Hydrates in Sediments: Their Role in Wellbore/Casing Integrity and CO_2 Sequestration

Manoochehr Salehabadi

Submitted for the degree of Doctor of Philosophy

Heriot-Watt University

Institute of Petroleum Engineering

Dec 2009

The copyright in this thesis is owned by the author. Any quotation from the thesis or use of any of the information contained in it must acknowledge this thesis as the source of the quotation or information.

ABSTRACT

Gas hydrates have attracted much interest among researchers recently because of their wide range of applications. The impact of natural gas hydrates in subsea sediments on the development of conventional hydrocarbon reservoirs in deep offshore and the potential role of CO_2 hydrates as a secondary safety factor in subsurface storage of CO_2 are the key areas in this thesis.

Several experiments were conducted on synthetic samples containing methane hydrate with different hydrate saturations to measure their geophysical properties, mechanical properties and understand their mechanical behaviour at realistic conditions. A numerical model was also developed with ABAQUS (a finite element package) to investigate the casing stability of the wellbore drilled in gas hydrate bearing sediments in deep offshore environments using the measured properties of gas hydrate bearing sediments under different scenarios.

The role of hydrates in subsurface storage of CO_2 was studied using a unique experimental set-up by simulating geothermal temperature gradient. The objective was to investigate whether CO_2 leaked from subsurface storage sites can be converted into hydrates, providing a secondary seal against further CO_2 leakage to ocean/atmosphere.

DEDICATION

This thesis is dedicated to

My mother, brother and sisters

And to the memories of my father

For their love and support

ACKNOWLEDGEMENTS

The author would first like to express his heartfelt thanks to Professor Bahman Tohidi for giving me this opportunity to work on a very interesting topic, his guidance, support and most important encouragement throughout the course of this study. My research could not have been completed without the constant help, suggestions and fruitful discussions offered by Dr.Jinhai Yang during the whole process of experimental investigations. I thank Dr.Min Jin for his guidance, suggestions and discussions during the whole process of numerical modeling. I would like to thank Dr.Antonin Chapoy for his valuable supports. I would like to express my gratitude to Dr.Ahmed Rehan for generously providing the license of ABAQUS for my study.

I thank Prof.John Rees and Dr.Ingo Pecher for spending their valuable time in reading this thesis and examination. Thanks are also due to my colleagues within the Institute of Petroleum Engineering, who have always attempted to answer my questions politely and sympathetically. More specific thanks are due to my colleagues within gas hydrate group. I had tremendous support from them. I would like to thank Brigitte McGregor, Pilvi-Helina Kivela and Alice Thompson for their valuable supports.

Thanks also go to the EPSRC (Engineering and Physical Sciences Research Council) and sponsors of the Wellbore Integrity in Gas Hydrate Bearing Sediments JIP (Joint Industry Project) for their financial support. None of this research would have been carried out without the financial assistance.

Last but not least, my deep love and appreciation goes to my mother, brother and sisters in Iran with whom I shared my childhood and whose love and support still sustain me today.

TABLE OF CONTENTS

LISTS OF TABLES

LISTS OF FIGURES

Chapter 1 – Introduction and Literature Review

1.1 Introduction

Gas hydrates have attracted much interest among researchers recently because of their wide range of applications. Many research projects are underway all over the world to study gas hydrates in natural and manmade environments with regard to their applications ranging from flow assurance, geohazards, source of energy, global warming and other petroleum engineering applications. The impacts of natural gas hydrates on the development of conventional hydrocarbon reservoirs in deep offshore environments and their applications in CO_2 sequestration are the key areas in this study.

The main object of this study is to investigate the role of gas hydrates sediments in wellbore integrity (i.e., casing stability) and CO_2 sequestration. The wellbore integrity is a general term including casing stability. In this study we focus on the casing stability analysis of a wellbore drilled in gas hydrate bearing sediments during drilling the next section of the wellbore (i.e., for a period of 8 days). The casing stability analysis is carried out using a numerical model. In order to provide reliable input data for the numerical model several experiments divided into two series were conducted. The results of the experiments were fed into the numerical model to analyse the casing stability of a wellbore drilled in gas hydrate bearing sediments. In order to examine the effects of GHSZ (Gas Hydrate Stability Zone) on the leakage of stored CO_2 in a geological structure beneath the GHSZ in deep offshore environments to seafloor, several experiments were conducted using a unique experimental apparatus simulating conditions in deep offshore environments.

The objective of this chapter is to provide some background information on gas hydrates, favourable conditions for gas hydrate formation, properties, their effects on the climate change and the development of hydrocarbon reservoirs in deep offshore environments. This chapter explains the various aspects of natural gas hydrates in relation to their definition, appearance in deep offshore environments, measurement of their properties, and the development of conventional hydrocarbon reservoirs in deep offshore environments and CO_2 sequestration.

1.1.1 Gas hydrates

Clathrate hydrates attracted much interest when Hammerschidt discovered a gas pipe line blocked by the formation of clathrate hydrate in 1934. Clathrate hydrates are crystalline compounds formed from the mixture of water and guest molecules with low molecular weight. The water molecules form a cage like structure encapsulating the guest molecules within its cavities. The water molecules are bonded together with hydrogen bonds but there is not any bonding between water molecules and guest molecules, as instead the water molecules interact with guest molecules through van der waals forces [1.1]. Clathrate hydrates can form three different crystalline structures, structure I, structure II and structure H. Structure I and structure II are the most commom and structure H is the least common type of hydrate crystal structures [1.1]. Structure H can form at high pressures and only in the laboratory. Structure I is made of two types of cages including dodecahedron and tetrakaidecahedron as shown in Figure 1.1. The size of dodecahedral cages are smaller than tetrakaidecahedral cages and therefore they are referred to as small cages and tetrakaidecahedral cages are referred to as large cages.

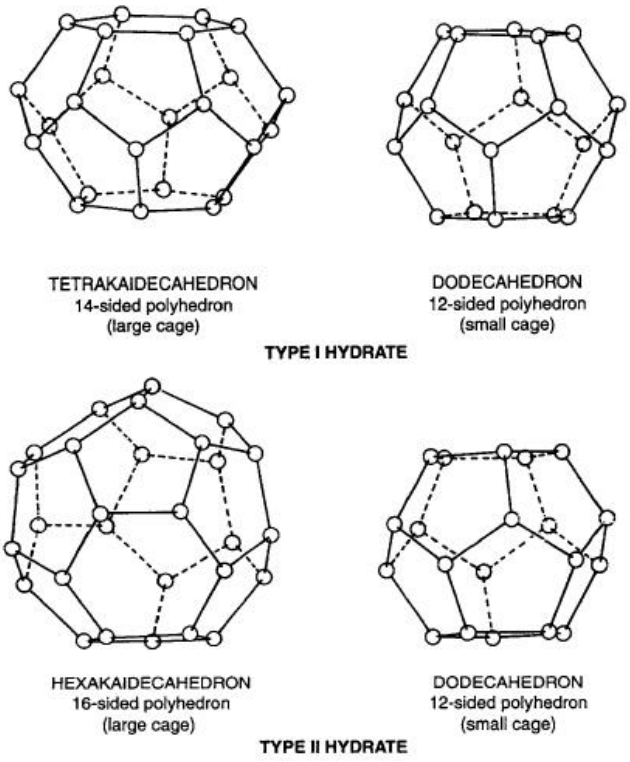

Figure 1.1 Schematic of cages in type I and type II hydrates [1.1]

The most common structure I hydrate formers are methane (CH_4), carbon dioxide (CO_2), hydrogen sulphide and ethane. CO_2 and CH_4 as guest molecules can occupy both the small and large cages in sI. Structure II is also made of two types of cages including dodecahedron and hexakaidecahedron. as shown in Figure 1.1 The size of dodecahedral cages are smaller than hexakaidecahedral cages therefore they are referred to as small cages and hexakaidecahedral cages are referred to as large cages in this structure. The most common structure II hydrate formers are nitrogen, propane and isobutene. Clathrate hydrates can be made of the components of natural gas including methane, carbon dioxide etc. These components are in a gaseous phase in ambient conditions therefore the clathrate hydrates of these components are normally referred to as gas hydrates. Methane hydrate can occupy either of the cavities in structure I and II due to the size of its molecule. Structure I is preferred because the methane molecules make structure I more stable and also structure I is more stable when its large cavities are occupied by methane molecules. Methane and carbon dioxide form structure I, and methane hydrate is the most common type of gas hydrate found in the nature. The ratio of the number of water molecules to the number of guest molecules is called hydration number; the hydration number for methane gas hydrate is 5.73-6.

From the thermodynamic perspective, temperature and pressure are the two main factors governing the formation or dissociation of gas hydrates. The phase boundary is a curve bounding the range of temperature and pressure in which gas hydrate forms and dissociates, as shown in Figure 1.2.

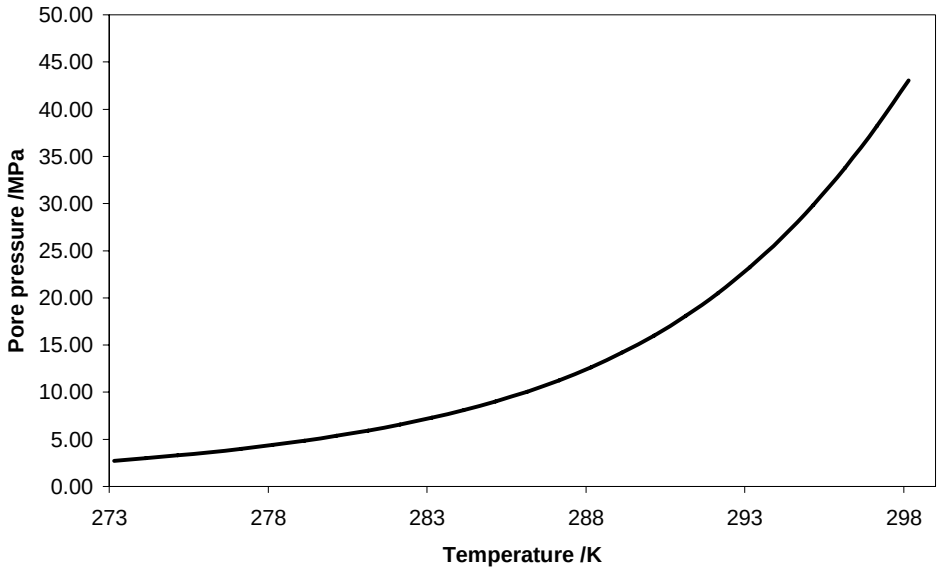

Figure 1.2 The phase boundary of methane hydrate

To the left of the phase boundary, the gas hydrate is stable and coexists with methane and/or water but to the right of the phase boundary gas hydrate is not stable and will dissociate to its original ingredients. The shape/position of the phase boundary depends on the composition of aqueous and non aqueous phases. For example the phase boundary of CO_2 is different from methane hydrate as shown in Figure 1.3.

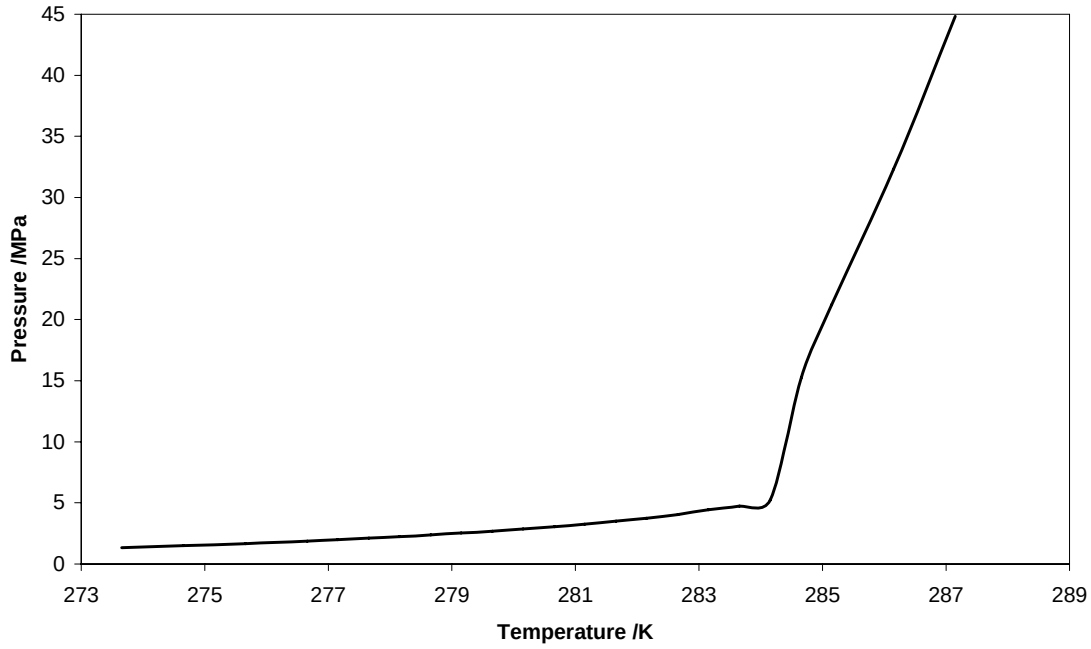

Figure 1.3 The phase boundary of CO_2 hydrate

1.1.2 Natural gas hydrates

Gas hydrates can also be found inside formations in deep offshore environments where the gas hydrate stability zone exists. The gas hydrate stability zone refers to a region in deep offshore environments where thermodynamic conditions are favourable for gas hydrate formation. The gas hydrate stability zone typically extends downward from the seafloor to a horizon called the base of gas hydrate stability zone. The base of the hydrate stability zone and the size of the gas hydrate stability zone is determined by overlapping the thermal gradient of sea water, the geothermal temperature gradient and the gas hydrate phase boundary, converted to depth, assuming the hydrostatic condition [1.1] as shown in Figure 1.4.

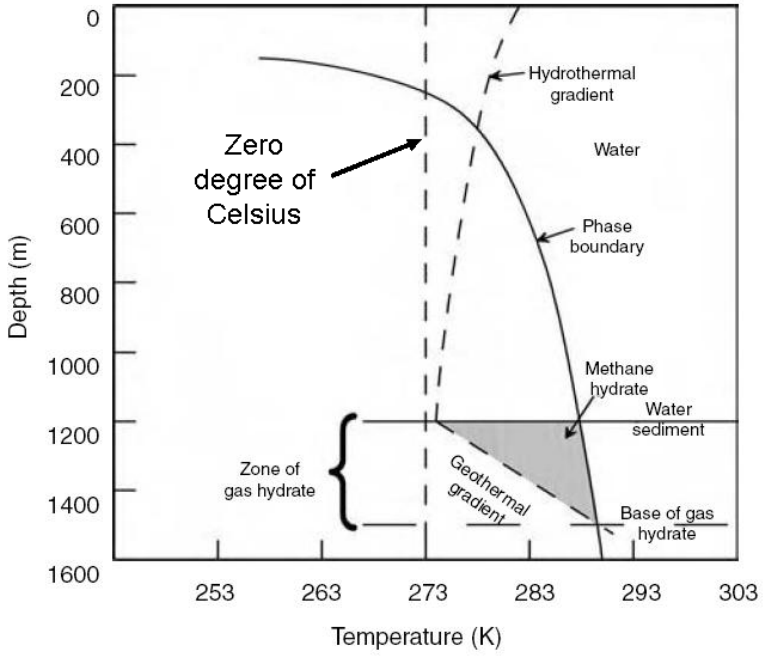

Figure 1.4 The phase boundary of gas hydrate in offshore environments [1.1]

The temperature in the water and the seafloor formations increases according to the thermal gradient of water and the geothermal temperature gradient, and therefore, set a lower boundary for gas hydrate stability zone and indeed limit the thickness of the gas hydrate stability zone. The upper boundary of the hydrate stability zone is set by the phase boundary converted to depth. In Figure 1.4 the gas hydrate is stable in the region between three lines including gas hydrate phase boundary, sea water hydrothermal gradient and geothermal temperature gradient. Normally, natural gas hydrates are

found in sediments within a few hundred meters of the seafloor, in water depths of around 500 m, depending on seabed temperature, gas composition, and geothermal temperature gradient. Figure 1.5 shows the wide geographical spread of natural gas hydrate reservoirs in the world.

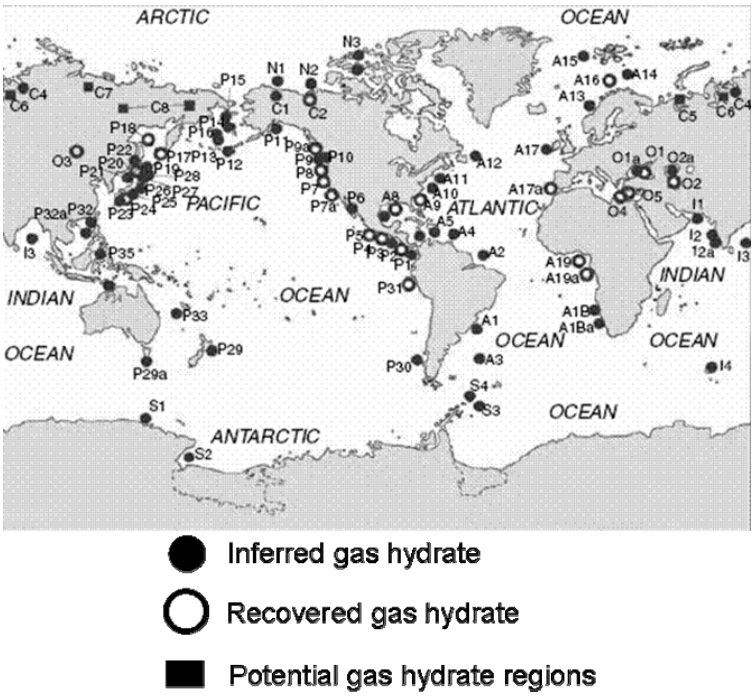

Figure 1.5 The global distribution of natural gas hydrates [1.1]

However, there are uncertainties in the evaluation of these reservoirs but even with very conservative estimata the volume of methane gas trapped in these reservoirs is 10 E15 m^3 [1.1], [1.2].

Source of methane

The methane gas required for gas hydrate formation in nature is either Biogenic or Thermogenic. Biogenic methane gas is generated by the microbial breakdown of organic matter in place within shallow seafloor formations. Thermogenic methane gas is generated by the breakdown of organic matter at greater depths and under high temperature. The generated methane gas migrates upward to the gas hydrate stability zone and forms gas hydrate. It has been, however, reported that the source of methane gas is both Biogenic and Thermogenic in some places like the Gulf of Mexico[1.3].

Bottom simulating reflector

Hydrate formations can be imaged using surface seismic data through the presence of BSR (Bottom Simulating Reflector). The BSR is a negative reflection from the phase contrast between free gas or water below the base of the hydrate stability zone and solid hydrates within the hydrate stability zone above. The BSR is therefore not structural reflectors but occurs at the phase transition of methane hydrates to free gas or water. One of the characteristics of the BSR is that it approximately follows the topography of the seafloor and cuts through the stratigraphy as shown in Figure 1.6

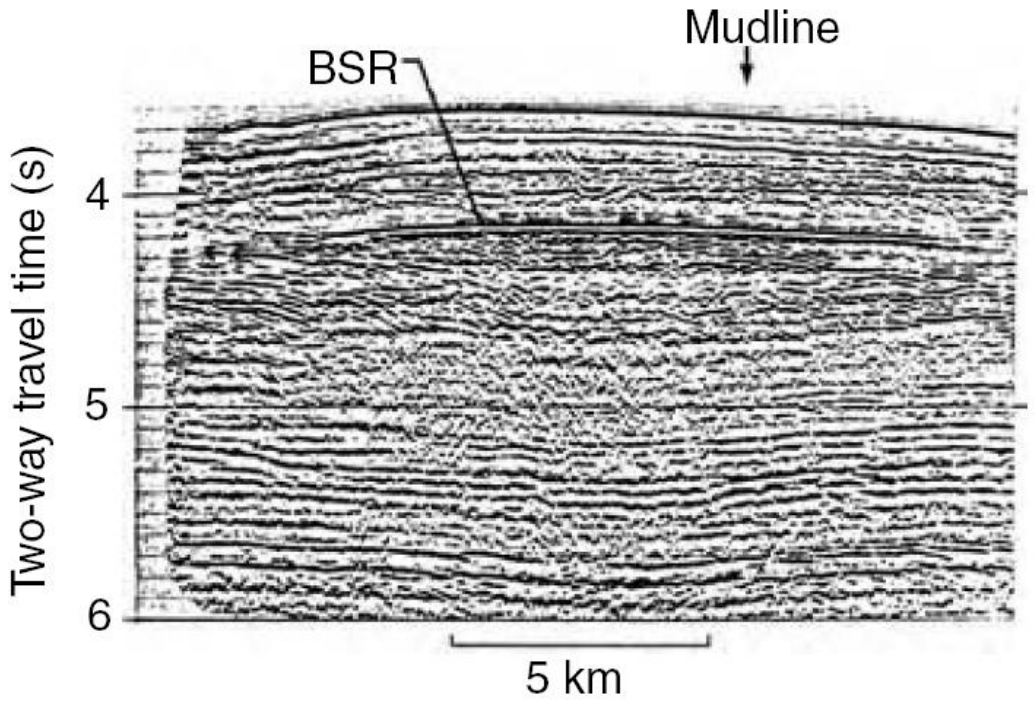

Figure 1.6 Bottom Simulating Reflector (BSR) [1.1]

Two models have been proposed for methane hydrate formation and BSR development. The first model considers that BSR is caused by methane hydrate overlying gas saturated sediments. The second model considers that BSR is caused by methane hydrate overlying water saturated sediments [1.4].

The first model assumes that the source of methane gas is local. Sedimentation leads to gradual thickening of the sediment column and causes hydrate-bearing sediments to subside out of the gas hydrate stability field leading to dissociation of hydrates to free

gas result free gas can be present there [1.5]. The second model assumes that the source of methane is methane removal from pore water saturated with methane and most of the methane gas was generated below the gas hydrate stability zone [1.6]. Therefore, free gas does not necessarily have to be present in this model.

The presence of bottom simulating reflector (BSR) has been considered for years as evidence of the occurrence of gas hydrate in deep offshore environments, although, it has been reported that the occurrence of gas hydrates does not require the presence of BSR [1.7]. It was suggested that the occurrence of gas hydrates without BSR could for example be explained with the presence of faults or fractures. Faults and fractures work like channels supplying methane gas from below to the gas hydrate stability zone. This process may lead to hydrate formation in small patches in the vicinity of the faults, too small to form continuous BSRs, [1.8].

Hydrate formation in the sediments

Natural gas hydrates occur in four main morphological types including disseminated, nodular, layered and massive [1.1] as shown in Figure 1.7 [1.1]. Small inclusions of gas hydrate are scattered in sediments in the disseminated gas hydrate formations. The nodular gas hydrate formations contain large lumps of gas hydrates up to a few centimetres. In the layered gas hydrate formations, thin layers of sediments sandwich and separated the gas hydrate layers. The massive gas hydrate formations contain small quantities of sediments scarred in the thick layers of gas hydrates. Natural gas hydrates store large quantities of methane gas (around 172 vol/vol), and therefore the release of this quantity of methane gas during gas hydrate dissociation may increase the pore pressure of very low permeability hosted formation significantly.

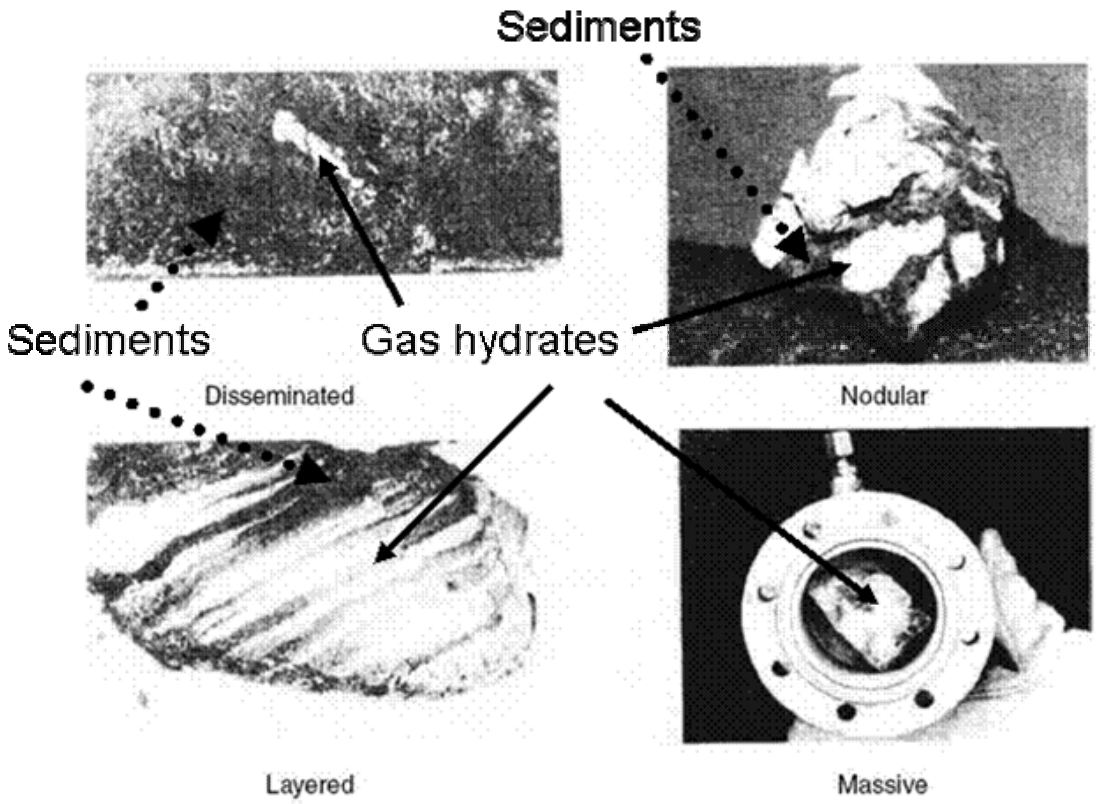

Figure 1.7 Four types of natural gas hydrates [1.1]

Hydrate growth models in pores of gas hydrate bearing sediments

The growth of hydrate within the pore space of host sediments has been a major controversial issue among researchers studying the geophysical and geomechanical properties of gas hydrate bearing sediments [1.9]. The hydrate growth in the pore space of the host formation has been described and classified in three models by Dvorkin, *et, al,* [1.10] as shown in Figure 1.8:

- Gas hydrate part of pore fluid model (i.e., pore filling)

  In this model, gas hydrate forms inside the pore space of the sediments. The elastic properties of sediments containing gas hydrates are the same as gas hydrate-free sediments.

- Gas hydrate part of the solid phase model (i.e., frame bearing)

  In this model, gas hydrate is part of the load bearing sediment structure. The elastic properties of sediments containing gas hydrates are higher than gas hydrate-free sediments.

- Gas hydrate as grain-contact cement and surface cement models

In this model, gas hydrate cements the sediment grains together. The elastic properties of sediments containing gas hydrates are significantly higher than gas hydrate-free sediments.

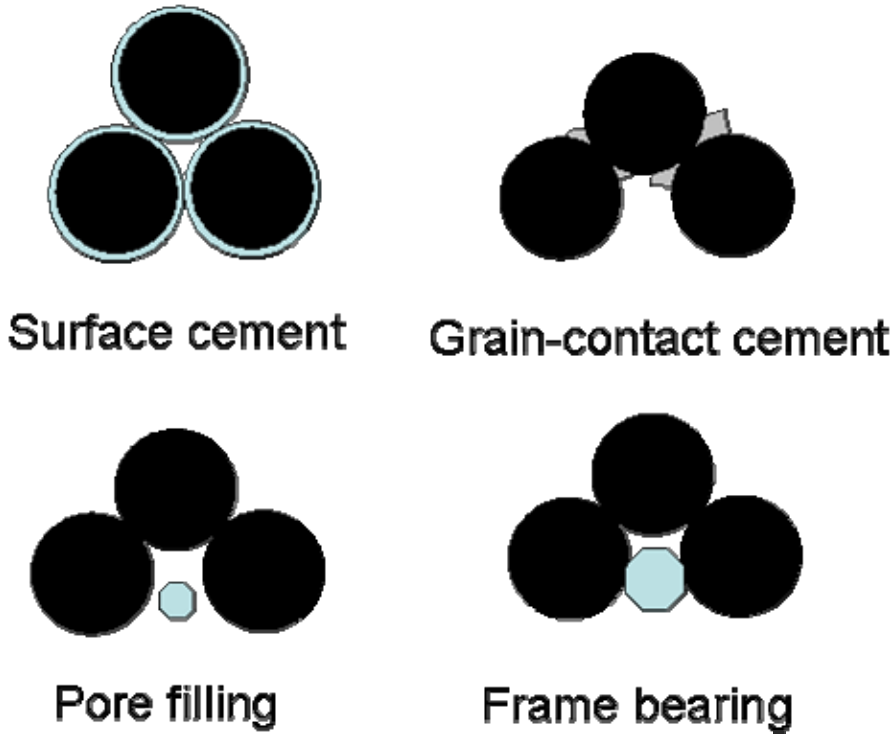

Figure 1.8 Schematic of hydrate growth in the pore space

The distribution of gas hydrates within the pore space of the host sediments (i.e., the above mentioned models) can have significant effects on the geomechanical and geophysical properties of the host sediments. For example, the contribution of the gas hydrates on the stiffness of the sediment (i.e., shear and bulk modulus) is much less in pore filling and frame bearing models than cementing models. In addition, the contribution of the gas hydrate on the stiffness of the sediment in frame bearing model is higher than the pore filling model.

Natural hydrates as a geohazard

There are many possible connections between natural gas hydrate dissociation and geohazards [1.11], [1.12], [1.13], [1.14], [1.15]. The impact of sea water level fluctuations on deep offshore environments are associated with a change of pressure in the seafloor sediments, resulting in the possible dissociation of natural gas hydrates. Wide spread gas hydrate dissociation releases a considerable amount of methane gas, a powerful greenhouse gas endangering the climate [1.16]. There has been reported

evidence that connects natural gas hydrate dissociation to submarine land slides on the Norwegian continental margin and seafloor slumps in west Africa [1.17]. These submarine land slides or seafloor slumps, caused by gas hydrate dissociation, can affect and damage petroleum facilities located in the region of failure. Natural gas hydrates may dissociate during the development of conventional hydrocarbon reservoirs, halting development operations or endangering the surface facilities installed on the seafloor [1.13], [1.18], [1.19], [1.20]. Hence, natural gas hydrates are geohazards of prime importance as the oil and gas industry move toward deep offshore environments.

Natural Gas hydrates and CO_2 sequestration

Climate change and global warming is a great concern for all countries. It is now widely accepted that the increase in CO_2 concentrations in the atmosphere is largely due to the combustion of fossil fuels, and is the main contributor to global climate change. Underground storage of CO_2 offers an interesting, and possibly environmentally safe, option for controlling the emission of greenhouse gases in the short to medium term. Natural gas hydrate reservoirs have attracted much interest over the years for underground CO_2 storage. Some researchers have studied the possibility of injection and sequestration of CO_2 in deep offshore environments to form CO_2 hydrate where favourable conditions for CO_2 hydrate exist [1.21], [1.22]. The injected CO_2 will convert into CO_2 hydrate and become trapped in the pore space within a formation, as an immobile phase. Based on the same principle, CO_2 sequestration in natural gas hydrate reservoirs and the production of methane gas has been investigated by some researchers [1.23], [1.24], [1.25], [1.26], [1.27]. The production of methane gas may well justify (pay for) the costs of the CO_2 capture and sequestration.

Principals of drilling operation including casing and cementing [1.28], [1.29]

The wellbore is created by drilling a hole with 36 inches diameter from the seafloor into the earth with a drilling rig which rotates a drill string with a bit attached in offshore environments. After the hole is drilled, sections of casing (steel pipe), slightly smaller in diameter than the hole, are placed in the hole. Cement is then circulated through the inside of the casing and out to the annulus between the casing and the hole. Cement fills the annulus between the hole and the casing. The casing provides structural integrity to the newly drilled hole in addition to isolating potentially dangerous high pressure zones from each other and from the surface. With these zones safely isolated

and formations protected by the casing, the hole can be drilled deeper with a smaller bit and also cased with a smaller casing.

1.2 Literature Review

Sections 1.2.1 to 1.2.3 present available information in the open literature. The results of this work are summarised in section 1.3 with detailed explanations in Chapters 2-6.

1.2.1 Review of wellbore integrity/casing stability in gas hydrate bearing sediments

The presence of gas hydrate in deep offshore environments has been considered as a source of geohazards [1.30], [1.11], [1.12], [1.14], [1.15]. Lane, et. al. [1.20] define offshore geohazards as "seafloor and substrate soil/rock conditions having the potential of developing into failure event causing loss of life or investments". They therefore classify gas hydrates as one of the geohazards encountered in deep water environments. Only defining the potential for geohazards is not a solution to the problems and it is necessary to both understand and evaluate geohazards correctly and thereafter design engineering programmes or other options to address those. Digby [1.31] concluded that the first step in dealing with a potential geohazard is to make a decision whether to avoid or mitigate it. As indications of gas hydrates are growing worldwide especially in deep offshore environments, so avoidance may not always be an available option. Williamson, et al. [1.18] reported that the degree of hazard of gas hydrate deposits depends on the thickness and lateral extent of these deposits as well as gas hydrate saturation inside pore spaces. Low gas hydrate saturation and disperse may result in a little amount of gas being released during gas hydrate dissociation. Likewise, high gas hydrate saturations may result in the release of large amounts of methane gas during gas hydrate dissociation posing a gas risk to activities in deep offshore environments. Sultan [1.32], studied the effect of gas hydrate dissociation and excess pore pressure generation during gas hydrate dissociation on seabed slope stability as one of the geohazards. He reported that excess pore pressures and gas hydrate dissociation under certain conditions could lead to catastrophic submarine landslides and slope failures.

The presence of gas hydrate is also one of the problems when developing conventional oil and gas fields in deepwater offshore. There have been reported documented cases of hole problems associated with drilling through gas hydrate bearing sediments in the arctic environments like stuck pipe, gas kicks, blowouts, subsidence, gas leaks outside the casing and poor cement jobs [1.33]. The reason for the low number of such cases

associated with gas hydrates reported in offshore environments may be related to the lack of identification of the presence of gas hydrate and the lack of knowledge of manifesting drilling induced gas hydrate dissociation in offshore drilling activities [1.33]. As mentioned above, the Bottom Simulator Reflector (BSR) is commonly accepted as a primary indication of gas hydrate in the offshore environments, suggesting an interface free gas zone and gas hydrate stability zone above [1.31]. Seismic surveys and drilling operations can not provide accurate data for gas hydrate deposits characterization. The first section of most deep offshore wellbores is drilled riser less so no cuttings are returned for examination. Logging data in this section is largely affected by hole washout and changes made in drilling mud, switching from seawater to weighted mud. These important issues must be taken into consideration to assess the drilling hazard potential of gas hydrate deposits [1.33].

The techniques commonly used to overcome drilling problems are reducing the drilling fluid temperature and/or increasing the hydrostatic mud pressure [1.34]. The potential casing failure of wellbores drilled in gas hydrate bearing sediments in deep offshore were flagged but still remain uncertain. The lack of a proper tool to predict the casing stability of wellbores drilled in gas hydrate bearing sediments, has largely resulted in a strategy of avoiding hydrate bearing sediments or drilling directional when locating deep offshore production platforms, as mentioned by A. J. Digby, to mitigate a hazard. These scenarios of course could increase the cost of development for deep offshore oil and gas fields. The potential for casing failure of wellbores drilled in gas hydrate bearing sediments could happen both during drilling of deeper sections of a wellbore and production of hot hydrocarbon after well completion.

Casing stability analysis is an important part of the well design, and therefore it is necessary to develop a tool to predict the casing behaviour for wellbores drilled in gas hydrate bearing sediments. Standard casing design considers the casing under uniform loadings coming from the formation without considering the interaction of casing-cement-formation on the required strength of casing [1.35]. There is indeed not a simple analytical method available to determine the magnitude of this effect. Berger, et al. [1.35] and Fleckenstein, et al. [1.36] developed a simple numerical model without considering the effects of the porous media and the presence of gas hydrate to study the effect of non-uniform loading on the casing stability.

Most modelling investigations conducted on gas hydrate bearing sediments so far, relate to methane gas production. Yousif, et al. [1.37] [1.38] studied the gas hydrate dissociation in Berea sandstone by depressurisation. They took into account the kinetics of gas hydrate dissociation using the Kim-Bishnoi kinetic model Kim, et al, [1.39]. Selim, et al, [1.40] developed an analytical model to simulate hydrate dissociation in porous media under thermal dissociation. The authors considered a moving interface in their model which separates dissociated and non-dissociated regions. They assumed that the dissociated region contains water and gas resulting from gas hydrate dissociation and the fact that water resulting from gas hydrate dissociation can not flow through porous media. Goel, et al, [1.41] presented a cylindrical model, representative of a gas hydrate reservoir, to simulate methane gas production from gas hydrate reservoirs using a depressurisation technique of coupling hydrate kinetic equation into radial diffusivity equations. Their model considered an interface which moves by hydrate dissociation and they only considered gas flow resulting from gas hydrate dissociation. Komai, et al, [1.42], disputed Kim`s kinetic equation as it can not be used for porous media. They conducted some experiments to modify this equation and as a result it can be used in numerical modelling of gas hydrate dissociation in the porous media. A small scale cell filled with sand saturated in water was used for the experiments, along with a microscope and Raman spectroscopic apparatus for observations. Distilled water was first injected into the cell and the cell pressure was increased to the desired value followed by the introduction of methane gas into the cell. Thereafter the cell was cooled down to form gas hydrate. They modified Kim`s equation based on the results of their experiments. Debendra, et al, [1.43], developed a model to simulate gas production from gas hydrate reservoirs in permafrost regions by thermal stimulation with the finite element method. They considered hydrate latent heat effect in their calculations and assumed heat transfer by conduction only. Gas flux was calculated in their model using the dissociation front at any point in time without considering any hydrate kinetic equation. Sun, et al, [1.44], developed a 3D simulator to model hydrate formation and dissociation in porous media, mainly based on the Kim`s kinetic equation. The simulator takes into consideration four components and five phases but is restricted to hydrate structure one. Moridis, et al, [1.45] developed a reservoir simulator considering multi-component, multiphase fluid and heat flow in the porous media. It can model the non-isothermal gas release, phase behaviour, heat and fluids flow in complex formations and it takes into account

calculations of up to four phases and nine components including salt and hydrate inhibitors. It considers gas hydrate dissociation, using both the equilibrium and kinetics reaction, and it can also model the effects of phase changes and the corresponding thermal effects. Gas hydrate dissociation can be obtained by all dissociation mechanisms including depressurisation and thermal stimulation. Ahmadi, et al, [1.46] modelled gas production from gas hydrate reservoirs using an axisymmetric model. Gerami, et al, [1.47] developed an analytical model to predict methane gas production from gas hydrate reservoirs by depressurisation without considering a sharp interface in the calculations. They reported that a sharp interface which divides the porous media into the hydrate and non-hydrate zones underestimates the gas generation from the gas hydrate reservoirs. The model considers the kinetics of gas hydrate dissociation using Kim` equation [1.48]. Nazirdoust, et al, [1.49] developed a finite element model to simulate methane gas production from sandstone core containing gas hydrate. The model considers three phases including gas hydrate as a solid phase, and gas and water as fluid phases. It also takes into consideration the effect of phase changes and their effects on the thermal analysis. The kinetics of hydrate dissociation is modelled using Kim`s model. The results of the model were positively compared with data resulting from a real sandstone core containing gas hydrate. Ji, et al, [1.50] studied the parameters affecting the rate of methane gas production from gas hydrate reservoirs. They conducted their studies using a one dimensional model considering a sharp interface dividing the hydrate and non-hydrate zones. In particular, they studied the effect of formation porosity and permeability on the rate of methane gas production, temperature and pressure distribution. The above modelling investigations as mentioned before are mainly focused on the production of methane from gas hydrate reservoirs and they consider gas hydrate bearing sediments as a rigid body in their calculations. It means that they have assumed that gas hydrate is found in such formations that these do not deform [1.51]. Recently potential wellbore failures during drilling through gas hydrate bearing sediments were studied. Yamamoto, et al, [1.52], based on the drilling campaign carried out from 1999 to 2000 in Nankai Trough, reported that the wellbore stability is an issue for drilling through unconsolidated formations containing no hydrate. They concluded that wellbore stability is even more critical during drilling in gas hydrate bearing sediments. Birchwood, et al, [1.53] developed a semi-analytical wellbore stability model to calculate the stress and strain caused during drilling in gas hydrate bearing sediments. They also conducted a thermal

analysis to determine temperature distributions and investigate the conditions under which gas hydrate will dissociate during drilling through gas hydrate bearing sediments. The thermal analysis was not coupled to the wellbore stability model. The formation mechanical behaviour was assumed to follow the Mohr-Coulomb criteria. The mechanical properties of sediments containing THF (TetraHydroFuran) hydrate were used by them in the calculations. Klar, et al, [1.54] developed a geomechanical model in FLAC code to study the wellbore stability during methane gas production from gas hydrate reservoirs by isothermal depressurisation. FLAC (Fast Lagrangian Analysis of Continua) is an explicit finite difference program for engineering mechanics computation. This program simulates the behaviour of structures built of soil, rock or other materials. Two-phase flow (water and gas) equations, assuming gas hydrate as a non-flowing phase, were used to model the two phase flow of liquid and gas during gas hydrate dissociation. The Kim-Bishnoi kinetic reaction equation is used to model gas hydrate dissociation during depressurisation. They did not nevertheless consider heat transfer in their model. The mechanical property of the formation was assumed to follow the Mohr-Coulomb type cohesion dependent on hydrate saturation. Rutqvist, et al, [1.55] coupled the numerical simulator of hydrate reservoir, developed by Moridis [1.45], with FLAC as a commercial geomechanical code to develop a numerical code considering the three essential terms (i.e., hydraulic, mechanical and thermal) for analysing the reservoir geomechanics of gas hydrate bearing sediments under mechanical and thermal stresses. They studied three different cases using the developed model. The first case involves gas hydrate dissociation due to production from deeper conventional hydrocarbon reservoirs. The second and third cases involved geomechanical effects during methane gas production from hydrate reservoirs and loading due to the weight of structures placed on the sea floor overlying gas hydrate bearing sediments. The developed model refers to the wellbore assembly as a rigid and fixed boundary condition. Kimoto, et al, [1.56] developed a chemo-thermo-mechanical finite element model to study the reservoir geomechanical effects of hydrate dissociation during thermal stimulation or depressurisation. In their model, Darcy's law is used to simulate gas and water (generated during hydrate dissociation) flow in porous media using relative permeability. An elasto-viscoplastic constitutive model adapted for modelling soil behaviour and considering the effect of hydrate, the Kim-Bishnoi kinetic reaction equation is used to model gas hydrate dissociation. The model was applied to study the geomechanical effects of one dimensional simple model containing

gas hydrates during dissociation by depressurisation and thermal stimulation with only few elements. Ng, et al, [1.57] continued developing Klar`s model [1.54]. They added the effect of heterogeneity of hosted formations and endothermic hydrate dissociation on the gas hydrate production from the hydrate bearing sediments by depressurisation. In spite of Klar`s model [1.54], in this work casing and cement were considered in the calculations. It was assumed that the cement has very good contact with the casing and formation without considering any contact element. The effect of sediment deformation/pore pressure on temperature distribution is assumed to be negligible. In other words, the coupling between hydraulic-mechanic and thermal models is one way or loose coupling in their study. They used the typical lithology found in the Nankai Trough region in their studies. They reported that the effect of heat transfer from the clay layer to sand layer has significant effects on the stress distribution and rate of hydrate dissociation. It is reported that the rate of hydrate dissociation is faster at the boundary between clay and sand layers than the middle of sand layer containing hydrate, and that this effect is more significant when the thickness of the layers are low. Rutqvist, et al, [1.58] used their previous coupled codes (Rutqvist, et al, [1.55]) to study the geomechanical response and gas production from gas hydrate reservoirs in permafrost region using horizontal wells. The wellbore assemblies were assumed rigid and the methane gas was produced by depressurisation. Freij-Ayoub, et al, [1.59] developed a model in FLAC finite difference code to study the stability of wellbore drilled in gas hydrate bearing sediments. The model assumes that the mechanical behaviour of sediments follow the Mohr-Coulomb constitutive model, with decreasing cohesion, corresponded to hydrate saturation decreasing in the pore space during dissociation. Hydrate dissociation is modelled using Boyle`s law with a very simplified method. Fluids, generated during hydrate dissociation, is considered as a single phase with Darcy law for fluid flow in the porous media.

Most of the developed geomechanical models in gas hydrate bearing sediments are mainly focused on open hole wellbore (i.e., wellbore without casing) stability analysis or cased hole wellbore (i.e. wellbore containing casing) stability analysis during the production of methane from gas hydrate reservoirs by depressurization. Recently, the casing stability analysis of wellbores drilled in gas hydrate bearing sediments during the drilling of deeper sections of the wellbore or production of hot hydrocarbon in deep offshore environments has attracted the interest of some researchers. Freij-Ayoub, et

al, [1.60] developed their initial model, by adding the casing elements to study the casing stability of wellbores drilled in gas hydrate bearing sediments during gas hydrate dissociation. However, the model does not consider non-uniform casing loading during gas hydrate dissociation.

1.2.2 Review of the mechanical properties of gas hydrate bearing sediments

Despite great interest in gas hydrate bearing sediments, their properties especially mechanical properties, are still fairly unknown [1.61], [1.62]. Taking real samples and conducting mechanical properties measurements in the laboratory, generally result in disturbance in the in-situ sample conditions even using new pressure coring techniques. To overcome the above problems, some scientists have suggested/used ice-bearing sediments in their measurements [1.63]. However, despite apparent similarities, the mechanical properties of ice and gas hydrates are very different [1.63]. It has been reported that gas hydrate shows different mechanical behaviour than ice [1.64] and therefore, the mechanical properties results from tests conducted with ice bearing sediments cannot be representative of samples containing gas hydrates.

The other important parameter is in-situ stresses and pore pressures. Clearly, studying the mechanical properties of synthetic gas hydrate bearing sediments formed in conditions close to in-situ gas hydrate bearing sediments remain the most reliable approach [1.61]. However, most researchers have conducted their investigations for measuring mechanical properties of gas hydrate bearing sediments under low in-situ stresses and pore pressure. These conditions are not representative of the real conditions in hydrate bearing sediments. Furthermore some researchers have used THF (Tetra-Hydro-Furan) as hydrate forming compound instead of hydrocarbon gases.

Nakagawa, et al, [1.65] conducted triaxial experiments on synthetic core samples made of sand and glass beads without gas hydrates and artificially cemented using sodium silicate. It has been reported that by increasing the cement content the mechanical behaviour of specimens is similar to the competent rocks. They mentioned that the fundamental difference between competent rock and loose sand (soil) is the Cohesion. Loose sands do not have significant cohesion therefore they undergo high deformation because of inter-granular slippage and rotation of the grains. The cohesion allows macroscopic transmission of tensile stress in granular materials leading to the formation of tensile fractures. They found a linear relationship between unconfined compression

strength and fracture toughness for specimens content below 0.5 % cementation. Edinima, et al, [1.66] conducted triaxial experiments on artificially made core samples containing gas hydrate with 9 MPa pore pressure and 10 MPa confining pressure. It was found from the experiments that core samples which contain gas hydrate show an increase in the maximum failure stress Yun, et al, [1.61] conducted comprehensive studies on the mechanical and geophysical properties of sediments containing THF (Tetra-Hydro-Furan) and under very low stress conditions. Formation of synthetic hydrate inside the sediments is the main challenge for conducting laboratory measurements on gas hydrate bearing sediments. As a result, Yun, et al, [1.61] used THF hydrate in their experiments as conducting experiment with THF hydrate is relatively straightforward and easy in comparison with gas hydrate. They conducted several experiments on different synthetic samples formed from sand, crushed silt, precipitated silt, kaolinite and THF hydrate with 0, 50 and 100 % hydrate saturation. This wide range of mineralogy represents the different lithologies found in the natural hydrate bearing systems. They found that at low hydrate concentrations (less than 40 % of pore space) the mechanical and geophysical properties of hydrate bearing sediments is controlled mainly by the soil structure. It was shown that hydrates increase the stiffness of the specimens when the hydrate concentration is more than 40 % of pore space. Therefore, at hydrate saturations higher than 40% hydrates have a great impact on the mechanical and geophysical properties of hydrate bearing sediments. Hato, et al, [1.67] conducted testes on real core samples taken from Nankai Trough in Japan to characterize their mechanical properties. One sample was with hydrate and another sample without hydrate (i.e., conducted after hydrate dissociation) under 1-3 MPa effective stress conditions. The authors did not mention the magnitude of confining pressure and pore pressure. They found that the strength of the sample containing gas hydrate at high saturation is 4 times higher than the dissociated one. The results were confirmed by comparing the calculated strength using well logging and calliper data from intervals containing gas hydrates and intervals without gas hydrates. Although, they conducted a couple of experiments with natural core samples, no information on the mineralogy of samples and the effect of the mineralogy of samples on the mechanical and geophysical properties of gas hydrate bearing sediments was reported.

Masui, et al, [1.68] conducted triaxial experiments on natural core samples without reporting the measurement of the geophysical properties. The authors found that gas

hydrate dissociation may reduce the mechanical strength of sediments containing gas hydrates. They conducted their tests at 10 MPa confining pressure and 9 MPa pore pressure. The trend of the Young modulus increase, due to an increase in hydrate saturation in natural core samples was similar to the previous experiments with synthetic core samples, although the deformations resulting from triaxial experiments on natural core samples were not similar to synthetic core samples. This phenomenon was related to the difference in the bounding structure of the sediments. Poisson's ratio is defined as the ratio of radial strain to axial strain [1.68]. The Poisson's ratio trend generated from conducting experiments on natural core samples versus gas hydrate saturation was also similar to synthetic core samples. Suzuki, et al, [1.69] conducted shear tests on natural core samples taken from the Nankai Trough in Japan. Their experiments were conducted under 1-3 MPa effective stress without mentioning the magnitude of confining stress and pore pressure. They also did not report the possible measurement of geophysical properties on the core samples and concluded that the stress-strain behaviour at low stress conditions was related to the gas hydrate carrying load and the increasing stiffness of the samples. Masui, et al, [1.62] conducted shear tests on both artificially formed gas hydrate core samples and natural gas hydrate core samples taken from the field. They made core samples by mixing Toyoura silica sand, and finer grains than Toyoura sand, to mimic the grain size distribution of gas hydrate bearing sediments. Gas hydrates were formed at the desired saturation by injecting methane gas into artificially made core samples and cooling them down to the appropriate temperature. The initial conditions of core samples before shearing were 8 MPa pore pressure, 278 K temperature and 9 MPa confining pressure. They observed that the strength of core samples with gas hydrate saturation ranging from 0 to 23 % did not change significantly and that the Young modulus of core samples containing gas hydrates increases in proportion to gas hydrate saturation. In general the Young modulus measurements of synthetic core samples were higher than natural core samples containing gas hydrates. They also reported that the Poisson`s ratio is not dependent on gas hydrate saturation and this is true for both synthetic and natural core samples containing gas hydrate.

The mechanical properties of gas hydrate bearing sediments have significant effects on the drilling and production activities from them as well as hydrocarbon reservoirs

underneath gas hydrate bearing sediments [1.62], [1.68], [1.64]. Two important scenarios are:

1. Drilling and production from conventional reservoirs below hydrate bearing sediments

2. Gas production from hydrates in sediments.

In both cases, gas hydrate dissociation, results in changes in the mechanical properties of hydrate bearing sediments. Therefore, it is essential to conduct comprehensive studies to quantify the properties of sediments containing gas hydrates especially mechanical properties. However, limited studies have been conducted/reported on the geomechanical behaviour and properties of gas hydrate bearing sediments, partly due to limited interest. As mentioned before, most experiments conducted on cores containing gas hydrate were under low stress and pressure.

1.2.3 Review of the self-sealing potential of CO_2 in gas hydrate bearing sediments

It is believed that in the short to medium term, fossil fuels will remain as the principal source of the World's energy and furthermore, the initial routes to a hydrogen economy will also require fossil fuels. In addition to increasing the efficiency of existing fossil fuel plants, carbon capture and storage is likely to be essential to reduce the effect of CO_2 emission on the climate. There are several options in storing CO_2 in geological structures. These include CO_2 injection into depleted oil/gas reservoirs, CO_2 use in EOR processes, coal-bed disposal, aquifer disposal and subsea sequestration in the form of gas hydrates.

Underground CO_2 storage offers interesting and environmentally safe possibilities. However, the main issue in underground CO_2 storage is the safety of long term sealing of stored CO_2. The choice of suitable reservoirs or geological formations is therefore critical to ensure storage integrity and safety with respect to gas leaks into the atmosphere or ocean [1.70].

Thermodynamic calculations show that CO_2 hydrates are stable at relatively low pressures (low water depths) at typical seabed temperature. Theoretically, hydrate formation in sediments could clog pore space and decrease sediment permeability. As a result underground structures (offshore) below sediments that have suitable pressure

and temperature conditions for CO_2 hydrate formation, could be regarded as the best candidates for underground storage of CO_2. If any CO_2 leakage happens during long term storage through the cap rock, theoretically the CO_2 would move upward through pore channels into the GHSZ (Gas Hydrate Stability Zone) and form solid CO_2 hydrates. The solid CO_2 hydrates would be immobile and could block the supply of CO_2 from below by pore clogging. The sedimentary formation containing the CO_2 hydrate may further hinder CO_2 leaking into the ocean [1.71] [1.72] [1.73] [1.74]. Numerous studies on the potential for storage of CO_2 in natural gas hydrate reservoirs and producing methane gas were reported by Chatti, et al, [1.23], Yang, et al, [1.24], Park, et al, [1.25], House, et al, [1.26], Kvamme, et al, [1.27].

The self-sealing potential of CO_2, in the form of CO_2 hydrate, in geological structures beneath the GHSZ and its benefits has been flagged by some researchers [1.75], [1.76] but actually, so far, no experimental apparatus or numerical model have been developed to investigate this phenomenon. Seol, et al, [1.75] simulated the relative permeability of sandstone cores containing gas hydrates by experimental and numerical modelling using TOUGH (Transport of Unsaturated Groundwater and Heat) code. TOUGH is a numerical code developed primarily at LBNL (Lawrence Berkeley National Laboratory) for studying flow and transport processes in porous media. The measurements and simulation again showed permeability reduction by hydrate formation in sandstone samples. Evernos, et al, [1.76] formed hydrate in sandstone cores by flowing natural gas and water through cores and measured the permeability of core samples containing gas hydrates. Based on the reduction in the permeability of core samples due to the formation of gas hydrates, they proposed to apply this phenomenon as a technique for CO_2 sequestration. If any CO2 leaked and migrated into the formations hosting favourable conditions for gas hydrate formation, the leaked CO_2 would be converted into CO_2 hydrate reducing the permeability of the hosted formation. Koide, et al, [1.74], [1.73] proposed this idea that if CO_2 is stored in permafrost region or cool submarine sediments, theoretically there is a possibility of forming secondary artificial cap rock due to CO_2 hydrate formation preventing further leakage of CO_2 into the atmosphere or ocean. Recently Kvamme, et al, [1.27] studied the replacement of methane gas in natural gas hydrate with CO_2 in Bentheim sandstone. MRI (Magnetic Resonance Imaging) technique was used in their experiments to visualise the conversion of gas hydrate to CO_2 hydrate. It was shown that their

experimental observations were consistent with the results of the numerical modelling using phase field theory. They concluded and reported that the hydrate and mineral matrix surfaces were separated by liquid-containing channels. These channels represented escape routes reducing the performance of hydrate sealing effects.

1.3 Summary and the organization of the thesis

Although there is much interest in gas hydrate bearing sediments, the available data related to properties is are still very limited. Most of the experiments conducted to quantify the properties of gas hydrate bearing sediments were either with THF (not normal constituents of in-situ gas hydrate) or at conditions far away from the realistic geomechanical conditions found in deep offshore environments. Although, some experiments were conducted on the natural core samples recovered from the Nankai Troguh region located in Japan, most of them were either conducted under unrealistic conditions or their conditions were not reported in the published literatures.

In this work, in order to provide data on the properties of gas hydrate bearing sediments, several experiments were conducted under realistic conditions on synthetic samples with varying mineralogy in the presence and absence of gas hydrates. Chapters 2 and 3 describe the mechanical and geophysical properties results from these experiments. The experimental apparatus used for quantifying the mechanical and geophysical properties of gas hydrate bearing sediments are described in Chapters 2 and 3 as these were based on a rigid body cell, which means that the confining stress was not under control during the experiments, An advanced Triaxial setup designed for gas hydrate bearing sediments was purchased. Chapter 3 also describes the results of a triaxial experiment conducted on sand without gas hydrate, to quantify the mechanical properties including the plastic properties of the sand used as host sediment for experiments described in Chapters 2 and 3.

The presence of natural gas hydrates, as potential geohazards, especially for the development of conventional hydrocarbon reservoirs in deep offshore environments have been discussed. Casing stability is an important issue in well design. Chapters 4 and 5 of this thesis describe the details of a finite element model developed for studying casing stability during drilling through gas hydrate bearing sediments under both uniform and non uniform loading. Numerical models were developed to take into account wellbore stability and casing stability in gas hydrate bearing sediments

particularly during the production of methane gas from gas hydrate bearing sediments. Furthermore, a model has been developed to address casing stability during drilling in gas hydrate bearing sediments under uniform casing loading.

CO_2 is the main source of greenhouse gas emissions and has an important impact on the climate change. Underground storage of CO_2 is described as one the interesting methods for CO_2 sequestration in the long term. The main issue in underground storage of CO_2 is the potential for CO_2 leakage over the long period of time. One option is to store CO_2 in a geological formation, beneath an interval hosting hydrate formation condition, in deep offshore environments. Theoretically, if any CO_2 leaked it would migrate upward into the interval with suitable conditions for hydrate formation. If CO_2 hydrates are formed, the leaked CO_2 hydrate becomes immobile and trapped in the pore spaces of the formation. The CO_2 hydrate, over time, will form a secondary cap preventing further leakage of CO_2. Chapter 6 describes the details of an experimental apparatus, and the experiments conducted, to examine the storage of CO_2 in a geological formation beneath an interval hosting hydrate formation conditions in deep offshore environments. Chapter 7 summarises the outcome of this thesis along with recommendations for further studies.

1.4 References

1.1 E. D. Sloan, *Clathrate hydrates of natural gases*, Marcel Dekker 641, 1990

1.2 A.V.Milkov, Global estimates of hydrate-bound gas in marine sediments:how much is really out there ?, Earth Science Reviews, 66, 183-197, 2004

1.3 K. A. Kvenvolden, T.D.Lorenson, *The global occurrence of natural gas hydrate*, *natural gas hydrate occurrence, distribution and detection*, American Geophysical Union, Washington, 2001

1.4 C.Ecker, *Seismic characterization of methane hydrate structures*, Stanford University, 2001

1.5 K.A.Kvenvolden, L.A.Barnard, *Hydrates of natural gas in continental margins*, AAPG, Mem, 34, 631-6640, 1983

1.6 R.Hyndman, E.Davis, *A mechanism for the formation of methane hydrate and seafloor bottom simulating reflectors by vertical fluid expulsion*, Journal of Geophysical Research, 97, 7025-7041, 1992

1.7 C. K. Paull, R. Matsumoto, P. J. Wallace, *Leg 164 science party: Ocean drilling program, initial reports in Ocean drilling program*, College Station, Texas, 1996

1.8 L.He, M.Osamu, X.Lei, *Methane hydrate accumulation model for the Central Nankai accretionary prism*, Marine Geology, 227, 201-214, 2006

1.9 S.Nakagawa, T.J. Kneafsey, and G.J.Moridis, *Mechanical strength and seismic property measurements of hydrate-bearing sediments (HBS) during hydrate formation and loading tests*, OTC 19559, Offshore Technology Conference ,Houston, Texas, U.S.A, 2008

1.10 J. Dvorkin, M. B. Helgerud, W. F. Waite, S. H. Kirby, A. Nur, *Natural gas hydrate in oceanic and permafrost environments*, 2003

1.11 M. Galavazi, R. Moore, M. Lee, D. Brunsden, B. Austin, *Quantifying the impact of deepwater geohazards.* OTC18083, Offshore Technology Conference, Houston, TX, U.S.A, 2006

1.12 T. J. Kvalstad, *What is the current "best practice" in offshore geohazard investigations? A State-of-the-art review*, OTC 18545, Offshore Technology Conference, Houston, TX, U.S.A, 2007

1.13 J. N. Nimblett, *Characterizing the accumulation and distribution of gas hydrate in marine sediments using numerical models and seismic data*, School of Earth and Atmospheric Sciences, Georgia Institute of Technology, 179, 2003

1.14 L. J. Peuchen, C. Raap, *Logging, sampling and testing for offshore geohazards*, OTC 18664, Offshore Technology Conference, Houston, TX, U.S.A, 2007

1.15 P. Bryn, E. S. Andersen, R. Lien , *The ormen lange geohazard experience: best Practice for geohazard evaluations of passive continental margins,* OTC 18712, Offshore Technology Conference, Houston, TX, U.S.A, 2007

1.16 R. G. Cicerone, R. S. Oremland, *Biogeochemical aspects of atmospheric methane*, Global Biochemical Cycles, 2, 299-327, 1988

1.17 K. A. Kvenvolden, *Gas hydrates-geological perspective and global change*, Review Geophysics, 31, 173-187, 1993

1.18 S. C. Williamson, D. R. McConnell, R. J. Bruce, *Drilling observations of possible hydrate-related annular flow in the deepwater gulf of mexico and implications on well planning*, OTC 17279, Offshore Technology Conference, Houston, TX, U.S.A, 2005

1.19 A. Lane, A. Taylor, *Geohazards: are we looking at them the right way? view from down under,* OTC 14106, Offshore Technology Conference, Houston, Texas U.S.A, 2002

1.20 A. Lane, *Overcoming deepwater geohazards in west africa,* OTC 17496, Offshore Technology Conference, Houston, TX, U.S.A, 2005

1.21 S.M.Masutani, G.C.Nihousi, *An update on the international field experiment on CO_2 ocean sequestration*, Proceeding of second international symposium on ocean sequestration of carbon dioxide, New Energy and Industrial Development Organization, Japan, 1999

1.22 E.Adams, M.Akai, L.Golmen, P.Haugan, H.Herzog, S.Masuda, S.M.Masutani, T.Ohsumi, C.S.Wong, *An international experiment on CO_2 ocean sequestration*, Green Gas Technologies, 293-298, 1998

1.23 I. Chatti, A. Delahaye, L. Fournaison, J. P. Petitet, *Benefits and drawbacks of clathrate hydrates: a review of their areas of interest*, Energy Conversion and Management, 1333-1343, 2005

1.24 J. Yang, B. Tohidi, B. M. Clennell, *Micro and macro-scale investigation of cementing characteristics of gas hydrates*, Proceeding of AAPG HEDBERG CONFERENCE, Gas Hydrates: Energy Resource Potential and Association Geologic Hazards, Vancouver BC, Canada, 2004

1.25 Y. Park, Kim. Do-Youn, J. W. Lee, D. G. Huh, K. P. Park, J. Lee, H. Lee, *Sequestering carbon dioxide into complex structures of naturally occurring gas hydrates,* The National Academy of Science of the USA , 103, 12690-12694, 2006

1.26 K. Z. House, P. S. Daniel, C. F. Harvey, K .S. Lackner *Permanent carbon dioxide storage in deep-sea sediments.* The National Academy of Science of the USA, 103, 12291-12295, 2006

1.27 B. Kvamme, A. Graue, T. Kuznetsova, G. Ersland, *Storage of CO_2 in natural gas hydrate reservoirs and the effect of hydrates as an extra sealing in cold aquifers,* International Journal of Greenhouse Gas Control, 236-246, 2007

1.28 H.Rabia, *Oilwell drilling engineering: principles and practice*, Kluwer Law International, 1986

1.29 Http://en.wikipedia.org/wiki/main_page

1.30 G. A. Wood, I.W. Hamilton, *Current geohazard problems and their geophysical interpretation - an international overview*, OTC 14102, Offshore Technology Conference, Houston, Texas U.S.A, 2002

1.31 A. J. Digby, *Assessment and quantification of the hydrate geohazard,* OTC 17223, Offshore Technology Conference, Houston, TX, U.S.A, 2005

1.32 N. Sultan, *Excess pore pressure and slope failures resulting from gas hydrates dissociation and dissolution*, OTC 18532, Offshore Technology Conference, Houston, TX, U.S.A, 2007

1.33 J. N. Nimb.lett, R. C. Shipp, F. Strijbos, *Gas hydrate as a drilling hazard: examples from global deepwater settings,* OTC 17476, Offshore Technology Conference, Houston, TX, U.S.A, 2005

1.34 C. P. Tan, R. Freij-Ayoub, M. B. Clennell, B. Tohidi, J. Yang, *Managing well bore instability risk in gas-hydrate-bearing sediments,* SPE 92960, Asia Pacific Oil & Gas Conference and Exhibition, Jakarta, Indonesia, 2005

1.35 A. Berger, W. W. Fleckenstein, A. W. Eustes, G. Thonhauser, *Effect of eccentricity, voids, cement channels, and pore pressure decline on collapse resistance of casing,* SPE 90045, SPE Annual Technical Conference and Exhibition, Houston, Texas, 2004

1.36 W. W. Fleckenstein, A. W. Eustes, W. J. Rodriguez, A. Berger, *Cemented casing: the true stress picture,* AADE-05-NTCE-14, National Technical Conference and Exhibition, Houston, Texas, 2005

1.37 M. H. Yousif, H. M. Abbas, M. S. Selim, E. D. Sloan, *Experimental and theoretical investigation of methane-gas-hydrate dissociation in porous media,* SPE Reservoir Engineering, 69-76, 1991

1.38 M. H. Yousif, P. M. Li, MS. Selim, E. D. Sloan, *Depressurization of natural gas hydrates in berea sandstone cores,* Journal of Inclusion Phenom, Mol.Recognit.Chem, 8,71-88, 1990

1.39 H. C. Kim, P. R. Bishnoi, R. A. Heidemann, S. S. H. Rizvi, *Kinetics of methane hydrate decomposition,* Chemical Engineering Science, 42,1645-1653, 1987

1.40 M. S. Selim, E. D. Sloan, *Hydrate dissociation in sediment,* SPE Reservoir Engineering, 1990

1.41 N. Goel, M. Wiggins, S. Shah, *Analytical modeling of gas recovery from in sit hydrates dissociation,* Journal of Petroleum and Engineering, 29, 115-127, 2001

1.42 T. Komai, Y. Sakamoto, T. Kawamura, Y. Yamamoto, *Dissociation rate of methane hydrates occupied in pore space of marine sediments,* Proceeding of The Sixth ISOPE Ocean Mining Symposium, Changsha, China, 2005

1.43 K. D. Debendra, S.Vineet, *Calculation of gas hydrate dissociation with finite-element model,* Journal of Energy Engineering, 3, 119, 1993

1.44 X. Sun, K. K. Mohanty, *Kinetics simulation of methane hydrate formation and dissociation in porous media,* Chemical Engineering Science, 61, 3476-3495, 2006

1.45 G. J. Moridis, *Numerical studies of gas production from methane hydrates,* SPE Gas Technology Symposium, Calgary, Canada, 2002

1.46 G. Ahmadi, C. Ji, D. H. Smith, *Natural gas production from hydrate dissociation: An axisymmetric model,* Journal of Petroleum and Engineering, 2007

1.47 S. Gerami, M. Pooladi-Darvish, *Predicting gas generation by depressurization of gas hydrates where sharp-interface assumption is not valid,* Journal of Petroleum Science and Engineering, 56,146-164, 2007

1.48 H. C. Kim, P.R. Bishnoi, R.A.Heidemann, S.S.H.Rizvi, *Kinetics of gas hydrate decomposition,* Chemical Engineering Science, 42, 1645-1653, 1987

1.49 K. Nazirdoust, G. Ahmadi, *Computational modeling of methane hydrate dissociation in a sandstone core,* Chemical Engineering Science, 62,6155-6177, 2007

1.50 C. Ji, G. Ahmadi, D. H. Smith, *Natural gas production from hydrate decomposition by depressurization,* Chemical Engineering Science, 56, 5801-5814, 2001

1.51 W. J. A. M. Swinkels, R. J. J. Drenth, *Thermal reservoir simulation model of production from naturally occurring gas hydrate accumulations,* SPE 68213, SPE Annual Technical Conference and Exhibition, Houston, 2000

1.52 K. Yamamoto, M. Yasuda, O. Osawa, *Geomechanical condition of deep water unconsolidated and hydrate related sediments of the pacific coast of central Japan*, Proceedings of the Fifth International Conference on Gas Hydrate, Trondheim, Norway, 2005

1.53 R. Birchwood, S. Noeth, P. Hooyman, W. Winters, *Well bore stability model for marine sediments containing gas hydrates,* AADE-05-NTCE-13, AADE National Technical Conference and Exhibition, Houston, Texas, 2005

1.54 A. Klar, K. Soga, *Coupled deformation-flow analysis for methane hydrate production by depressurized wells,* 3rd Biot Conference on Poromechanics, Norman, Oklahoma, 2005

1.55 J. Rutqvist, G. J. Moridis, *Numerical studies on the geomechanical stability of hydrate-bearing sediments,* OTC 18860, Offshore Technology Conference, Houston, Texas, 2007

1.56 S. Kimoto, F. Oka, T. Fushita, M. Fujiwaki, *Chemo-thermo-mechanically coupled numerical simulation of the subsurface ground deformations due to methane hydrate dissociation,* Computers and Geotechnics, 34, 216-228, 2007

1.57 M. Y. A. Ng, A. Klar, K. Soga, *Coupled soil deformation-flow-thermal analysis of methane production in layered methane hydrate soils*, in OTC 19364, Offshore Technology Conference, Houston, Texas, U.S.A, 2008

1.58 J. Rutqvist, G. J. Moridis, T. Grover, T. Collett, *Geomechanical response of permafrost-associated hydrate deposits to depressurization-induced gas production,* Journal of Petroleum Science and Engineering, 67, 1-12, 2009

1.59 R. Freij-Ayoub, C. Tan, B. Clennell, B. Tohidi, J. Yang, *A well bore stability model for hydrate bearing sediments,* Journal of Petroleum Science and Engineering, 57, 209-220, 2007

1.60 R. Freij-Ayoub, B. Clennell, B. Tohidi, J. Yang, R. Hutcheon, *Casing integrity in hydrate bearing sediments,* Offshore Site Investigation and Geotechnics, London, 2007

1.61 T. S. Yun, J. C. Santamarina, C. Rupple, *Mechanical properties of sand, silt, and clay containing tetrahydrofuran hydrate,* Journal of Geophysics Research, 12, 2007

1.62 A. Masui, K. Miyazaki, H. Haneda, Y. Ogata, K. Aoki, *Mechanical characteristics of natural and artificial gas hydrate bearing sediments,* Proceedings of the 6th International Conference on Gas Hydrates (ICGH 2008), Vancouver, British Columbia, Canada, 2008

1.63 L. A. Stern, , S. H. Kirby, W. B. Durham, *Peculiarity of methane clathrate hydrate formation and solid-state deformation, including possible superheating of water ice,* Science, 273, 1843-1848, 1996

1.64 S. Nakagawa, T. J. Kneafsey, and G. J. Moridis, *Mechanical strength and seismic property measurements of hydrate-bearing sediments (HBS) during hydrate formation and loading tests,* OTC 19559, Offshore Technology Conference, Houston, Texas, U.S.A, 2008

1.65 S. Nakagawa, L. R. Myer, *Mechanical and acoustic properties of weakly cemented granular rocks*

1.66 T. Edinima, Y. Kamata, H. Minagawa, R. Ogmura, J. Nagao, H. Narita, *Mechanical properties of sandy sediment containing methane hydrate,* Proceedings of the Fifth International Conference on Gas Hydrate, Trondheim, Norway, 2005

1.67 M. Hato, T. Matsuoka, H. Ikeda, T. Inamori, T. Saeki, K. Suzuki, *Geomechanical property of gas hydrate sediment in the Nankai Troug,* Proceedings of the 6th International Conference on Gas Hydrates (ICGH 2008),Vancouver, British Columbia, Canada, 2008

1.68 A. Masui, K. Miyazaki, H. Haneda, Y. Ogata, K. Aoki *Mechanical properties of natural gas hydrate bearing sediments retrieved from eastern Nankai Trough,* OTC 19277, Offshore Technology Conference, Houston, Texas, U.S.A, 2008

1.69 K. Suzuki, T. Ebinuma, H. Narita, *Shear strength of natural gas hydrate bearing sediments of Nankai Trough,* Proceedings of the 6th International Conference on Gas Hydrates (ICGH 2008), Vancouver, British Columbia, Canada, 2008

1.70 Y. L. Gallo, P. Couillens, T. Manai, *CO_2 Sequestration in depleted oil or gas reservoirs,* SPE 74104, 2002

1.71 R. L. Kleinberg, *New deposit accumulation model for marine gas hydrates,* OTC 18246, 2006

1.72 A. I. Evernos, J. Heathman, J. Ralstin, *Impermeation of porous media by forming hydrates in situ,* SPE 2881, 1971

1.73 H. Koide, M. Takahashi, H. Tsukamoto, Y. Shindo, *Self-trapping mechanisms of carbon dioxide in the aquifer disposal,* Energy Conversion and Management, 36, 505-508, 1995

1.74 H. Koide, Y. Shindo, Y. Tazaki, M. Iijima, K. Ito, N. Kimura, K. Omata, *Deep sub-seabed disposal of co_2 the most protective storage,* Energy Conversion Management, 38, S253-S258, 1997

1.75 Y. Seol, T. J. Kneafsey, L. Tomutsa, G. J. Moridis, *Preliminary relative permeability estimates of methane hydrate bearing sand*, *Proceeding of TOUGH symposium*, California, USA, 2006

1.76 A. I. Evernos, J. Heathman, J. Ralstin, *Impermeation of porous media by forming hydrates in-Situ*, SPE 2881, SPE Third Biennial Gas Industry Symposium, 1971

Chapter 2 – Mechanical and Geophysical Properties of Gas Hydrate Bearing Sediments

2.1 Introduction

There is little reliable data regarding the properties of sediments containing gas hydrates in the open literature. Gas hydrate dissociation will decrease the mechanical properties of gas hydrate bearing sediments. However, there are not data available quantifying the mechanical degradation of these sediments as a function of temperature in the open literature. As a result, in order to provide reliable input data for numerical model that investigate casing stability in the wellbores drilled in gas hydrate bearing sediments, and to quantify mechanical degradation of sediments containing gas hydrate as a function of temperature, several experiments were conducted in this study. The experiments, conducted to measure the geophysical and mechanical properties of gas hydrate-bearing sediments, are new in the composition of samples and experimental conditions they cover. The experiments were conducted under 29 MPa axial stress and 24 MPa pore pressure (i.e., 5 MPa effective stress) simulating real conditions found in deep offshore environments (i.e., Gulf of Mexico). Sediments compositions included sand, silt and clay, containing different saturations of methane hydrates, to represent the lithology of natural gas hydrate bearing sediments. The experimental methodology was designed to keep the effective stress constant during the injection of methane gas and water to ensure the integrity of the sample.

2.2 Experimental apparatus

All the experiments were conducted using the ultrasonic set-up developed at the Centre for Gas Hydrate Research at the Institute of Petroleum Engineering, Heriot-Watt University. Figure 2.1 shows a schematic of the ultrasonic set-up. It consists of a cylindrical cell, ultrasonic signal system, a LVDT (linear variable differential transformer), gas separator and backpressure regulator, Quizix pump and a personal computer. The test cell is 300 mm long with an inner diameter of 75 mm. It can work up to 40 MPa and is surrounded by a cooling jacket connected to a temperature control bath (Cryostat). The cooling jacket is filled with a mixture of water and ethylene glycol as a coolant fluid. The cooling jacket temperature can be kept stable to within ± 0.05 K. One end of the test cell is fitted with a movable piston that makes overburden pressure adjustable. The LVDT is fixed to the rod tail of the movable piston to

determine the displacement during depressurisation and compression, or expansion due to gas hydrate formation or dissociation. The ultrasonic system includes two ultrasonic transducers (a pulser and a receiver) and a digital storage oscilloscope for measuring the velocities of P-wave and S-wave through the hydrate-bearing sediment samples, as well as for frequency analysis of acoustic signals. The gas separator and backpressure regulator are used for measuring gas production/release by heating or depressurisation driven by a Quizix pump. A set of test data including pore pressure, overburden pressure, temperature, displacement of the piston, and ultrasonic waveforms, are acquired by the personal computer. The high pressure transducer measuring pore pressure is calibrated using a dead-weight-tester with an accuracy of ± 0.008 MPa in the range of 0 to 138 MPa. The thermal probe is a platinum resistance thermometer (PRT) which is calibrated using a PREMA Precision Thermometer 3040 over a range from 273.15 to 323.15 K. The deviation is within 0.1 K. The PRT thermal probe is inserted inside the cell to measure the temperature of the system. All the measurements except for sonic data are logged using a LabView programme. The time interval of data logging is adjustable through the interface of the LabView programme (set to one to two minutes in all experiments).

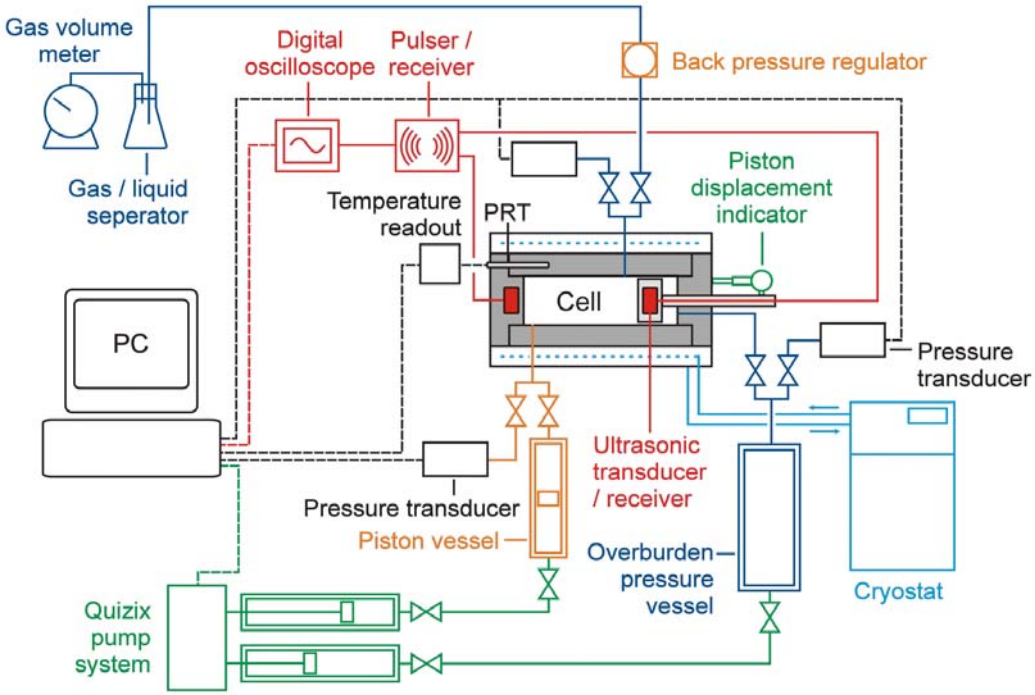

Figure 2.1 Schematic diagram of the ultrasonic set-up

2.3 Test material

2.3.1 Methane

The methane gas used in the experiments was supplied by Air Products PLC, with a certified purity 99.995 vol %.

2.3.2 Sand

Sand made of pure quartz was selected for the experiments to minimize the effect of the presence of other minerals and impurities on the results. The presence of small quantities of other minerals may alter the mechanical properties of sands by the chemical reaction of pore fluid with skeleton material [2.1]. The sand used in the experiments was provided from a mine at Lochaline in Scotland [2.1]. The sand from Lochaline in Scotland is made of quartz and it was analysed by Scanning Electron Microscope (SEM). The SEM analysis showed that the sand is composed of 99.65% to 99.85 % quartz by weight; with the remaining fraction consisting of opaque, tourmaline, glauconite and clay minerals [2.1].

2.3.3 Silt

The silt used in the experiments was prepared by crushing the sand to the desired size using a milling machine at the University of Edinburgh. The particle size distribution for both silt and sand was determined by using Malvern Mastersizer (shown in Figure 2.2) which measures the particle size distribution based on the principal of laser scattering [2.1]. The particle size distribution of the prepared silt and original sand is shown in Figure 2.3. The prepared silt has a particle size distribution between 1 to 140 μm, with a mass medium size 8.9 μm.

Figure 2.2 Malvern Mastersizer particle size distribution analyser

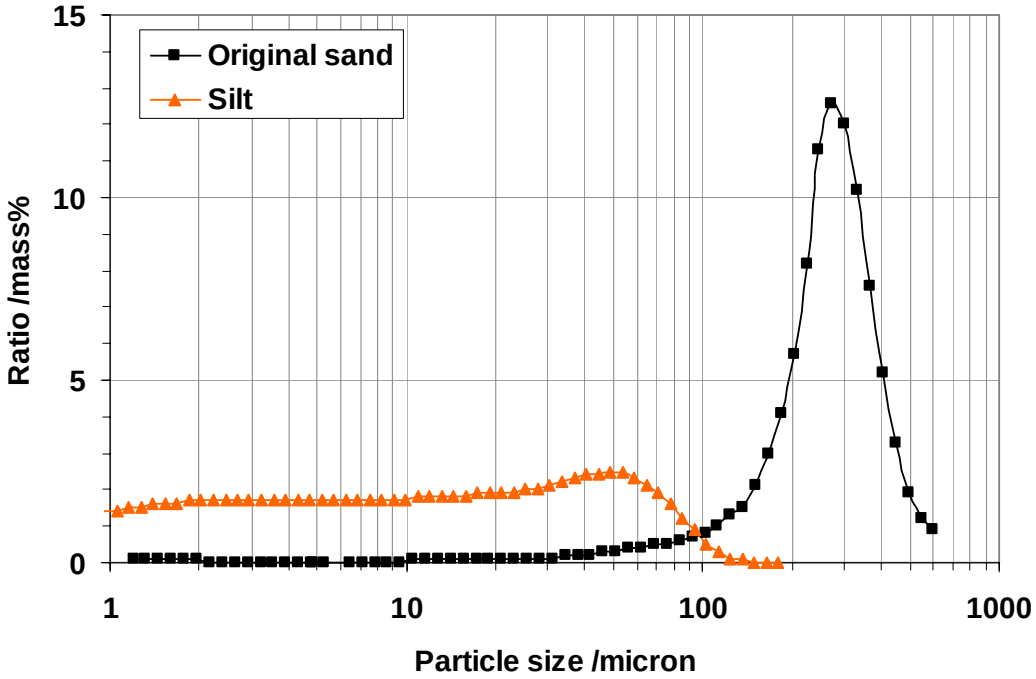

Figure 2.3 Particle size distributions of the sand and silt

2.3.4 Clay

Two types of clay, kaolinite and montmorillonite, were used in the experiments. The reason for selectingwas that montmorillonite, rather than the more commonly used illite, was that it absorbs more water (i.e., expands more) than kaolinite in contact with water. It is expected that illite absorbs significantly very less water than kaolinite. The kaolinite was supplied by WBB Minerals, and the montmorillonite was supplied by colleagues in at the University of Moscow as part of an INTAS project (grant number 03-51-4259) funded by the EU.

2.4 Experimental methodology

Figure 2.4 shows the procedure used to conduct this series of experiments.

2.4.1 Sample preparation

The experiments were conducted at 24 MPa pore pressure and 29 MPa overburden pressure (i.e., 5 MPa effective stress) to simulate deep water environments, i.e., 400 m below the seabed in 2000 m of water depth. It was also assumed that the temperature in the hydrate-bearing sediments is 277.15 K. The sediments were loaded into the cell until it was completely filled. Once filled with sediments the cell top was closed and vacuum was applied.

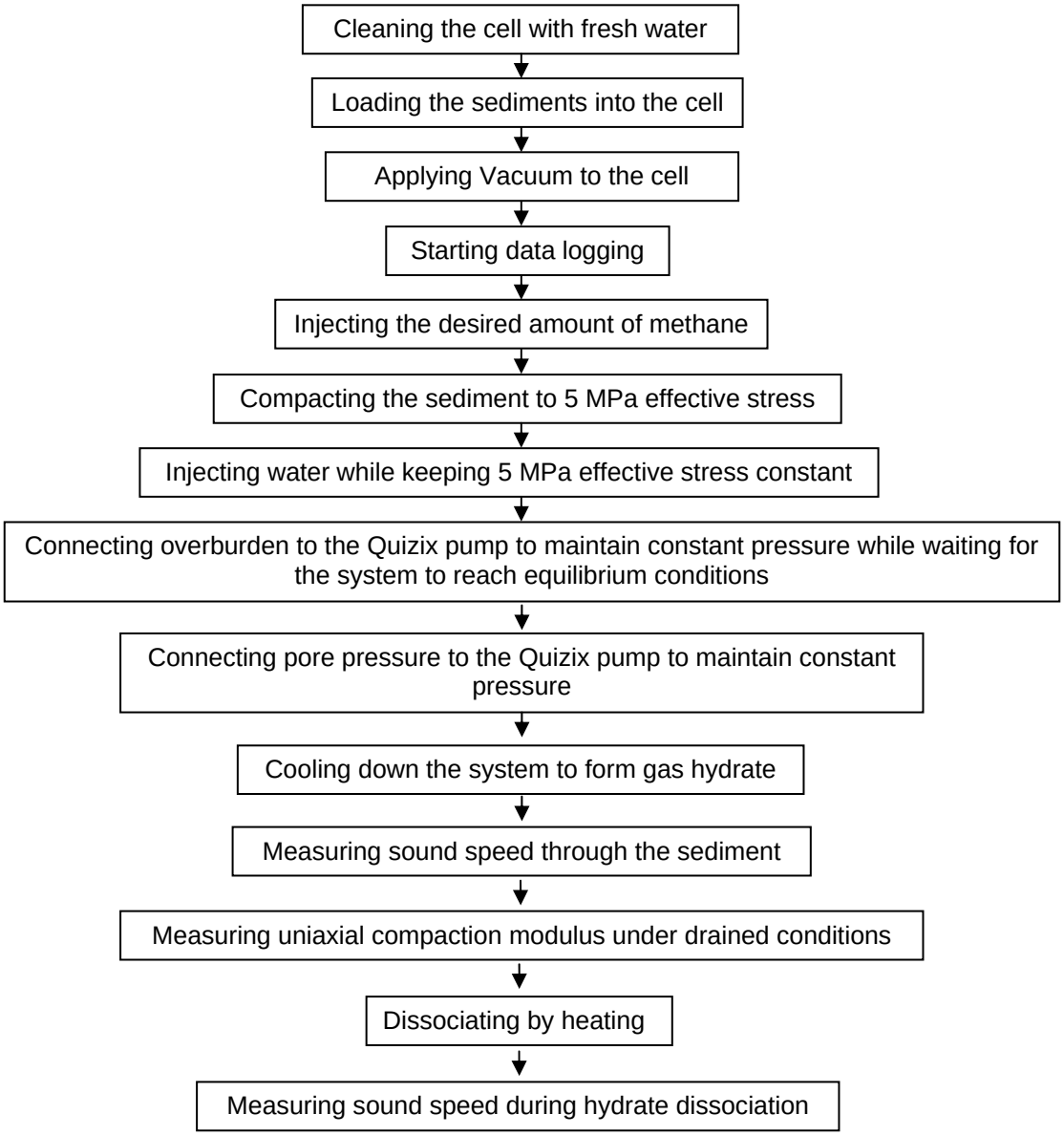

Figure 2.4 Summary of the experimental procedure applied

Afterwards the data logging programme was started. The desired quantity of methane gas was introduced into the cell at room temperature. Then the sediment inside of the cell was compacted to reach 5 MPa effective stress by moving the piston while the piston displacement was recorded. Distilled water was introduced into the system during which time the effective stress was kept constant at 5 MPa by moving the piston and applying controlled overburden pressure. The system was left undisturbed overnight, to reach equilibrium while the overburden pressure was kept constant 29 MPa. It was assumed that after this period, water was saturated with the injected methane.

2.4.2 Hydrate formation procedure

Once the system reached equilibrium the pore pressures was maintained constant by a Quizix pump. The system was cooled down to 277.15 K to form methane gas hydrate. The pore pressure was kept constant during the hydrate formation by injecting water into the cell using the Quizix pump. The rate of water injection was high during the initial hours of cooling, indicating that methane gas was being converted into gas hydrate. This process was continued for 6-7 days. It was assumed that this process was completed when the water injection rate remained constant at zero. Figure 2.5 shows the phase boundary of gas hydrate, and the thermodynamic conditions for gas injection and hydrate formation. The hydrate phase boundary was predicted by use of the in-house thermodynamic model (HWHYD). Details of gas hydrate calculations are presented in Appendix A.

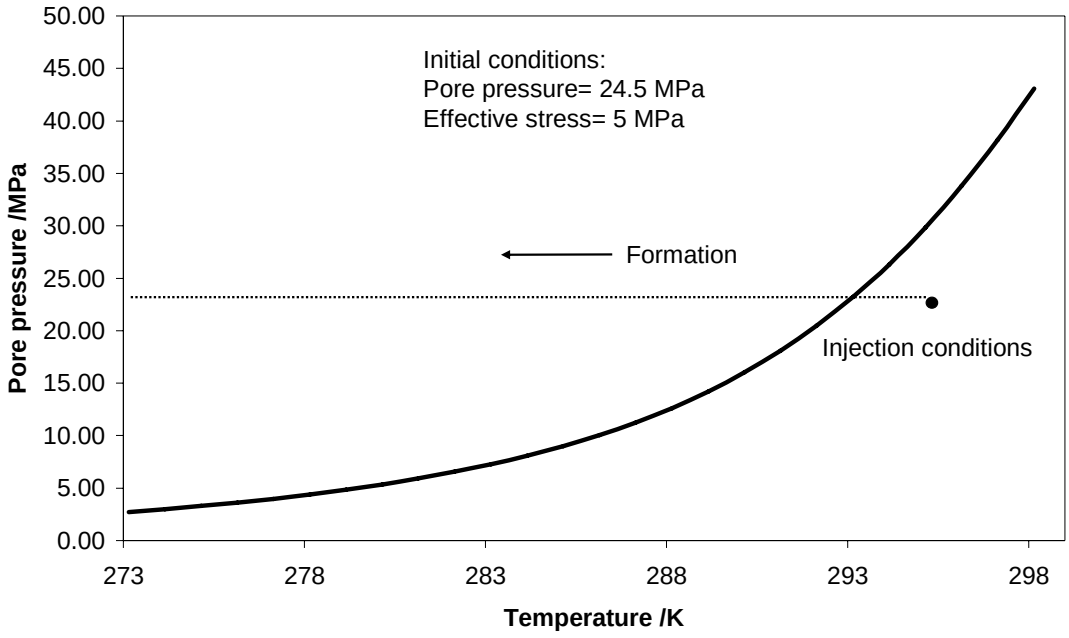

Figure 2.5 Hydrate formation condition at 277.15 K

2.4.3 Measurements of sound velocity (Geophysical Properties)

Compressional (P-Wave) and shear waves (S-Wave) are often used in the laboratory measurements to characterise the geophysical properties of gas hydrate-bearing sediments. Propagation of waves through gas hydrate-bearing sediments produces particle motion. The compressional wave propagates in the direction of the particle

motion resulting in longitudinal strain. In contrast, the shear wave propagates in the perpendicular direction of the particle motion resulting in shear strain. The velocity of compressional and shear waves is related to bulk density (ρ), bulk modulus (K) and shear modulus (G) of the sediments [2.2]:

$$V_p = \sqrt{\frac{K + \frac{4}{3}G}{\rho}} \tag{2.1}$$

$$V_s = \sqrt{\frac{G}{\rho}} \tag{2.2}$$

where

V_p = the velocity of P-Wave

V_s =the velocity of S-Wave

In the experiments once the gas hydrate formation was completed, the P-wave and S-wave velocities were measured through the cell containing the sediments by dividing the length of sediment inside the cell over the travelling time of P-wave and S-wave. The travelling time was determined by picking up the first arrival of the received wave form as shown in Figures 2.6 and 2.7. The sound velocity measurements were made using ultrasound of 1 MHz frequency.

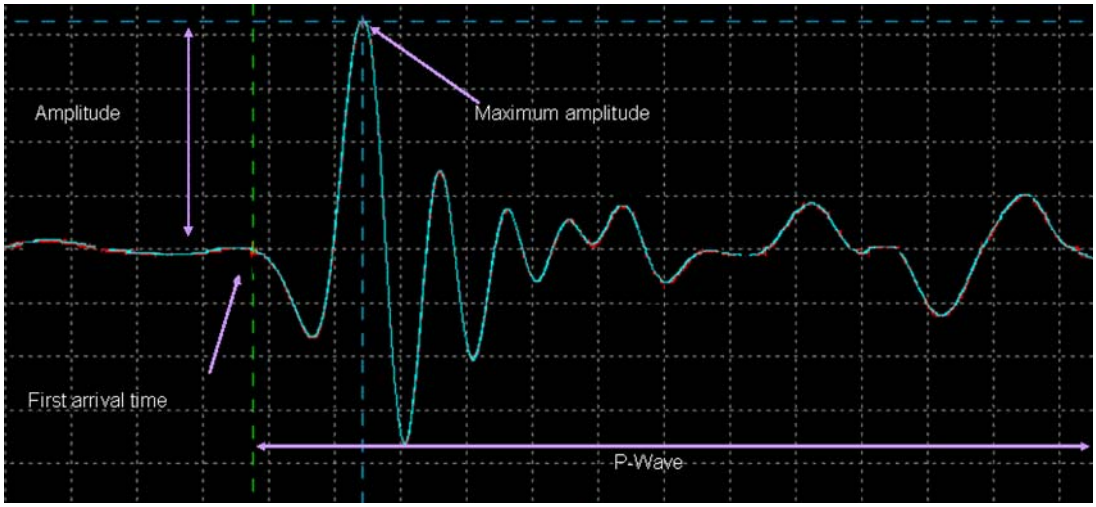

Figure 2.6 Determining the first arrival time of P-Wave

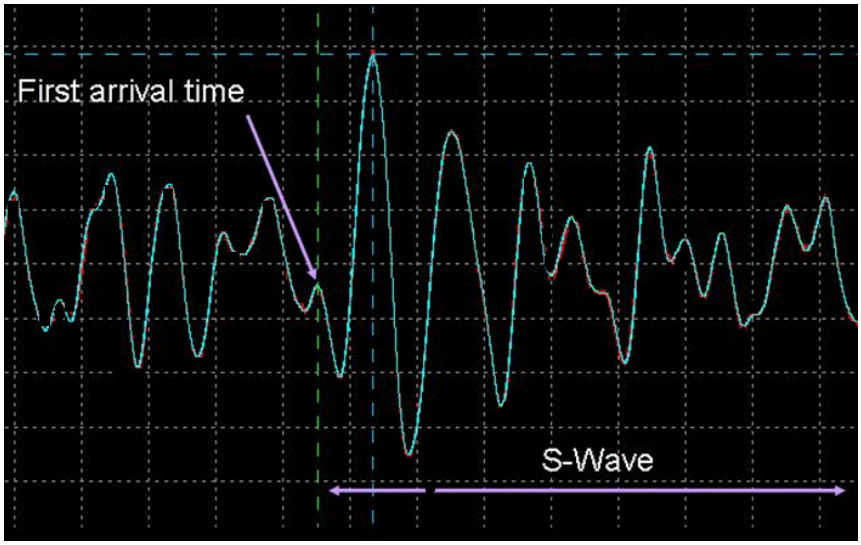

Figure 2.7 Determining the first arrival time of S-Wave

2.4.4 Dynamic moduli

As shown in Equations 2.1 and 2.2, the velocity of shear and compressional waves depends on elastic moduli. Therefore, the bulk modulus and shear modulus can be calculated based on elastic theory as [2.3]:

$$G = \rho V_s^2 \tag{2.3}$$

$$K = \rho V_p^2 - \frac{4}{3}\rho V_s^2 \tag{2.4}$$

where

G = Dynamic shear modulus

K = Dynamic bulk modulus

V_p = the velocity of compressional wave

V_s =the velocity of shear wave

ρ = bulk density

The bulk modulus and shear modulus obtained from the above equations are dynamic elastic properties. In theory, the bulk modulus and shear modulus measured in the laboratory (static bulk and shear modulus) are identical to the dynamic bulk and shear modulus calculated from the velocities of sonic waves. However, there have been some experiments reported that static bulk and shear modulus obtained from stress-strain

measurements are different from dynamic bulk and shear modulus obtained from the velocities of sonic waves using the above equations [2.3].

2.4.5 Static uniaxial compaction modulus

As shown in Figure 2.8, the sediment inside the cell of the ultrasonic set-up is not deformed radically as it is confined by the body of the cell. In other words, the lateral deformation of the sediment is zero while applying axial pressure by moving the piston (i.e., uniaxial compaction). In this type of test, the slope of axial stress (load) versus axial strain is used to calculate the static uniaxial compaction modulus.

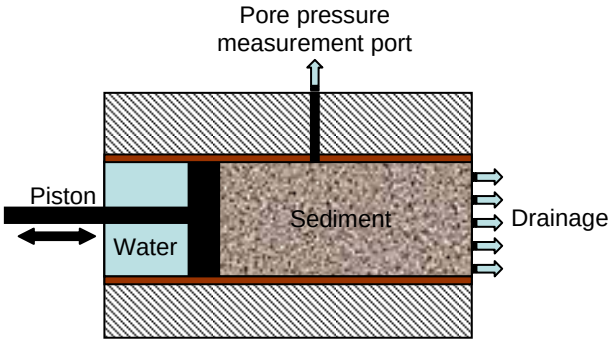

Figure 2.8 Schematic of the test cell of the ultrasonic set-up

The uniaxial compaction modulus ($\frac{\Delta\sigma}{\Delta\varepsilon}$) can be calculated based on the theory of elasticity and Hooke`s law as [2.3]:

$$\frac{\Delta\sigma}{\Delta\varepsilon} = \frac{E(1-\nu)}{(1+\nu)(1-2\nu\nu} \tag{2.5}$$

$$\frac{\Delta\sigma}{\Delta\varepsilon} = K' + \frac{4}{3}G' \tag{2.6}$$

where

σ =axial stress

ε =axial strain

ν =poisson`s ratio

E =Young modulus

G' = static shear modulus

K' = static bulk modulus

The modulus $\frac{\Delta\sigma}{\Delta\varepsilon}$ is called the oedometer modulus or static uniaxial compaction modulus. In this study, the axial stress (load) was increased to a desired value before reducing it to its original value, i.e., loading and unloading cycle. This process was repeated three times through three loading-unloading cycles. The piston movement and axial stress (load) were measured during the three cycles. The pore pressure was kept constant with the aid of the Quizix pump. An average value of the three calculated static uniaxial compaction modulus resulting from each cycle of loading-unloading was reported as the final value of static uniaxial compaction modulus for each experiment.

2.4.6 Hydrate dissociation by heating under drained conditions

Once the loading and unloading cycles were finished, the gas hydrate within the sediment was dissociated by step heating (i.e., increasing the temperature stepwise). The gas hydrate dissociation process was conduced at constant overburden pressure and almost constant pore pressure. The pore pressure fluctuated within a range of ± 0.5 MPa in most experiments although it was regulated against a backpressure regulator. The pressure regulator is a one way valve which is used to control or limit the pressure in a system. The regulator is set to open at a predetermined set pressure. When the set pressure is exceeded, the regulator opens and allows a portion of the fluid passes through it and closes when the set-pressure is reached.

Sonic velocities were measured during gas hydrate dissociation to investigate the effect of gas hydrate dissociation on the mechanical and geophysical properties of the sediment sample containing gas hydrates. Figure 2.9 shows the phase boundary of methane hydrate, and the thermodynamic path of the hydrate dissociation process.

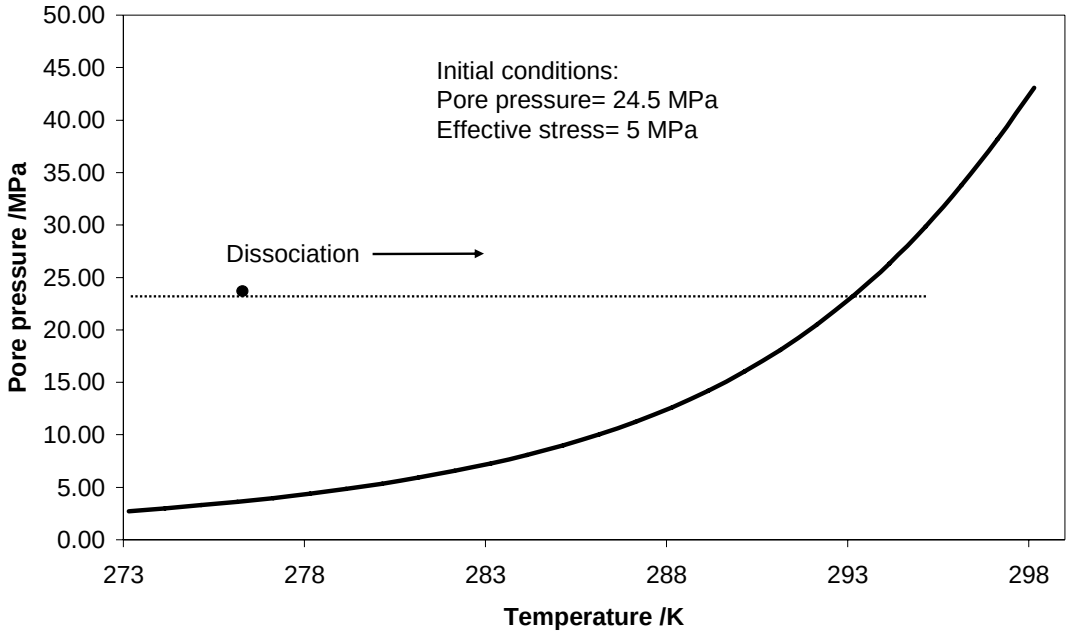

Figure 2.9 Hydrate dissociation conditions

2.4.7 Hydrate dissociation by heating under undrained conditions

Similar to hydrate dissociation under drained conditions, the temperature inside the sample was increased stepwise to dissociate gas hydrate in the sediment sample but the excess gas and water generated due to gas hydrate dissociation was not allowed to drain. Therefore, the pore pressure was increased during hydrate dissociation. The pore pressure and sonic velocities were measured during this process.

2.5 Results

Eight experiments were planned to understand the effect of gas hydrate on the geophysical and geomechanical properties of gas hydrate bearing sediments. They were also planned to quantify the mechanical degradation of gas hydrate bearing sediments during gas hydrate dissociation. As a result, the experiments were conducted with different sediment textures and gas hydrate saturations. The gas hydrate saturation is defined as the ratio of the volume of gas hydrate over the volume of the pore. Hydrate formation was such a slow process that each experiment took more than two weeks to be completed. Because of time constraints, it was decided to form gas hydrate with low (i.e., <20%), middle(i.e., 20%< <40%) and high (i.e., >40%) gas hydrate saturations Experiments 1 to 3 and 8 were conducted with silt and Experiments 4 to 7 with mixtures of clay and silt. In Experiments 1 through 7, after conducting the

required measurements on the samples containing gas hydrate, the gas hydrate was dissociated under drained conditions by heating. Therefore, the excess pore pressure generated during gas hydrate dissociation was allowed to dissipate. Experiment 8 was dissociated under undrained conditions to simulate the pore pressure increase in a very low permeability formation where fluids generated during gas hydrate dissociation can not flow, hence increasing the formation pore pressure. The results of the experiments are reported based on saturations in Tables 2.1 to 2.4 to facilitate comparison.

2.5.1 Mechanical and geophysical properties of hydrate-bearing sediments

Table 2.1 shows the properties of samples used in this series of experiments. Initial porosity (i.e., φ_0) was calculated based on the volume of injected gas after compaction of a sample and before gas hydrate formation. It was assumed that the injected gas occupies the total pore space of the sample after compaction. The porosity of the sample after hydrate formation was calculated as:

$$\varphi_h = \frac{V_p - V_h}{V_t} \tag{2.7}$$

where

φ_h =porosity after hydrate formation

V_h =volume of gas hydrate (as explained in Appendix A)

V_p =pore volume

V_t =total volume

Table 2.1 Properties of the sediment samples used in the experiments

Experiment Number	Sediment Composition	Hydrate saturation (S_h)/ %	Initial porosity φ_0 / %	Porosity after hydrate formation (φ_h)/ %	Remaining free gas/ %
1	Silt	7.4	38.1	34.10	1.8
8	Silt	23.3	37.3	27.31	0.9
2	Silt	25.6	37.7	27.26	1.4
3	Silt	43.6	38.8	21.19	8.2
4	90 % Silt+10 % Ka	18.8	39.1	30.29	5.1
5	80 % Silt+20 % Ka	21.3	39.6	28.98	3.1
6	90 % Silt+10 % Mo	24.1	38.0	27.87	1.8
7	80 % Silt+20 % Mo	21.4	38.2	28.32	3.7

In the experiments conducted with silt, four different saturations of gas hydrate were formed, from 7.4% up to 43.6%. For the highest gas hydrate saturation 43.6%, 8.2% of free gas remained in the sediments. This may be due to the entrapment of the remaining free gas in individual hydrate crusts, which resulted in separation of the remaining gas from water so that no further hydrate formation can occur in lab time-scale.

In Experiments 4 to 7 with mixtures of silt and clay, it was intended to form gas hydrate with 20% saturation. However, as shown in Table 2.1, the actual gas hydrate saturations achieved were in a range from about 19 to 24%, and with noticeably higher remaining free gas saturations in comparison to Experiments 1, 2, and 8. The high saturation of remaining free gas might be due to the presence of clays that reduces water mobility needed for hydrate growth.

Measured sound velocities (Geophysical Properties)

Table 2.2 shows the velocities of shear and compressional waves measured in this series of experiments.

Table 2.2 Measured sound speed in the samples

Experiment Number	Sediment Composition	Hydrate saturation (S_h)/ %	Remaining free gas/ %	Velocity of P-wave/ km/s	Velocity of S-wave/ km/s
1	Silt	7.4	1.8	1.81	1.05
8	Silt	23.3	0.9	1.98	1.04
2	Silt	25.6	1.4	1.93	1.15
3	Silt	43.6	8.2	2.29	1.08
4	90 % Silt+10 % Ka	18.8	5.1	1.99	1.13
5	80 % Silt+20 % Ka	21.3	3.1	2.12	1.19
6	90 % Silt+10 % Mo	24.1	1.8	1.92	1
7	80 % Silt+20 % Mo	21.4	3.7	1.97	1.19

The compressional velocity in samples made by silt slightly increased as the saturation of gas hydrate increased from 7.4 to 25.6%. When the gas hydrate saturation increases from 25.6 to 43.6%, the compressional velocity increased more significantly. However, no meaningful increase in the shear velocity was measured which could be related to the high concentration of remaining free gas affecting the shear wave velocity or/and an error occurred in determining the arrival time of S-wave. As shown in Table 2.2 the shear wave velocities are similar in samples made by silt and clay with similar gas hydrate saturation regardless the type of the clay.

Dynamic moduli

Table 2.3 shows the calculated dynamic bulk and shear modulus based on Equations 2.3 and 2.4.

Table 2.3 Calculated dynamic moduli

Experiment Number	Sediment Composition	Hydrate saturation (S_h)/ %	Remaining free gas/ %	Dynamic Shear modulus/ GPa	Dynamic Bulk modulus/ GPa
1	Silt	7.4	1.8	2.58	4.22
8	Silt	23.3	0.9	2.52	5.77
2	Silt	25.6	1.4	3.05	4.53
3	Silt	43.6	8.2	2.67	8.44
4	90 % Silt+10 % Ka	18.8	5.1	2.92	5.17
5	80 % Silt+20 % Ka	21.3	3.1	3.20	5.89
6	90 % Silt+10 % Mo	24.1	1.8	2.29	5.39
7	80 % Silt+20 % Mo	21.4	3.7	3.20	4.51

It can be found from Table 2.3 that the dynamic bulk modulus and shear modulus for the samples made with silt, changed with gas hydrate saturation in a way similar to that of the acoustic velocities.

The dynamic bulk modulus of samples made mixtures of silt and kaolinite increases by increasing the concentration of kaolinite. The dynamic shear modulus does not have a noticeable change as a result of an increase in the concentration of kaolinite due to the errors associated with shear wave measurements. For the samples made by mixtures of silt and montmorillonite, the dynamic bulk modulus decreases and the dynamic shear modulus increases by increasing the concentration of montmorillonite

Static uniaxial compaction modulus

Table 2.4 shows the static uniaxial compaction modulus calculated based on equation 2.5 for Experiments 1 to 8.

Table 2.4 Calculated uniaxial compaction modulus of samples containing gas hydrate

Experiment Number	Sediment Composition	Hydrate saturation (S_h)/ %	Static uniaxial compaction modulus/ GPa
1	Silt	7.4	3.79
8	Silt	23.3	47.22*
2	Silt	25.6	3.05
3	Silt	43.6	12.21
4	90 % Silt+10 % Ka	18.8	27.25
5	80 % Silt+20 % Ka	21.3	32.34
6	90 % Silt+10 % Mo	24.1	16.90
7	80 % Silt+20 % Mo	21.4	18.26

***** *The measured value is very high. The exact reason for this could not be ascertained, though internal friction between the internal body of the cell and the piston.*

In order to measure the static uniaxial compaction modulus, the axial stress (load) was increased by 0.69 MPa during loading and reduced to the original value during unloading. The piston displacement was in a range from 0.002 to 0.007 mm using a LVDT transducer. The loading and unloading cycles were conducted under drained conditions. Therefore, the static uniaxial compaction modulus was calculated for drained conditions.

Table 2.4 also shows the effect of sample texture on the uniaxial compaction modulus. It was very difficult to get identical gas hydrate saturation in the clay-silt experiments and the corresponding reference silty experiment with similar gas hydrate saturation (i.e., Experiment 2). Gas hydrate saturation and the texture (sediment composition) of the sediment affect the static uniaxial compaction modulus. The increase in clay content, regardless of the type of the clay, increases the static uniaxial compaction modulus of the samples. The samples containing montmorillonite showed lower static

uniaxial compaction modulus than the samples containing kaolinite, although they had similar gas hydrate saturations.

2.5.2 Mechanical and geophysical properties of gas hydrate-bearing sediments during heating

Hydrate dissociation under drained conditions

With the exception of Experiment 8, in which the gas hydrate was dissociated by heating under undrained conditions, the gas hydrates in the rest of the experiments were dissociated under drained condition. Special care was taken to maintain the pore pressure constant during hydrate dissociation and the pore pressure was measured at a different port from the drainage port as shown in Figure 2.8. However, the pore pressure during hydrate dissociation in Experiments 3 and 5 fluctuated more than 2-2.5 MPa as shown in Figures 2.10 and 2.11. The possible reason for this fluctuation could be the movement of fine particles that blocked the drainage port.

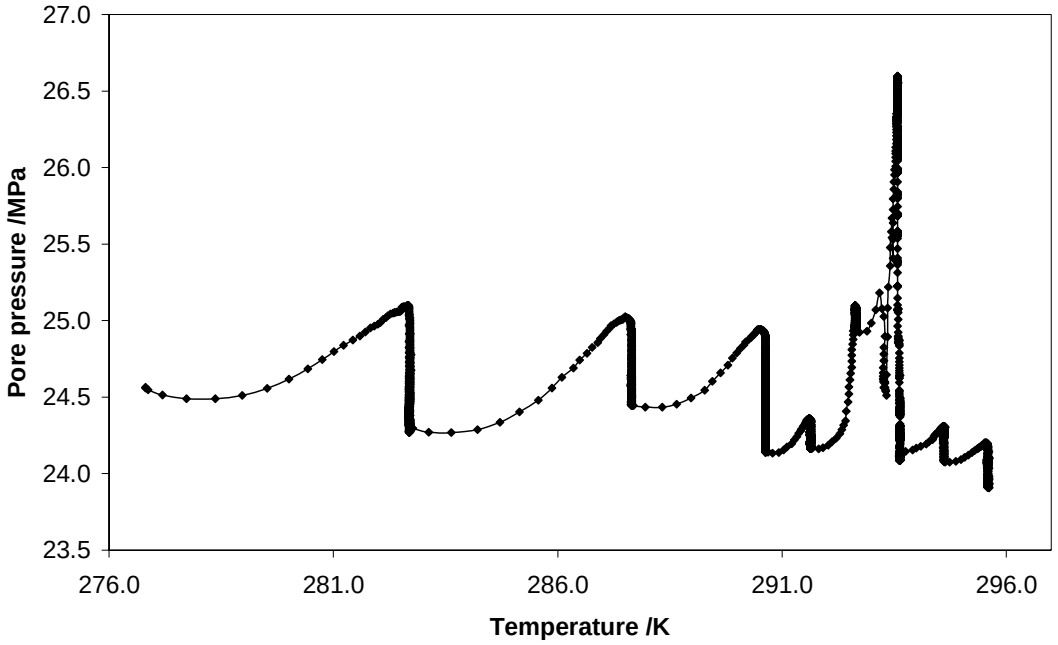

Figure 2.10 Pore pressure changes in Experiment 3 during hydrate dissociation under drained conditions

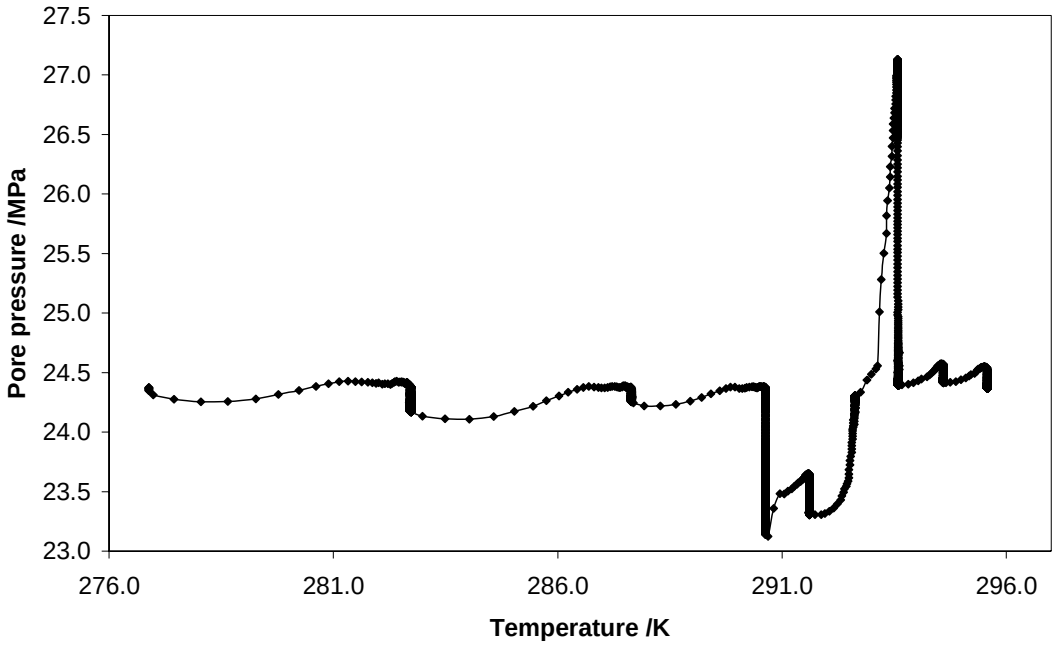

Figure 2.11 Pore pressure changes in Experiment 5 during hydrate dissociation under drained conditions

Dynamic moduli measured

Tables 2.5 to 2.8 show the dynamic bulk and shear modulus measured at different temperatures during gas hydrate dissociation by heating.

Table 2.5 Dynamic bulk and shear modulus measured during hydrate dissociation in Experiments 1 and 2

Temperature /K	Experiment 1		Experiment 2	
	Dynamic Shear modulus/ GPa	Dynamic Bulk modulus/ GPa	Dynamic Shear modulus/GPa	Dynamic Bulk modulus/ GPa
276.85	2.58	4.22	3.05	4.53
282.65	2.68	4.18	3.07	4.56
287.55	2.63	4.25	3.02	4.63
290.55	2.63	4.33	3.02	4.72
291.55	2.58	4.40	3.02	4.72
292.65	N/A		3.02	4.72
293.55	1.35	4.56	0.55	1.85
294.55	1.31	3.79	0.55	1.85
295.55	1.35	3.45	0.55	1.85

Table 2.6 Dynamic bulk and shear modulus measured during dissociation in Experiments 3 and 4

Temperature /K	Experiment 3		Experiment 4	
	Dynamic Shear modulus/ GPa	Dynamic Bulk modulus/ GPa	Dynamic Shear modulus/ GPa	Dynamic Bulk modulus/ GPa
276.85	2.67	7.02	2.90	5.23
282.65	2.67	7.02	2.88	5.28
287.55	2.62	6.89	2.87	5.24
290.55	2.62	6.69	2.84	5.28
291.55	2.62	6.69	2.84	5.28
292.65	2.67	6.53	2.84	5.28
293.55	N/A		1.74	5.39
294.55	N/A		N/A	
295.55	N/A		N/A	

Table 2.7 Dynamic bulk and shear modulus measured during dissociation in Experiments 5 and 6

Temperature /K	Experiment 5		Experiment 6	
	Dynamic Shear modulus/ GPa	Dynamic Bulk modulus/ GPa	Dynamic Shear modulus/ GPa	Dynamic Bulk modulus/ GPa
276.85	3.19	5.90	2.31	5.37
282.65	3.21	5.79	2.29	5.44
287.55	3.21	5.71	2.28	5.55
290.55	3.32	5.54	2.01	5.90
291.55	3.34	5.48	1.96	5.97
292.65	3.34	5.30	1.73	5.47
293.55	0.41	2.04	N/A	
294.55	0.41	2.04	0.55	1.85
295.55	0.42	2.03	0.55	1.85

Table 2.8 Dynamic bulk and shear modulus measured during dissociation in Experiment 7

Temperature /K	Experiment 7	
	Dynamic Shear modulus/ GPa	Dynamic Bulk modulus/ GPa
276.85	3.20	4.60
282.65	3.12	4.60
287.55	3.09	4.63
290.55	3.04	4.82
291.55	2.95	4.76
292.61	1.68	3.67
293.55	1.81	3.31
294.55	1.76	3.38
295.55	1.76	3.31

Figures 2.12 and 2.13 show the dynamic bulk and shear modulus for Experiments 1-3 which were conducted on sediments containing silts only.

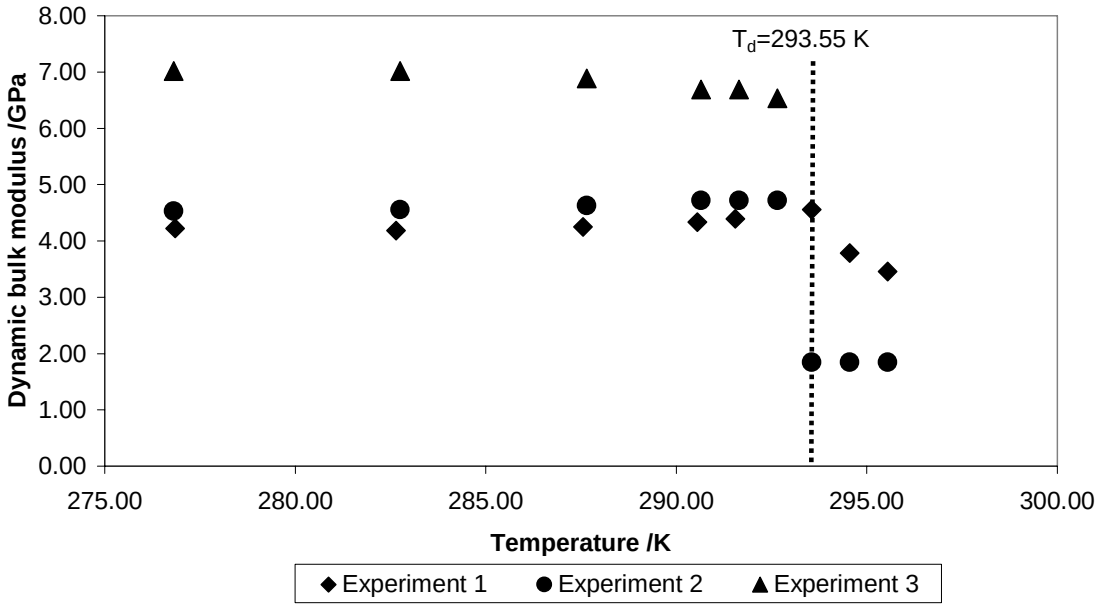

Figure 2.12 Dynamic bulk modulus of Experiments 1, 2 and 3 with silt containing 7.4, 25.6 and 43.6 vol% gas hydrate, respectively (T_d represents dissociation temperature at 25 MPa pore pressure)

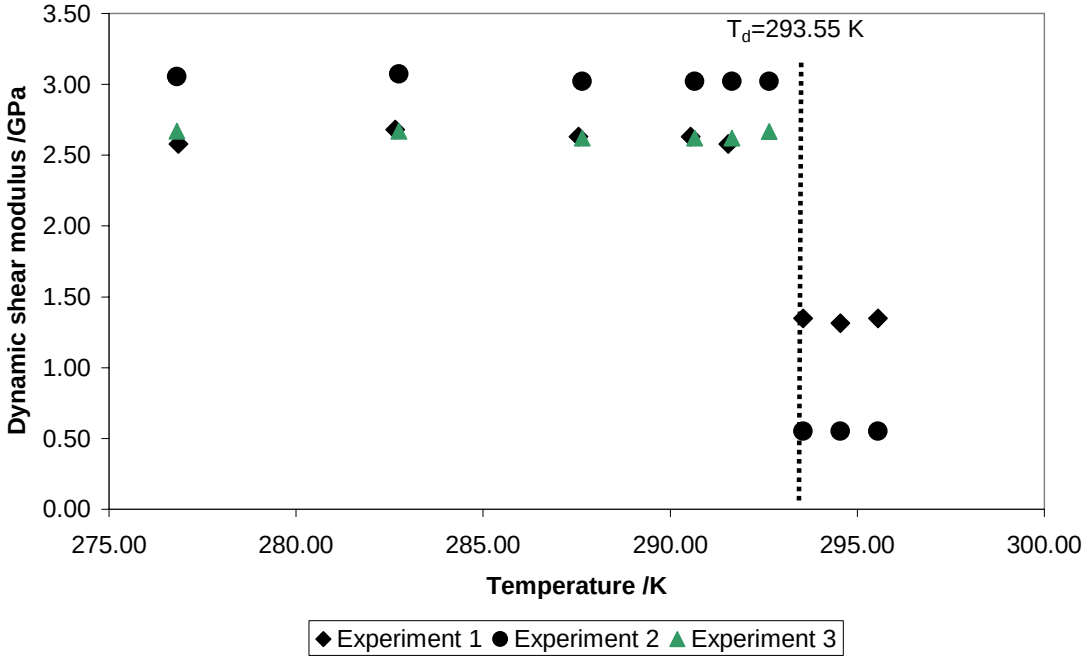

Figure 2.13 Dynamic shear modulus of Experiments 1, 2 and 3 with silt containing 7.4, 25.6 and 43.6 vol% gas hydrate, respectively (T_d represents dissociation temperature at 25 MPa pore pressure)

It is clearly demonstrated that the system temperature does not have a significant effect on dynamic bulk and shear moduli below hydrate dissociation temperature (in this case, 293.55 K). However, once the system condition reaches the dissociation point, both the dynamic bulk modulus and the dynamic shear modulus are sharply decreased. Additionally, it was observed that the acoustic signals disappeared when the system temperature reached the dissociation point of gas hydrate in Experiment 3, where a large amount of methane gas was suddenly released due to gas hydrate dissociation.

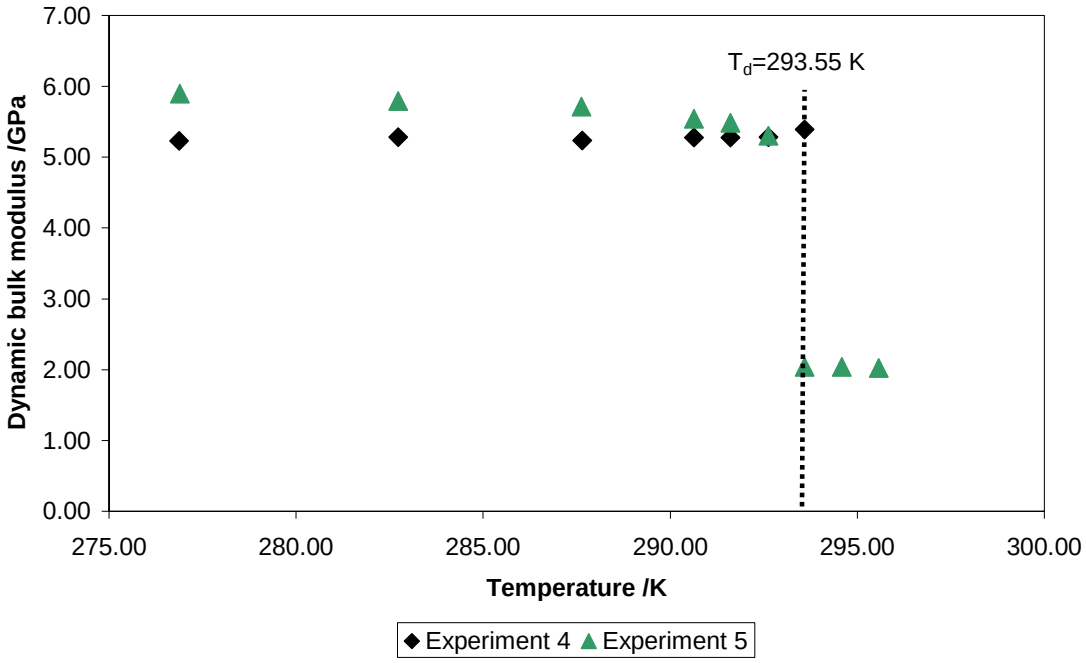

Figure 2.14 Dynamic bulk modulus of Experiments 4 (90 % Silt+10 % Ka) and 5 (80 % Silt+20 % Ka), (T_d represents dissociation temperature at 25 MPa pore pressure)

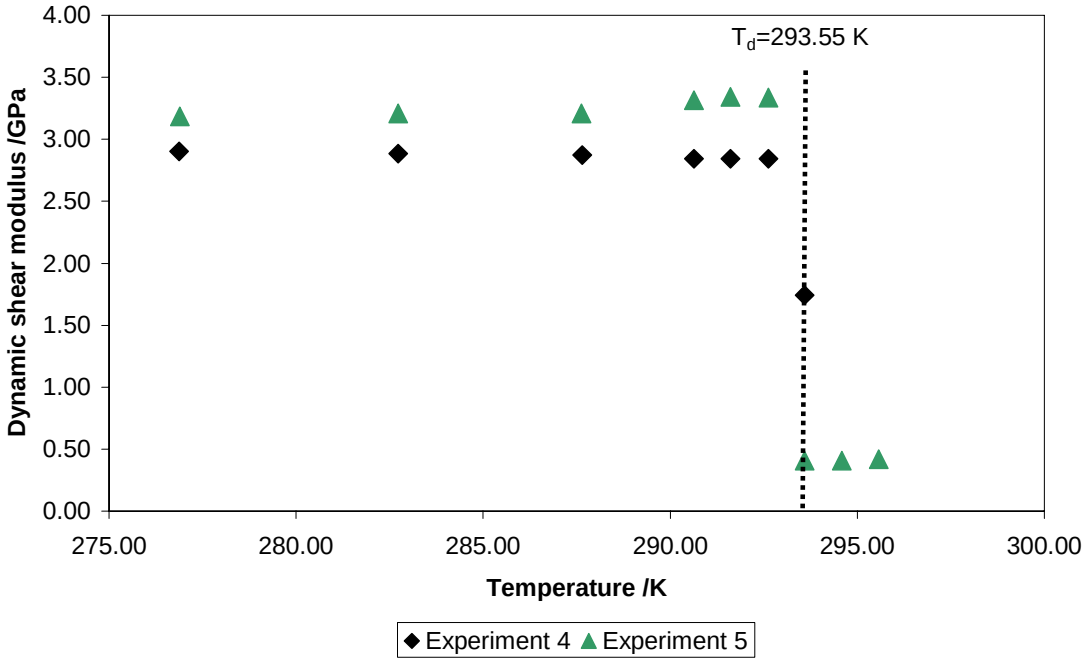

Figure 2.15 Dynamic shear modulus of Experiments 4 (90 % Silt+10 % Ka) and 5 (80 % Silt+20 % Ka), (T_d represents dissociation temperature at 25 MPa pore pressure)

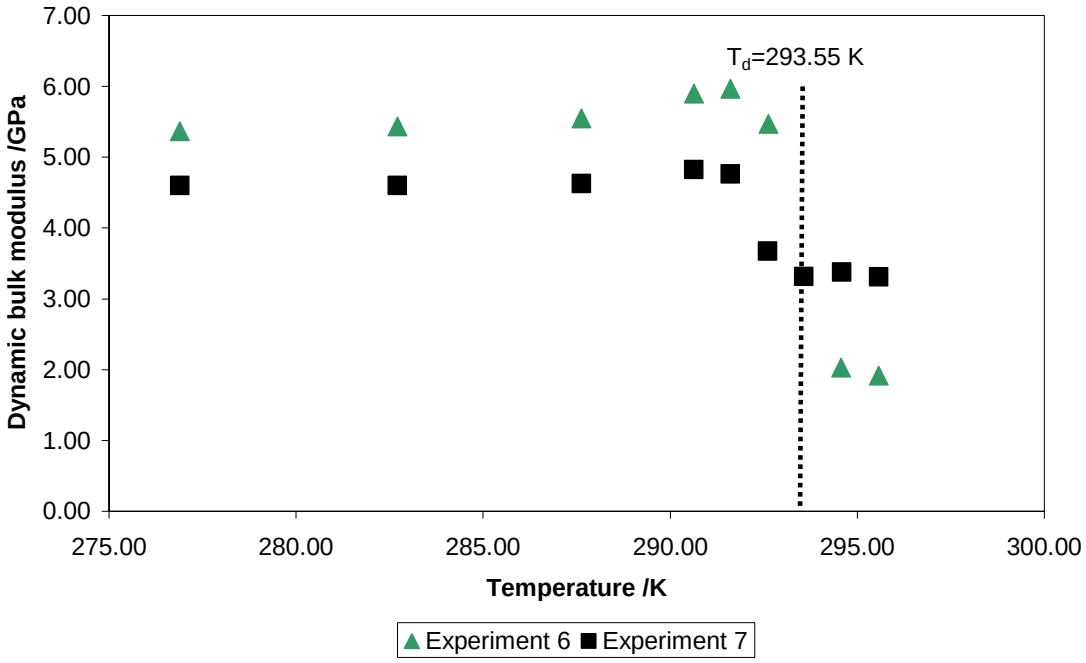

Figure 2.16 Dynamic bulk modulus of Experiments 6 (90 % Silt+10 % Mo) and 7 (80 % Silt+20 % Mo), (T_d represents dissociation temperature at 25 MPa pore pressure)

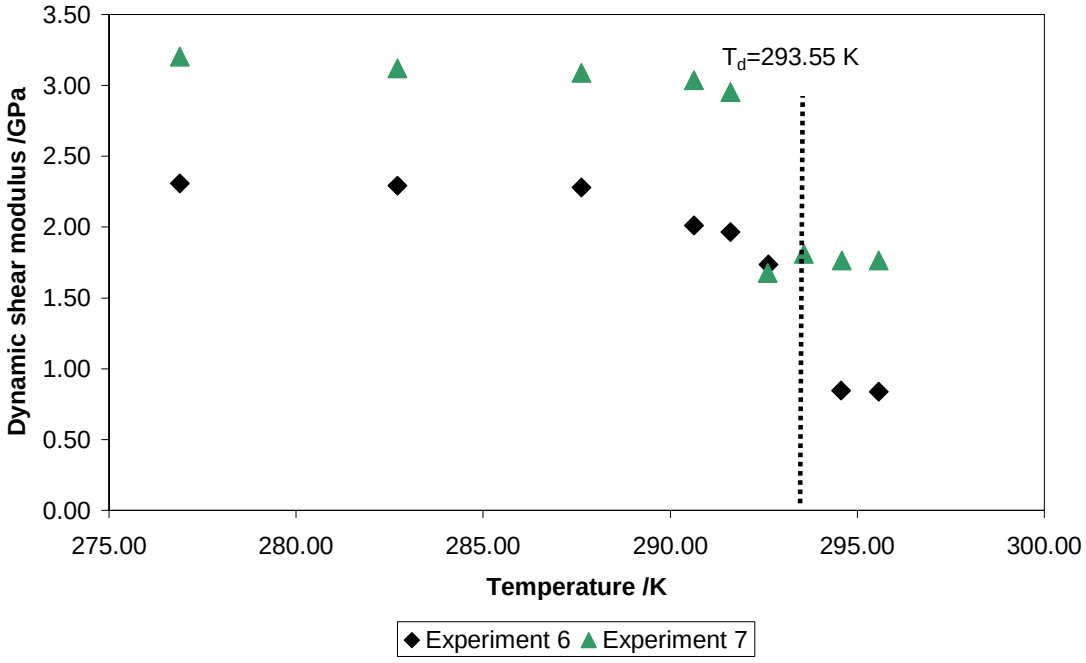

Figure 2.17 Dynamic shear modulus of Experiments 6 (90 % Silt+10 % Mo) and 7 (80 % Silt+20 % Mo), (T_d represents dissociation temperature at 25 MPa pore pressure)

Hydrate dissociation under undrained conditions

When the formation permeability is very low the fluids generated during gas hydrate dissociation cannot dissipate in the formation very quickly. As a result the pore pressure in the formation will increase. Therefore, to simulate these conditions, in Experiment 8 the hydrates were dissociated under undrained conditions to measure the magnitude of pore pressure increase during gas hydrate dissociation.

Pore pressure

Figure 2.18 shows the pore pressure changes during gas hydrate dissociation under undrained conditions. The pore pressure increases sharply after the gas hydrate dissociation point. The experiment was stopped when the pore pressure was close to the maximum working pressure of the set-up for safety reasons.

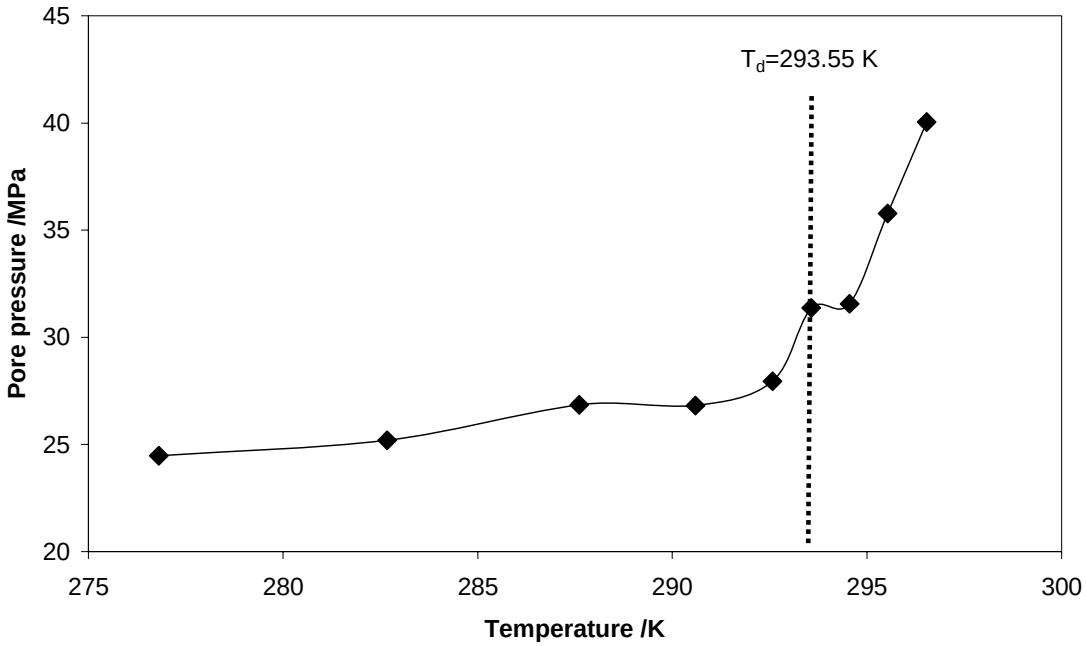

Figure 2.18 Pore pressure increases during gas hydrate dissociation at undrained conditions (T_d represents dissociation temperature at 25 MPa pore pressure)

- ***Dynamic moduli***

Table 2.9 shows the dynamic moduli measured in Experiment 8 which was conducted with silt only at undrained condition. It can be found from this table that the dynamic bulk modulus decreased at approximately the hydrate dissociation temperature. It decreased sharply after the dissociation point (293.55 K). The shear bulk modulus

decreased at 1 K before the dissociation temperature, but the decrease was very small even after the dissociation point.

Table 2.9 Dynamic bulk and shear modulus measured during gas hydrate dissociation in Experiment 8.

Temperature /K	Experiment 8	
	Dynamic Shear modulus/ GPa	Dynamic Bulk modulus/ GPa
276.85	2.51	5.76
282.75	2.49	5.75
287.65	2.49	5.70
290.65	2.48	5.70
292.65	2.45	5.72
293.55	2.42	5.59
295.55	2.36	4.56

2.6 Discussion

As mentioned before, P-wave propagates in the direction of the particle motion resulting in longitudinal strain. In contrast, S-wave propagates in the perpendicular direction of the particle motion resulting in shear strain. Therefore, P-wave can propagate through fluids but S-wave requires a medium with shear stiffness to propagate. The results presented in Table 2.2 show no significant increase in the velocity of S-wave as a function of gas hydrate saturation particularly in gas hydrate saturations from 7.4 to 25.6% in silt samples. It means that the presence of gas hydrates does not add to the shear stiffness of the medium. In addition the velocity of P-wave does not increase significantly with the increase in gas hydrate saturation from 7.4 to 25.6% in silt samples. The changes in the velocities of P-wave and S-wave in silt samples could suggest that hydrates grow within the pore space as in the pore filling model. In other words, the pore filling model is suggested as a dominating model for gas hydrates growth in silt samples as shown in Figure 2.19. It should be mentioned that once gas hydrate formation is completed free gas may be enclosed by gas hydrates as shown in Figure 2.20.

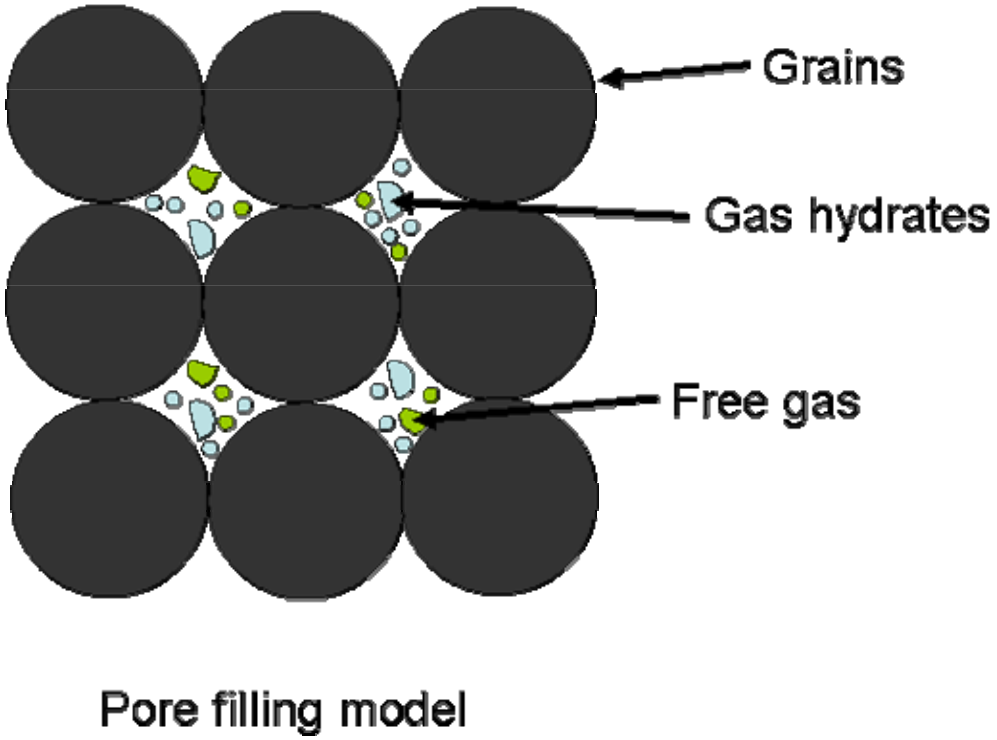

Figure 2.19 Schematic of gas hydrate growth in silt samples with gas hydrate saturation from 7.4 to 25.6%

As shown in Table 2.2, the velocity of P-wave increases with the increase in gas hydrate saturation from 25.6 to 44.6 %. However, the velocity of S-wave decreases. The decrease in the velocity of S-was was related to the presence of free remaining gas and an error occurred in determining the arrival time of S-wave. It was also shown in Table 2.2 that the concentration of free remaining gas (most likely trapped in hydrate crystals) increases with the increase in gas hydrate saturations. The effects of free remaining gas on the velocity of S-wave could be explained by the fact that free gas bubbles formed within hydrate crystals (as shown in Figure 2.20) weakening the stiffness of hydrate crystals surrounding the gas bubbles resulting in the decrease in the velocity of S-wave. This phenomenon is manifested by shear modulus decrease in Experiment 3 as shown in Table 2.3.

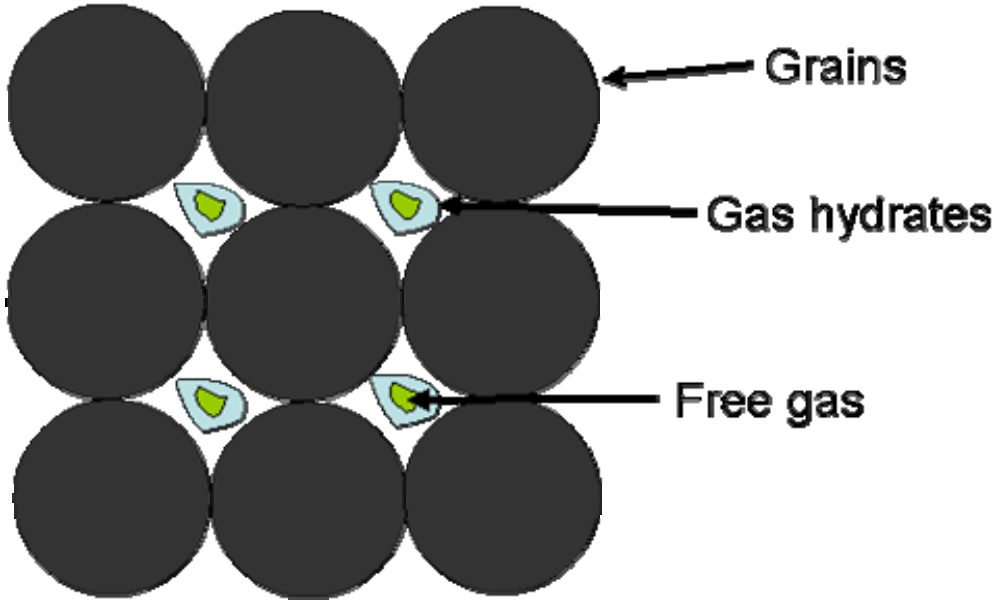

Figure 2.20 Schematic of trapped gas bubbles within gas hydrate crystals

There is a fluctuation in the results of the static uniaxial compaction modulus in the silt samples as shown in Table 2.4. It was expected that the static uniaxial compaction modulus of Experiment 2 would be higher than that of Experiment 1 but the reverse is shown in Table 2.4. This can be explained by the fact that the loading and unloading in this series of experiments was conducted by controlling the pressure of injected water behind the piston in the piston assembly by a Quizix pump. The result of this series of experiments showed that controlling the axial load by the pressure of injected water does not have high performance. It was improved by controlling the rate of water injection in the second series of experiments as explained in the next chapter. The average rate of loading in Experiment 1 was 2.344 kPa/second and the average rate of loading in the rest of experiments was 0.2 to 0.55 kPa/second. It means that although Experiment 1 has lower gas hydrate saturation than Experiment 2, the rate of loading in Experiment 1 was higher than Experiment 2 and as a result the static uniaxial compaction modulus in Experiment 1 is higher than Experiment 2.

For the samples made of silt and different type of clays, there were different responses by the dynamic bulk and shear moduli to gas hydrate dissociation as shown in Figures 2.14 to 2.17. As shown in Figures 2.14 and 2.15, both dynamic shear and bulk moduli of samples made of silt and kaolinite are decreasing at a point very close to the

dissociation point. Figures 2.16 and 2.17 show that as the system temperature approaches the dissociation point (about 1.5 K below the hydrate dissociation point), the dynamic shear modulus of the samples containing montmorillonite are gradually decreased, while the dynamic bulk modulus are slightly increased. The increase in the bulk modulus as a function of temperature before dissociation point has not been clearly understood yet and as a result further investigations are required.

2.7 Summary

In this chapter, the results of a series of experiments conducted on synthetic samples containing gas hydrates with different gas hydrate saturations were presented. The compressional wave velocity in the samples made with silt slightly increased without changes in the shear wave velocity as the saturation of gas hydrate increased from 7.4 to 25.6 %. The increases were more noticeable when the gas hydrate saturation increased from 25.6 to 43.6 %. This indicates the pore filling nature of gas hydrates. The dynamic bulk and shear modulus slightly increased as the gas hydrate saturation increased in samples made of silt.

The rate of loading seemed to alter the results of static uniaxial compaction modulus measurements. A higher rate of axial loading resulted in a higher magnitude of static uniaxial compaction modulus. Increasing clay contents increased the magnitude of the static uniaxial compaction modulus. The samples made by a mixture of montmorillonite and silt resulted in lower static uniaxial compaction modulus than samples made by a mixture of kaolinite and silt with the same gas hydrate saturation.

The dynamic shear and bulk modulus in the samples made in this series of experiments did not noticeably change by increasing the temperature until the system temperature approached the dissociation point of gas hydrate. Once hydrate is dissociated both dynamic shear and bulk modulus decreased sharply.

The pore pressure in the experiment conducted under undrained condition (i.e., very low permeability formations) increased significantly during gas hydrate dissociation. It almost followed the hydrate phase boundary of the methane hydrate (P versus T plot).

2.8 References

2.1 R. Narayanasamy, *Quantifying the effects of partial saturation on sand production prediction and geomechanical responses of reservoirs*, Institute of Petroleum Engineering, Heriot-Watt: Edinburgh, 2007

2.2 E. Spangenberg, J. Kulenkampff, *Physical properties of gas hydrate bearing sediments,* Proceedings of the Fifth International Conference on Gas Hydrate, Trondheim, Norway, 2005

2.3 E. Fjaer, R. M. Holt, P. Horsrud, A. M. Raaen, R. Risnes, *Petroleum related rock mechanics*, Elsevier, 2008

Chapter 3 –Mechanical Behaviour and Geophysical Properties of Gas Hydrate-Bearing Sediments

3.1 Introduction

The first series of experiments explained in the previous chapter were conducted to quantify the mechanical and geophysical properties of sediments containing gas hydrate and mechanical degradation of those sediments as a function of temperature during gas hydrate dissociation. The second series of experiments were conducted with a different procedure to quantify the mechanical and geophysical properties of sediments containing gas hydrate before gas hydrate dissociation, as well as investigating the mechanical behaviour of sediments containing gas hydrate under uniaxial loading. The aim of this series of experiments was mainly to understand the behaviour of sediments containing gas hydrate under uniaxial loading (i.e., compaction). As a result, unlike the first series of experiments, in this series of experiments after measuring the static uniaxial compaction modulus, the sediments were loaded up to the maximum working pressure of the equipment. The continuous loading was applied by injecting hydraulic fluid (water) behind the overburden piston at rates from 0.001 to 0.005 cm^3/min, while the pore pressure was maintained constant using a backpressure regulator, which simulates drained conditions. Finally, after completion of the continuous loading step, the gas hydrate inside the samples was dissociated by depressurisation, instead of heating in order to investigate the mechanical behaviour of the sediments containing gas hydrate during depressurisation.

The experiments described in Chapters 2 and 3 were conducted using the same ultrasonic set-up explained in Section 2.2. As mentioned before, the ultrasonic set-up limits the radial deformation of a sample. As a result, a Triaxial setup was purchased and customised to meet the requirements of studying geophysical and mechanical properties/behaviour of sediments containing gas hydrate under real conditions found in deep offshore environments (e.g., Gulf of Mexico). The Triaxial setup can be used to measure the static modului and plastic parameters of a sample. The results of experiments conducted with the Triaxial setup are presented at the end of this chapter.

3.2 Experimental apparatus

All the experimental were conducted using the ultrasonic set-up developed at the Centre for Gas Hydrate Research at the Institute of Petroleum Engineering, Heriot-Watt University. The details of this setup were described in Section 2.2.

3.3 Test material

The test materials used in these experiments are the same as those in the first series of experiments explained in Section 2.3.

3.4 Experimental methodology

Figure 3.1 shows the procedure used to conduct this series of experiments. The sample preparation, hydrate formation, measuring sound speeds and calculating dynamic moduli are exactly identical to Section 2.4 and therefore they are not explained in this section. The last two steps, shown in Figure 3.1, are the only differences in this series of experiments.

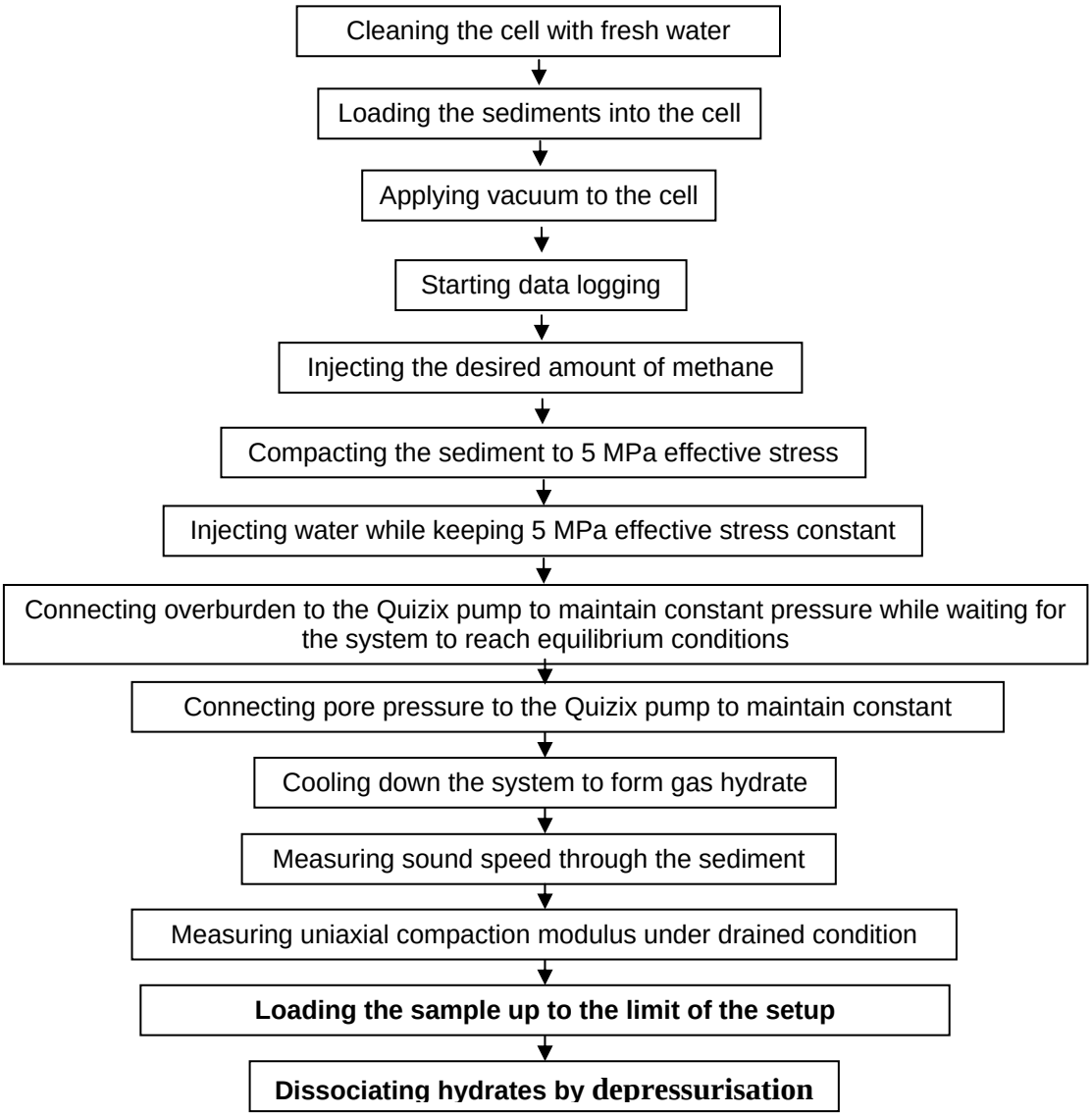

Figure 3.1 Summary of experimental procedure

3.4.1 Static uniaxial compaction modulus

In this series of experiments, the static uniaxial compaction modulus was measured at drained conditions at a controlled rate of loading. The loading and unloading were conducted by pumping water behind the moving piston of the vessel at a controlled rate as shown in Figure 3.2. The rate of water injection behind the piston was kept constant during measuring uniaxial compaction modulus in this series of experiments.

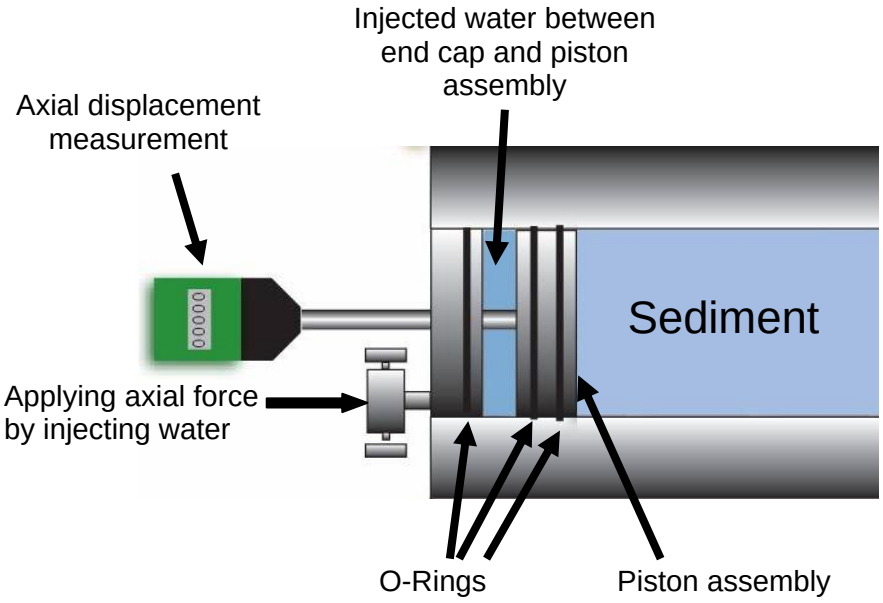

Figure 3.2 Schematic of the piston assembly

The rate of fluid injection/withdrawal behind the moving piston during loading and unloading were set at 0.001-0.005 cm^3/min and 0.0005-0.0025 cm^3/min, respectively. These rates were selected through trial and error with the aim of maintaining the pore pressure at a near constant value (the pore pressure was kept constant to within ± 0.01 MPa) . The piston movement (i.e., axial strain) and axial load were measured through three cycles of loading and unloading. The samples were loaded up to 0.69 MPa during the loading of each cycle. The piston movement was in a range of 0.001 to 0.05 mm. The axial strain and load were used to calculate static uniaxial compaction modulus using Equation 2.5. The average value of the three calculated the static uniaxial compaction modulus measurements resulting from each cycle of loading-unloading and was reported as the final value of static uniaxial compaction modulus for each experiment.

3.4.2 Continuous loading under drained conditions

After completing the static uniaxial compaction modulus measurements, the samples made were continuously loaded using the same loading rate used for measuring static compaction modulus (i.e., 0.001-0.005 cm^3/min) to understand their mechanical behaviour in the presence of gas hydrates. The loading was continued at a near constant rate until the axial load reached the maximum working pressure of the set-up (i.e., 42 MPa). As before, the pore pressure was kept near constant with the aim of the

Quizix pump. However, fluctuations within ± 0.2 MPa in the pore pressure were observed due to the partial blockage of the drainage ports by fine grains during drainage. The axial load, axial displacement, pore pressure and temperature were logged during continuous loading.

3.4.3 Hydrate dissociation by depressurisation at drained conditions

Once continuous loading was completed the gas hydrate inside the pore space was dissociated by depressurisation. The temperature was kept constant and the pore pressure was decreased by continuous withdrawal of the fluids from the test cell at a constant rate 0.01 cm^3/min. Figure 3.3 shows the phase boundary of methane hydrate and the thermodynamic conditions for gas hydrate dissociation by depressurisation.

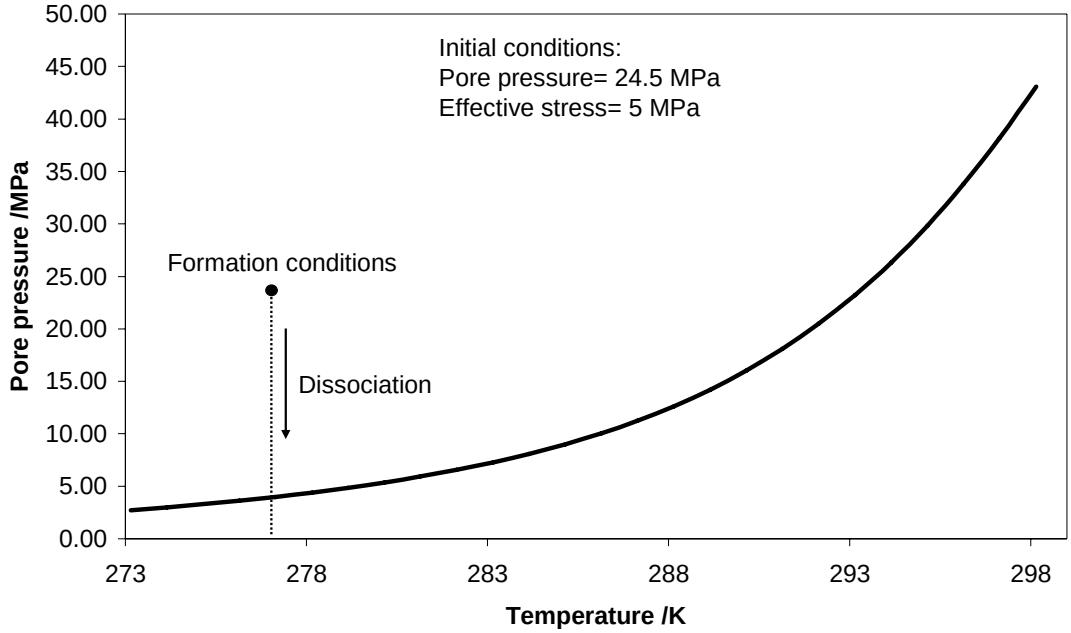

Figure 3.3 Hydrate phase boundary and hydrate formation conditions for the system investigated in this work.

3.5 Experiments conducted with Triaxial setup

In the previous sections, the experiments conducted on sediments with different mineralogy containing gas hydrate were explained. Those experiments were conducted using the setup includes a rigid stainless steel cylinder with a piston assembly as shown in Figure 2.8. The sediment inside the cylinder can be loaded and unloaded axially using the piston assembly without any control on the magnitude of the radial displacements (i.e., lateral stresses), as the sediment is surrounded by the rigid stainless

steel cylinder. In order to measure the static moduli and plastic properties of sediments containing gas hydrate, a Triaxial setup was purchased and modified specifically for conducting triaxial experiments on sediments containing gas hydrates. The setup was not available until recently (i.e., the end of this study), and therefore there was not enough time to conduct experiments using sediments of different mineralogy, containing gas hydrate. The installation and commission of the setup took some considerable time and consequently only the results of experiments conducted with sand without gas hydrate are presented in this study. These results can be compared with the results of experiments conducted with sand containing gas hydrate in the future.

3.5.1 Triaxial setup

The Triaxial setup was purchased from VJTech ltd for conducting the experiments on samples containing gas hydrates. The setup includes the standard components used in soil mechanics. The specifications of the setup meet BS 1377 standards. The setup however was modified to meet the requirements of this study. The technical specifications of the setup are presented in Table 3.1. To summarise, the setup includes a rigid 250 kN load frame, a high pressure stainless steel cell with a working pressure up to 40 MPa and two high pressure, high volume, syringe pumps to control the confining pressure and pore pressure. The horizontal stresses in deep offshore environments are high, and as a result, in order to measure the mechanical properties of the sediments containing gas hydrate under realistic conditions, the Triaxial cell was built with stainless steel to withstand the high confining pressure applied in this study. Most of the Triaxial cells used in soil mechanics are designed to withstand very low confining pressures and are made of special plastic. The setup also includes 50 kN and 250 kN load cells to measure the axial load with high accuracy, a displacement transducer to measure axial displacement, a temperature probe to measure the cell fluid temperature and on sample radial displacement transducers to measure the lateral displacements of the sample. The schematic of the setup is shown in Figure 3.4.

Table 3.1 Technical description of the Triaxial setup

Description	Details
General	
De-Airing tank	
Capacity	19 litre
Operating pressure	Atmospheric-Vacuum
Vacuum pump	
Capacity	2 stages 40 litre/min
Syringe pumps	
Capacity	260 cm^3
Operating pressure	40 MPa
Flow rate	0.001-107 cm^3/min
Accuracy	0.5% of full scale
Triaxial cell	
Operating pressure	40 MPa
Tested pressure	70 MPa
Capacity	For samples up to 100 mm diameter
Current base pedestal	50 mm diameter with 5 ports
Current top cap	50 mm diameter with one port
Reserve top cap and based pedestal	50 m diameter top cap with two ports, housing a sonic transducer. 50 mm diameter based pedestal with 5 ports, housing a sonic transducer
Special feature	Balanced ram
Displacement transducers	
Axial displacement	25 mm displacement transducer with 5-pin DIN plug
Radial displacement	High pressure on-sample calliper set 50 mm diameter

Table 3.1 Technical description of the Triaxial setup (contd.)

Description	Details
Load frame	
Model	TriScan 250 Advanced
Capacity	250 kN
Height	2300 mm
Width	900 mm
Length	850 mm
Vertical clearance	1100 mm
Horizontal clearance	550 mm
Platen diameter	158 mm
Speed range	0-10 mm/min
Weight	600 kg
Power supply	110-240 V AC
Width	900 mm

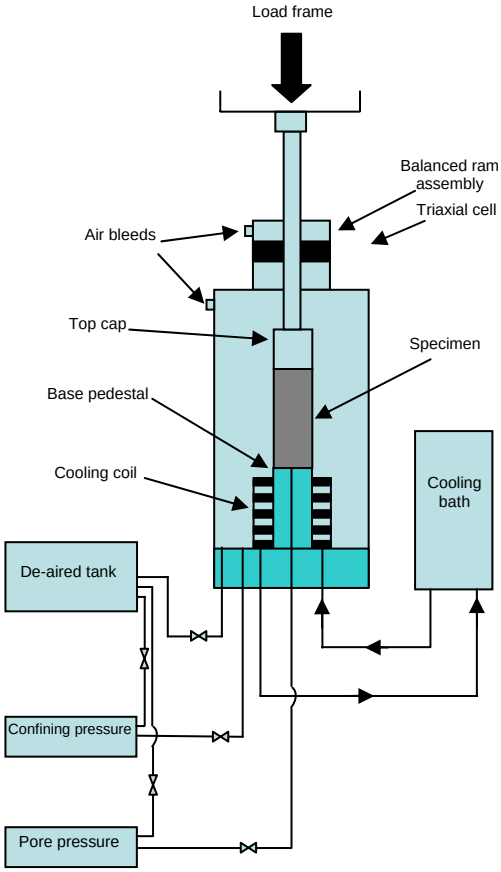

Figure 3.4 Schematic of the Triaxial setup

The setup is controlled by a computer using a microprocessor based system incorporating a large graphic display and a 20 key membrane key pad for data entry. The built-in four stand alone data logger allows data acquisition from load, displacement, pore pressure and volume change transducers. Various components of the setup monitor different measurements whilst running an experiment, and can be controlled using the software package provided with the computer.

The base pedestal and top cap are designed to house ultrasonic transducers for measuring sonic velocities during the running of an experiment. The sonic velocities however were not measured during this study as the system was just commissioned. The other feature that makes this setup ideal for measuring the mechanical properties of the sediments containing gas hydrates is its capability of cooling down the sample to the desired temperature. The sample can be cooled down using the cooling coil provided inside the cell around the base pedestal, and the cooling bath connected to the cooling coil as shown in Figure 3.5.

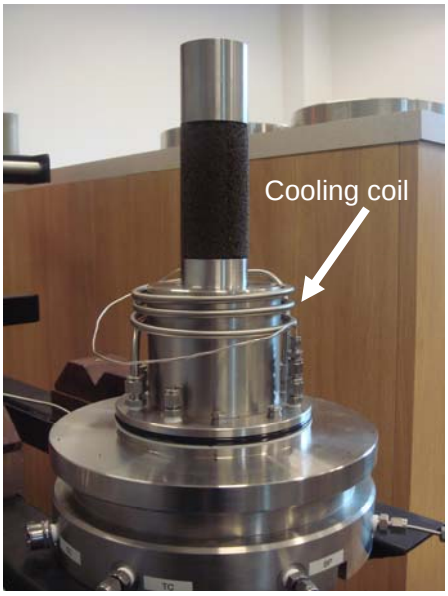

Figure 3.5 Picture of cooling coil inside the cell

The cooling bath circulates coolant of low temperature inside the cooling coil, and as a result, the temperature inside the cell containing the sample is decreased. The Triaxial cell is equipped with balanced ram technology which facilitates the use of the full loading capacity of the Triaxial frame.

3.5.2 Calibration of the setup

The pressure transducers, displacement transducers, load cell and volume measurement transducers were calibrated by the manufacturer and also by VJTech ltd prior to installation at the laboratory. The experiments were conducted soon after the installation and the commission of the setup (i.e., less than 6 months) and therefore the setup was not recalibrated.

3.5.3 Sample preparation method

A dry non-cemented samples were prepared for conducting triaxial experiments. A 50 mm rubber membrane was stretched over the base pedestal and was fixed on the base pedestal using three O-rings. The first porous disc was placed on the base pedestal. A three piece split mould was placed around the membrane and the top portion of the membrane was stretched over the mould. The test material (i.e., sand) was poured into the mould. Once the mould was filled with the test material, the sample was tapped slightly to provide a smooth surface on the top. The second porous disc was placed on top of the sample followed by the top cap with ports connecting it to the base pedestal.

The rubber membrane was then folded over the top cap and fixed with three O-rings. All the valves connected to the sample were closed and vacuum with 0.096 MPa pressure was applied to the sample from ports connected to the base pedestal. After applying the vacuum, the three-piece split mould was removed. The dimensions of the sample were measured using a digital calliper and a ruler. The radial displacement transducer was mounted on the sample and the sample was ready for starting the experiment as shown in Figure 3.6. The stainless steel cell was fitted onto the base pedestal and held in place using the special locking system as shown in Figure 3.7. The cell was filled with de-aired water. The valve of the supplied de-aired water was closed once the cell was filled. The axial displacement transducer was installed. The program was started to log the axial displacement, radial displacement, axial load, confining pressure, pore pressure, cell volume and pore volume.

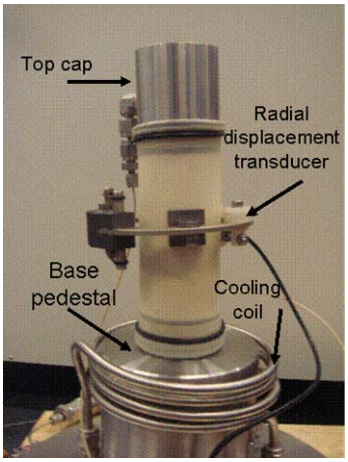

Figure 3.6 Picture of a prepared sample

Figure 3.7 Locking system of the Triaxial cell to the base pedestal

Once the confining pressure was set to the desired level, the sample was saturated with de-aired water. The pore pressure was increased to 24 MPa by injecting water. The confining pressure was increased at the same time as the pore pressure by injecting de-aired water whilst keeping the initial effective stress constant. The system was then cooled down to 278.05 K to simulate the seabed temperature in deep offshore environments. The sample was sheared by applying axial load at a speed of 0.01% strain/second at drained condition as reported by Edinima, et al [3.1].

The initial aim was to apply 5 MPa confining pressure on dry samples (i.e., 5 MPa effective stress) and conduct triaxial experiments under the same conditions used in the previous experiments. Figures 3.8 and 3.9 show the results of the first two experiments.

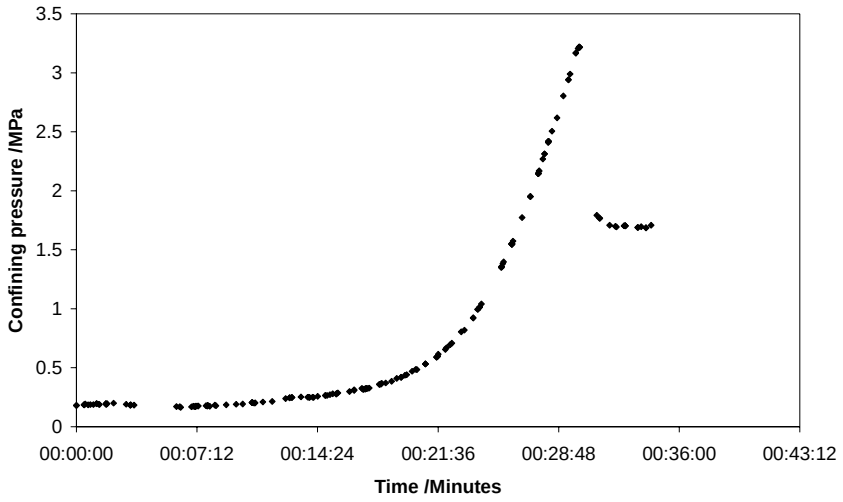

Figure 3.8 Confining pressure versus time

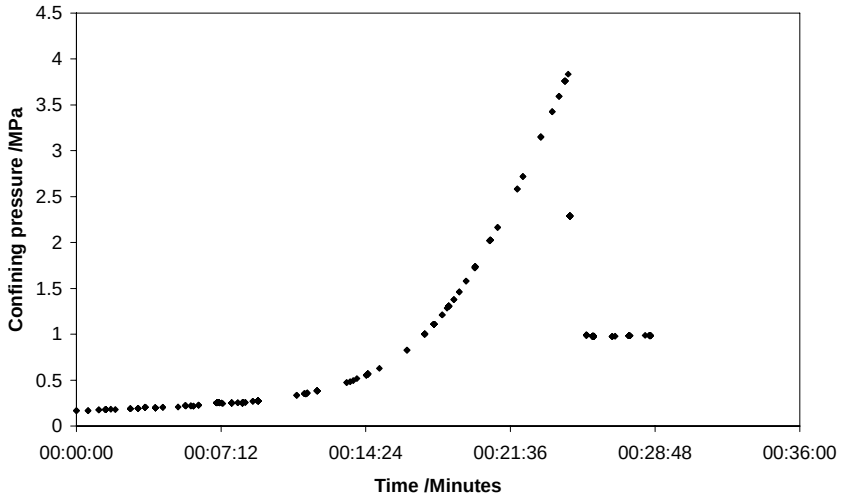

Figure 3.9 Confining pressure versus time

As shown in the above figures the effective pressure cannot be increased to more than 3 MPa. Above 3 MPa, the confining fluid (i.e., de-aired water) breaks through the sample, leading to communication between the pore fluid and confining fluid. It was decided to conduct a multi-stage triaxial experiment with 1 MPa initial effective confining pressure and 0.5 MPa pressure increments till the confining fluid breaks through the sample. In addition to the multi-stage triaxial experiment, two single-stage triaxial experiments were conducted under 1.5 and 2 MPa effective confining pressure. The conventional triaxial experiment (single-stage triaxial experiment) involves the breakage of at least three samples under three different confining pressures and

obtaining their peak strengths. Obviously, this technique requires three identical samples. As mentioned before, preparing samples containing exactly the same gas hydrate saturation is very difficult. However, several peak strengths can be obtained from a single sample in a multistage triaxial experiment. The multistage triaxial experiment involves applying the first confining pressure and then applying axial load until the sample deforms plastically. The confining pressure is then increased and axial loading is continued until the sample starts deforming plastically under new confining pressure conditions. This procedure is continued for as many stages as desired [3.2], [3.3]. In this study, the peak strengths of the multistage triaxial experiment were compared with those of single-stage triaxial experiments (conducted under 1.5 and 2 MPa confining pressures) to examine the reliability of multistage triaxial experiments. The results of the experiments are detailed below.

3.6 Results

The results of experiments conducted using the Triaxial setup are presented in Section 3.6.3. Eight experiments were conducted using the ultrasonic setup including four experiments conducted with silica sand with different gas hydrate saturations, three more experiments conducted with silt with different methane hydrate saturations, and the last experiment conducted with a mixture of silt and clay. Three of the eight experiments were conducted without forming gas hydrate. The aim was to understand the mechanical and geophysical properties of those sediments without gas hydrate. The results of these experiments were compared with the results of experiments conducted with the same sediments containing gas hydrate. The difference shows the effect of the gas hydrate on the mechanical and geophysical properties of the gas hydrate bearing sediments. The results of the experiments conducted using the ultrasonic setup are reported based on saturations in Tables 3.2 to 3.5 to facilitate comparison.

3.6.1 Mechanical and geophysical properties before hydrate dissociation

Parameters of the sediments used

Table 3.2 shows the properties of samples used in this series of experiments. Initial porosity (i.e., φ_0) was calculated based on the volume of injected gas/water, after compaction of a sample and before gas hydrate formation. Porosity of the sample after

hydrate formation (i.e., φ_h) was calculated using equation 2.7 which was explained in the previous chapter.

Table 3.2 Properties of the sediment samples used in the experiments

Experiment number	Sediment composition	Hydrate saturation (S_h)/ %	Initial porosity φ_0 / %	Porosity after hydrate formation (φ_h)/ %	Free gas/ %
13	Sand	0	44.9	45	2
9	Sand	3.8	45	43.52	1.8
10	Sand	10	47	42.29	4.1
11	Sand	44.6	45.8	25.41	8
14	Silt	0	35.32	34.39	2
12	Silt	5.4	36.7	33.67	1.5
15	Silt	52.9	37.2	16.88	9.1
16	80 % Silt+20 % Ka	0	36.53	36.54	2

Measured sound speed (Geophysical Properties)

The measured sound velocities in this series of experiments are shown in Table 3.3. The velocity of shear wave in Experiment 13 was not logged as the communication between the ultrasonic transducer and receiver was lost during the experiment.

Table 3.3 Measured sound velocities in the experiments

Experiment Number	Sediment Composition	Hydrate saturation (S_h)/ %	Free gas / %	Velocity of P-wave / km/s	Velocity of S-wave / km/s
13	Sand	0	2	1.69	N/A
9	Sand	3.8	1.8	1.76	1.3
10	Sand	10	4.1	1.8	1.15
11	Sand	44.6	8	1.96	1.20
14	Silt	0	2	1.6	0.79
12	Silt	5.4	1.5	1.82	1.08
15	Silt	52.9	9.1	3.20	1.58
16	80 % Silt+20 % Ka	0	2	1.74	0.97

As shown in Table 3.3, the velocity of compressional wave in sand samples increases with the increase in gas hydrate saturation from 0 % to 44.6 %. However, the measured velocity of shear wave does not show a meaningful increase with gas hydrate saturation.

Figure 3.10 shows the velocity of compressional waves in silt samples, presented in Tables 2.2 and 3.3. As shown in this figure the velocity of the compressional wave increases by increasing the gas hydrate saturation from 0% to 52.9 %. Furthermore, it increases significantly when the gas hydrate saturation is more than 40 %. This agrees with the result of experiments conducted with the samples containing THF hydrate [3.4]. The velocity of shear waves in silt samples, presented in Tables 2.2 and 3.3 are shown in Figure 3.11. They do not increase significantly until the gas hydrate saturation is higher than 40%. The velocity of shear waves in the sample with 52.9% gas hydrate saturation is significantly higher than others.

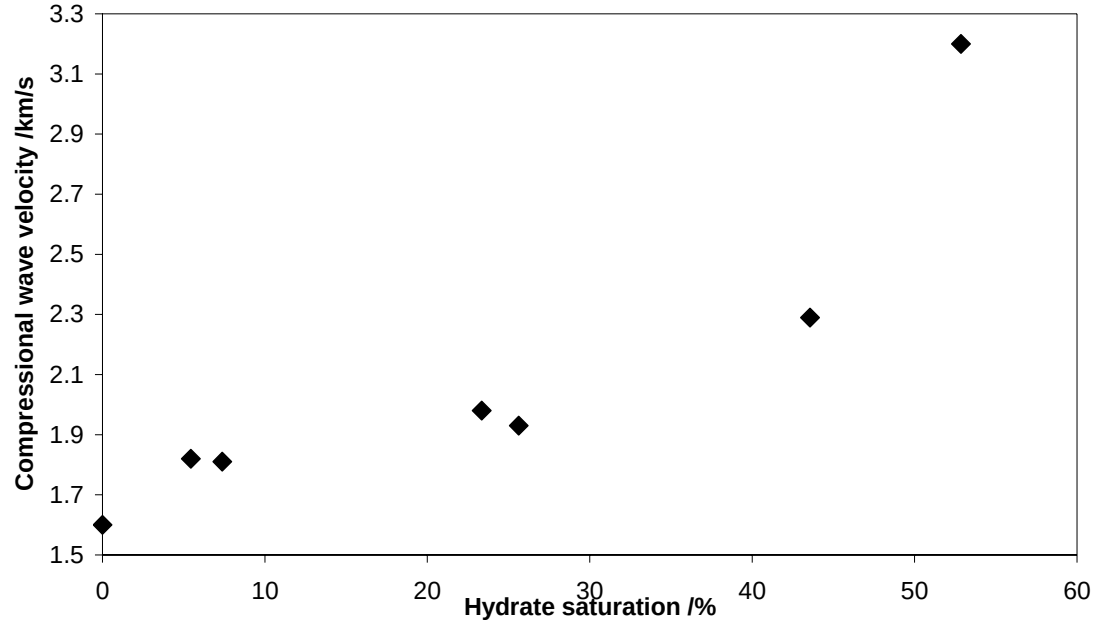

Figure 3.10 Measured compressional wave velocities as a function of hydrate saturation in the sediments containing silt and gas hydrate (i.e., Experiments 1, 2, 3, 8, 12, 14, 15).

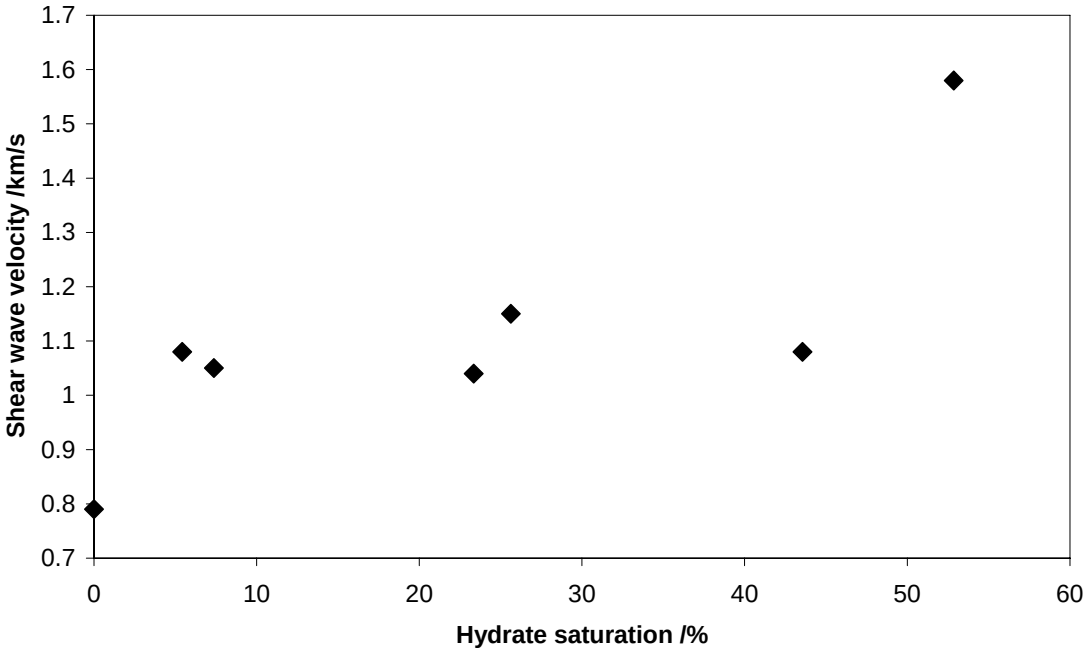

Figure 3.11 Measured shear wave velocities as a function of hydrate saturation in the sediments containing silt and gas hydrate (i.e., Experiments 1, 2, 3, 8, 12, 14, 15).

Dynamic moduli

The dynamic bulk and shear modulus, calculated using Equations 2.3 and 2.4, are shown in Table 3.4 for this series of experiment.

Table 3.4 Calculated dynamic moduli

Experiment Number	Sediment Composition	Hydrate saturation (S_h)/ %	Dynamic Shear modulus/ GPa	Dynamic Bulk modulus/ GPa
13	Sand	0	N/A	N/A
9	Sand	3.8	3.54	1.77
10	Sand	10	2.84	3.17
11	Sand	44.6	3.18	4.25
14	Silt	0	1.47	4.08
12	Silt	5.4	2.73	4.12
15	Silt	52.9	5.80	16.07
16	80 % Silt+20 % Ka	0	2.27	4.29

As mentioned before shear wave velocity was not recorded, and as a result, the dynamic bulk modulus and shear modulus were not calculated in Experiment 13. The dynamic bulk modulus of sand samples increased with an increase in gas hydrate saturation from 3.8% to 44.6%. Therefore the presence of gas hydrate strengthens the sediments' stiffness and improves their mechanical properties. Figure 3.12 shows the dynamic bulk modulus in silt samples with different gas hydrate saturation obtained from Tables 2.3 and 3.4.

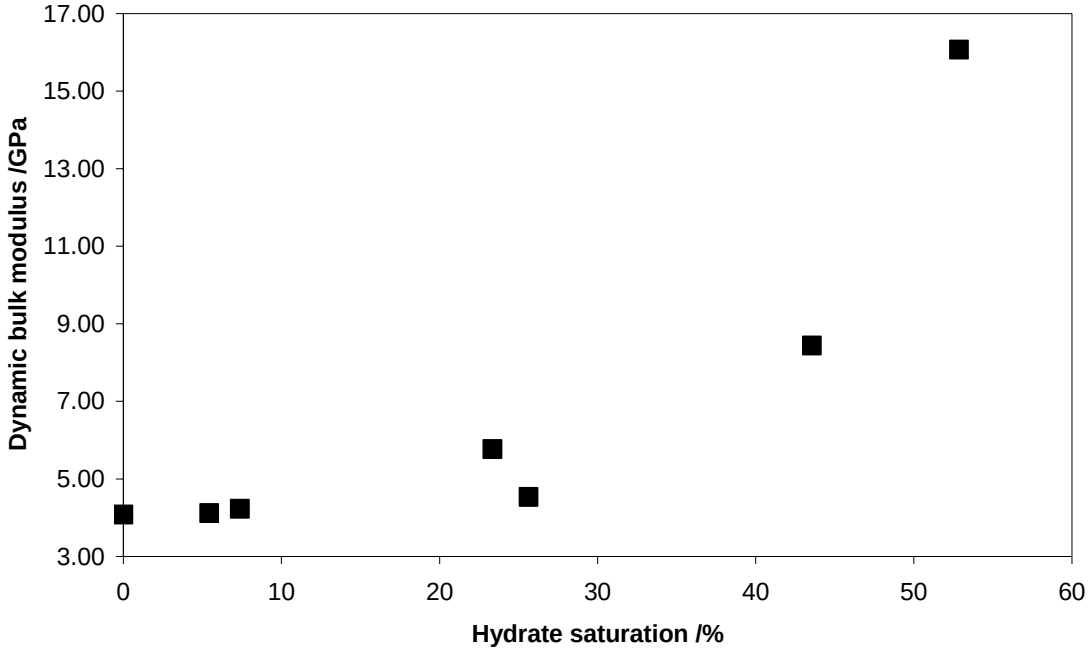

Figure 3.12 Dynamic bulk modulus of the sediments containing silt and gas hydrate as a function of hydrate saturation (i.e., Experiments 1, 2, 3, 8, 12, 14, 15)

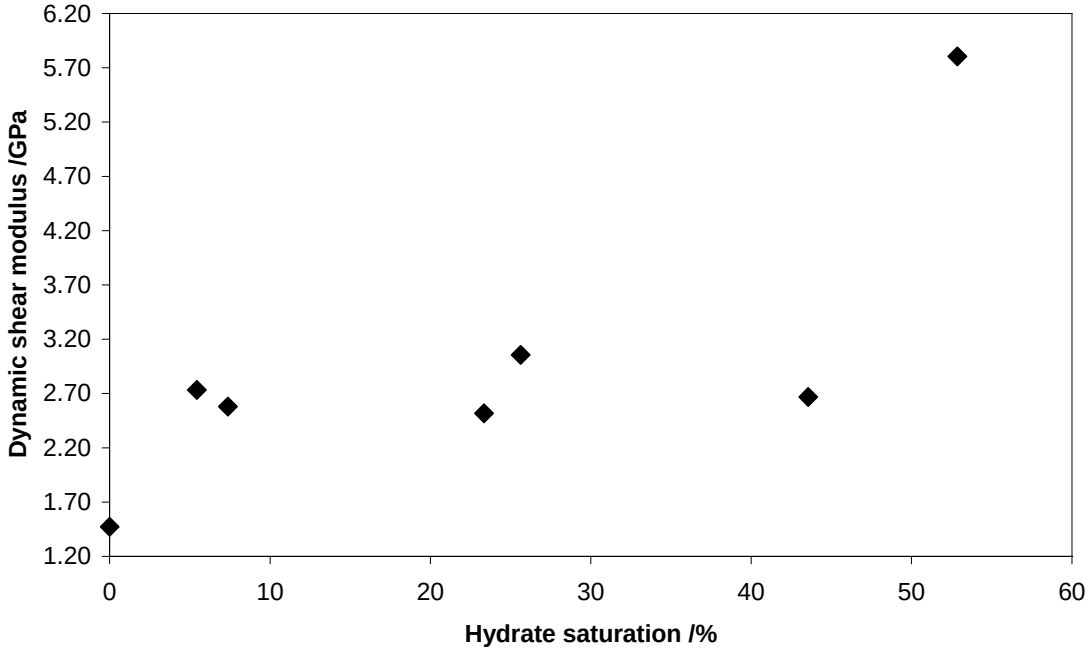

Figure 3.13 Dynamic shear modulus of the sediments containing silt and gas hydrates as a function of hydrate saturation (i.e., Experiments 1, 2, 3, 8, 12, 14, 15)

The dynamic bulk modulus in silt samples increases gradually with an increase in gas hydrate saturation with an exception at 25.6% which was possibly due to the presence of free remaining gas or/and the error in determining arrival time of S-wave (i.e., velocity measurement). It increases significantly when the gas hydrate saturation is more than 40%.

The dynamic shear modulus of the silt samples shown in Figure 3.13 was generated from results shown in Tables 2.3 and 3.4. The dynamic shear modulus in these samples increases slightly with an increase in gas hydrate saturation, with some fluctuations. The dynamic shear modulus (similar to the dynamic bulk modulus) increases significantly when gas hydrate saturation in the silt samples is more than 40%. Tables 2.3 and 3.4 show that the dynamic bulk modulus and the shear modulus increases with an increase in gas hydrate saturation and clay content in samples composed of mixtures of silt and kaolinite.

- ***Effects of sample mineralogy on the dynamic moduli***

Figures 3.14 and 3.15 show the dynamic bulk and shear modulus for sand and silt samples. As shown in these figures, the presence of gas hydrate has different effects on samples with different mineralogies as the dynamic bulk modulus of silt samples in the presence of gas hydrate is higher than sand samples. Also, it seems the dynamic bulk modulus of silty sediments containing high gas hydrate saturations is strongly affected by the presence of gas hydrate in comparison to the sand samples. However, there is no significant difference between the results of dynamic shear modulus in silt and sand samples.

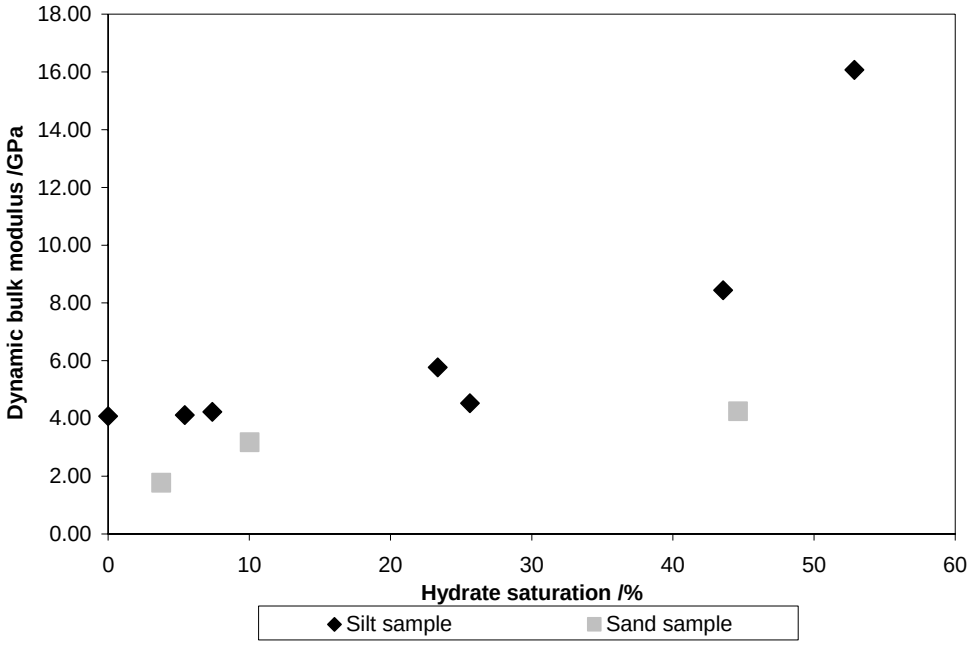

Figure 3.14 Dynamic bulk modulus of silt and sand samples containing gas hydrate as a function of hydrate saturation.

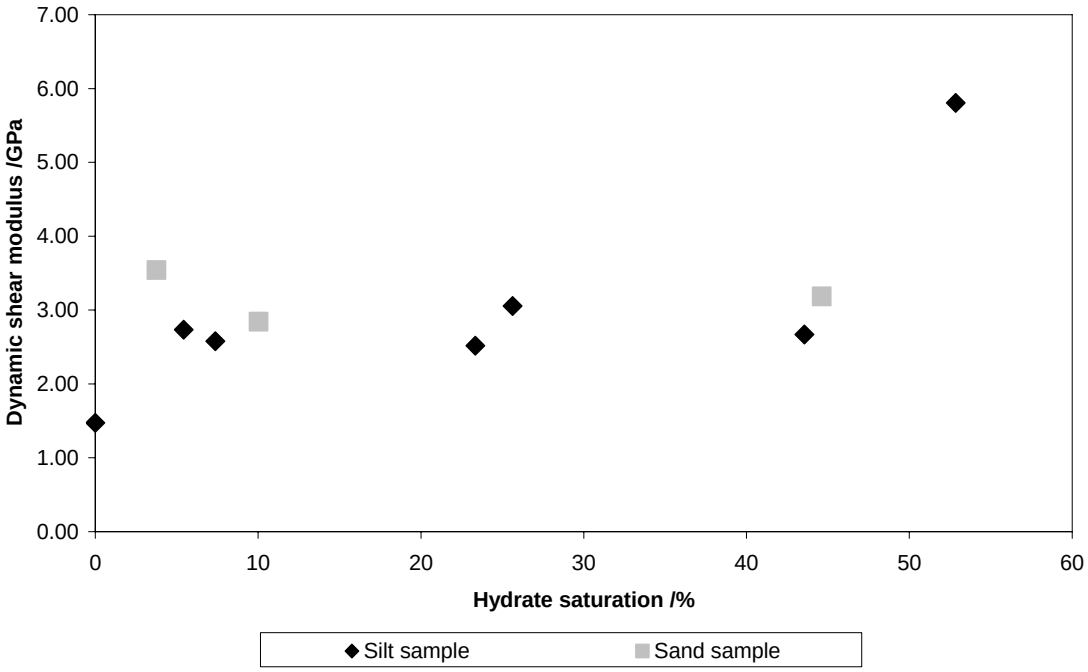

Figure 3.15 Dynamic shear modulus of silt and sand samples containing gas hydrate as a function of hydrate saturation.

Figures 3.16 and 3.17 show dynamic bulk and shear modulus of silt and clay-silt samples regardless of the type of the clay. It can be found from the figures that the

addition of 20 % clay to the silt samples in the present of gas hydrate does not have a significant effect on the dynamic bulk and shear modulus of the samples.

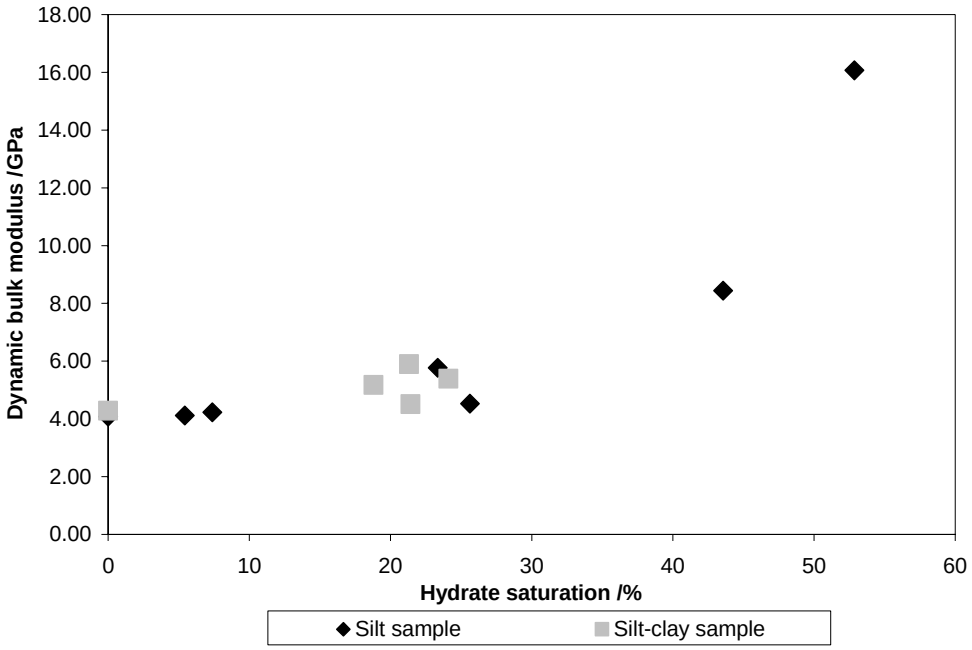

Figure 3.16 Dynamic bulk modulus of silt and clay-silt samples as a function of gas hydrate saturation.

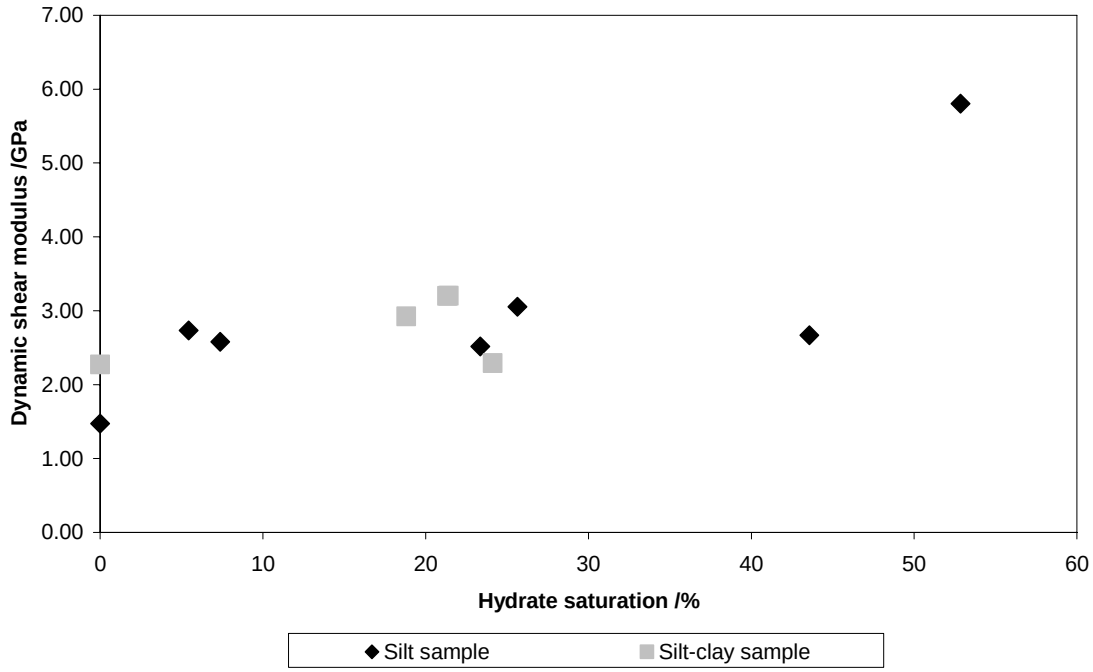

Figure 3.17 Dynamic shear modulus of silt and clay-silt samples as a function of gas hydrate saturation.

Static uniaxial compaction modulus

The results of static uniaxial compaction modulus measurements are shown in Table 3.5 for each experiment.

Table 3.5 The static uniaxial compaction modulus of samples containing gas hydrate

Experiment Number	Sediment Composition	Hydrate saturation (S_h)/ %	Static uniaxial compaction modulus/ GPa
13	Sand	0	15.41
9	Sand	3.8	15.00
10	Sand	10	18.83
11	Sand	44.6	30.64
14	Silt	0	1.38
12	Silt	5.4	21.35
15	Silt	52.9	37.80
16	80 % Silt+20 % Ka	0	14.44

As is shown in the above table, static uniaxial compaction modulus in silt samples increases as gas hydrate saturation increases, therefore, the presence of gas hydrate improves the mechanical properties of sediments composed of silt. The rate of loading and unloading during the measurement of static uniaxial compaction modulus in this series of experiments was different from the first series and therefore, the results of these experiments were not compared with the results of previous experiments conducted with silt.

The static uniaxial compaction modulus should be measured within elastic range of hydrate-bearing samples. Initially, the aim was to measure the static uniaxial compaction modulus with higher axial loads than the previous series (> 0.69 MPa) and therefore in Experiment 9 (the first experiment of this series of experiments), the sand sample with 3.8% gas hydrate was continuously loaded. It was found that the sample failed at 6.4 MPa (i.e., 1.4 MPa higher than initial effective stress) as shown in Figure 3.18. As a result, the static uniaxial compaction modulus in the rest of the experiments was conducted with 0.69 MPa maximum axial load to avoid sample failure.

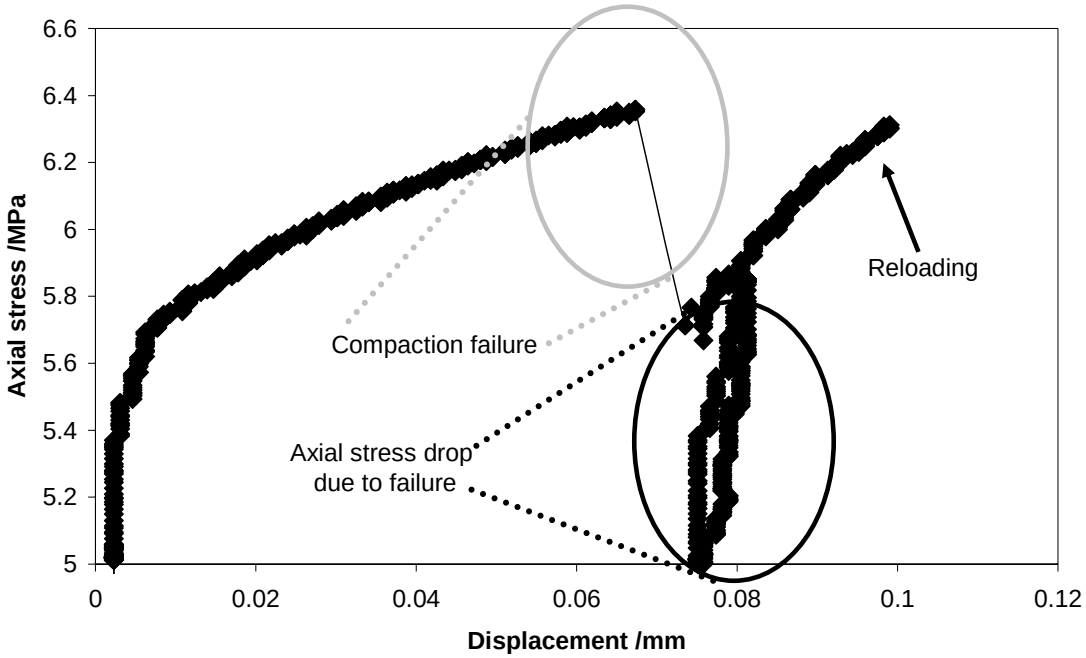

Figure 3.18 Determination of the maximum load for measuring static compaction modulus by continuous axial load after hydrate formation in Experiment 9.

Figure 3.19 shows the results of static uniaxial compaction modulus measurements in silt and sand samples containing gas hydrate. As expected, the static uniaxial compaction modulus in sand and silt increases as gas hydrate saturation increases, therefore, the presence of gas hydrates improves mechanical properties of sand and silt samples. It was observed that static uniaxial compaction modulus in sand with 3.8% gas hydrate is unexpectedly low. It could be explained by the fact that the values of static uniaxial compaction modulus shown in Table 3.5 for sand are an average of three static uniaxial compaction measurements for three cycles. However, static uniaxial compaction in Experiment 9 is obtained from only one cycle of loading-unloading as the sample failed after the first cycle. It should be mentioned here that the value of static uniaxial compaction in the first cycles in all experiments with sand were lower than the average value of the three cycles which might be related to relative low compaction of the loaded sediments.

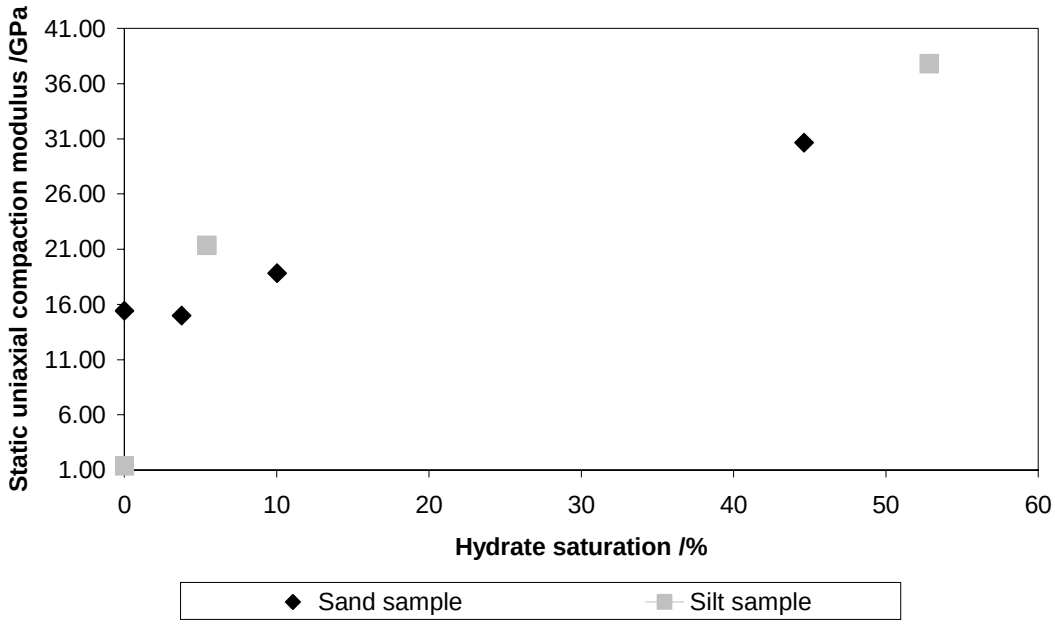

Figure 3.19 Static uniaxial compaction modulus as a function of hydrate saturation in the experiments with sand and gas hydrates

Continuous loading

Figures 3.20 to 3.24 show the axial load versus axial displacement in the experiments with sand.

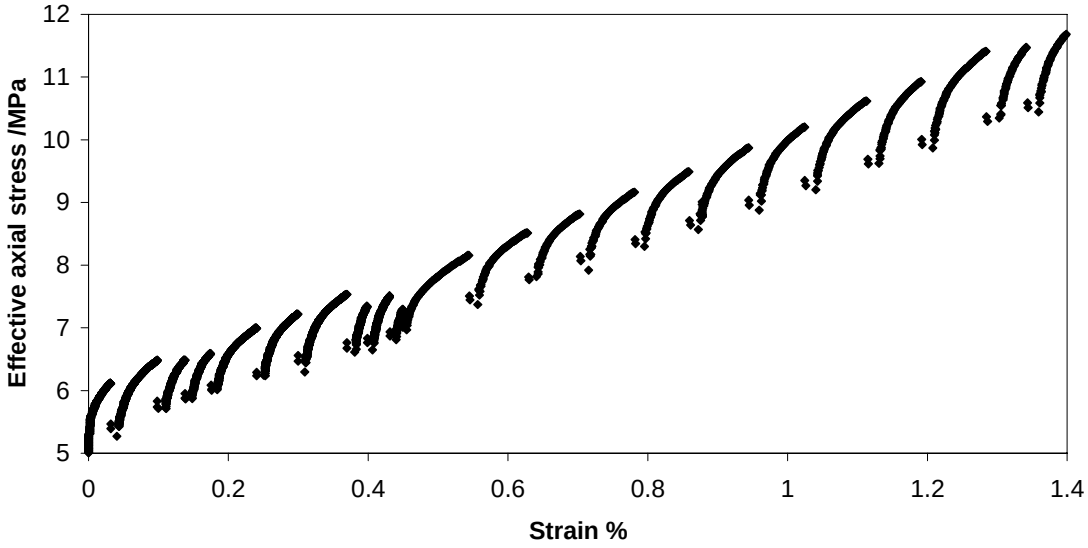

Figure 3.20 Uniaxial compaction of Experiment 13 (sand without gas hydrate) during continuous loading.

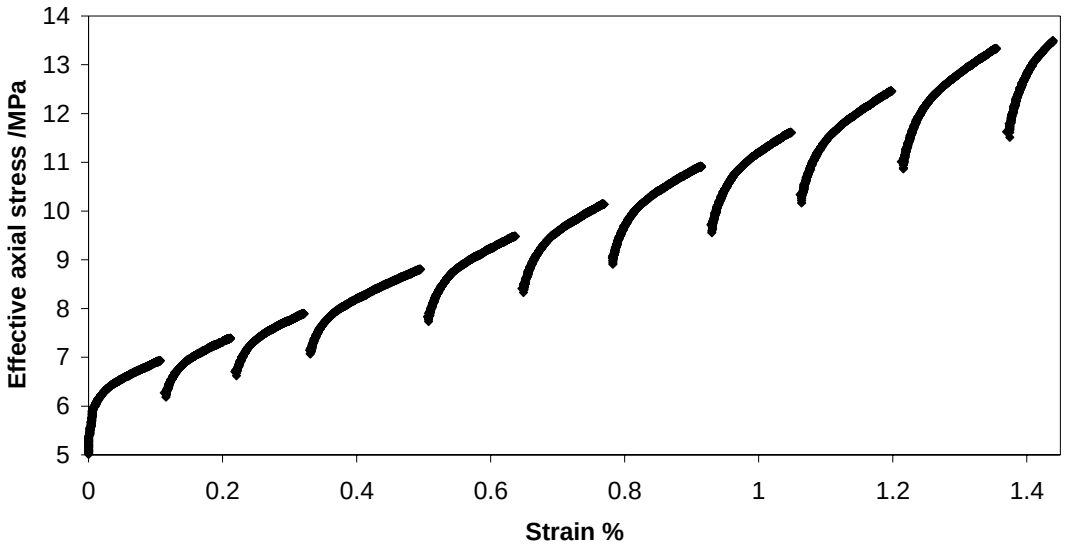

Figure 3.21 Uniaxial compaction of Experiment 9 (sand containing 3.8 % gas hydrate) during continuous loading.

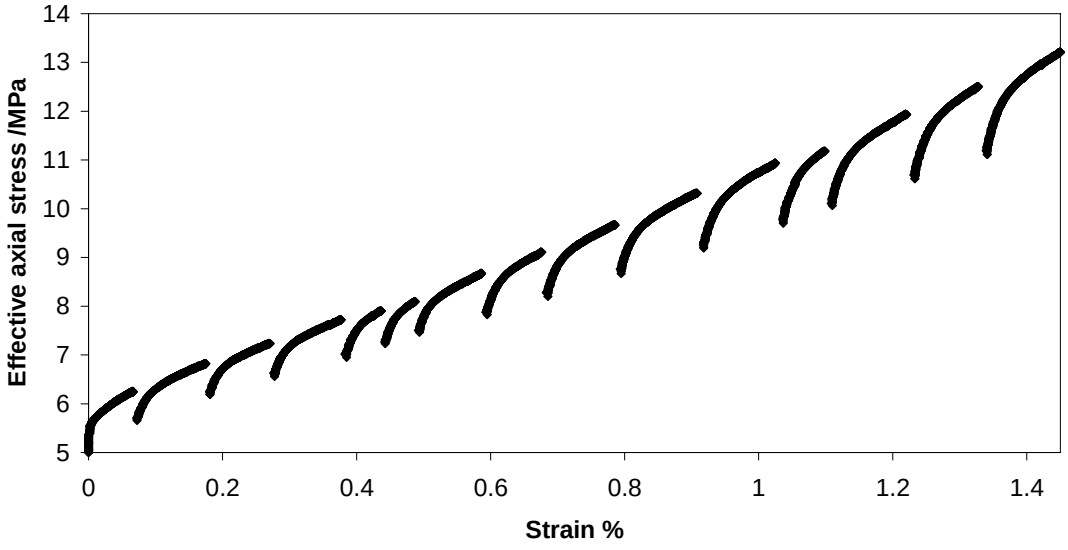

Figure 3.22 Uniaxial compaction of Experiment 10 (sand containing 10 % gas hydrate) during continuous loading.

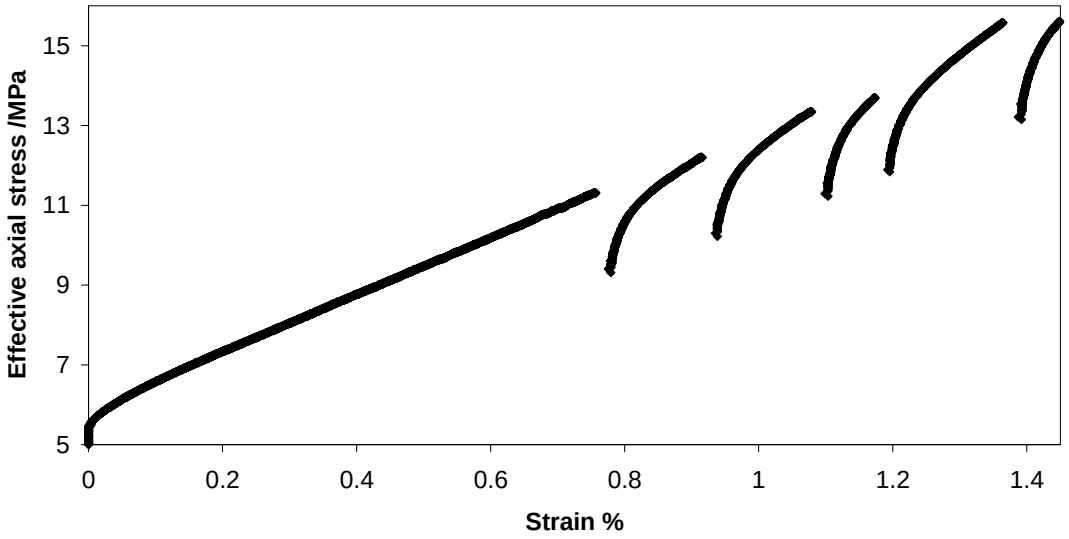

Figure 3.23 Uniaxial compaction of Experiment 11 (sand containing 44.6 % gas hydrate) during continuous loading.

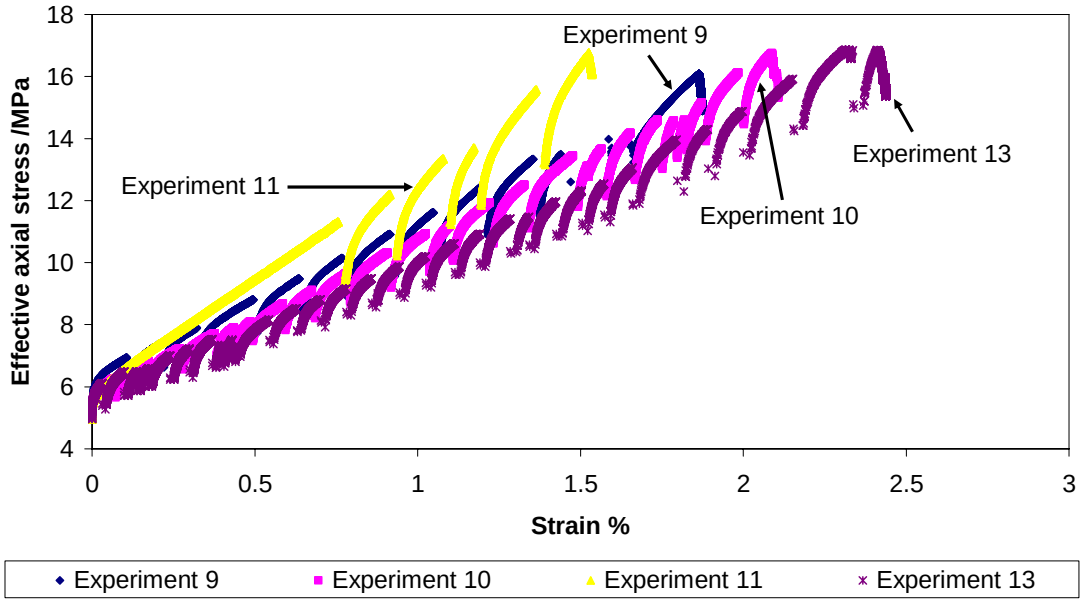

Figure 3.24 Uniaxial compaction of Experiment 9 (sand containing 3.8% hydrate), Experiment 10 (sand containing 10% hydrate), Experiment 11 (sand containing 44.6 % hydrate) and Experiment 13 (sand without hydrate) during continuous loading.

As shown in Figures 3.20 to 3.24, several stress drops occurred during continuous loading. The multiple stress drops might be a result of static versus dynamic friction factors. In other words, the piston assembly needed a threshold pressure difference to start moving inside (due to static friction factor between the moving piston and the internal cell body), and when that threshold pressure difference met, the piston assembly moved suddenly (due to the fact that dynamic friction factor between the moving piston and the internal cell body is lower than static friction factor) inside and caused dropping in the axial stress (i.e., pressure behind the moving piston). Therefore, an extra experiment was conducted in order to clarify this assumption. The experiment was conducted by filling the cell with a mixture of water and 2% nitrogen gas to simulate the presence of water and free gas without any sand (hence, no mechanical failure). The reason that nitrogen was used is that the solubility of nitrogen in water is negligible. The axial load was increased with a constant rate to the maximum working pressure of the setup. The axial load and displacement were logged during loading. Figure 3.25 shows the effective axial stress versus axial strain measured in this experiment. As can be seen, there are no such stress drops during loading. Therefore, the multiple stress drops in the previous experiments might be related to the mechanical behaviour of the sediment samples in the presence and absence of gas hydrate.

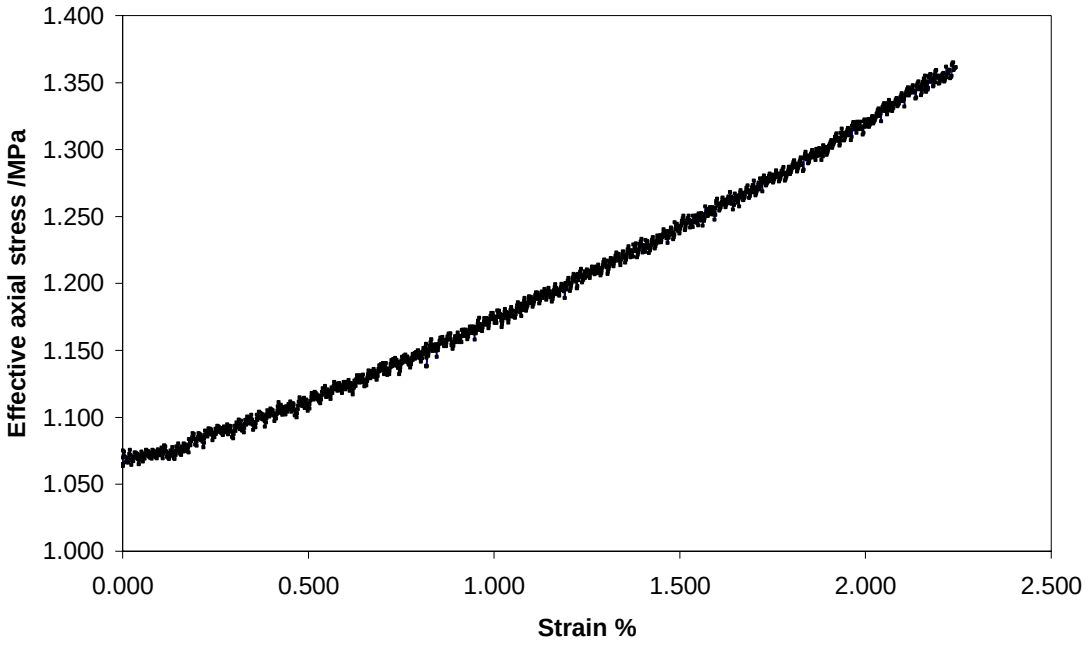

Figure 3.25 Uniaxial compaction of water with 2% Nitrogen gas

The slope of axial stress versus axial strain is defined as compaction stiffness in this study. Figure 3.24 shows that the compaction stiffness increases in sand samples by increasing the saturation of gas hydrate. It means that the presence of gas hydrate strengthens the structure and skeleton of a sand sample and as a result, increases the load bearing capacity of sediments. However, this improvement is not significant when the gas hydrate saturation is low as there is no noticeable difference in the compaction stiffness between Experiments 9 and 10.

Figure 3.26 shows the result of continuous loading for the experiments without gas hydrate. It can be found that the compaction stiffness of the experiment with sand (i.e., Experiment 13) is higher than silt (i.e., Experiment 14) and a mixture of silt with kaolinite (i.e., Experiment 16). Figure 3.27 shows the result of continuous loading for experiments presented in Table 3.2. It can be found that Experiment 15 has the highest compaction stiffness and Experiment 16 has the lowest compaction stiffness. The compaction stiffness is decreasing by moving from the left to the right of Figure 3.27.

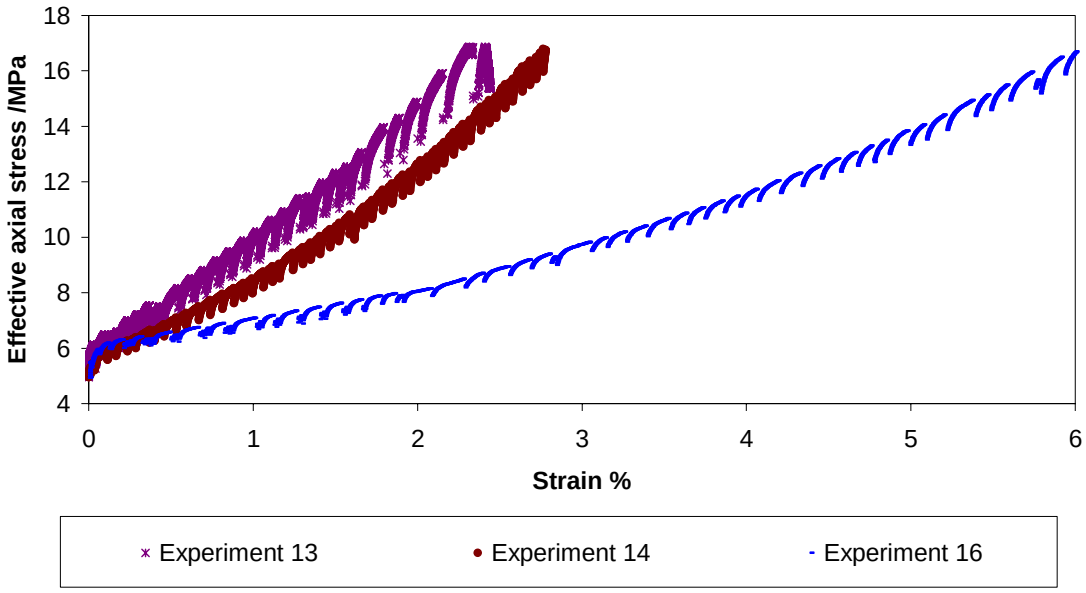

Figure 3.26 Uniaxial compaction of Experiment 13 (sand without hydrate), Experiment 14 (silt without hydrate) and Experiment 16 (silt and 20% kaolinite without hydrate)

.

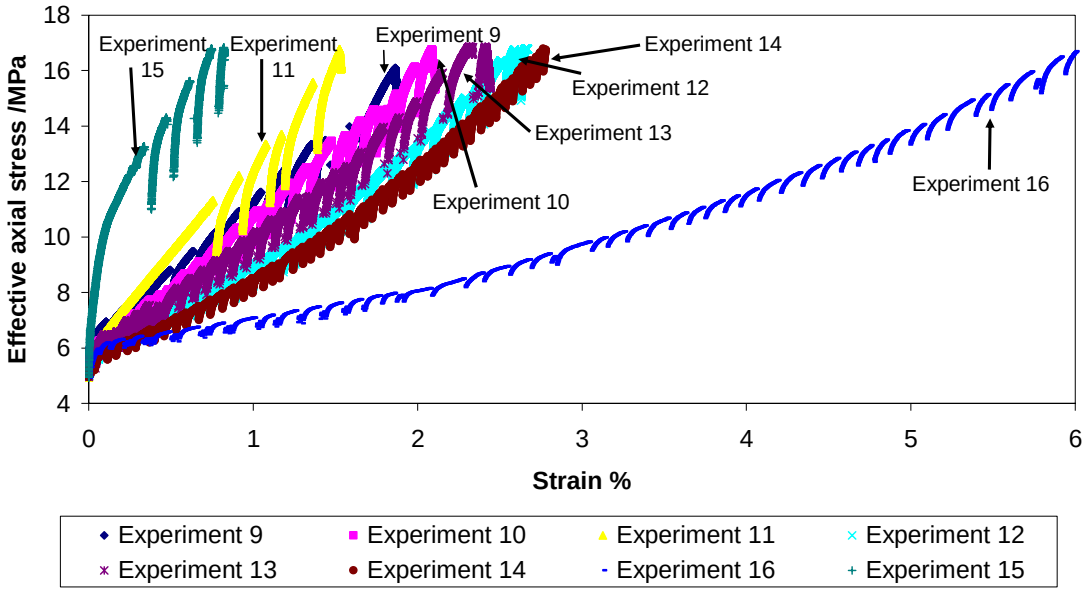

Figure 3.27 Uniaxial compaction of Experiment 9 (sand containing 3.8% hydrate), Experiment 10 (sand containing 10% hydrate), Experiment 11 (sand containing 44.6% hydrate), Experiment 12 (silt containing 5.4% hydrate), Experiment 13 (sand without hydrate), Experiment 14 (silt without hydrate), Experiment 15 (silt containing 52.9% hydrate) and Experiment 16 (silt with 20% kaolinite without hydrate).

3.6.2 Dissociation by depressurisation

After completion of the continuous loading, the pore pressures in Experiments 14, 15 and 16 were decreased to dissociate gas hydrates and to investigate the effect of hydrate dissociation on the geomechanical properties of hydrate-bearing sediments. The depressurisation process was continued even after sample failure in the compaction process. During depressurisation the axial stress (overburden pressure) was kept constant and pore pressures were reduced by withdrawing fluids from the test cell at constant rate of 0.01 cm^3/min. The axial stress and pore pressure were logged during depressurisation.

Figures 3.28 to 3.30 show axial deformation versus effective stress during depressurisation process in the experiments. A axial deformation increases as effective stress increases due to a decrease in the pore pressure.

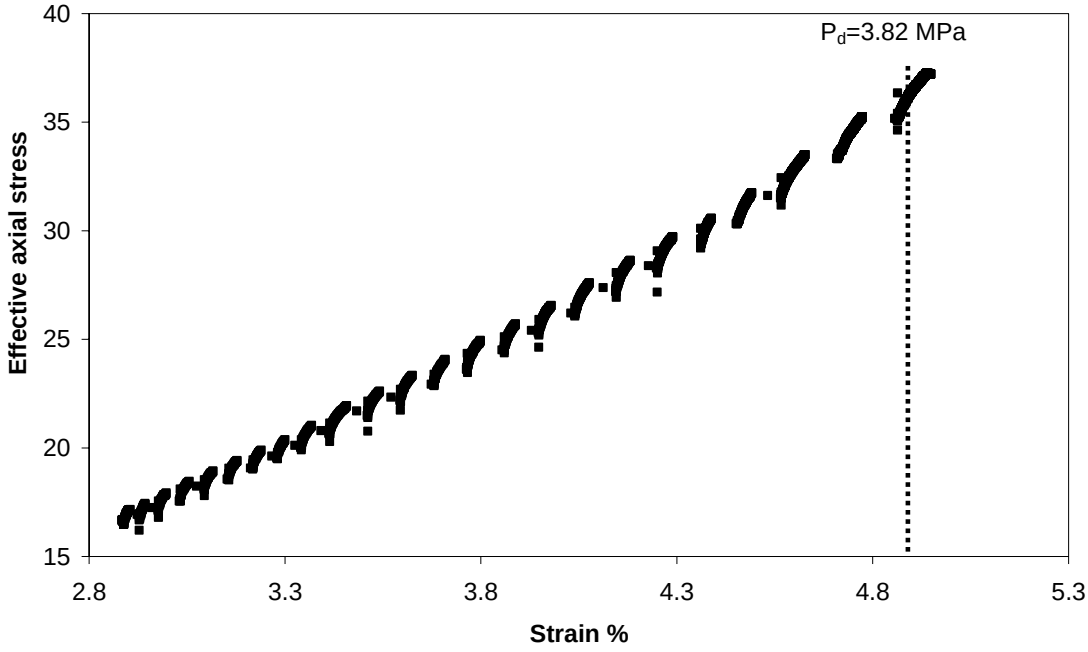

Figure 3.28 Uniaxial compaction in Experiment 14 (silt without gas hydrate) during depressurisation (P_d represents dissociation pressure at 277.15 K temperature).

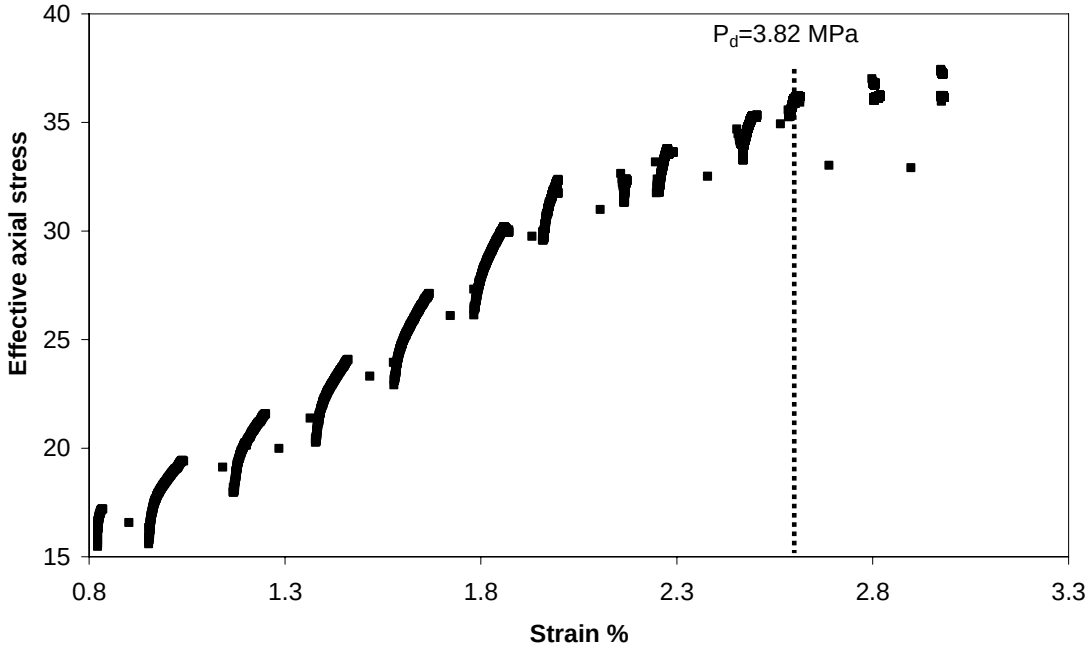

Figure 3.29 Uniaxial compaction in Experiment 15 (silt containing 52.9% hydrate) during depressurisation (P_d represents dissociation pressure at 277.15 K temperature).

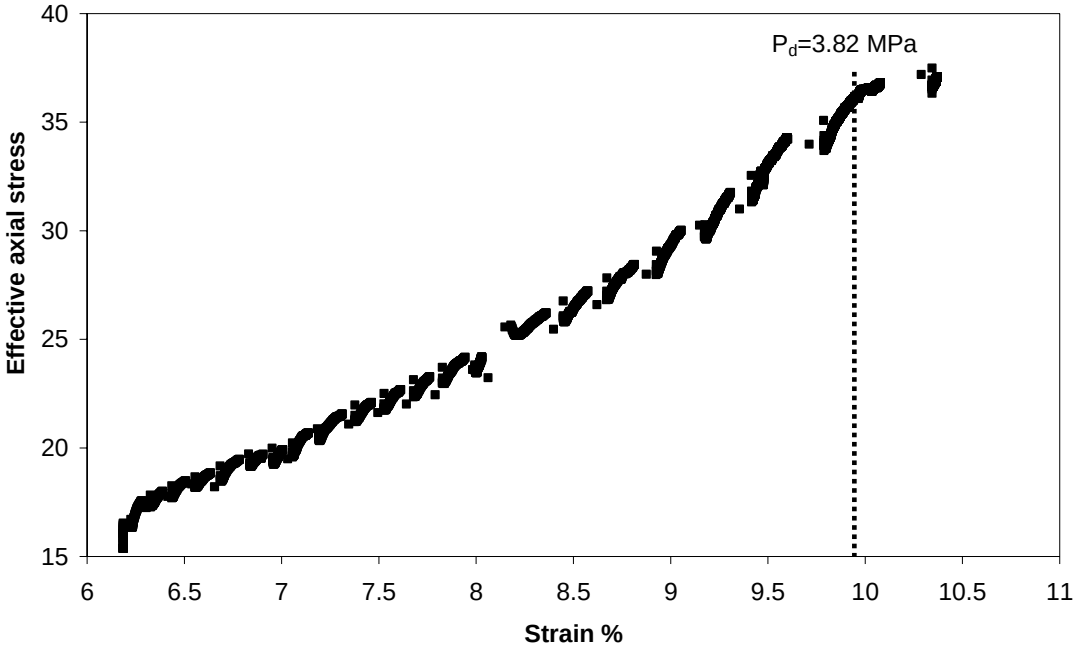

Figure 3.30 Uniaxial compaction in Experiment 16 (silt and 20% kaolinite without hydrate) during depressurisation (P_d represents dissociation pressure at 277.15 K temperature).

3.6.3 Results of the triaxial experiments

Figure 3.31 shows the pore and confining pressure profiles during water injection in a multistage triaxial experiment. As the figure shows, the effective stress was kept constant at 1 MPa during increasing the pore and confining pressure. Similar to the multistage triaxial experiment, the effective confining pressure was kept constant in two single-stage experiments conducted under 1.5 and 2 MPa effective confining stress.

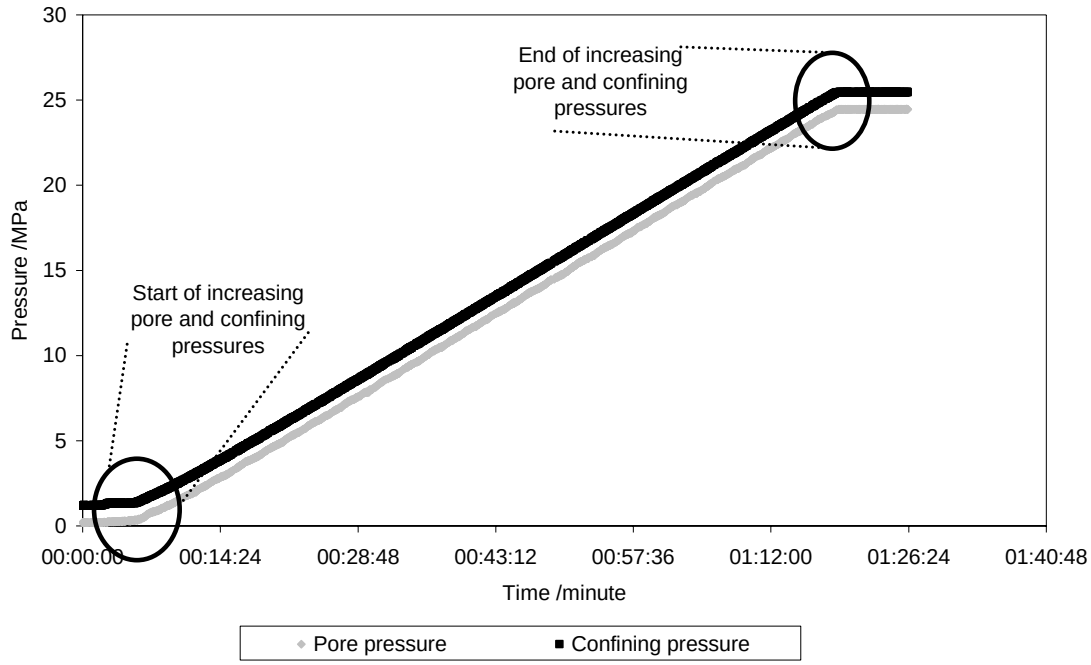

Figure 3.31 The pore and confining pressure profile during water injection

Figure 3.32 and 3.33 show the deviatoric stress versus axial strain in a multi stage and two other single-stage triaxial experiments. The deviatoric stress is defined as:

$$q = \sigma_1 - \sigma_3 \tag{3.1}$$

σ_1 =maximum principle stress

σ_3 = minimum principle stress

The peak deviatoric stress and its confining pressure at each stage in multistage triaxial experiment are presented in Table 3.6. The values presented in Table 3.6 can be used to calculate the plasticity parameters of the sample.

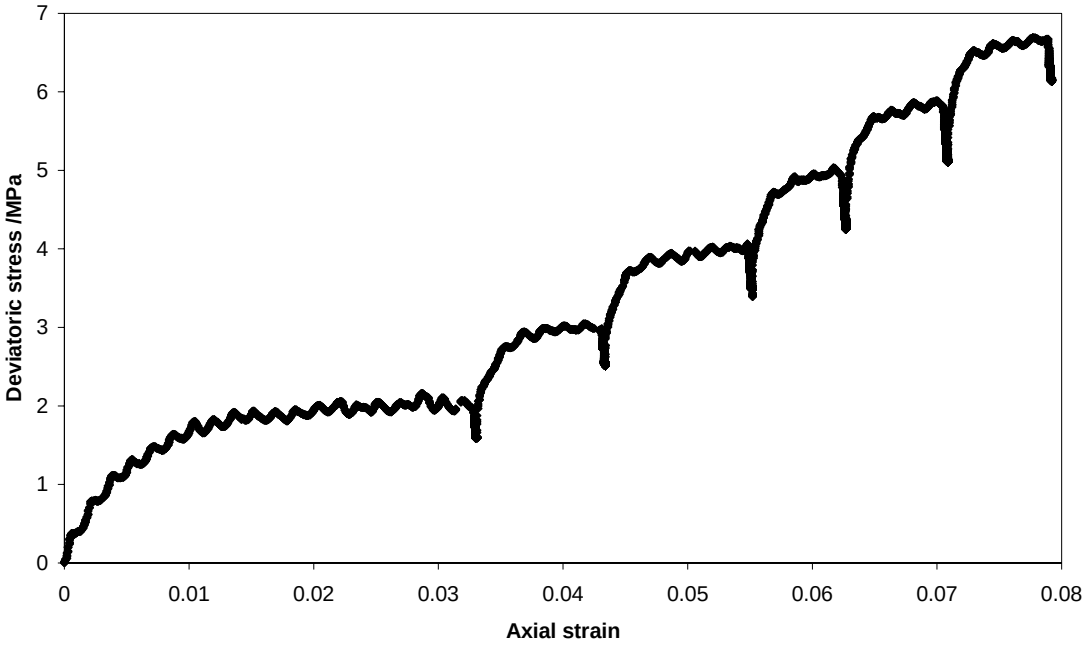

Figure 3.32 Deviatoric stress versus axial strain in the multistage triaxial experiment

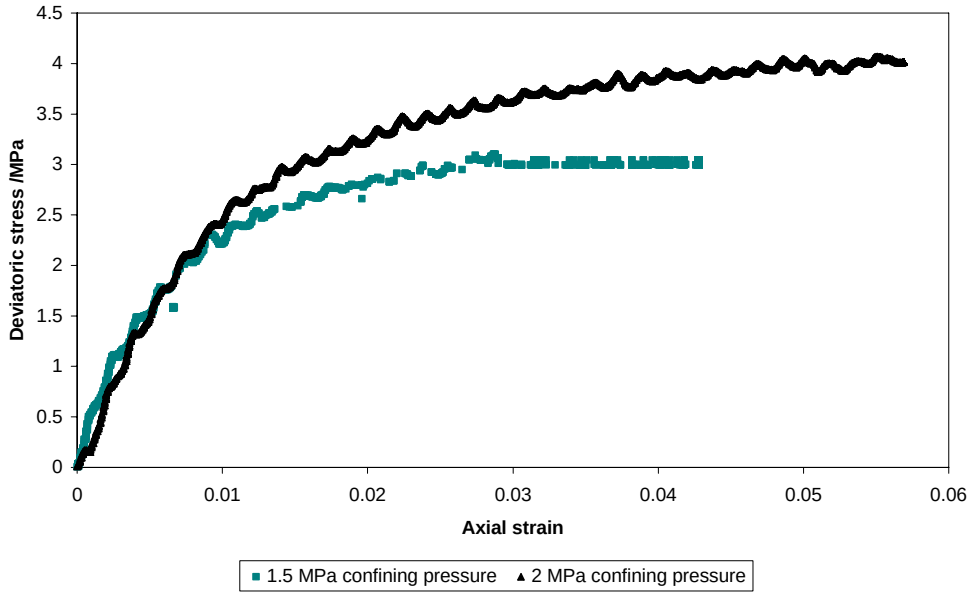

Figure 3.33 Deviatoric stress versus axial strain in triaxial experiments conducted under 1.5 and 2 MPa effective confining pressures

Table 3.6 Deviatoric stress and effective confining pressure at each stage

Stage	Effective confining stress /kPa	Pore pressure /kPa	Deviatoric stress /kPa
1	1000	24460	2072
2	1500	24460	2987
3	2000	24460	3977
4	2500	24460	4927
5	3000	24460	5825
6	3500	24460	6636

Figure 3.34 shows the result of first three stages of the multistage triaxial experiment and two triaxial experiments conducted under 1.5 and 2 MPa effective confining pressures. Figure 3.34 also shows that peak strengths resulted from the multistage triaxial experiment agree with the results of two single-stage triaxial experiment conducted under 1.5 and 2 MPa effective confining pressure respectively. As a result, the results of the multistage triaxial experiment can be representative of several single-stage triaxial experiments conducted under different effective confining pressures (as mentioned before).

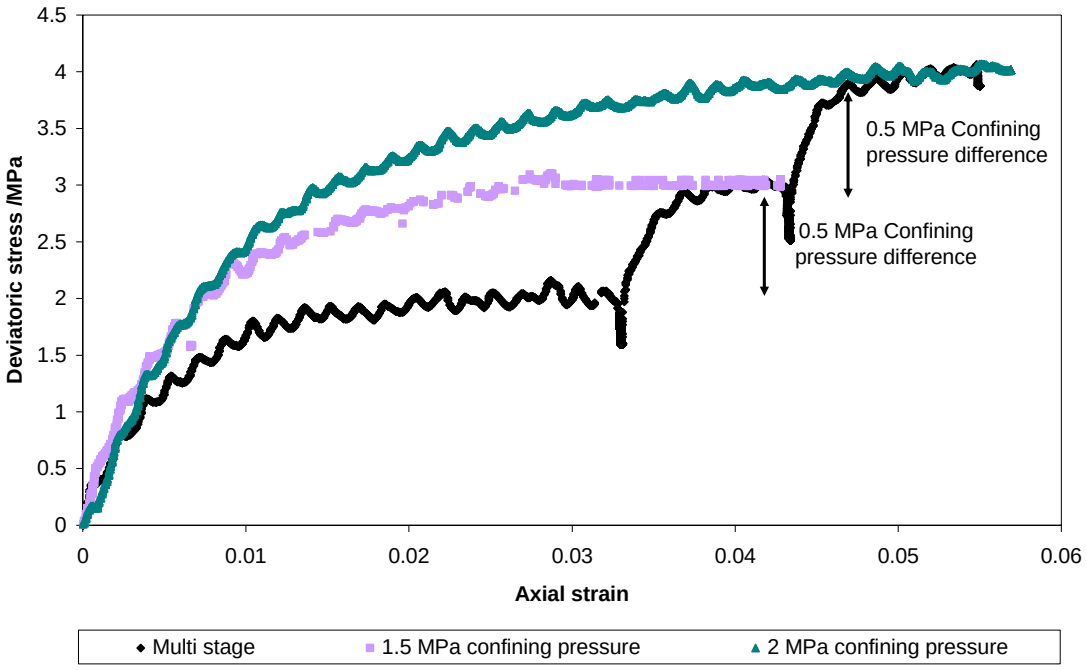

Figure 3.34 Deviatoric stress versus axial strain in triaxial experiments

The cohesion and friction angel as parameters of Mohr-Coulomb criterion can be calculated as [3.5]:

$$\sigma_1^{'} = C_0 + \sigma_3^{'} tan^2 \beta \tag{3.2}$$

$$C_0 = 2S_0 \tan \beta \tag{3.3}$$

$$\beta = \frac{\pi}{4} + \frac{\phi}{2} \tag{3.4}$$

where

$\sigma_1^{'}$=maximum effective principle stress

$\sigma_3^{'}$= minimum effective principle stress

S_0=cohesion

ϕ=friction angle

Figure 3.35 shows the maximum effective principle stress versus the minimum effective principle stress obtained from Table 3.6. The cohesion and friction angle were calculated as 75.06 kPa and 28.67^o respectively based on Figure 3.35 and Equations 3.2 to 3.4.

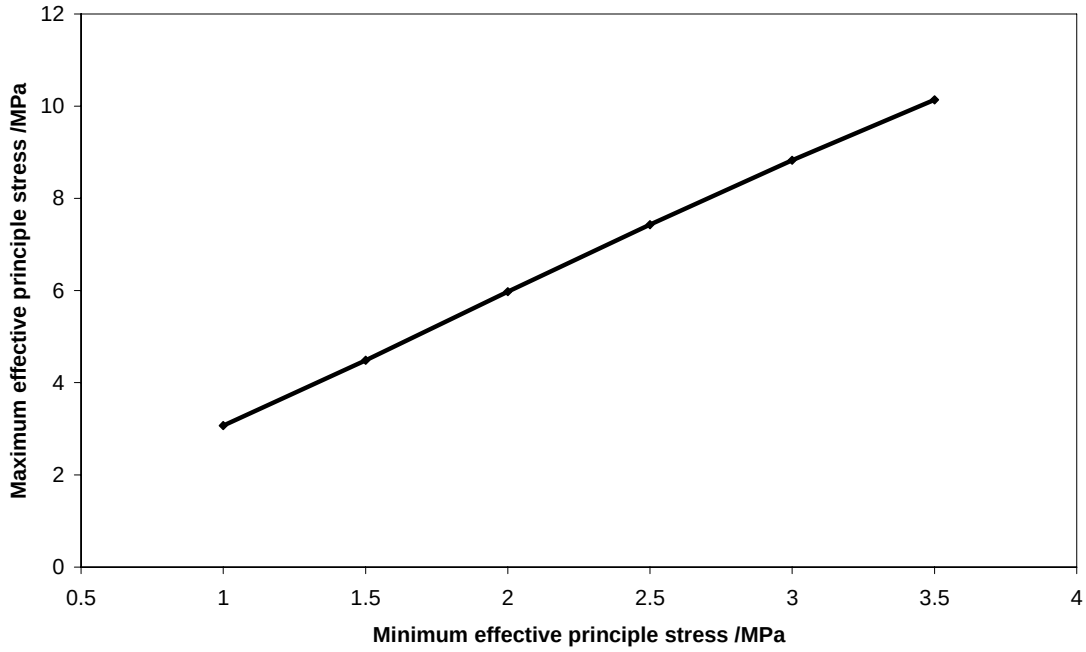

Figure 3.35 Maximum effective principle stress versus the minimum effective principle stress.

Figure 3.36 shows the deviatoric stress versus axial strain of the sample during the first stage. The material stiffness is defined as the resistance of material to deformation. The Young modulus is always used to describe the material stiffness. There are different definitions for Young modulus including tangential and secant [3.6]. The tangential modulus is the slope of stress versus strain curve at any specific stress or strain along the curve. The secant modulus (E_{50}) can be determined at the half peak deviatoric stress drawn through the origin of the stress versus strain curve as shown in Figure 3.36. The calculated secant Young modulus in the experiment was 286.044 MPa. This value agrees with the results of triaxial experiment conducted by Yun [3.6].

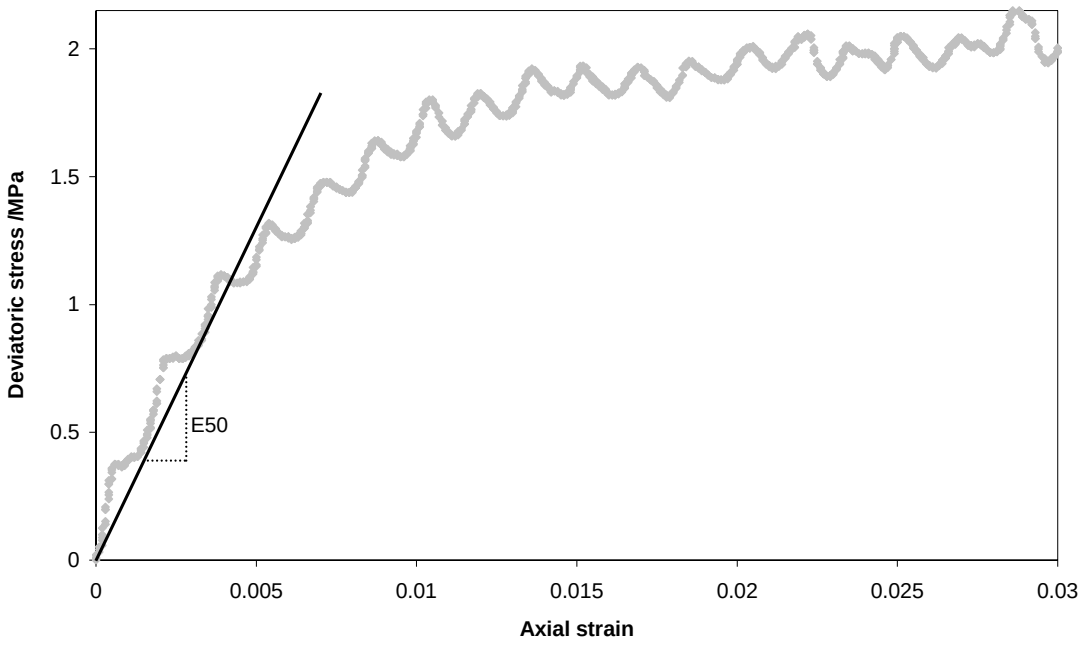

Figure 3.36 Deviatoric stress versus axial strain at the first stage

Figure 3.37 shows the radial (lateral) strain versus axial strain for the first stage. It shows that the sample experienced large lateral deformation caused by either deformation under constant volume in barrel shape due to the frictions against the ends or developing shear bands.

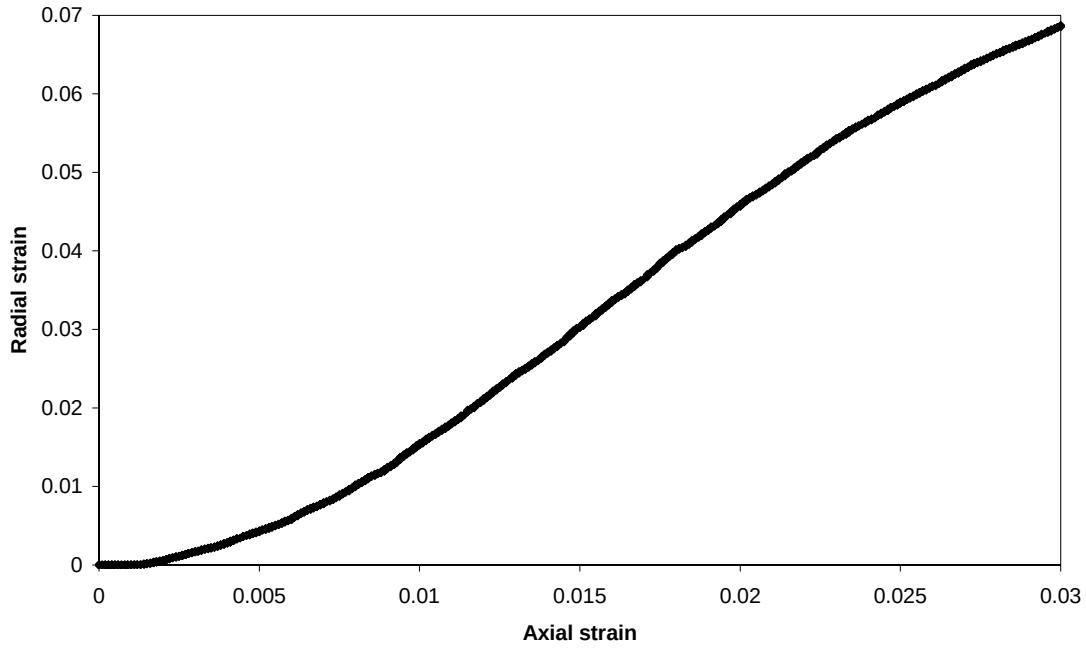

Figure 3.37 Radial (lateral) strain versus axial strain

3.7 Discussion

Like the experiments with silt samples presented in the previous chapter, the results presented in Table 3.3 show no significant increase in the velocity of S-wave as a function of gas hydrate saturation in sand samples. Therefore, the presence of gas hydrates does not create a medium with enough shear stiffness for S-wave to propagate. Moreover the velocity of P-wave does not increase significantly with the increase in gas hydrate saturation. Therefore, it can be suggested that gas hydrates form within pore space as the pore filling model and gas hydrate crystals are suspended inside pore fluid without contribution to the stiffness of sediments.

The initial porosity of silt samples is lower than sand samples as shown in Table 3.2. In general, the differences in initial porosities affect direct comparison of experiments. It was expected that the velocity of P-wave in the silt sample without gas hydrate (i.e., Experiment 14) to be higher than the sand sample without gas hydrate (i.e., Experiment 13) due to lower initial porosity in the silt sample however, the reverse of this fact is shown in Table 3.3. The exact reason has not been clearly understood yet and as a result further investigations, conducting more experiments without gas hydrate with silt and sand samples, are required

The velocity of both S-wave and P-wave in Experiment 15 is significantly higher than Experiment 11 as shown in Table 3.3 at almost the same gas hydrate saturation. As mentioned above, the gas hydrate growth within pore space in Experiment 11 (i.e., sand sample with 44.6% gas hydrate saturation) is dominated by the pore filling model. Therefore high sound velocities, particularly P-wave, in Experiment 15 can be explained by the fact that in silt samples at very high gas hydrate saturation (i.e., >50%), the gas hydrates may cement the sediments grains as shown in Figure 1.8. It means that gas hydrates contribute to the stiffness of the sediment manifested by the significant increase in dynamic bulk and shear modulus as shown in Table 3.4.

As shown in Figures 3.14 and 3.15, dynamic bulk modulus of sand samples is lower than silt samples in low gas hydrate saturation (i.e., comparing Experiments 12 and 9 presented in Table 3.3). However, the difference between dynamic shear modulus of Experiments 9 and 12 is not significant and it is believed that dynamic shear modulus is affected by the presence of free gas and/or an error associated with determining the first arrival time of S-wave. Porosity and grain size in silt samples is less than sand samples as shown in Figure 2.3 and Table 3.2. It was suggested that gas hydrate growth in Experiments 9 and 12 is dominated by the pore filling model. However, it seems that gas hydrate growth within pore spaces is not uniform throughout the sample. It means that although the pore filling model is dominating in both Experiments 9 and 12, there might be some pore spaces that gas hydrates form like in the frame bearing model as shown in Figure 3.38.

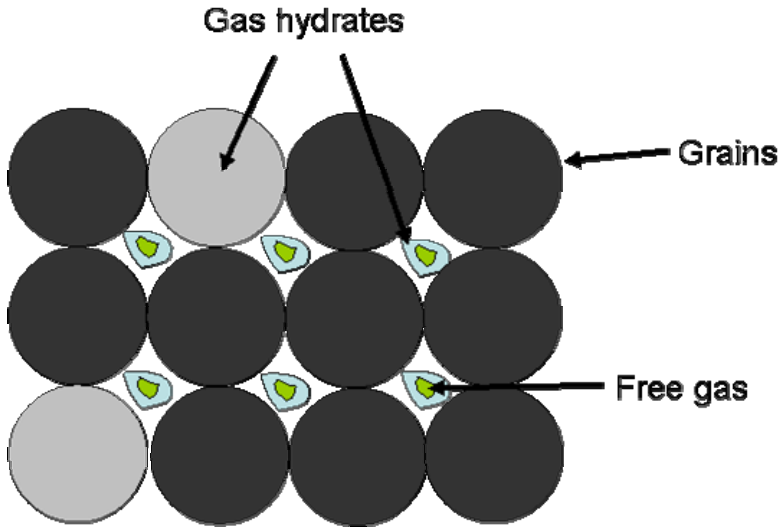

Figure 3.38 Schematic of co-existing of pore filling and frame bearing hydrate growth models

In other words, gas hydrate growth is not suggested to be uniform throughout the sediment. The difference in the dynamic bulk modulus of Experiments 9 and 12 might be explained by the fact that the number of pore spaces in which gas hydrates grow as frame bearing is higher in Experimen12 (i.e., silt sample) than Experiment 9 (i.e., sand sample) due to low porosity and grain size in silt samples. It was expected that the velocity of S-wave in silt samples to be higher than sand samples like the velocity of P-wave at low gas hydrate saturations as shown in Table 3.3. Therefore, further investigations, conducting more experiments containing low gas hydrate saturations with silt and sand samples, are required.

The failures (stress drops) during continuous loading (compaction) can be explained by the compaction failure [3.5]. It is based on the pore collapse failure mode which is observed in high porosity materials. The porosities of all samples used in this series of experiments are high as shown in Table 3.2. When these samples are loaded and compressed the grains may loosen or gas hydrate crystals separate from the grains and are then pushed or twisted into the open pore space resulting in the compacting of the material [3.5]. This process is schematically shown in Figure 3.39 where the black spots are gas hydrate crystals.

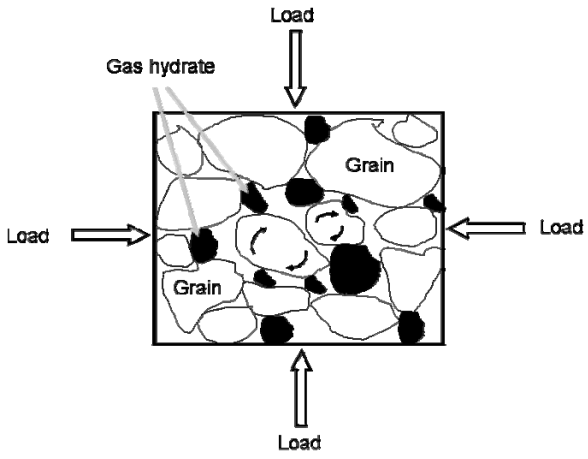

Figure 3.39 Schematic of compaction failure theory

It is observed in Figures 3.20 to 3.24 that the axial load increases by increasing the axial deformation during compaction (continuous loading). It can be explained by the fact that the rearrangement of the grains resulted from compaction, leading to a dense structure [3.5]. A sample with dense structure is able to carry more load, hence compaction increases the load carrying capacity

It has been reported that soils containing sand compact less than soils containing silt or clay and that even small quantities of silt or clay-size particles have a large effect on soil compaction [3.7]. Therefore, it is to be expected that the compaction stiffness of sand samples is higher than that of silt samples. This would explain the results of Experiment 13 conducted with sand (without gas hydrates) which showed the highest compaction stiffness as depicted in Figure 3.26. Figure 3.26 also shows that stress drops can occur without the presence of gas hydrates. This can be explained by the fact that sediment grains are twisted or pushed into the open pore space resulting in the compacting of the material under loading. It should be mentioned that such compaction has not been reported in literatures as soil consolidation (i.e., compaction) is normally measured using Oedometer in soil mechanics which is different from the setup used in the experiments. In addition, loading in Oedometer is incremental using seating load instead of continuous.

The sediments in Experiment 16 are made of a mixture of silt and clay and the average particle size of clay is smaller than silt. This Experiment shows the least compaction stiffness (Figure 3.26) which can be explained by the fact that smaller particles like clay can roll and fill the pores between silt particles during compaction resulting in low compaction stiffness [3.8]. As mentioned before, at high gas hydrate saturations, hydrates may cement the sediments grains and behave similar to a contact cement model. Therefore, it is expected that the effect of cementation is higher when porosity is low. This might explain the results of Experiment 15 (conducted with silt and high saturation of gas hydrate) where the highest compaction stiffness was observed (as shown in Figure 3.27)

The depressurisation causes further sediment compaction, manifested by the observed increase in axial deformation. The axial deformation in Experiments 14, 15 and 16 before the dissociation point is 2 %, 1.79 % and 3.7 %, respectively. It can be inferred that silt samples containing high gas hydrate saturation in comparison with silt samples without hydrate, compact less during depressurisation and before reaching the dissociation point and also that the addition of 20 % clay to silt samples without hydrate, causes further deformation during pore pressure decrease (i.e., depressurisation). As a result, it is suggested that subsidence could be an important issue in gas production from sediments containing gas hydrate by depressurisation.

Subsidence in gas hydrate bearing sediments during methane gas production from natural gas hydrate reservoirs can cause casing buckling or shearing leading to wellbore loss or damage surface facilities placed on the seafloor. Further investigation is required for quantifying subsidence as a result of gas production from gas hydrate bearing sediments.

3.8 Summary

In this chapter, the results of the second series of experiments conducted on synthetic samples containing gas hydrates with different gas hydrate saturations were presented. In this series of experiments (unlike the first series), the samples were loaded axially up to the maximum working capacity of the setup when measuring the static uniaxial compaction modulus in this series. At the end of the loading stage, the gas hydrates inside the pore space were dissociated by depressurisation (compared to heating in the previous chapter).

The results show that the velocity of compressional waves in samples made with sand increased as a direct function of gas hydrate saturation within the sample. However, the velocity of shear wave did not show a similar pattern with an increase in gas hydrate saturation. However, at hydrate saturations higher than 50% the velocity of shear waves increased in samples made of silt. It was suggested that gas hydrate form within pore space of sand samples as the pore filling model without contribution to the stiffness of sample. It was also suggested that gas hydrate growth within pore space in silt samples at high gas hydrate saturation (i.e., >50%) is dominated by the cementing model. Therefore, gas hydrates at high gas hydrate saturation in silt samples increase the stiffness of the samples significantly manifested by increase in dynamic bulk and shear modulus.

The static uniaxial compaction modulus increased by increasing the gas hydrates saturation. This means that the gas hydrate improves the mechanical properties of samples made with sand.

The stress drops occurred during continuous loading could be related to the interaction between grains of sediments and gas hydrate particles. It was suggested that when the samples were loaded, the grains may loosen or gas hydrate particles separate from the grains and then are pushed or twisted into the pore space resulting in the compaction of

the samples. The presence of gas hydrate improves the compaction stiffness of the sediments and this effect is stronger when gas hydrate saturation is high. The compaction stiffness of sediments made with silt containing high gas hydrate saturations is higher than the sediments made with sand containing high gas hydrate saturation. The presence of clay decreases the compaction stiffness of samples made with silt.

Gas hydrate dissociation by depressurisation increases the effective stress due to the resulting decrease in the pore pressure, hence further compaction. This means that subsidence caused by further deformation due to compaction is an important issue in methane gas production from sediments containing gas hydrate by the depressurisation method.

In order to control the confining pressure and lateral displacement a Triaxial setup was purchased and commissioned. The design of the setup was modified so that it can be used to study the properties (including mechanical properties, permeability) of gas hydrate bearing sediments under realistic conditions. The results of experiments conducted with the setup were presented in this chapter.

3.9 References

3.1 T. Edinima, Y. Kamata, H. Minagawa, R. Ogmura, J. Nagao, H. Narita, *Mechanical properties of sandy sediment containing methane hydrate,* Proceedings of the Fifth International Conference on Gas Hydrate, Trondheim, Norway, 2005

3.2 A. Bro, *Analysis of multistage triaxial test results for a strain-hardening rock*, International Journal of Rock Mechanics and Mining Sciences, 34, 143-145, 1997

3.3 M. M. Kim, H-Y.Ko, *Multistage triaxial testing of rocks*, Geotechnical Testing Journal, 2, 1979

3.4 T. S. Yun, F.M.Francisca, J.C.Santamarina, C.Ruppel, *Compressional and shear wave velocities in uncemented sediment containing gas hydrate,* Geophysical Research Letters, 32, 2005

3.5 E. Fjaer, R. M. Holt, P. Horsrud, A. M. Raaen, R. Risnes, *Petroleum related rock mechanics*, Elsevier, 2008

3.6 T. S. Yun, J. C. Santamarina, C. Rupple, *Mechanical properties of sand, silt, and clay containing tetrahydrofuran hydrate,* Journal of Geophysics Research, 12, 2007

3.7 H-Y. Fang, H.F.Winterkorn, *Foundation engineering handbook*, Kluwer Academic Publisher, 1995.

3.8 H. Kok, R. K. Taylor, R. E. Lamond, S.Kessen, *Soil compaction problems and solutions*, Cooperative Extension Service, Kansas State University, 1996

Chapter 4 – Casing Stability Modelling in Gas Hydrate Bearing Sediments with Very Low Permeability

4.1 Introduction

wellbore integrity is defined as the long term ability of the wellbore to produce. Casing is a pipe used to line the drilled wellbore to protect the wellbore from collapse, to isolate geological formation (after cementing) and to carry the weight of the completion system and subsequent casing strings. Therefore, it is the foundation of a well and its stability is a key issue in the wellbore integrity analysis. A conductor pipe is the first casing which is usually put into the wellbore to prevent caving and collapse of the wellbore (and shallow sediment washout in onshore wells). This casing, particularly in land wellbores, is relatively short (30-60 m) and most of the times is hammered into the ground. However, the conductor pipe is much longer and is drilled and cemented in deep offshore drilling operations. In a data set of 344 wellbores drilled in the deepwater Gulf of Mexico 89 percent of the conductor pipes were set at depths greater than 304 m [4.1]. The average setting depth of the conductor pipe in the above data set was 563 m which in most areas is near or below the base of GHSZ (Gas Hydrate Stability Zone) [4.1].

The necessary conditions for gas hydrate formation exist at water depth higher than a few hundred meters (300-500m). Depending on the water depth, seabed temperature and geothermal temperature gradient, gas hydrate bearing sediments could be found in the first few hundred metres of subsea sediments. Drilling through gas hydrate bearing sediments could dissociate gas hydrates resulting in the release of gas. The released gas reduces the density of drilling mud and as a result the mud pressure exerted on the wellbore is reduced. The drilling mud pressure provides mechanical supports to the wellbore. Further reduction in the drilling mud pressure could lead to wellbore collapse or drilling string stuck. Other challenges associated with drilling operations in gas hydrate bearing sediments includes casing stability in resuming the drilling operations after running the first casing (i.e., conductor pipe) and/or production of hot hydrocarbons. In this study, we focus on the modelling of the casing (conductor pipe) stability after running the conductor pipe and during drilling of the deeper sections of the wellbores drilled in gas hydrate bearing sediments (i.e., for a period of 8 days). The

circulation of hot drilling mud during drilling operations of the wellbore could further result in dissociation of gas hydrate in subsea sediments. The fluids generated during gas hydrate dissociation cannot flow away if the permeability of the formation is very low causing high pore pressure behind the conductor pipe. The high pore pressure may endanger the stability of the conductor pipe depending on the magnitude of the trapped pressure and the mechanical strength of the conductor pipe.

After drilling through gas hydrate bearing sediments, the conductor pipe is run to mainly protect the gas hydrate bearing sediments from washing out (though preventing in-situ hydrate dissociation during drilling deeper sections of the wellbore is also very important). As the drilling operation progresses and the wellbore depth increases, the temperature of the drilling mud inside the conductor pipe increases due to the geothermal temperature gradient. Generally, the drilling mud inside the conductor pipe is warmer than the formation containing gas hydrates behind the conductor pipe (unless it is deliberately cooled) and therefore, there is a heat transfer between the drilling mud inside the conductor pipe and gas hydrate bearing sediments behind the conductor pipe as shown in Figure 4.1.

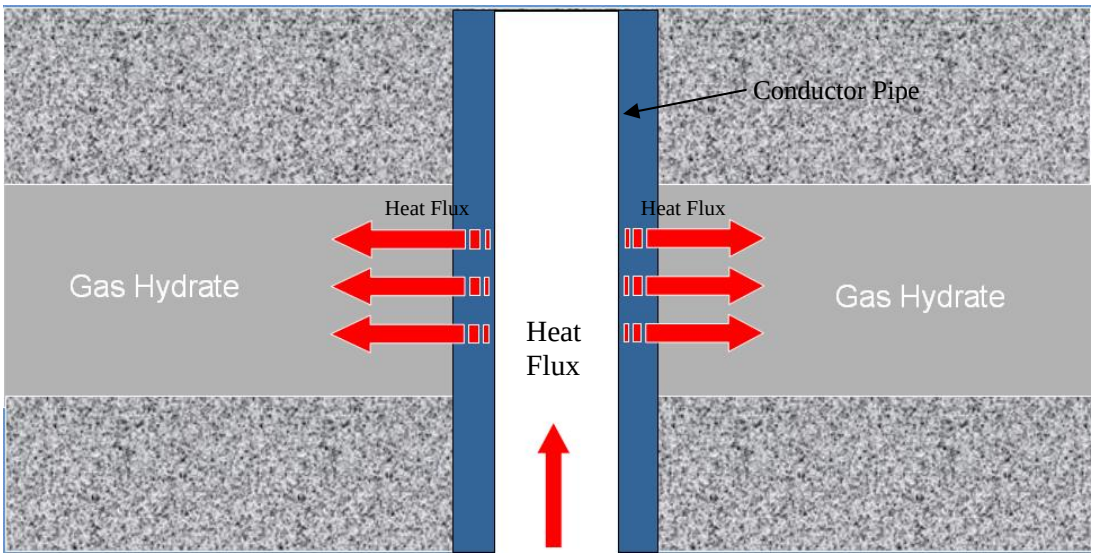

Figure 4.1 Schematic of heating formation behind conductor pipe during drilling

The heat flux will increase the temperature in gas hydrate bearing sediments behind the conductor pipe leading to gas hydrate dissociation. The dissociation process decreases the mechanical strength of gas hydrate bearing sediments due to the removal of gas

hydrates from the host formation. The fluids generated during gas hydrate dissociation increases the formation pore pressure behind the cement and conductor pipe depending on the formation permeability (as mentioned before) as shown in Figure 4.2.

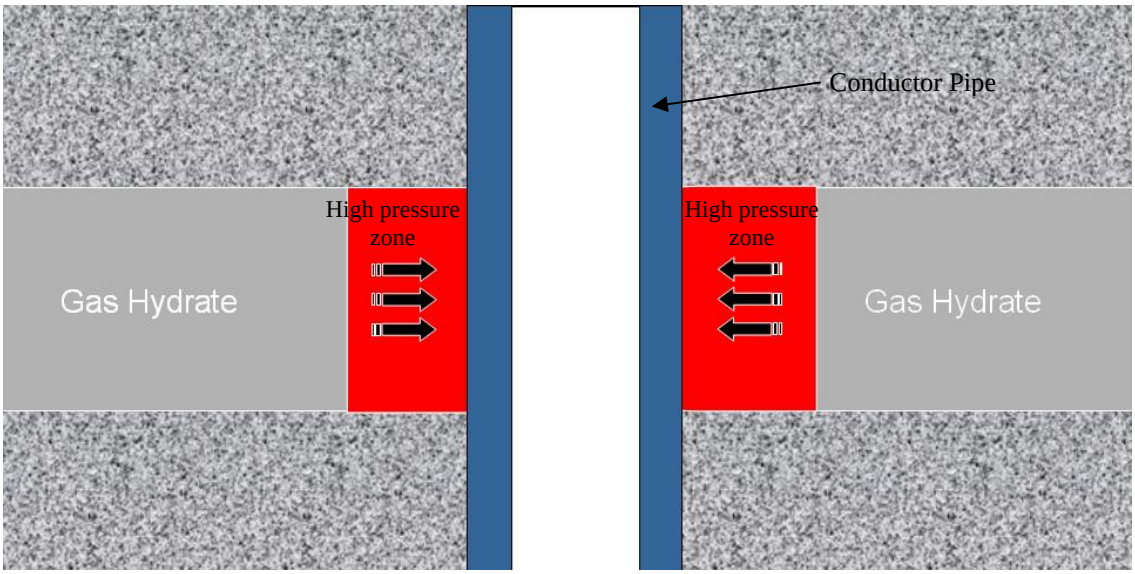

Figure 4.2 Schematic of increasing pore pressure behind conductor pipe during drilling due to gas hydrate dissociation

As shown in Figure 4.2, there is a high pressure zone behind the conductor pipe. From the drilling engineering point of view, the conductor pipe, as a surface casing, is designed to withstand high internal or burst pressure, although in this case, the conductor pipe is used under conditions for which it is not designed (i.e., high external pressure), and therefore, the casing stability analysis is an important issue in the development of conventional oil and gas fields in deep offshore.

In this chapter, a new procedure is used in developing a numerical model with ABAQUS to investigate casing stability in a wellbore drilled in gas hydrate bearing sediments in deep offshore environment. ABAQUS is a robust finite element package specifically developed for solving non linear problems. It has a capability that allows the users to customise it for their particular applications. The model is new as it considers the interaction between formation, cement and casing. In addition it takes into consideration the effects of non-uniform loading on the casing, and that ABAQUS is a finite element package and was developed to be used for the geomechanical study of gas hydrate bearing sediments. In this work, different numerical models were

developed to study casing stability in gas hydrate bearing sediments under different scenarios including uniform, and as mentioned before, non-uniform loadings. The developed models are detailed in the following sections.

4.2 Developed model

The model was developed to simulate casing stability for wellbores drilled in gas hydrate bearing sediments. Gas hydrate bearing sediments are normally under three dimensional stresses; vertical stress due to the weight of formations lying above the zone of interest, minimum and maximum horizontal stresses due to constraints from unlimited horizontal displacements in two perpendicular directions or geological structures. The model considers the state of the wellbore at the some specific depth. The wellbore was modelled as plain strain. Plain strain assumes that the model is of infinite length normal to the plane section of the analysis. As a result, in plane strain analysis, the stress in the perpendicular direction to the plane section of the analysis is not zero, but the stain in that direction is zero. It was assumed that there is no heterogeneity in the formation and the wellbore is completely vertical. The in-situ stresses were assumed isotropic as assumed by Birchwood, et al, [4.2]. The effect of drilling fluid inside the casing (i.e., internal pressure) on the mechanical strength of the casing was taken into account (the drilling fluid pressure in addition to the collapse strength of casing). It was assumed that heat transfer takes place by conduction only and the formation permeability is low enough that water and gas generated as a result of gas hydrate dissociation cannot flow away. The heat transfer term was coupled to hydraulic and mechanical deformation terms using one-way coupling. All material properties used in the modelling were obtained from Tables 2.5 to 2.8 and available literatures [4.3], [4.2], [4.4], [4.5], [4.6], [4.7].

4.2.1 Governing Equations

Hydraulic- Mechanic Analysis

The hydraulic-mechanic coupling consists of porous medium and pore fluid and is based on equilibrium, constitutive equation and mass conservation using the effective stress theory.

- ***Equilibrium***

Equilibrium is expressed by writing the principle of virtual work for the volume under consideration in its current configuration at time *t*:

$$\int_V \sigma : \delta\varepsilon \, dV = \int_S t.\delta v \, dS + \int_V f.\delta\delta \, dV \tag{4.1}$$

where

δv =virtual velocity field

$\delta\varepsilon$ =the deformation

σ =the stress

t =surface tractions per unit area

f =body forces per unit volume

S=surface on which forces apply

V =the volume with surface area S

The effective stress equation is:

$$\bar{\sigma} = \sigma + u_w \tag{4.2}$$

where

$\bar{\sigma}$ =the effective stress

σ =the total stress

u_w =the pore pressure

In ABAQUS, pore pressure is stored with positive sign and stress components are stored with negative signs.

- ***Constitutive equations***

The constitutive equation for the solid is expressed as:

$$d\tau = H : d\varepsilon + g \tag{4.3}$$

where

$d\tau$ =the stress increment

H =the material stiffness

$d\varepsilon$ =the strain increment

g =any strain independent contribution (thermal expansion)

- ***Mass Conservation***

A continuity equation equates the rate of increase in liquid mass stored at a point to the rate of mass of liquid flowing into the point within the time increment:

$$\frac{d}{dt}\left(\int_V \rho_w \varphi dV\right) = -\int_S \rho_w \varphi N V_w dS \tag{4.4}$$

where

ρ_w =density of liquid

φ =porosity

N =outward normal vector

V =volume of porous media

S=surface on which surface fluxes apply

V_W = liquid velocity in pore space

The continuity equation is integrated in time by using the backward Euler approximation.

Uncoupled heat transfer

- ***Energy balance***

The basic energy balance is:

$$\int_V \rho U dV = -\int_S q dS + \int_V r dV \tag{4.5}$$

where

V =the volume with surface area S

S=surface on which surface fluxes apply

ρ =the density

U =the rate of the internal energy

q=the heat flux per unit area of the body

r=the heat supplied externally into the body per unit volume

It is assumed that the thermal and mechanical terms are one-way coupled such that porous medium deformation does not affect heat transfer and temperature distribution.

- ***Constitutive definition***

Heat conduction is assumed to be governed by the Fourier law:

$$f = -k\frac{\partial T}{\partial x} \tag{4.6}$$

where

k =the conductivity matrix

f =the heat flux

x=the position

4.2.2 Thermal/hydraulic-mechanical coupling

ABAQUS does not have an element with fully THM (Thermal-Hydraulic-Mechanical) coupling, which means that the Jacobian matrix for hydraulic-mechanical equations and thermal equations is derived separately [4.8]. The one-way coupling technique was used to couple thermal and hydraulic-mechanical analysis. It was assumed that pore fluid flow and displacements do not affect the temperature distribution.

ABAQUS provides predefined subroutines that users can develop using FORTRAN to customize the ABAQUS for a particular case. Although ABAQUS has a lot of flexibility by providing the above subroutines (compared with other finite element packages) each subroutine in ABAQUS is specific for a particular analysis and therefore, for special cases which are not covered in ABAQUS, like this study, the users need to find the relevant subroutines and couple them internally. The coupling of hydraulic-mechanic and thermodynamic models was conducted by coupling two available subroutines in ABAQUS [4.9], [4.10]. USDFLD (user defined field variables) and DISP are the two subroutines used in this study. USDFLD provides access to many variables including; temperature, pore pressure, stress, strain and etc. at each time increment. This subroutine can be used to define field variables and

introduce solution-dependent material properties. Field variables are parameters used mainly to change real properties by making the properties dependant on them. DISP is a subroutine called for all degrees of freedom in the model and can be used to define the magnitudes of prescribed boundary conditions including pore pressure.

The thermal model was first run to calculate temperature distribution in the model over the simulation time. The thermal model breaks the simulation time into multiple time increments and the temperature distribution at the end of each time increment was written to an output file. In this study, the material properties of the casing were defined to be dependent on one dummy field variable in order to gain access to the temperature distribution through USDFLD during the analysis. The temperature distribution was passed to USDFLD by calling GETVRM which is an internal subroutine within USDFLD and reading the output file. After reading the output file containing temperature distribution over the simulation time, the temperature distribution was passed to the DISP in order to be used for gas hydrate phase boundary calculations using HWHYD (in-house developed thermodynamic software) [4.11]. Finally, the pore pressure was increased to be equal to the calculated equilibrium pressure using HWHYD in the model by DISP as a fixed pore pressure boundary condition. This process continued till the total time reached simulation time [4.10]. The schematic of the coupling algorithm is shown in Figure 4.3. A sample of the input file inclusive of the developed subroutines is provided in Appendix B.

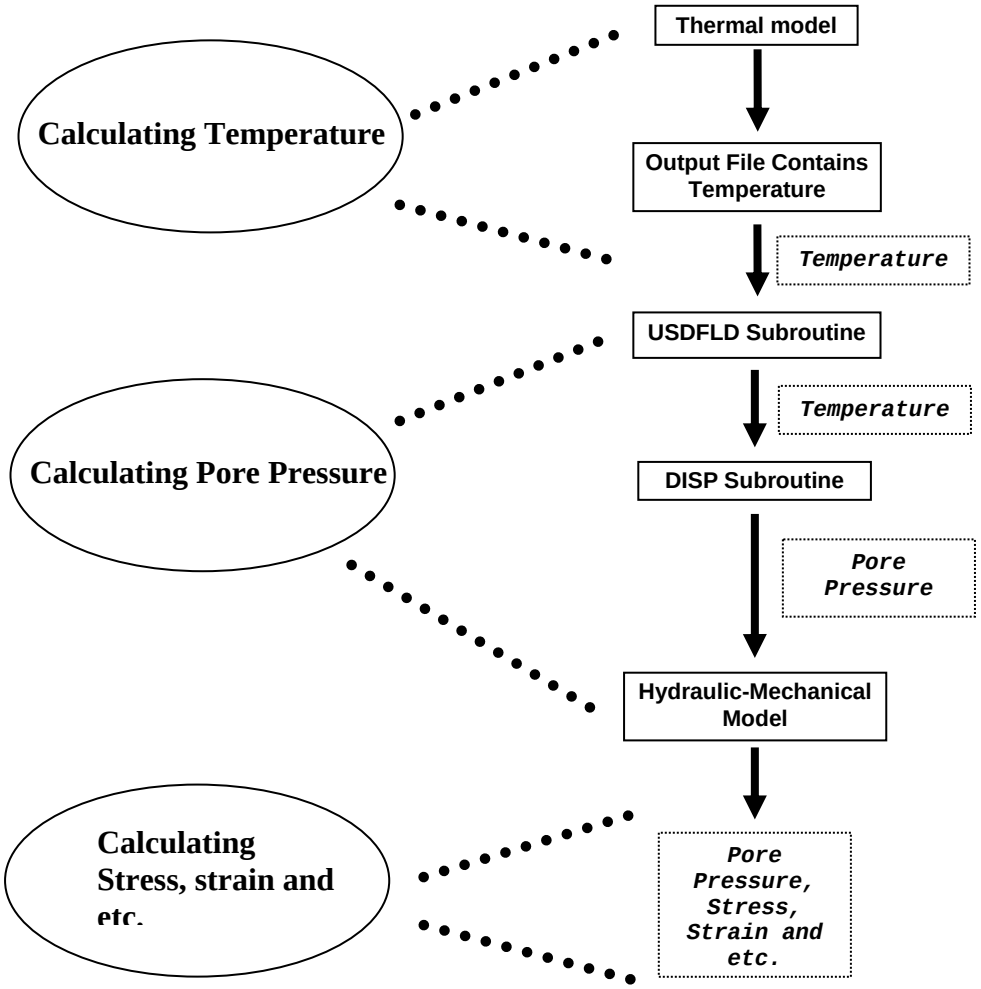

Figure 4.3 Schematic of coupling process

Interpolation in time

While reading the temperature from the external file, ABAQUS obtains the value of temperature at the time increments used by the analysis. However, if the data corresponding to the above time increments are not available in the file, ABAQUS will interpolate linearly between the time increments stored in the file to obtain values at the time increments required by the analysis. Therefore, sufficient data is provided in the temperature file to make the interpolation meaningful [4.9].

Gas hydrate phase boundary

When the formation is heated, gas hydrate behind the cement sheath will dissociate and result in an increase in the formation pore pressure. The magnitude of pore pressure changes during gas hydrate dissociation in very low permeability formations as shown in Figure 4.4.

Figure 4.4 shows the phase boundary prediction by HWHYD and the pore pressure changes obtained from Experiment 8. As shown in Figure 4.4, the difference between the prediction of HWHYD and the experimental results is small. In addition, conducting an experiment to quantify pore pressure changes during gas hydrate dissociation is a time consuming task.

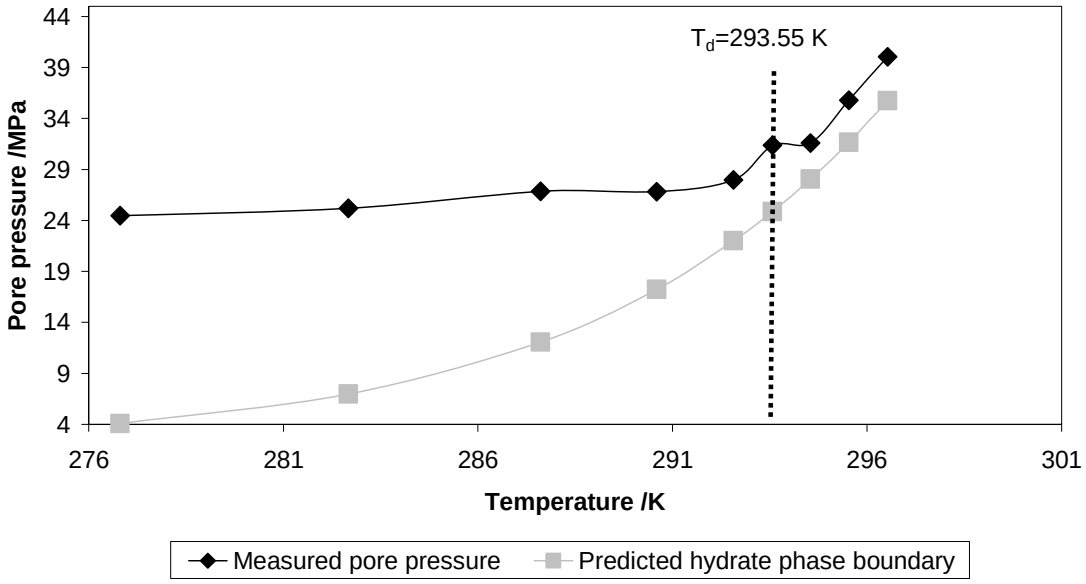

Figure 4.4 Methane hydrate phase boundary predicted with HWHYD and pore pressures results from Experiment 8.

Therefore, HWHYD was used and implemented into the model to predict the phase boundary of methane hydrate and quantify the pore pressure increase due to hydrate dissociation by thermal stimulation (i,e,. circulating hot mud or production of hot hydrocarbon fluids). HWHYD models hydrates using the solid solution theory of van der Waals and Platteeuw. More information on the thermodynamic modelling used in HWHYD can be found elsewhere [4.11].

4.2.3 Contact interactions

The interaction between the cement and formation surfaces is modelled by defining an interaction model as shown in Figure 4.5. The interaction model can be modified so that formation and cement surfaces cannot pass through each other but they are allowed to debond. A predetermined tension stress can be transmitted before debonding. More information on the interaction model can be found elsewhere [4.9]. In this model no

transmitted tension stress was considered. Also the contact interaction model can be modified so that the cement and formation surfaces can slide one along the other. In this model, we assume that the cement has good bonding with the formation so that there is not a sliding between those surfaces. The casing and cement were assumed perfectly bonded in this study.

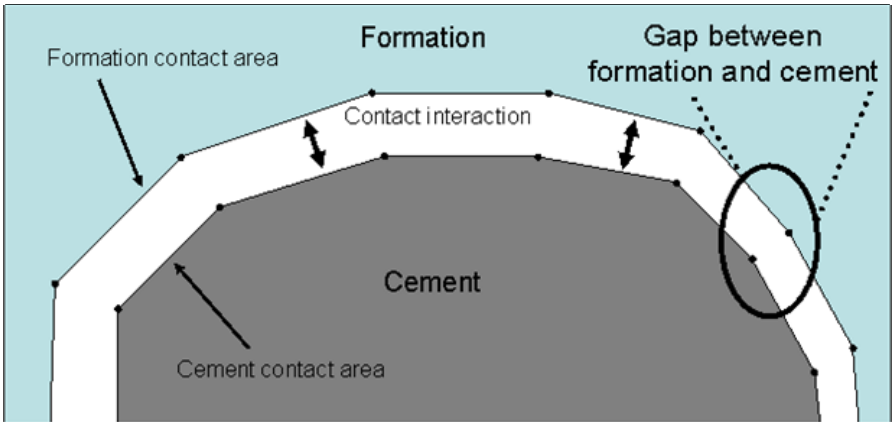

Figure 4.5 Schematic of contact interaction

4.2.4 The properties of materials

Formation

The physical and mechanical properties of the formation were obtained from Tables 2.5 to 2.8 with different gas hydrate saturations. As a result, it was assumed that the formation is elastic with degradable elastic properties as a function of temperature during gas hydrate dissociation as shown in Tables 2.5 to 2.8.

Casing

The mechanical properties of the casing are shown in Table 4.1. The casing was modelled as elastic/perfect plastic material using Von Mises criterion.

In engineering, the Von Mises is defined as [4.12]:

$$\sigma_{vm} = \sqrt{\frac{(\sigma_1 - \sigma_2)^2 + (\sigma_2 - \sigma_3)^2 + (\sigma_1 - \sigma_3)^2}{2}} \tag{4.7}$$

where

σ_{vm} =Von Mises stress

σ_1 =maximum principal stress

σ_2 =intermediate principal stress

σ_3 =minimum principal stress

The material (i.e., casing) starts to yield when Von Mises stress reaches the yielding strength of the material which is a characteristic material property.

Table 4.1 Properties of casing

Thickness /m	0.025 or 1 in
Yield Stress /MPa	375
Weight ($kg.m^{-1}$)	494
Young's Modulus /GPa	210
Poisson Ratio	0.3
Density /$kg.m^{-3}$	8000
Thermal Expansion /K^{-1}	12.42 E-6
Thermal Conductivity /$Wm^{-1}K^{-1}$	15
Heat Capacity /$JK^{-1}kg^{-1}$	450

Cement

When the principal stress components are dominantly compressive, the response of the cement is modelled by an elastic-plastic. When the principal stress components are tensile, the response of the cement is modelled by cracking. Cracking is assumed to occur when the stress reaches a cracking failure surface. When a crack has been detected, its orientation is stored for subsequent calculations and it is irrecoverable and remains for the rest of the calculation but the crack may open and close following its detection. More information on the cement model can be found elsewhere [4.9].

The mechanical properties of the cement affect the magnitude of the stress generated in the casing. As a result, in order to investigate the effect of cement with different mechanical properties on the casing stability, the mechanical properties of two different cement formulations designed for shallow depths are used in the modelling.

Formulation 1 contains a cement/siliceous material mixture, 30% latex by weight of water (BWOW), mixed at 1481.43 kg/m^3 (i.e., 12.1 ppg) with 0.04 m^3 mix water per sack of cement. Formulation 2 contains a cement/pozzolan mixture, 4.5 kg/sack silica flour, 30% latex (BWOW), mixed at 1689.56 kg/m^3 (i.e., 13.8 ppg) with 0.02 m^3 mix water per sack of cement [4.6]. During drilling the next section of a wellbore in gas hydrate bearing sediments, the amount of heat flux that passes through the cement is directly related to the thermal properties of the cement. If the thermal properties of the cement are high more heat flux will pass to the formation causing more gas hydrate to dissociate and the reverse is true if the thermal properties of the cement are low. In order to investigate the effect of cement with different thermal properties on the casing stability, the thermal properties of two different cement systems are used in the modelling. System A has high thermal conductivity and low heat capacity whereas system B has low thermal conductivity and high heat capacity. The properties cement slurries are presented in Tables 4.2 to 4.5.

The cement used for cementing exploration wellbores in the Nankai Trough region was TLC cement developed by the Halliburton [4.13]. It had the characteristic of low density, low hydration heat, low thermal conductivity and desired compressive strength under the low temperature environment. It is general practice in engineering to use cement with low thermal conductivity. It will be shown throughout this study that using cement with low thermal conductivity in a wellbore drilled in gas hydrate bearing sediments is not recommended under all conditions.

Table 4.2 Properties of cement with thermal properties according to System A and mechanical properties according to Formulation-1

General properties	
Thickness /m	0.05 or 2 in
Density /kg.m^{-3}	2200
Weight / kg.m^{-3}	1481.43
Mechanical properties, Formulation #1	
Young's Modulus /GPa	4.75
Poisson Ratio,	0.42
Compressive Strength /MPa	6.89
Tensile Strength /MPa	0.207
Thermal properties, System A	
Thermal Expansion /K^{-1}	4.33 E-6
Thermal Conductivity /Wm^{-1}K^{-1}	2.4
Heat Capacity /JK^{-1}kg^{-1}	835

Table 4.3 Properties of cement with thermal properties according to System B and mechanical properties according to Formulation-1

General properties	
Thickness /m	0.05 or 2 in
Density /kg.m^{-3}	2200
Weight / kg.m^{-3}	1481.43
Mechanical properties, Formulation #1	
Young's Modulus /GPa	4.75
Poisson Ratio,	0.42
Compressive Strength /MPa	6.89
Tensile Strength /MPa	0.207
Thermal properties, System B	
Thermal Expansion /K^{-1}	4.33 E-6
Thermal Conductivity /Wm^{-1}K^{-1}	0.66
Heat Capacity /JK^{-1}kg^{-1}	2100

Table 4.4 Properties of cement with thermal properties according to System A and mechanical properties according to Formulation-2

General properties	
Thickness /m	0.05 or 2 in
Density /kg.m^{-3}	2200
Weight / kg.m^{-3}	1689.56
Mechanical properties, Formulation #2	
Young's Modulus /GPa	5.51
Poisson Ratio	0.32
Compressive Strength /MPa	17.24
Tensile Strength /MPa	1.37
Thermal properties, System A	
Thermal Expansion /K^{-1}	4.33 E-6
Thermal Conductivity /Wm^{-1}K^{-1}	2.4
Heat Capacity /JK^{-1}kg^{-1}	835

Table 4.5 Properties of cement with thermal properties according to System B and mechanical properties according to Formulation-2

General properties	
Thickness /m	0.05 or 2 in
Density /kg.m^{-3}	2200
Weight / kg.m^{-3}	1689.56
Mechanical properties, Formulation #2	
Young's Modulus /GPa	5.51
Poisson Ratio	0.32
Compressive Strength /MPa	17.24
Tensile Strength /MPa	1.37
Thermal properties, System B	
Thermal Expansion /K^{-1}	4.33 E-6
Thermal Conductivity /Wm^{-1}K^{-1}	0.66
Heat Capacity /JK^{-1}kg^{-1}	2100

Formation fluid

The formation fluid is assumed single phase (i.e., water) throughout the analysis, but with pressure contributions from gas liberation due to hydrate dissociation [4.4]. The properties of formation fluid used in the model are presented in Table 4.6

Table 4.6 Properties of formation fluid

Density /kg.m^{-3}	1000
Thermal Expansion /K^{-1}	0.0003
Thermal Conductivity /Wm^{-1}K^{-1}	0.6
Heat Capacity /JK^{-1}kg^{-1}	4181.3

Drilling fluid (mud)

The density of drilling fluid was assumed 1040.67 kg/m^3 (8.5 ppg).

4.3 Uniform Case

In this case, the casing stability of a wellbore drilled in gas hydrate bearing sediments is modelled with uniform and circular geometry. The initial conditions used in this case are presented in Table 4.7 obtained from the available literature. It was assumed that the wellbore was drilled with a 36 inch diameter drill bit and cased with 30 inch conductor pipe. The grade of conductor pipe was assumed J-55 [4.10] with maximum 375 MPa Yield strength. The initial temperature of the gas hydrate bearing sediments was assumed 288 K as assumed by Moridis, et al [4.7] and the temperature of the drilling mud during drilling the deeper sections of the wellbore was assumed 298 K as assumed by Freij-Ayoub, et al, [4.4].

Table 4.7 Initial conditions

In-situ Temperature /K	288
In-situ Pore Pressure /MPa	18
In-situ horizontal stresses /MPa	24

4.3.1 Geometry of the model

The wellbore is modelled in 2D considering casing, cement and formation as concentric circles, as shown in Figure 4.6.

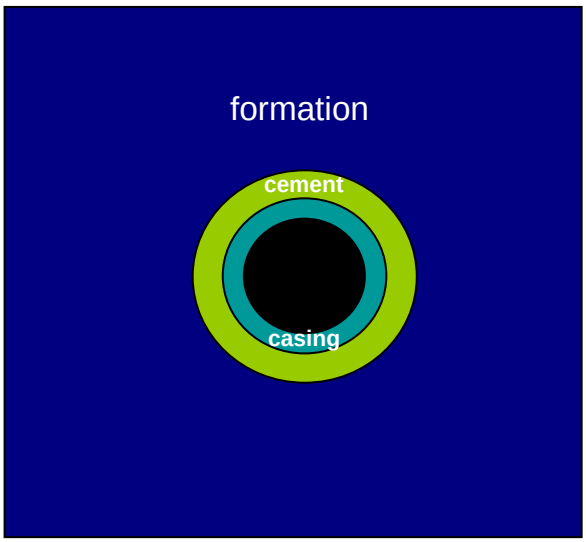

Figure 4.6 Geometry of the uniform circular model used in this work

The appropriate boundary conditions were applied to the far field faces to simulate far field conditions. The size of the total model is 100 times bigger than the wellbore size to accurately represent the effects of far field conditions on the region of wellbore [4.14]. The casing, cement and formation elements were plane strain, eight node continuum elements. The formation elements contained an additional degree of freedom to accommodate pore pressure. Finite element analysis uses a complex system of points called nodes which make a grid called a mesh as shown in Figures 4.13 to 4.16. This mesh is programmed to contain the material properties which define how the model will react to certain loading conditions.

4.3.2 Modelling sequence

Equilibrium step

The model was brought to equilibrium by executing an initial load step specifying initial effective stresses, temperature and pore pressure and fixing displacements along far field boundaries. The initial conditions are presented in Table 4.7. The far field stresses remained constant throughout the subsequent steps. The initial displacements

were zero. This is very important since the casing and cement should only deform by loadings resulting from operations after drilling. The casing and cement should not deform by initial loadings.

Drilling step

During a drilling operation, a cylindrical volume of the formation is removed. This volume was under the initial state of stresses described in the equilibrium step and therefore was exerting forces on the surrounding formation. The removal of the cylindrical volume leads to the removal of the force exerted by this volume on the surrounding formation. Drilling fluid which replaces the removed cylindrical volume exerts hydrostatic pressure (due to the density of drilling fluid which is higher than the density of formation fluid) on the surrounding formation. The pressure of drilling fluid is not sufficient to maintain the original equilibrium. This leads to the creation of additional stresses in the surrounding formation to achieve equilibrium. To simulate the creation of additional stresses in the surrounding formation due to the drilling operation, elements within the wellbore in the model were removed in this step.

Running the casing and cementing step

It was assumed that casing was run and cemented immediately after drilling, therefore, in this step after adding cement and casing elements into the model, a force equal to the hydrostatic pressure of the drilling mud was applied on the inner surface (i.e., internal pressure) of the casing. The interaction between cement and casing was tied after activating casing and cement elements. Also, the interaction model between cement and formation surface was activated after running the casing and cementing.

Drilling the next section step

At this step, the wellbore temperature is increased by 10 K to simulate the heat transfer from drilling mud inside the casing. It is assumed that formation permeability is low enough that gas and water released as a result of gas hydrate dissociation cannot flow out of the wellbore region, resulting in an increase in the formation pore pressure.

4.3.3 Thermal model

The size of the thermal model is the same as the hydraulic-mechanical model but with different elements. Also, the density of the mesh and shape of the elements used in the thermal model is exactly the same as the hydraulic-mechanical model. The thermal

analysis was conducted as a transient heat transfer by conduction only by increasing the temperature of casing nodes to 10 K higher than their initial temperature. The heat absorption during gas hydrate dissociation was not considered in the calculations. The thermal model was first run for the same total period of time that the hydraulic-mechanical was going to run but the temperature rising started after running the casing and cementing step. The temperature distribution as an output of this model was saved in a file at each time increment. Finally the file was imported into the hydraulic-mechanical model during analysis of that model and the temperature at each node was called to calculate the gas hydrate dissociate pressure. The time increment in the hydraulic-mechanical model was adjusted properly in order to accurately capture the temperature changes.

4.3.4 Validity of the hydraulic-mechanical model and mesh analysis

The stress redistribution around a wellbore in the cylindrical coordinates due to the drilling operations can be calculated with analytical solution by considering non permeable mud cake as [4.15]:

$$\sigma_r = \left(1 - \frac{R_w^2}{r^2}\right)\sigma_h + \frac{R_w^2}{r^2} P_w \tag{4.8}$$

$$\sigma_\theta = \left(1 + \frac{R_w^2}{r^2}\right)\sigma_h - \frac{R_w^2}{r^2} P_w \tag{4.9}$$

$$\sigma_z = \text{Constant} \tag{4.10}$$

where

σ_r =radial stress

R_w =wellbore radius

r =distance from the sand face

σ_h =horizontal stress

P_w =pore pressure

σ_θ =tangential stress

σ_z =vertical stress

Figures 4.7 and 4.8 show the effective stress distribution around the wellbore resulting from the analytical calculation and numerical modelling (i.e., model with 7120 elements). The mud pressure was assumed 20 MPa in the wellbore and in-situ stresses were obtained from Table 4.7. The effective stress with negative sign in Figures 4.7 and 4.8 means that the effective stress is in compression. The effective stress in tension has a positive sign meaning that pore pressure is higher than total stress.

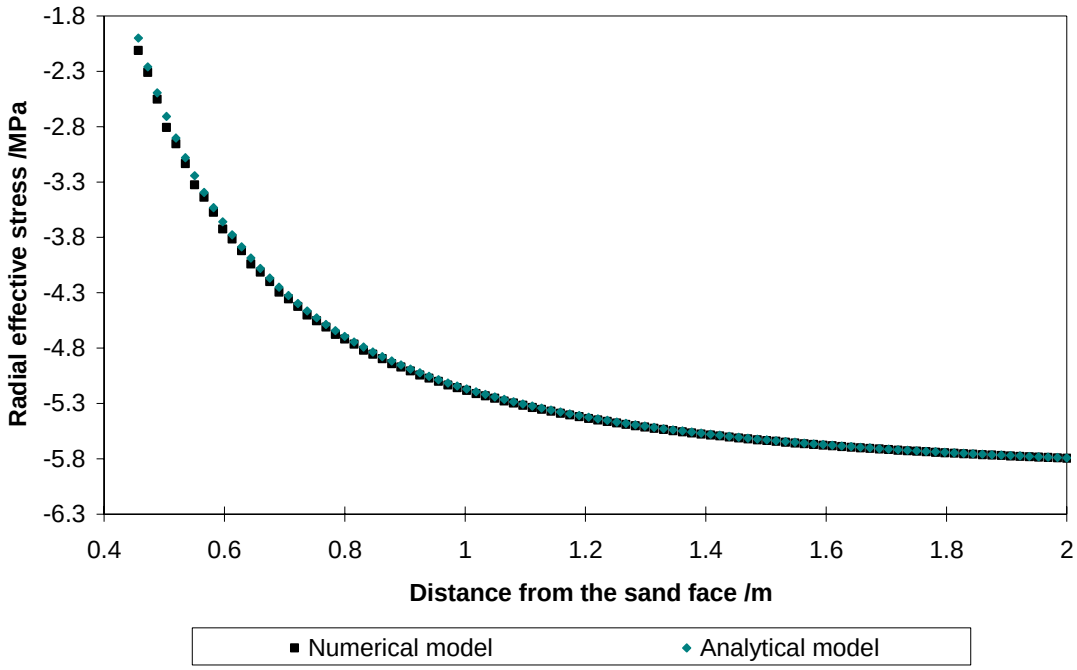

Figure 4.7 Radial effective stresses around the wellbore after drilling operations

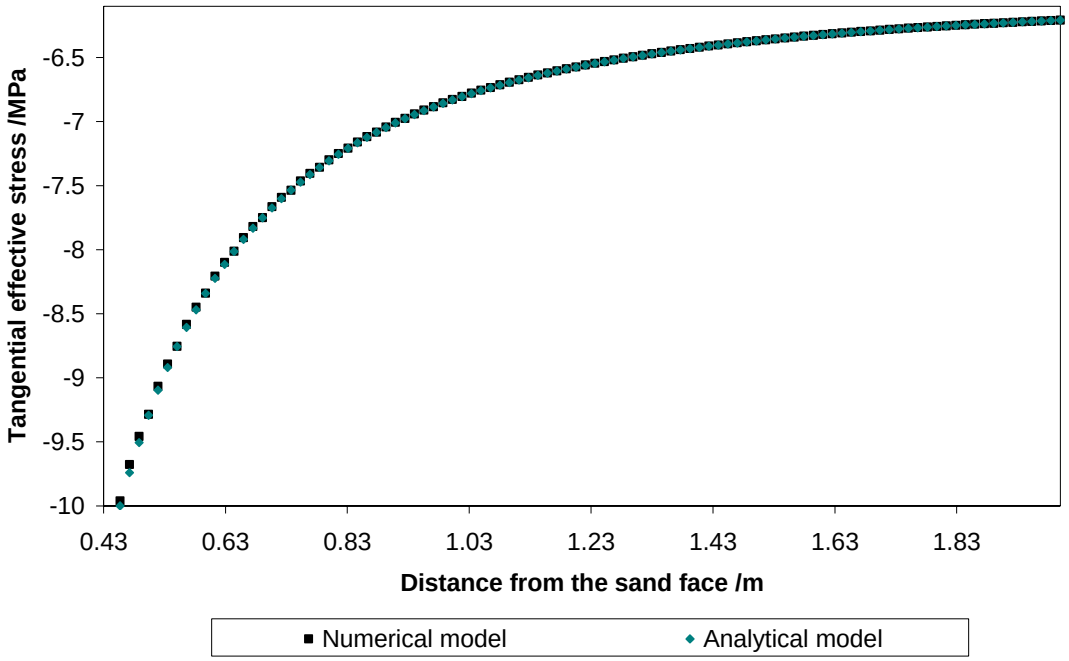

Figure 4.8 Tangential effective stresses around the wellbore after drilling operations

Figures 4.7 and 4.8 show that the results of the numerical model agree with the results of the analytical model. In order to find the best mesh density, three models with different mesh densities were made. The results of those three models were compared with the result of the analytical model to identify the accuracy of the results as shown in Figures 4.9 and 4.10. There are fluctuations in the result of the model with low mesh density but the results of two other fine models are very close to the results of the analytical solution. However, the model with 22051 elements took a very long time to complete the analysis in comparison with the time taken by the model with 7120 elements. Therefore, the model with 7120 elements was used throughout this study for numerical modelling purposes as its results had much agreement with the results of the analytical solutions and also its running time was not too long.

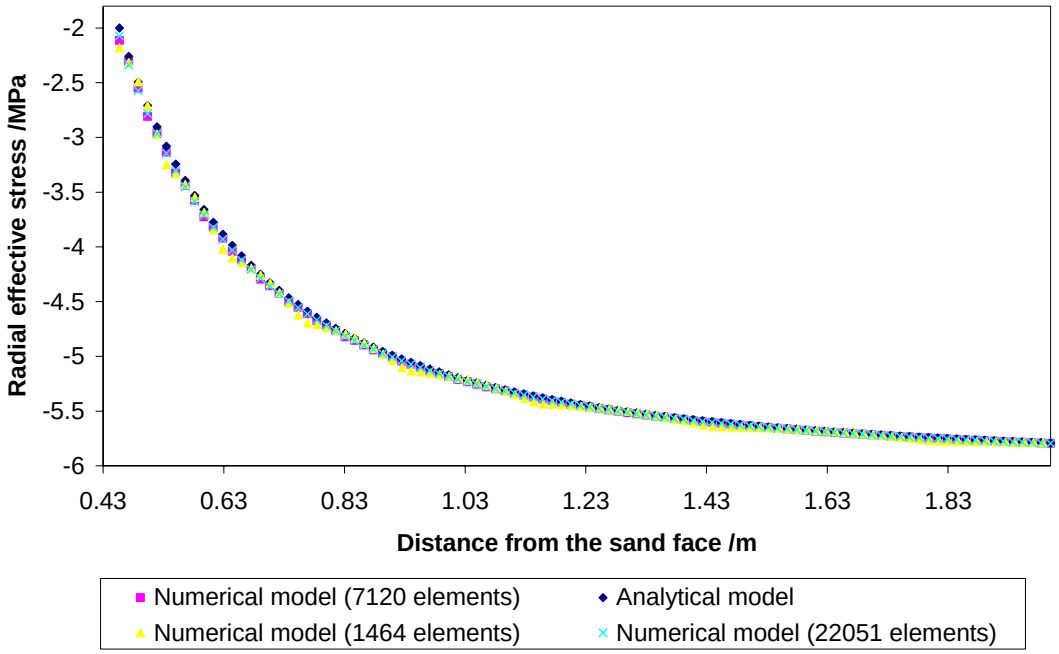

Figure 4.9 Radial effective stresses around the wellbore after drilling operations for models with different mesh density

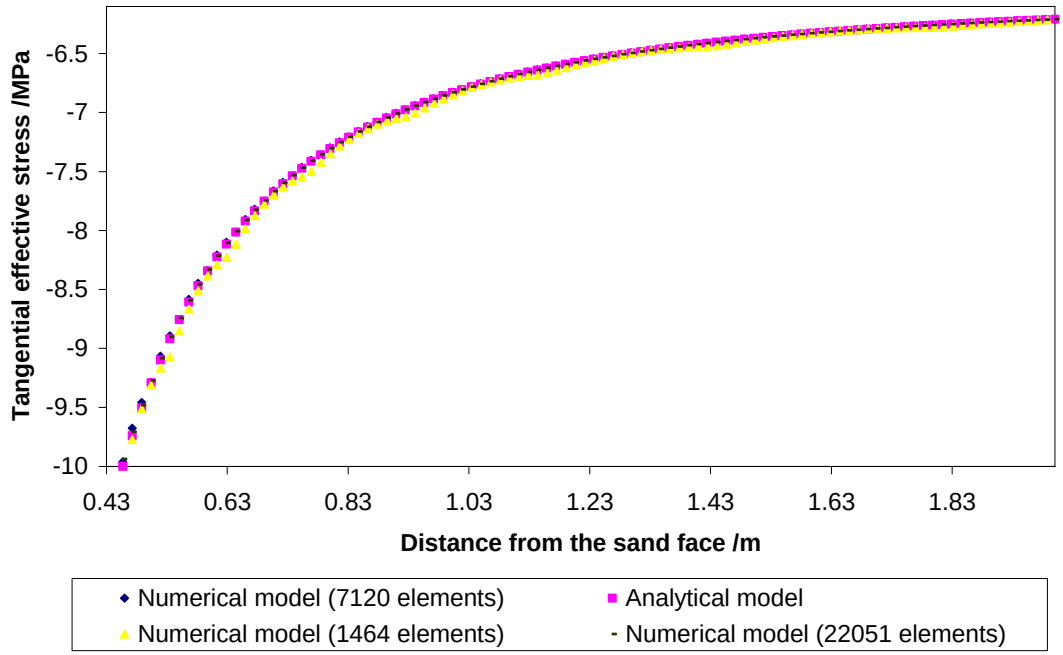

Figure 4.10 Tangential effective stresses around the wellbore after drilling operations for models with different mesh density

4.4 Non-uniform Case

The conventional casing design is based on uniform loading of the casing and does not take into account the interactions between the casing, the cement and the formation; therefore, conventional casing design fails to account for non uniform loading of the casing. There are several reasons for non uniform loading of the casing. Casing eccentricity and voids in the cement (gasified cement by gas migration) are the two main sources of non uniform loading of the casing [4.10], [4.16].

4.4.1 Casing eccentricity

The casing eccentricity is defined as not placing the casing at the centre of the wellbore at the end of the casing running operation. The casing eccentricity is very important especially from the cementing operation point of view. Cementing is performed by circulating a calculated volume of cement slurry through the inside of the casing and out into the annulus (i.e., the volume between the casing and the wellbore). The cement slurry should fill the entirety of the annulus between the casing and the wellbore from the bottom up to the surface. It is called cement return in drilling engineering. One of the reasons that cement slurry does reach the surface (i.e., no cement return) is the hole enlargement which happens in unconsolidated formations frequently. If the casing is not at the centre of the wellbore, the cement sheath around the casing after the cementing operation will not be uniform leading to safety issues and other problems during subsequent wellbore operations. Centralizers are accessory tools called casing jewellery and are used to keep the casing at the centre of the wellbore. The place and number of the centralizers on the casing are very important. If many centralizers are installed on the casing, the friction force generated during running the casing will be so high leading to stuck pipe. On the other hand, if the number of centralizers is too low, the casing will not stay at the centre of the wellbore causing subsequent problems. Determining the number and place of the centralizers are out of the scope of this study. The results of the cementing operation in exploration wellbores drilled in gas hydrate bearing sediments offshore Japan (Nankai Trough) showed no cement return to the surface. It was most likely due to hole enlargement. Gas hydrate bearing sediments are usually very soft and unconsolidated formations. Therefore, hole enlargement and wash out are problems during drilling and cementing of this type of formation. As a result, it is necessary to use enough centralizers on the casing to keep the casing at the centre of the wellbore. If the hole is washed out and there are not enough centralizers

placed on the casing, the casing eccentricity is inevitable [4.13]. In this study, the casing stability of a wellbore, drilled in gas hydrates bearing with insufficient number of centralizers, is of interest and therefore, two numerical models were made to investigate the effect of the casing eccentricity (i.e., non uniform loading) on casing stability in wellbores drilled in gas hydrate bearing sediments [4.16]. The initial conditions and material properties in this case are the same as the uniform case.

Degree of the eccentricity

Figures 4.11 and 4.12 show the schematic of a centric and eccentric casing [4.16].

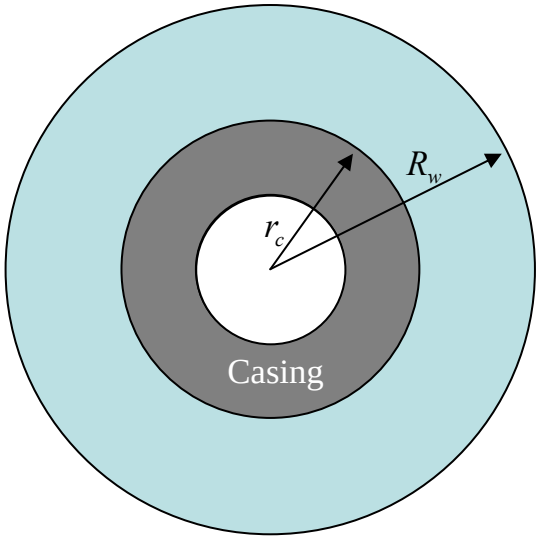

Figure 4.11 Schematic of centric casing

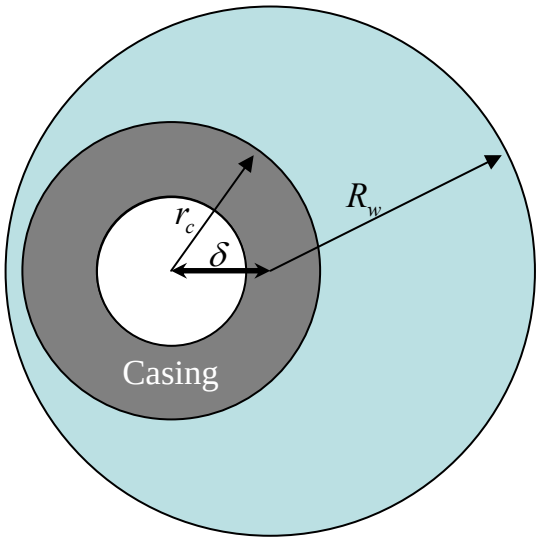

Figure 4.12 Schematic of eccentric casing

The degree of the eccentricity in percent is defined in this study as:

$$\text{Eccentricity\%} = \frac{\delta}{(R_w - r_c)} * 100 \tag{4.11}$$

where

δ =difference between centre of the wellbore and the casing

R_w =radius of the wellbore

r_c =radius of the casing

The degree of the eccentricity varies from zero to 100% in which the casing touches the inner wall of the wellbore (sand face) and the thickness of the cement sheath is zero.

Geometry

Two casing eccentricities were considered in this study including 20% and 40% eccentricity. The size of the models, type of elements and mesh density are equal to the uniform model as explained in Section 4.3.1.

Thermal model

The temperature distribution was different for models with different degrees of eccentricity as the thickness of the cement sheath were different. As a result, two different thermal models were developed corresponding to each hydraulic-mechanic model. The mesh density and element types were the same as Hydraulic-Mechanic models to prevent mesh incompatibility problems during reading temperature values from an external file.

Modelling sequence

The modelling sequence is the same as uniform case explained in Section 4.3.2.

4.5 Results

4.5.1 Uniform case

Temperature distribution and pore pressure generated due to gas hydrate dissociation during 8 days of drilling the next section of the wellbore with mechanical properties according to Experiment 2 are presented in Figures 4.13 to 4.16.

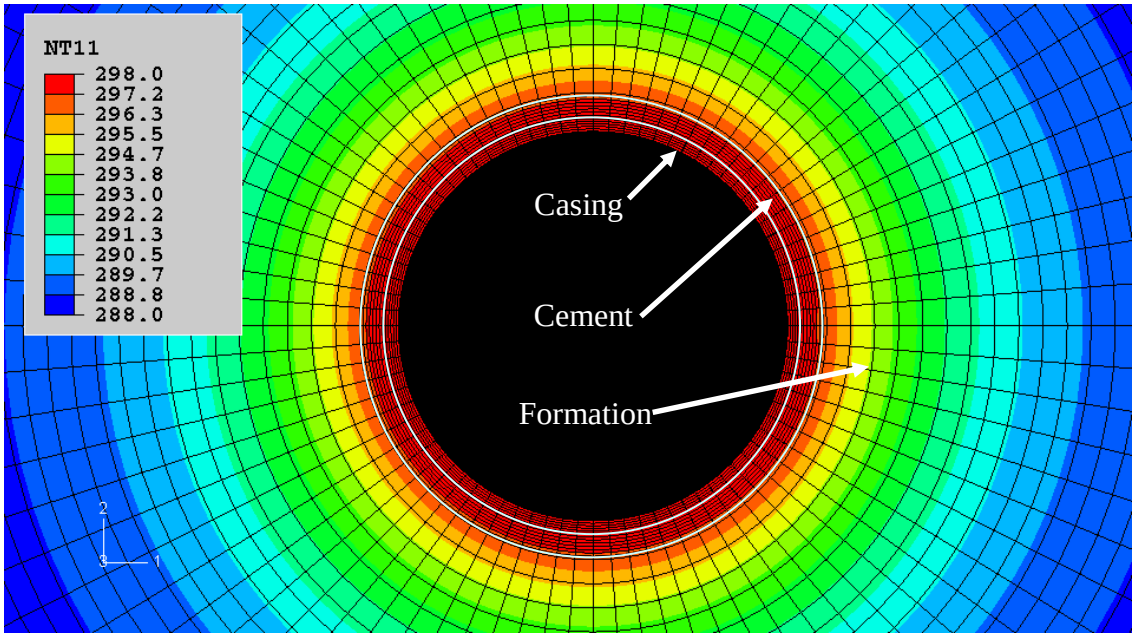

Figure 4.13 Temperature (in K) distribution around the wellbore with cement thermal properties according to System A.

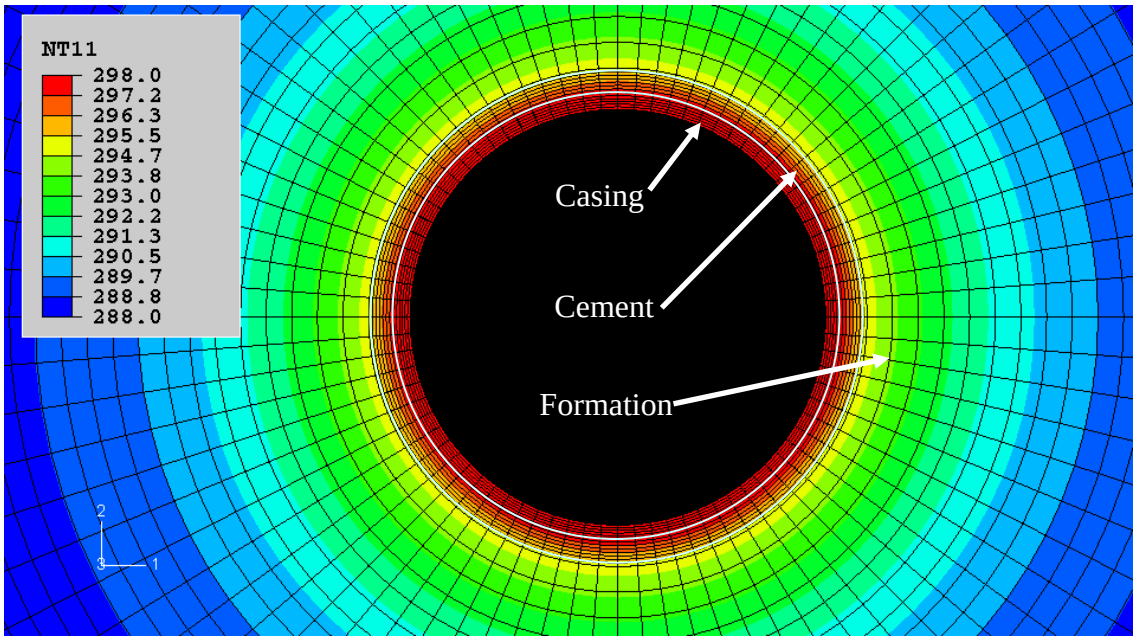

Figure 4.14 Temperature (in K) distribution around the wellbore with cement thermal properties according to System B.

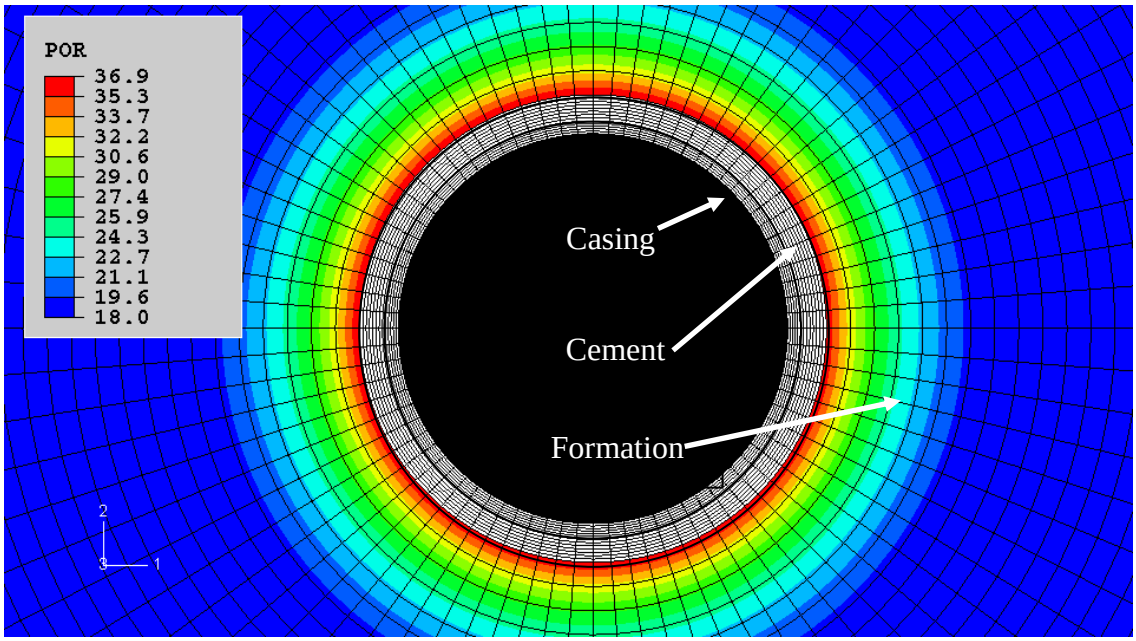

Figure 4.15 Pore pressure (in MPa) distribution around the wellbore with cement thermal properties according to System A.

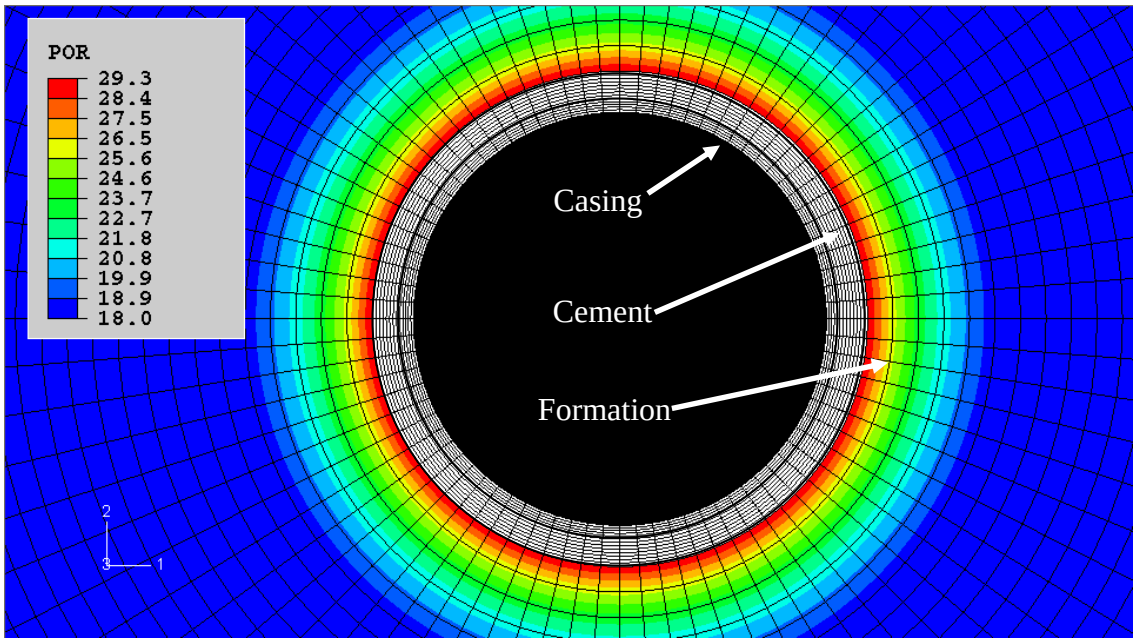

Figure 4.16 Pore pressure distribution (in MPa) around the wellbore with cement thermal properties according to System B.

As shown in these figures, temperature and pressure are uniformly distributed in the formation as expected. The magnitudes of temperature and pore pressure are higher when the cement thermal properties are according to System A. These figures also

show that the pore pressure is higher near the wellbore. It decreases to the in-situ pore pressure in the surrounding formation by moving away from the wellbore.

Pore pressure calculations by ABAQUS agree well with the results of HWHYD as shown in Figures 4.17 and 4.18. The results of HWHYD are methane gas hydrate equilibrium pressures calculated manually at different selected temperatures. Figures 4.17 and 4.18 also show that the HWHYD has been coupled properly with the Hydraulic-Mechanic model in ABAQUS.

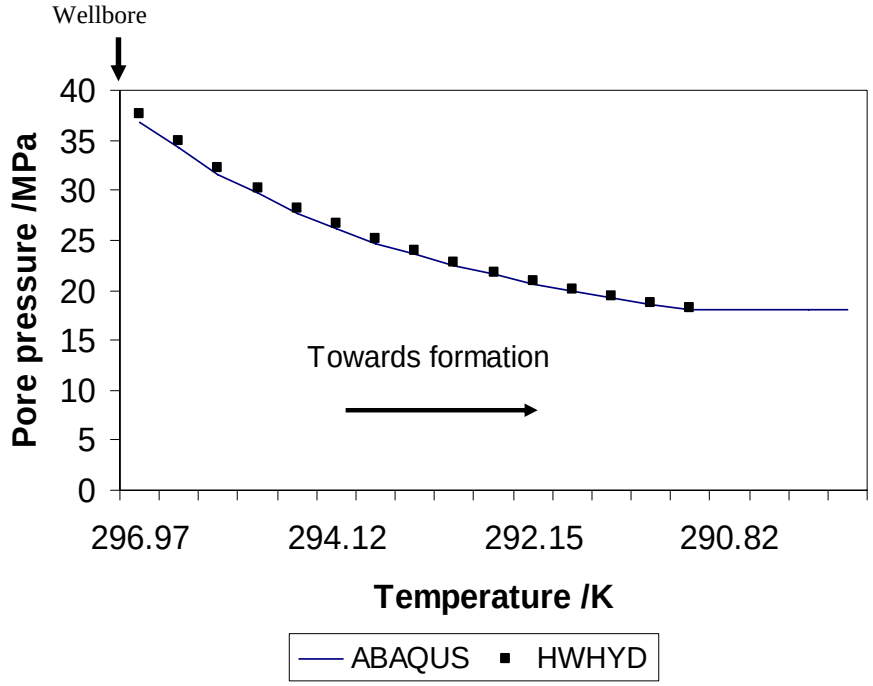

Figure 4.17 Pore pressure distribution from the wellbore toward the formation when cement has thermal properties according to System A

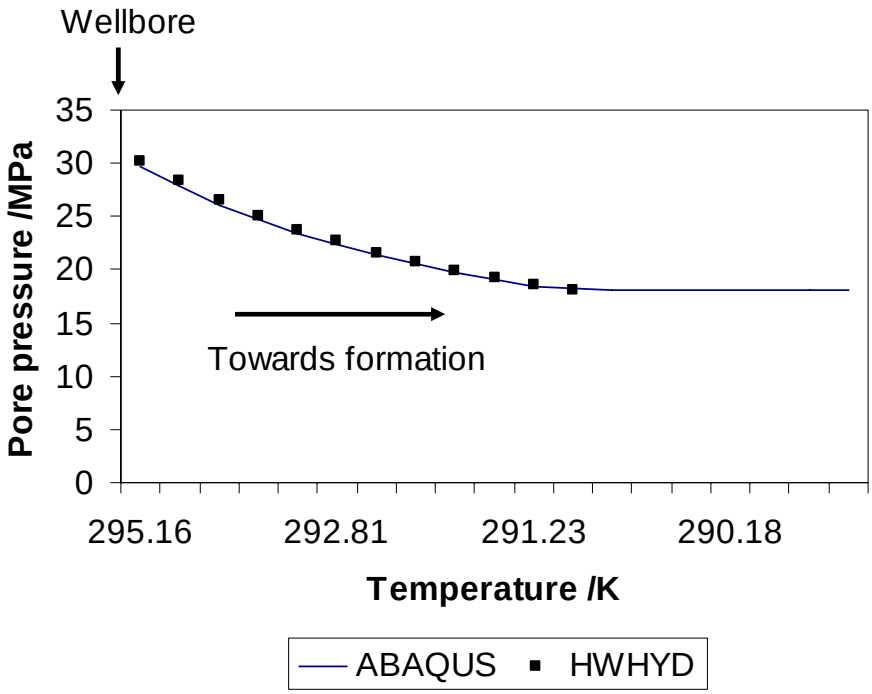

Figure 4.18 Pore pressure distribution from the wellbore toward the formation when cement has thermal properties according to System B

Tables 4.8 to 4.11 show the maximum Von Mises stress generated in the casing after drilling the next section of the wellbore in formations with mechanical properties corresponding to Experiments 1 to 7.

Table 4.8 Maximum Von Mises stress in the casing of the wellbore with cement thermal properties according to System A and mechanical properties according to Formulation-1

Experiment Number	Sediment Composition	Hydrate saturation (S_h)/ %	Maximum Von Mises stress / MPa Formulation-1
1	Silt	7.4	68.17
2	Silt	25.6	90.51
3	Silt	43.6	46.11
4	90 % Silt+10 % Ka	18.8	61.16
5	80 % Silt+20 % Ka	21.3	95.15
6	90 % Silt+10 % Mo	24.1	74.49
7	80 % Silt+20 % Mo	21.4	62.84

Table 4.9 Maximum Von Mises stress in the casing of the wellbore with cement thermal properties according to System A and mechanical properties according to Formulation-2

Experiment Number	Sediment Composition	Hydrate saturation (S_h)/ %	Maximum Von Mises stress / MPa
			Formulation-2
1	Silt	7.4	70.22
2	Silt	25.6	94.05
3	Silt	43.6	46.17
4	90 % Silt+10 % Ka	18.8	62.03
5	80 % Silt+20 % Ka	21.3	98.79
6	90 % Silt+10 % Mo	24.1	78.06
7	80 % Silt+20 % Mo	21.4	63.82

Table 4.10 Maximum Von Mises stress in the casing of the wellbore with cement thermal properties according to System B and mechanical properties according to Formulation-1

Experiment Number	Sediment Composition	Hydrate saturation (S_h)/ %	Maximum Von Mises stress / MPa
			Formulation-1
1	Silt	7.4	59.48
2	Silt	25.6	68.43
3	Silt	43.6	45.83
4	90 % Silt+10 % Ka	18.8	53.84
5	80 % Silt+20 % Ka	21.3	70.13
6	90 % Silt+10 % Mo	24.1	61.42
7	80 % Silt+20 % Mo	21.4	55.92

Table 4.11 Maximum Von Mises stress in the casing of the wellbore with cement thermal properties according to System B and mechanical properties according to Formulation-2

Experiment Number	Sediment Composition	Hydrate saturation (S_h)/ %	Maximum Von Mises stress / MPa
			Formulation-2
1	Silt	7.4	70.22
2	Silt	25.6	70.53
3	Silt	43.6	45.91
4	90 % Silt+10 % Ka	18.8	54.29
5	80 % Silt+20 % Ka	21.3	72.08
6	90 % Silt+10 % Mo	24.1	64.17
7	80 % Silt+20 % Mo	21.4	56.65

4.5.2 Non-uniform case

Figures 4.19 to 4.22 show temperature distribution and the resulting pore pressure due to gas hydrate dissociation for 20 and 40 percent casing eccentricity, respectively around the wellbore with cement thermal properties according to System A.

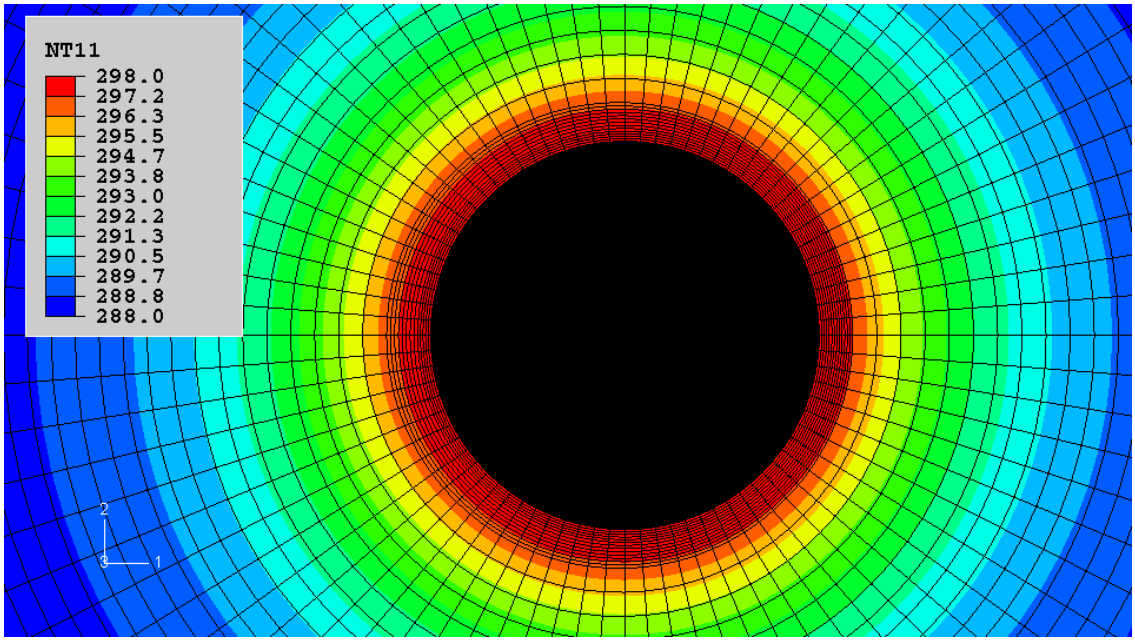

Figure 4.19 Temperature (in K) distribution around the wellbore with cement thermal properties according to System A and 20 percent casing eccentricity

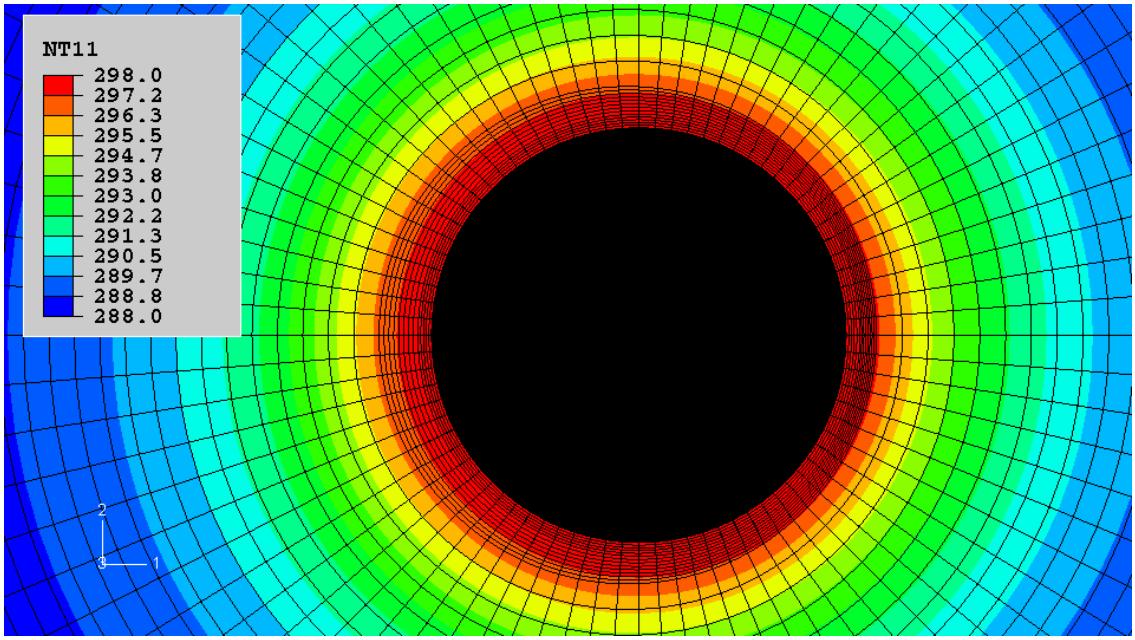

Figure 4.20 Temperature (in K) distribution around the wellbore with cement thermal properties according to System A and 40 percent casing eccentricity

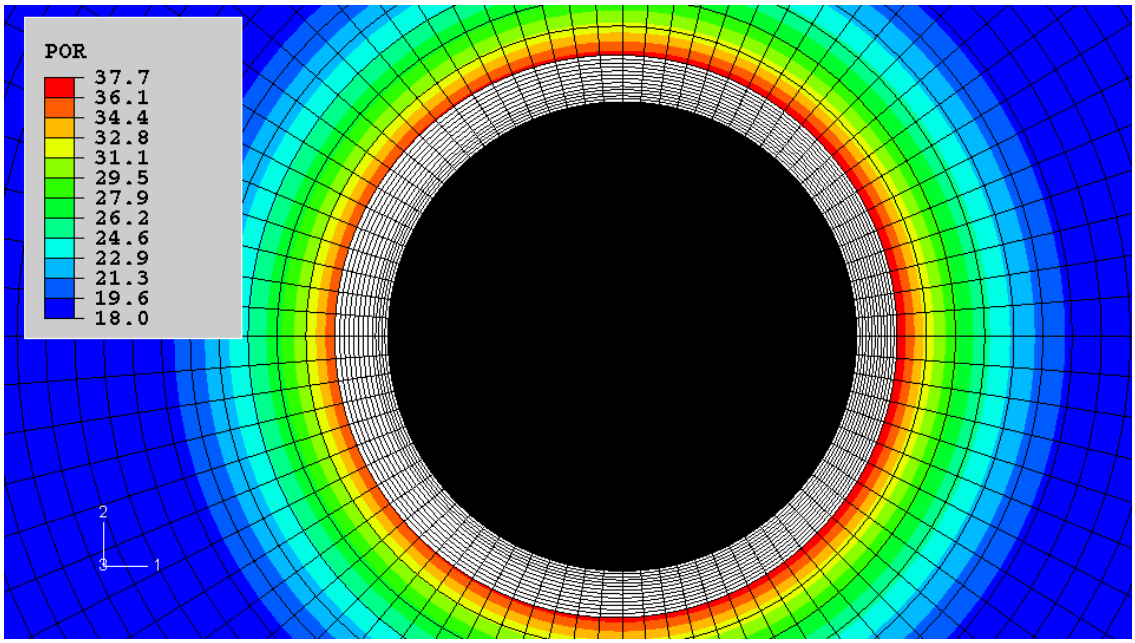

Figure 4.21 Pore pressure (in MPa) distribution around the wellbore with cement thermal properties according to System A and 20 percent casing eccentricity

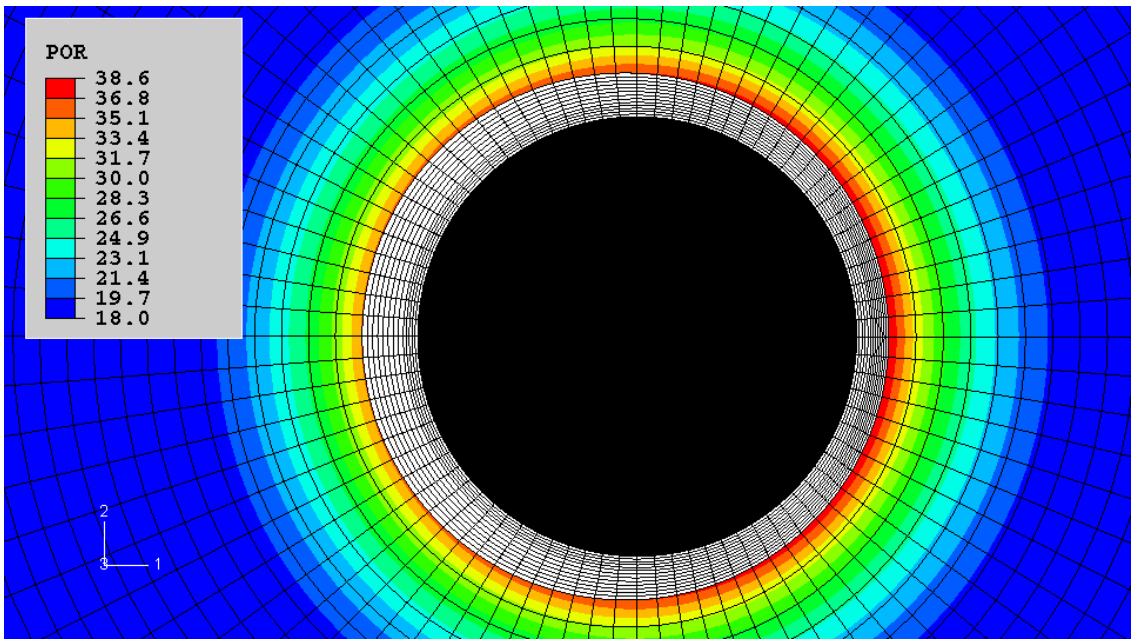

Figure 4.22 Pore pressure (in MPa) distribution around the wellbore with cement thermal properties according to System A and 40 percent casing eccentricity

The temperature distribution in the formation is non uniform around the circumference of the wellbore with eccentric casing, as the thickness of the cement sheath is not

uniform in the annulus. As shown in the figures, the temperature on the right side of the casing is higher than on the left side as the cement sheath on the right side of the casing is thinner than the left side. The pore pressure distribution follows the same pattern of temperature distribution, as shown in Figures 4.21 and 4.22. The magnitudes of pore pressure (similar to the magnitudes of the temperature) are higher on the right side of the casing than the left side and therefore, the casing is not uniformly loaded around its circumference [4.16]. The maximum Von Mises stress generated in the casing for 20 and 40 percent casing eccentricity in the wellbore drilled in different formations are presented in Tables 4.12 to 4.15.

Table 4.12 Maximum Von Mises stress in the casing of the wellbore with cement thermal properties according to System A and mechanical properties according to Formulation-1 under uniform and non-uniform loadings.

Experiment Number	Sediment Composition	Hydrate saturation (S_h)/ %	Maximum Von Mises stress /MPa		
			Formulation-1		
			Non-eccentric casing	20% eccentric casing	40% eccentric casing
1	Silt	7.4	68.17	67.68	67.84
2	Silt	25.6	90.51	89.92	90.14
3	Silt	43.6	46.11	45.90	46.18
4	90 % Silt+10 % Ka	18.8	61.16	60.93	61.17
5	80 % Silt+20 % Ka	21.3	95.15	94.63	94.86
6	90 % Silt+10 % Mo	24.1	74.49	73.86	74.02
7	80 % Silt+20 % Mo	21.4	62.84	62.44	62.60

Table 4.13 Maximum Von Mises stress in the casing of the wellbore with cement thermal properties according to System A and mechanical properties according to Formulation-2 under uniform and non-uniform loadings

Experiment Number	Sediment Composition	Hydrate saturation (S_h)/ %	Maximum Von Mises stress /MPa		
			Formulation-2		
			Non-eccentric casing	20% eccentric casing	40% eccentric casing
1	Silt	7.4	70.22	70.17	70.48
2	Silt	25.6	94.05	94.43	95.08
3	Silt	43.6	46.17	45.72	45.86
4	90 % Silt+10 % Ka	18.8	62.03	61.67	61.74
5	80 % Silt+20 % Ka	21.3	98.79	99.47	100.4
6	90 % Silt+10 % Mo	24.1	78.06	78.09	78.57
7	80 % Silt+20 % Mo	21.4	63.82	63.51	63.60

Table 4.14 Maximum Von Mises stress in the casing of the wellbore with cement thermal properties according to System B and mechanical properties according to Formulation-1 under uniform and non-uniform loadings

Experiment Number	Sediment Composition	Hydrate saturation (S_h)/ %	Maximum Von Mises stress /MPa		
			Formulation-1		
			Non-eccentric casing	20% eccentric casing	40% eccentric casing
1	Silt	7.4	59.48	60.27	61.01
2	Silt	25.6	68.43	70.08	71.77
3	Silt	43.6	45.83	46.03	46.44
4	90 % Silt+10 % Ka	18.8	53.84	54.78	55.63
5	80 % Silt+20 % Ka	21.3	70.13	71.60	73.37
6	90 % Silt+10 % Mo	24.1	61.42	62.69	63.93
7	80 % Silt+20 % Mo	21.4	55.92	56.55	57.23

Table 4.15 Maximum Von Mises stress in the casing of the wellbore with cement thermal properties according to System B and mechanical properties according to Formulation-2 under uniform and non-uniform loadings

Experiment Number	Sediment Composition	Hydrate saturation (S_h)/ %	Maximum Von Mises stress /MPa		
			Formulation-2		
			Non-eccentric casing	20% eccentric casing	40% eccentric casing
1	Silt	7.4	61.04	61.36	61.98
2	Silt	25.6	70.53	71.37	72.70
3	Silt	43.6	45.91	46.02	46.44
4	90 % Silt+10 % Ka	18.8	54.29	54.84	55.46
5	80 % Silt+20 % Ka	21.3	72.08	72.81	74.19
6	90 % Silt+10 % Mo	24.1	64.17	64.88	65.95
7	80 % Silt+20 % Mo	21.4	56.55	56.83	57.45

Tables 4.12 to 4.15 show that the maximum Von Mises stress generated in the casing after drilling the next section of the wellbore (i.e., gas hydrate dissociation) is higher when the cement mechanical properties are in accordance with Formulation-2 under both uniform (i.e., non-eccentric casing) and non-uniform loadings (i.e., eccentric casing). The table also shows that regardless of the cement mechanical properties the maximum Von Mises stress in the casing in wellbore cemented with low thermal properties (i.e., System B) is lower than cement with high thermal properties (i.e., System A) under uniform conditions. This confirms the benefits of using this type of cement in gas hydrate sections of the wellbore.

Figures 4.23 to 4.26 show maximum Von Mises stress in the casing in wellbores under uniform and non-uniform loadings.

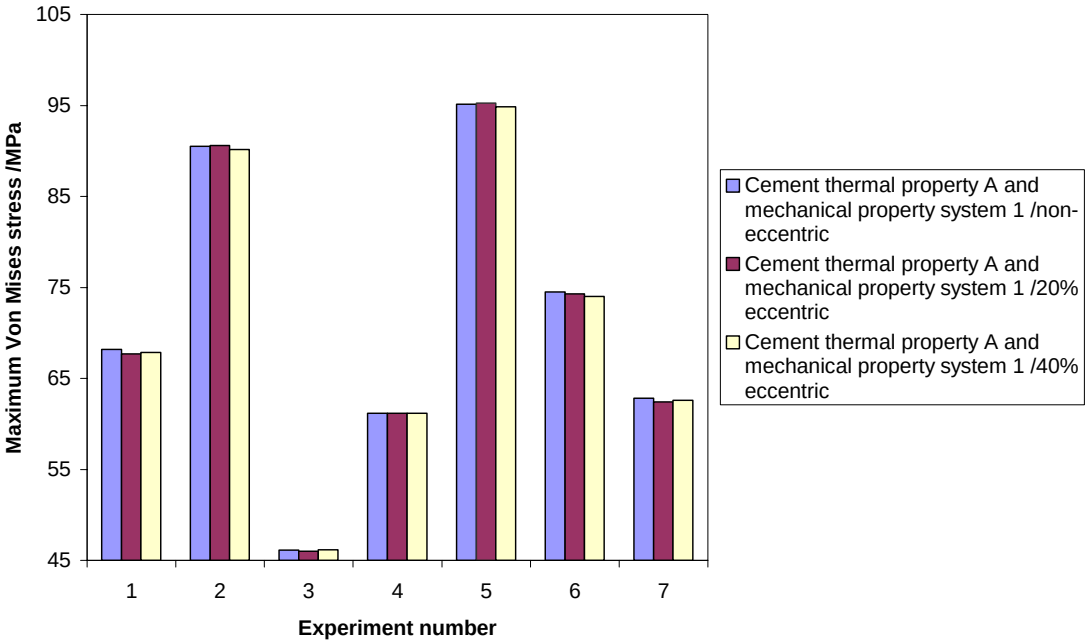

Figure 4.23 Maximum Von Mises stress in the casing with Cement A thermal properties and Formulation-1 mechanical properties under uniform and non uniform loadings.

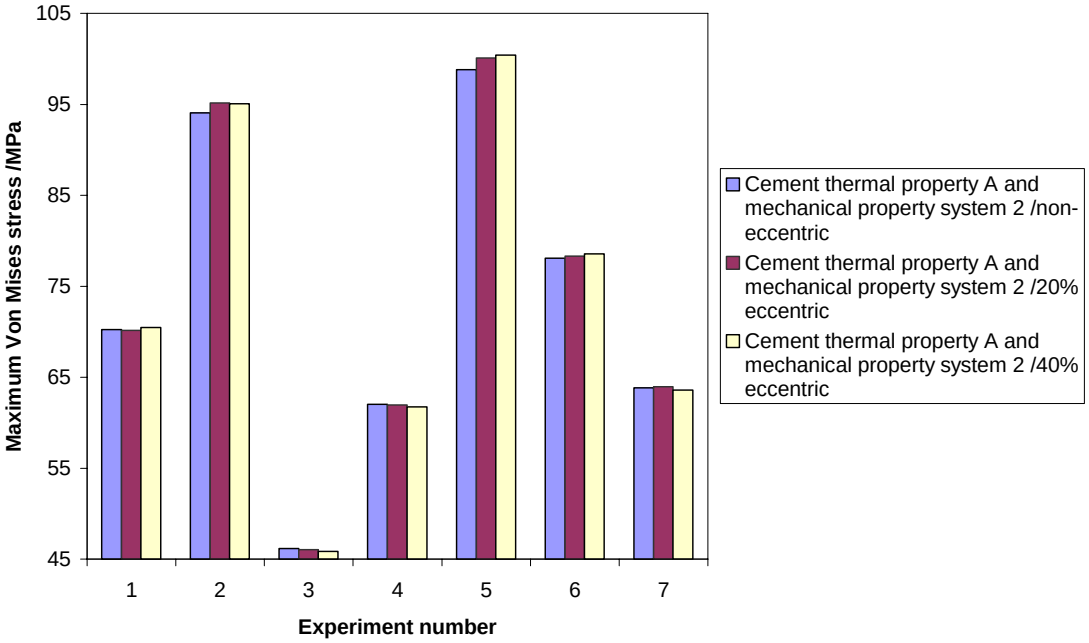

Figure 4.24 Maximum Von Mises stress in the casing with Cement A thermal properties and Formulation-2 mechanical properties under uniform and non uniform loadings

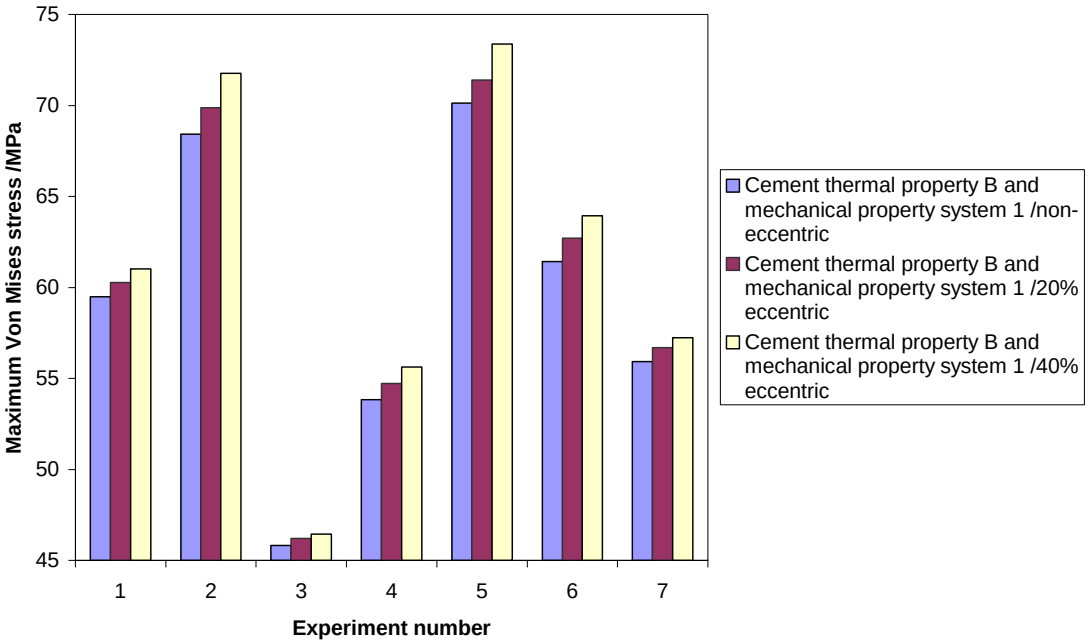

Figure 4.25 Maximum Von Mises stress in the casing with Cement B thermal properties and Formulation-1 mechanical properties under uniform and non uniform loadings

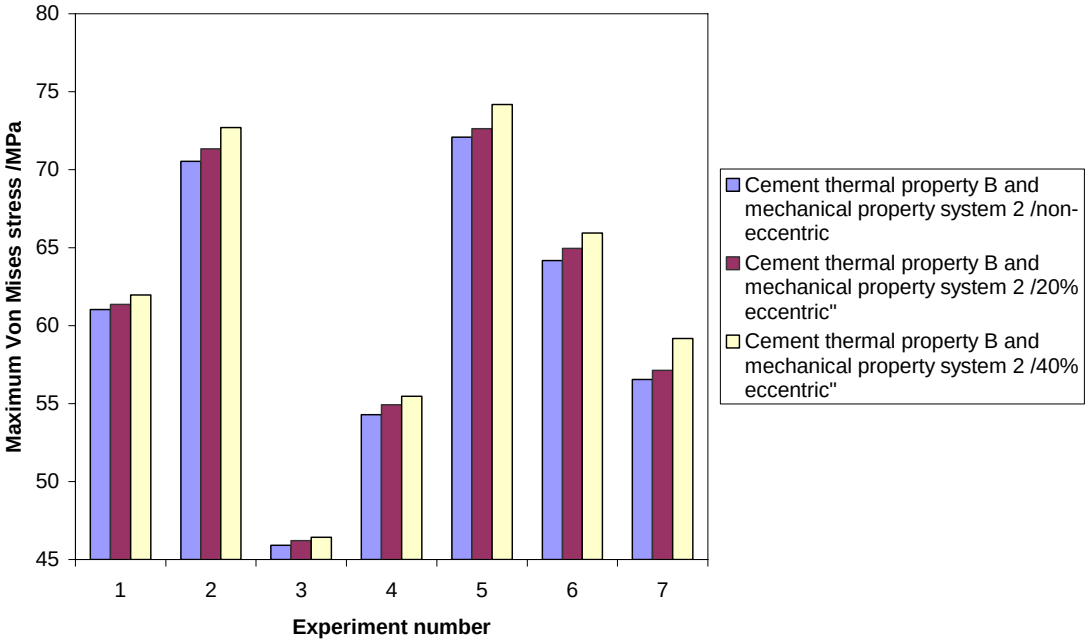

Figure 4.26 Maximum Von Mises stress in the casing with Cement B thermal properties and Formulation-2 mechanical properties under uniform and non uniform loadings

The above figures show that regardless of the mechanical properties of the cement, the maximum Von Mises stress in casings in wellbores cemented using high thermal properties cements (i.e., System A) does not increase by increasing the degree of casing eccentricity. However, the maximum Von Mises stress in casings in wellbores cemented using the low thermal properties cements (i.e., System B) increases by increasing the casing eccentricity.

4.6 Discussion

As shown in Tables 4.8 to 4.11 maximum Von Mises stress in the casing of a wellbore drilled in gas hydrate bearing sediments, regardless of the sediments mineralogy, increases with an increase in gas hydrate saturation. This is suggested to the following two factors; 1) the drilling operation dissociates gas hydrate in the formation behind the casing resulting in an increase in the formation pore pressure, 2) the dissociation of hydrates decreases the mechanical strength of hydrate bearing sediments [4.10] as shown in Tables 2.5 to 2.8. However, the Von Mises stress in Experiment 3 is unexpectedly low. This is suggested to the fact that mechanical degradation was not considered in the calculations, as it could not be measured in this experiment (no S-Wave signal in the receiver).

It is common in drilling practices to use cement with low thermal properties in hydrate bearing sections to decrease the heat transfer through cement and consequently to decrease hydrate dissociation and pore pressure increase behind the casing. The results of this study confirm the benefits of using this type of cement in gas hydrate sections of the wellbore, provided the casing job is good and the casing is placed at the centre of the wellbore. If casing is eccentric then the reverse of the above is true. As mentioned before, in this study the formation was modelled as elastic with degradable elastic properties as a function of temperature. It is expected that gas hydrate bearing sediments behave as elasto-plastic materials under loading instead of just elastic. As a result, it is believed that the maximum Von Mises stress generated in the casings (i.e., shown in Figures 4.23 to 4.26) of a wellbore cemented using a cement with low thermal properties increases significantly by increasing the casing eccentricity and may lead to casing collapse.

4.7 Summary

A numerical model that couples a well-proven thermodynamic PVT-Hydrate model (i.e., HWHYD) with ABAQUS has been developed. The model was used to analyse casing stability in wellbores drilled in gas hydrate bearing sediments under uniform and non-uniform loading due to the casing eccentricity. In the developed model it was assumed that the fluids generated during gas hydrate dissociation cannot flow away from the wellbore region. The mechanical properties of different sediments, containing methane hydrates obtained from Chapter 2, were used in the modelling.

Under the assumed boundary conditions and parameters used in the modelling, it was found that when the cement's thermal properties are low (regardless of the mechanical properties of the cement) the maximum Von Mises stress generated in a centred casing is lower than a casing cemented with a high thermal properties cement as shown in Figure 4.27. However, when the casing is eccentric, the reverse of the above is true.

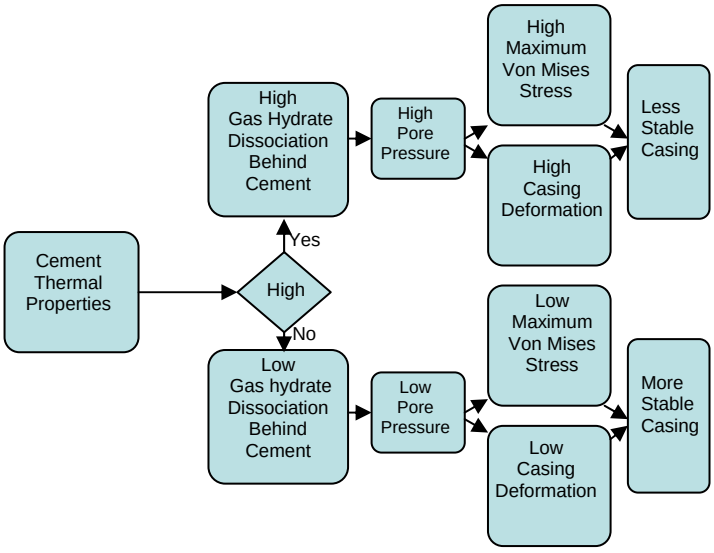

Figure 4.27 Summary of results in uniform model

4.8 References

4.1 M. A. Smith, W.Kou, A.Ahmed, R.Kuzela, *The significance of gas hydrate as a geohazard in Gulf of Mexico exploration and production*, OTC 17655, Offshore Technology Conference, Houston, U.S.A, 2005

4.2 R. Birchwood, S. Noeth, P. Hooyman, W. Winters, *Well bore stability model for marine sediments containing gas hydrates,* AADE-05-NTCE-13, AADE National Technical Conference and Exhibition, Houston, Texas, 2005

4.3 W. D. Callister, *Material Science and Engineering, An Introduction.* John Wiley & Sons, 2007.

4.4 R. Freij-Ayoub, B. Clennell, B. Tohidi, J. Yang, R. Hutcheon, *Casing integrity in hydrate bearing sediments,* Offshore Site Investigation and Geotechnics, London, 2007

4.5 R. Freij-Ayoub, C. Tan, B. Clennell, B. Tohidi, J. Yang, *A well bore stability model for hydrate bearing sediments,* Journal of Petroleum Science and Engineering, 57, 209-220, 2007

4.6 W. W. Fleckenstein, A. W. Eustes, W. J. Rodriguez, A. Berger, *Cemented casing: the true stress picture,* AADE-05-NTCE-14, National Technical Conference and Exhibition, Houston, Texas, 2005

4.7 G. J. Moridis, G. J. Moridis, M. B. Kowalsky, *Response of oceanic hydrate bearing sediments to thermal stresses,*OTC 18193, Offshore Technology Conference, Houston, Texas, 2006

4.8 J. Rutqvista, L. B. Rgessonb., M. Chijimatsuc, A. Kobayashic, L. Jingd, T. S. Nguyene, J. Noorishada, C-F. Tsang, *Thermohydromechanics of partially saturated geological media: governing equations and formulation of four finite element models,* International Journal of Rock Mechanics & Mining Sciences, 38,105-127,2001

4.9 *ABAQUS User`s Manual, Version 6-7, Http://www.simulia.com/*

4.10 M. Salehabadi, M. Jin, J. Yang, H. Haghighi, R. Ahmed, B. Tohidi, *Finite element modelling of casing stability in gas hydrate bearing sediments*, SPE Drilling & Completion Journal, 2009

4.11 B. Tohidi, A. Danesh, A. C. Todd, *Modelling single and mixed electrolyte-solutions and its applications to gas hydrates,* Chemical Engineering Research & Design, 73, 464-472, 1995

4.12 A.J.M.Spencer, Continuum mechanics, Longman Group Limited, 1980

4.13 M. Matsuzawa, S. Umezu, K. Yamamoto, *Evaluation of experiment program 2004: natural hydrate exploration campaign in the nankai-trough offshore japan*, IADC/SPE Drilling Conference, Miami, USA, 2006

4.14 A. Bobet, *Effect of pore water pressure on tunnel support during static and seismic loading.* Tunneling and Underground Space Technology, 18, 377-393, 2003

4.15 E. Fjaer, R. M. Holt, P. Horsrud, A. M. Raaen, R. Risnes, *Petroleum related rock mechanics*, Elsevier, 2008

4.16 M. Salehabadi, M. Jin, J. Yang, R. Ahmed, B. Tohidi, *The effect of casing eccentricity on the casing stability analysis of the wellbore drilled in gas hydrate bearing sediments*, Submitted to SPE/EUROPEC Conference, Barcelona, Spain, 2010

Chapter 5 – Developing a Numerical Model with Consideration to the Kinetics of Hydrate Dissociation

5.1 Introduction

It was assumed in the model developed in the previous chapter that the permeability of the formation is very low, and as a result, the fluids generated during gas hydrate dissociation cannot flow away, resulting in an increase in the formation pore pressure. In other words, it was assumed that the formation pore pressure follows the equilibrium pressure of gas hydrate phase boundary at the calculated system temperature until all the gas hydrates inside the pore space are dissociated. To summarise, in the previous model, the pore pressure was forced to follow the equilibrium pressure of the gas hydrate phase boundary using the DISP subroutine. If the formation is permeable, then the pore pressure during gas hydrate dissociation does not necessarily follow the equilibrium pressure of the gas hydrate phase boundary. The gas hydrate dissociation process, in permeable formations, continues either to the point where the pore pressure reaches the equilibrium pressure of the gas hydrate phase boundary at the given temperature, or, a lower value depending on the kinetics of hydrate dissociation and the flow behaviour in the porous media (until all of the gas hydrates inside the pore space are dissociated). In this chapter, a model is developed by considering the kinetics of hydrate dissociation, in order to remove the assumption related to very low permeability for gas hydrate bearing sediments.

5.2 The developed model

In order to improve the model developed in the previous chapter and consider formation permeability in the casing stability analysis, the fixed pore pressure boundary conditions (i.e., low permeability), assumed in the previous chapter, was relaxed. The fixed pore pressure boundary condition was relaxed by taking into account the fluid flux generated during gas hydrate dissociation. In other words, instead of forcing pore pressure in the Hydraulic-Mechanic model to follow the equilibrium pressure of the gas hydrate phase boundary obtained from HWHYD, fluid flux generated during gas hydrate dissociation was considered in the Hydraulic-Mechanic model. The fluid flux generated during gas hydrate dissociation was obtained using the kinetics of gas hydrates dissociation.

5.2.1 Kim`s hydrate dissociation kinetics model

Kim, et al, [5.1] suggested a model for considering the kinetics of gas hydrate dissociation. They suggested that the rate of gas and water generated inclusive of dissociated gas hydrate during the dissociation process can be calculated as:

$$\frac{dm_g}{Vdt} = -K_d M_g A_h \varphi S_h (P_{eq} - P) \tag{5.1}$$

$$K_d = -K_d^0 Exp(-\frac{9400}{T}) \tag{5.2}$$

A_h =3E5 (m^{-1})

K_d^0 =3.6 E4 ($kmolm^{-2}kPa^{-1}s^{-1}$)

$$\frac{dm_w}{dt} = \frac{M_w N_h}{M_g}\frac{dm_g}{dt} \tag{5.3}$$

N_h =5.7-6

$$\frac{dm_h}{dt} = \frac{M_h}{M_g}\frac{dm_g}{dt} \tag{5.4}$$

where

K_d =hydrate dissociation constant

K_d^0 =hydrate dissociation constant

A_h =hydrate surface area for unit volume of hydrate

M_g =molecular mass of methane gas

M_w =molecular mass of water

M_h =molecular mass of hydrate

P_{eq} =gas hydrate phase boundary pressure

P =pore pressure

φ =porosity

S_h =gas hydrate saturation

V =porous media volume

$\frac{dm_g}{dt}$ =rate of gas generated

$\frac{dm_w}{dt}$ =rate of water generated

$\frac{dm_h}{dt}$ =rate of gas hydrate dissociation

Values of A_h and K_d^0 were obtained from S. Gerami and M. Pooladi-Darvish [5.2]. Hydrate dissociation results in gas hydrate lattice destruction (i.e., $\frac{dm_h}{dt}$) and the release of water (i.e., $\frac{dm_w}{dt}$) and methane gas (i.e., $\frac{dm_g}{dt}$) which are the initial ingredients of most in-situ gas hydrate. According to the Kim's kinetics model (i.e., Equation 5.1), the hydrate lattice destruction or hydrate dissociation rate is a function of a driving force (i.e., $(P_{eq} - P)$) and surface area (i.e., $A_h \varphi S_h$) to which the driving force applies. As a result, hydrate lattice which is close to the surface on which a driving force is applied will destruct first releasing gas and water. The driving force is the difference between the gas hydrate equilibrium pressure and the current pore pressure [5.3].

Hydrate dissociation results in the release of gas and water. The release of methane gas and water during the hydrate dissociation process can be considered as source terms (i.e., volume flux) in the numerical modelling. The rate of source terms as a function of time can be calculated based on the hydrate kinetics equations [5.4]. The gas hydrate dissociation process continues until all gas hydrates inside the pore space are consumed.

In this study, multiphase flow was not considered as the finite element package (ABAQUS) used in this work did not have this capability. ABAQUS only takes into consideration liquid phase (i.e., water). To enable the existing model to simulate gas hydrate dissociation in porous media the following reaction was assumed:

Hydrates----------water + Gas

The density of hydrates is very close to that of water; therefore, the produced gas could be regarded as the net volume increase at system pressure and temperature conditions. This means that the volume of water produced is equivalent to the volume of

dissociated hydrates, hence, the pore pressure increase is solely due to produced gas. As a result, in this study the volume of methane generated during gas hydrate dissociation is considered to be the source of fluid flux. It was assumed that pore pressure contributions come from the volume of methane at system pressure and temperature. The volume of methane gas was calculated by knowing the density of methane gas at the given pressure and temperature as:

$$\frac{dV_g}{Vdt} = -\frac{1}{\rho_g} K_d M_g A_h \varphi S_h (P_{eq} - P) \tag{5.5}$$

where

ρ_g = methane gas density, which is a function of pressure and temperature

5.2.2 Gas hydrate saturation calculation

The hydrate dissociation process continues until either all the hydrates inside the pore space are consumed or the conditions of the system (i.e., the temperature and pressure) reach the hydrate equilibrium conditions. As a result, the hydrate saturation changes during dissociation are required to determine the end of the hydrate dissociation process.

The gas hydrate saturation changes during the dissociation process were calculated as:

$$\frac{dm_g}{Vdt} = -K_d M_g A_h \varphi S_h (P_{eq} - P) \tag{5.6}$$

If both side of the above equation are divided by ρ_h and V_p we get:

$$\frac{1}{\rho_h}\frac{1}{V_p}\frac{dm_g}{Vdt} = -\frac{1}{\rho_h}\frac{1}{V_p} K_d M_g A_h \varphi S_h (P_{eq} - P) \tag{5.7}$$

where

ρ_h =density of hydrate

V_p =volume of pore space

By considering that $\varphi = \frac{V_p}{V}$ (porosity) we get:

$$\frac{1}{\rho_h}\frac{1}{V_p}\frac{dm_g}{Vdt} = -\frac{1}{\rho_h}\frac{1}{V_p}\frac{V_p}{V}K_d M_g A_h S_h (P_{eq} - P) \tag{5.8}$$

Considering $\frac{dm_h}{Vdt} = \frac{M_h}{M_g}\frac{dm_g}{Vdt}$:

$$\frac{1}{\rho_h}\frac{1}{V_p}\frac{dm_h}{Vdt} = -\frac{M_h}{M_g}\frac{1}{\rho_h}\frac{1}{V_p}\frac{V_p}{V}K_d M_g A_h S_h (P_{eq} - P) \tag{5.9}$$

$$\frac{1}{V_p}\frac{dV_h}{Vdt} = -\frac{M_h}{M_g}\frac{1}{\rho_h}\frac{1}{V_p}\frac{V_p}{V}K_d M_g A_h S_h (P_{eq} - P) \tag{5.10}$$

After rearrangement and considering $\frac{dS_h}{dt} = \frac{dV_h}{V_p dt}$:

$$\frac{dS_h}{dt} = -\frac{M_h}{M_g}\frac{K_d}{\rho_h}M_g A_h S_h (P_{eq} - P) \tag{5.11}$$

$\frac{dS_h}{dt}$ = Gas hydrate saturation as a function of time

5.2.3 Thermal model as an analogy of hydraulic model

The typical mass balance equation containing the source term is:

$$\frac{d}{dt}(\int_V \rho_w \varphi dV) = -\int_S \rho_w \varphi N V_w dS + \int_V q dV \tag{5.12}$$

where

q = mass generation rate of aqueous phase per volume of the porous media (source term)

The mass balance equation provided in the ABAQUS package for Hydraulic-Mechanic module is:

$$\frac{d}{dt}(\int_V \rho_w \varphi dV) = -\int_S \rho_w \varphi N V_w dS \tag{5.13}$$

It can be found by comparing Equations 5.12 and 5.13 that the source term is not considered in the governing equations of this module of the ABAQUS package and therefore, there was a limitation imposed by the governing equations used in the ABAQUS package for implementing the kinetics of gas hydrate dissociation into the Hydraulic-Mechanic model.

The mass balance equation containing source term in the hydraulic model can be derived by applying the mass conservation law to a control volume for fluid flow in porous media in the Cartesian coordinates as shown in Figure 5.1. q_{fx}, q_{fy} and q_{fz} are mass inflow entering the control volume, $q_{fx+\Delta x}$, $q_{fy+\Delta y}$ and $q_{fz+\Delta z}$ are mass outflow leaving the control volume. According to the Taylor series, with neglecting second and higher order terms, it can be shown that [5.5]:

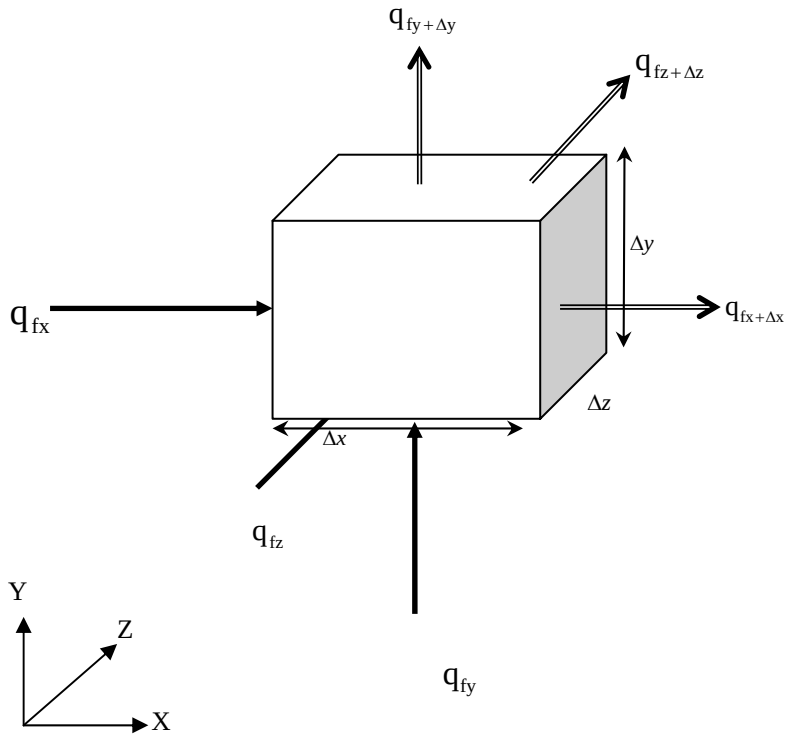

Figure 5.1 Schematic of the control volume

$$q_{fx+\Delta x} = q_{fx} + \frac{\partial q_{fx}}{\partial_x}\Delta x \tag{5.14}$$

$$q_{fy+\Delta y} = q_{fy} + \frac{\partial q_{fy}}{\partial_y}\Delta y \tag{5.15}$$

$$q_{fz+\Delta z} = q_{fz} + \frac{\partial q_{fz}}{\partial_z}\Delta z \tag{5.16}$$

The source term (mass generated in the control volume) is $G\Delta x\Delta y\Delta z$ and the rate of mass storage in the control volume is $\frac{\partial(\rho\varphi)}{\partial t}\Delta x\Delta y\Delta z$ [5.6].

Now the mass balance equation with reference to Figure 5.1 can be written as:

(Inlet Mass - Exit Mass)+ Mass Generated= Mass Stored

$$-\frac{\partial q_{fx}}{\partial_x}\Delta x-\frac{\partial q_{fy}}{\partial_y}\Delta y-\frac{\partial q_{fz}}{\partial_z}\Delta z+G\Delta x\Delta y\Delta z=\frac{\partial(\rho\varphi)}{\partial t}\Delta x\Delta y\Delta z \tag{5.17}$$

According to the Darcy law:

$$-\frac{\partial q_{fx}}{\partial_x}\Delta x-\frac{\partial q_{fy}}{\partial_y}\Delta y-\frac{\partial q_{fz}}{\partial_z}\Delta z+G\Delta x\Delta y\Delta z=\frac{\partial(\rho\varphi)}{\partial t}\Delta x\Delta y\Delta z \tag{5.18}$$

$$q_{fx}=\frac{\rho K_x}{\mu}\Delta y\Delta z\frac{\partial P}{\partial x} \tag{5.19}$$

$$q_{fy}=\frac{\rho K_y}{\mu}\Delta x\Delta z\frac{\partial P}{\partial y} \tag{5.20}$$

$$q_{fz}=\frac{\rho K_z}{\mu}\Delta x\Delta y\frac{\partial P}{\partial z} \tag{5.21}$$

By substituting Equations 5.19 to 5.21 into 5.18 and dividing by the volume we get:

$$\left[\frac{\partial}{\partial x}(\frac{\rho K_x}{\mu}\frac{\partial P}{\partial x})+\frac{\partial}{\partial y}(\frac{\rho K_y}{\mu}\frac{\partial P}{\partial y})+\frac{\partial}{\partial z}(\frac{\rho K_z}{\mu}\frac{\partial P}{\partial z})\right]+G=\frac{\partial(\rho\varphi)}{\partial t} \tag{5.22}$$

where

P =pressure

K_x =permeability in direction of X

K_y =permeability in direction of Y

K_z =permeability in direction of Z

ρ =density

φ =porosity

μ =viscosity of the water

G =source term

The heat balance equation containing source term in the thermal model can be derived by applying the energy conservation law to a control volume in the Cartesian coordinates as shown in Figure 5.2.

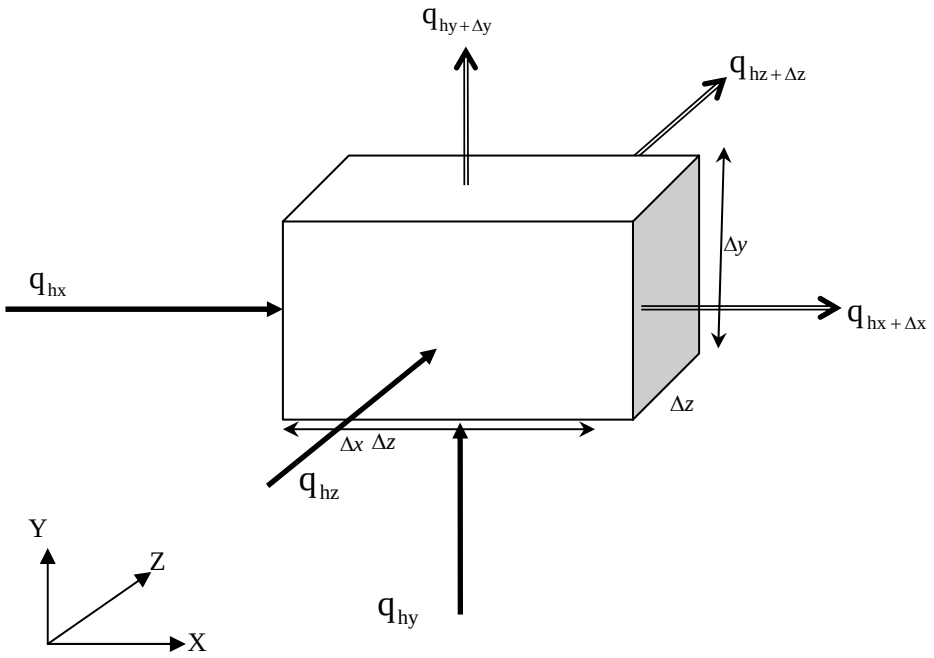

Figure 5.2 Schematic of the control volume

q_{hx}, q_{hy} and q_{hz} are heat inflow entering the control volume, $q_{hx+\Delta x}$, $q_{hy+\Delta y}$ and $q_{hz+\Delta z}$ are heat outflow leaving the control volume. According to Taylor series with neglecting second and higher order terms, it can be shown that [5.5]:

$$q_{hx+\Delta x} = q_{hx} + \frac{\partial q_{hx}}{\partial_x}\Delta x \tag{5.23}$$

$$q_{hy+\Delta y} = q_{hy} + \frac{\partial q_{hy}}{\partial_y}\Delta y \tag{5.24}$$

$$q_{hz+\Delta z} = q_{hz} + \frac{\partial q_{hz}}{\partial_z}\Delta z \tag{5.25}$$

The source term (heat generated in the control volume) is $G\Delta x\Delta y\Delta z$ and the rate of heat storage in the control volume is $\rho C_p \frac{\partial T}{\partial t}\Delta x\Delta y\Delta z$.

Now the heat balance equation with reference to Figure 5.2 can be written as:

(Inlet Heat - Exit Heat)+ Heat Generated= Heat Stored

$$-\frac{\partial q_{hx}}{\partial_x}\Delta x-\frac{\partial q_{hy}}{\partial_y}\Delta y-\frac{\partial q_{hz}}{\partial_z}\Delta z+G\Delta x\Delta y\Delta z=\rho C_p\frac{\partial T}{\partial t}\Delta x\Delta y\Delta z \tag{5.26}$$

According to the Fourier's law:

$$q_{hx}=H_x\Delta y\Delta z\frac{\partial T}{\partial x} \tag{5.27}$$

$$q_{hy}=H_y\Delta x\Delta z\frac{\partial T}{\partial y} \tag{5.28}$$

$$q_{hz}=H_z\Delta x\Delta y\frac{\partial T}{\partial z} \tag{5.29}$$

By substituting Equations 5.27 to 5.29 into 5.26 and dividing by volume we get:

$$\left[\frac{\partial}{\partial x}(H_x\frac{\partial T}{\partial x})+\frac{\partial}{\partial y}(H_y\frac{\partial T}{\partial y})+\frac{\partial}{\partial z}(H_z\frac{\partial T}{\partial z})\right]+G=\rho C_p\frac{\partial T}{\partial t} \tag{5.30}$$

where

T =temperature

H_x =thermal conductivity in direction of X

H_y =thermal conductivity in direction of Y

H_z =thermal conductivity in direction of Z

ρ =density

C_p =specific heat capacity

G =heat volume flux term

Equations 5.22 and 5.30 show that the heat balance equation in the thermal model including conduction only, is similar to the material balance of the hydraulic model including Darcy flow. As a result the thermal model in ABAQUS which contains the heat volume flux term in its heat balance equation was used as an analogy of the hydraulic model in order to overcome the mentioned limitation of the mass balance equation in the hydraulic model. Details of the finite element form of heat balance and mass balance equations are provided in Appendix C.

By comparing Equations 5.22 and 5.30, it can be found that temperature (*T*) and thermal conductivity (*H*) in the thermal analysis are analogues of pressure (*P*) and hydraulic conductivity ($\frac{\rho K}{\mu}$) in the hydraulic model, respectively. However, no clear analogue can be found for specific heat capacity (C_p) in hydraulic analysis.

In order to identify the analogue of specific heat capacity (C_p) in the hydraulic model, two models, including a thermal model (with a known value of thermal conductivity) and a hydraulic model (with known values of porosity and fluid density) were built. Then the wellbore temperature in the thermal model and sand face (it is referred to the area of a formation exposed to the wellbore) pore pressure in the hydraulic model were increased by 28 units (i.e., 28 K and 28 MPa in thermal and hydraulic models, respectively). The specific heat capacity in the thermal model was tuned to achieve the best match between the temperature distribution (from the thermal model) and pore pressure distribution (from the hydraulic model), as shown in Figure 5.3. Consequently, the thermal model with tuned specific heat capacity and known thermal conductivity was used as an analogue to the hydraulic model.

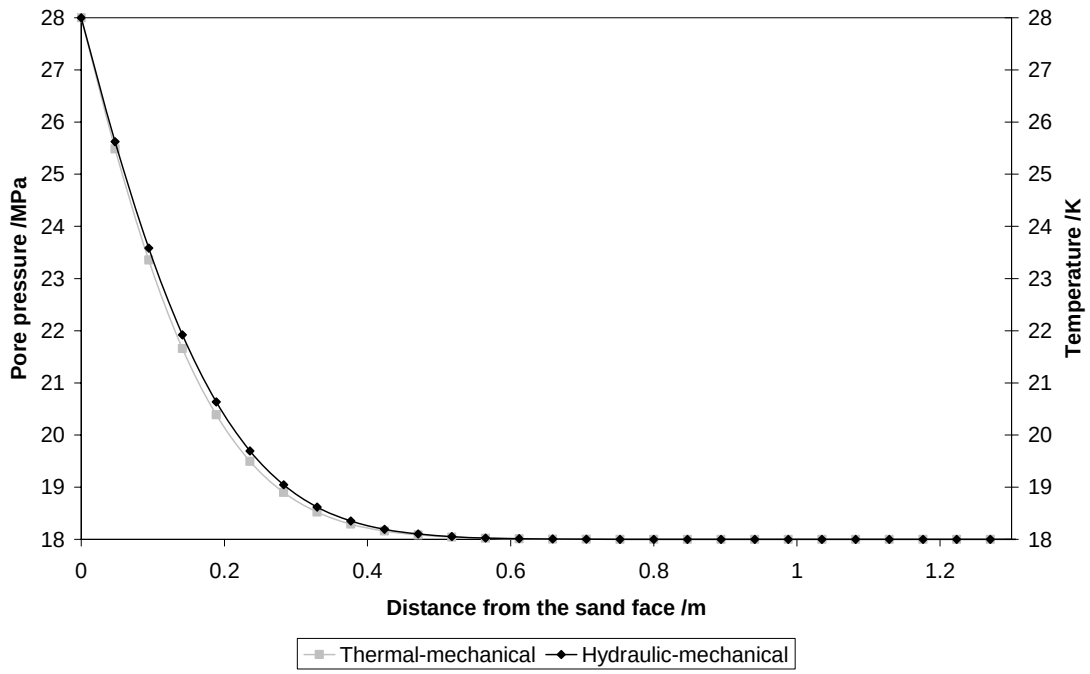

Figure 5.3 Pore pressure and temperature generated from the hydraulic model and its analogue thermal model

The same procedure was used for identifying the coupling term in the thermal-mechanical model analogue to the coupling term in the hydraulic-mechanical model. As a result the thermal expansion in the thermal-mechanical model was tuned to achieve the best match between the displacement distribution from the thermal-mechanical model with the displacement distribution from the hydraulic-mechanical model, as shown in Figure 5.4

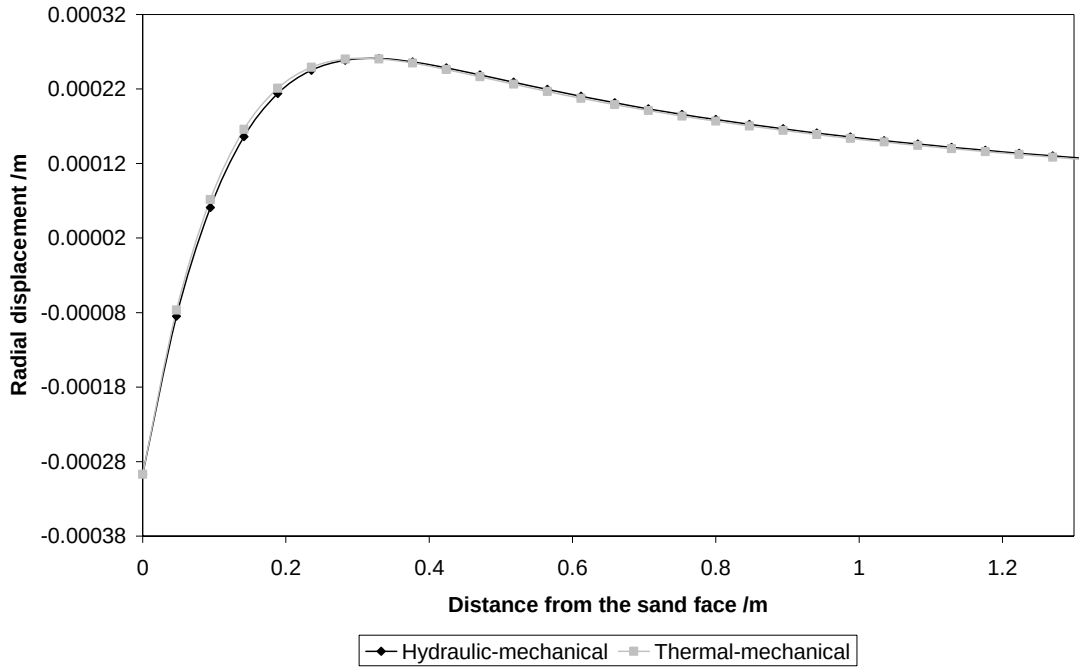

Figure 5.4 Displacement distribution in hydraulic-mechanical and thermal-mechanical models

Figures 5.5 and 5.6 show the radial and tangential effective stress distributions in hydraulic-mechanical and thermal-mechanical models resulting from the tuned displacements in the models.

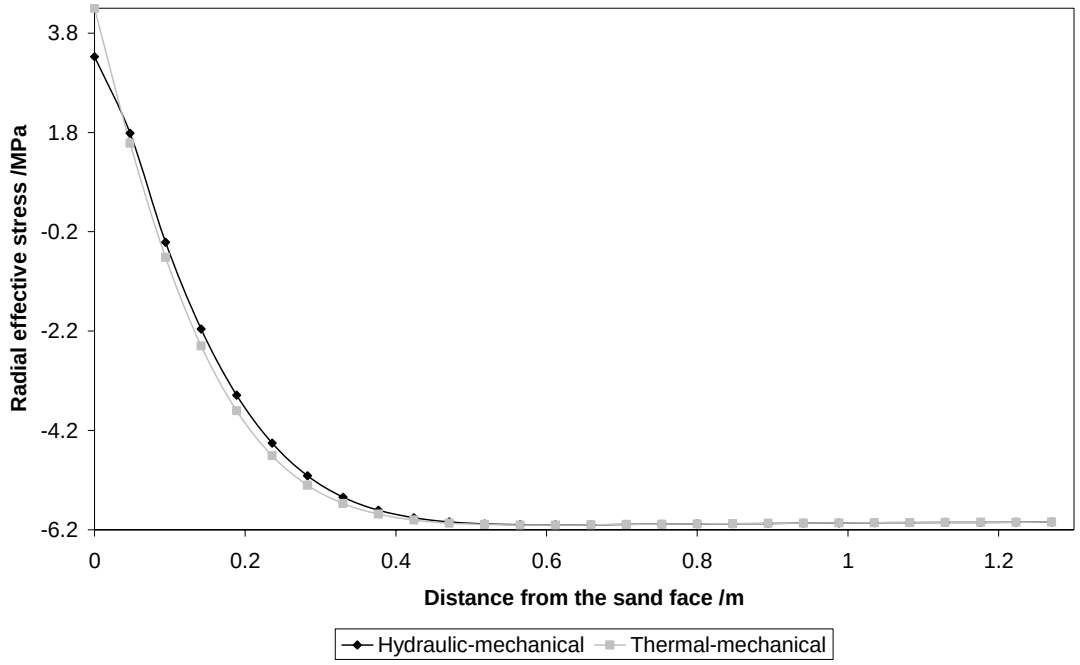

Figure 5.5 Radial effective stress distribution in hydraulic-mechanical and thermal-mechanical models

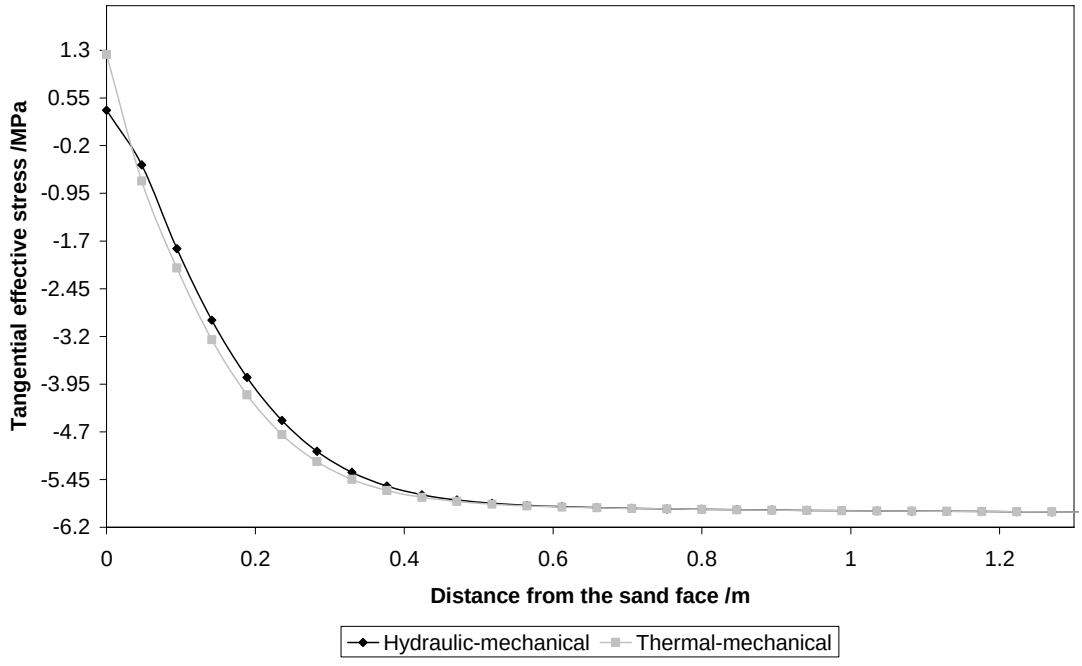

Figure 5.6 Tangential effective stress distribution in hydraulic-mechanical and thermal-mechanical models

Figures 5.4 to 5.6 show that the thermal-mechanical model can be used as the analogue for the hydraulic-mechanical model to which it was tuned.

5.2.4 Implementing the kinetics of gas hydrates dissociation into the thermal-mechanical analysis of ABAQUS

In order to take into consideration the kinetics of gas hydrate dissociation, two subroutines in ABAQUS including DFLUX (body flux) and USDFLD were developed and internally coupled. The developed subroutines are presented in Appendix D.

DFLUX is a subroutine which can be used to define a flux as a function of position, time and temperature. It is called at each integration point in the analysis [5.7]. USDFLD is a subroutine which can be used to define not only field variables as discussed in Section 4.2.2 but also to define the solution-dependent state variables. The solution-dependent state variables are parameters that can be defined within the USDFLD subroutine to evolve with the solution of an analysis. They can be defined as a function of position, time and temperature as well as other parameters within the subroutine and are different from field variables. The detailed explanations regarding these variables can be found elsewhere [5.7].

USDFLD invokes an internal subroutine called GETVRM (get variables) in order to access the pore pressure and temperature at each element during analysis. Changes in gas hydrate saturation are calculated using kinetics of hydrate dissociation (Kim's equation) within USDFLD by taking into account the pore pressure and temperature at each element and stored as a solution-dependent state variable. Gas hydrate saturation along with pore pressure and temperature are passed to the DFLUX subroutine in order to calculate fluid flux generated during gas hydrate dissociation. The formation permeability is updated during analysis as a function of gas hydrate saturation as shown in Equation 5.31 obtained from Nazirdoust, et al [5.8]:

$$K_D = K_{D0}(1 - S_h)^N \tag{5.31}$$

where

K_D=the absolute permeability of the sediments containing gas hydrate

K_{D0}=the initial absolute permeability of the sediments without gas hydrate

S_h=the hydrate saturation

N is determined experimentally and it was assumed equal to 15 in this study as assumed by Nazirdoust, et al [5.8]. Equation 5.31 was originally reported by Masuda, et al [5.9] by studying methane hydrate dissociation in Berea sandstone cores. As a result,

the formation permeability is defined to be dependent on a field variable which is gas hydrate saturation. USDFLD calculates gas hydrate saturation during analysis and stores it as both a field variable to update formation permeability and a solution-dependent state variable to pass on to DFLUX subroutine.

5.2.5 Thermal/thermal-mechanical coupling algorithm

The staggered solution method was used to couple thermal and thermal-mechanical models. The thermal model was first run to calculate temperature distribution in the model over the simulation time. The thermal model breaks the simulation time into multiple time increments and the temperature distribution at the end of each time increment was written to an output file as field variables. The thermal-mechanical model is the analogue of the hydraulic-mechanical model therefore the temperature is the analogue of pore pressure. As a result it was not possible to pass the temperature distribution from the thermal model to the USDFLD subroutine directly as the temperature in the thermal-mechanical model was a degree of freedom. In order to overcome this limitation, the temperature distribution which resulted from the thermal model was written as a field variable. The USDFLD subroutine contains the HWHYD model and the kinetics of hydrate dissociation (Kim's equation) and is being invoked repeatedly within the thermal-mechanical model. HWHYD was used to calculate the hydrate phase boundary while the kinetics model was used to calculate hydrate saturation. Pore pressure and calculated hydrate saturation at each element of the USDFLD subroutine were passed on to the DFLUX subroutine. The thermal-mechanical model updates the formation permeability using calculated hydrate saturation and imposes the calculated fluid flux in the model by invoking the DFLUX subroutine. It should be mentioned that the thermal-mechanical model first invokes the USDFLD subroutine and then the DFLUX subroutine at the beginning of each time increment and before running. The thermal-mechanical model calculates strain, stress and pore pressure distribution. The pore pressure distribution is calculated based on the imposed fluid flux and updated formation permeability. The calculated pore pressure distribution from the thermal-mechanical model was then passed back to the USDFLD subroutine in order to calculate the hydrate saturation for the next time increment. This process continues till the total time reaches the simulation time. The schematic of the coupling algorithm is shown in Figure 5.7.

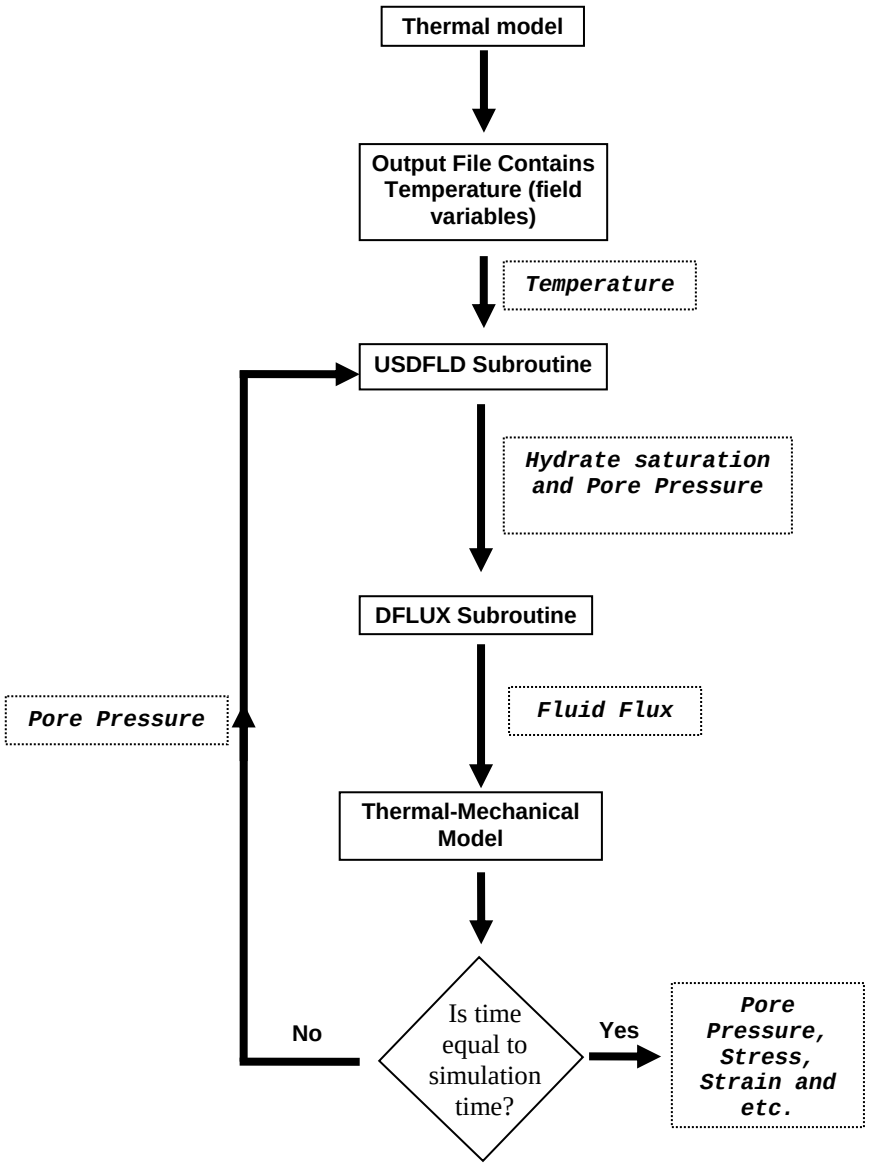

Figure 5.7 Schematic of coupling process

5.2.6 Contact interactions

The contact interaction model is the same as the model explained in Section 4.2.3. In this model it is assumed that the cement has good bonding with the formation so that there is no sliding between these surfaces. Furthermore, it is assumed that the casing and cement were perfectly bonded.

5.2.7 The properties of materials

Formation

The physical and mechanical properties of the formation including the plastic properties were obtained from available literature and three different magnitude of absolute permeability were used for the parametric study as shown in Table 5.1.

Table 5.1 Assumed properties of hydrate bearing formation

General properties	
Density /kgm^{-3}	2200
Hydrate saturation / %	20
Mechanical properties	
Young's Modulus /MPa	807.6
Poisson Ratio	0.4
Cohesion /MPa	3.2
Friction angle /^{o}	30
Absolute permeability /m^2	97.98 E-13
Absolute permeability /m^2	97.98 E-14
Absolute permeability /m^2	97.98 E-15
Thermal properties	
Thermal Conductivity /Wm^{-1}K^{-1}	1.4
Heat Capacity /JK^{-1}kg^{-1}	1900

Casing

The physical and mechanical properties of the casing were the same as Table 4.1.

Cement

The thermal and mechanical properties of the cement used in the model are presented in Table 5.2.

Table 5.2 Properties of cement

Mechanical properties	
Young's Modulus /GPa	5.51
Poisson`s Ratio	0.32
Compressive Strength /MPa	17.241
Tensile Strength /MPa	1.379
Thermal properties	
Thermal Expansion $/K^{-1}$	4.33 E-6
Thermal Conductivity $/Wm^{-1}K^{-1}$	0.66
Heat Capacity $/JK^{-1}kg^{-1}$	2100

Formation fluid

The properties of the formation fluid were the same as Table 4.6.

5.2.8 Geometry of the model

The geometry of the model used in this study is similar to the uniform case explained in Section 4.3. The formation elements contained an additional degree of freedom to accommodate temperature (i.e., as analogue of pore pressure).

5.2.9 Modelling sequence

The modelling sequence are the same as Section 4.3.2.

5.3 Results

The models in which the absolute formation permeability is 97.98 E-13, 97.98 E-14 and 97.98 E-15 are named Case-1, Case-2 and Case-3 respectively throughout this study. The permeability of Case-3 was obtained from Nazirdoust, et al [5.8]. As mentioned before, permeabilities in Cases-1 and 2 were used only for parametric study. The temperature distribution in the models is presented in the Figure 5.8.

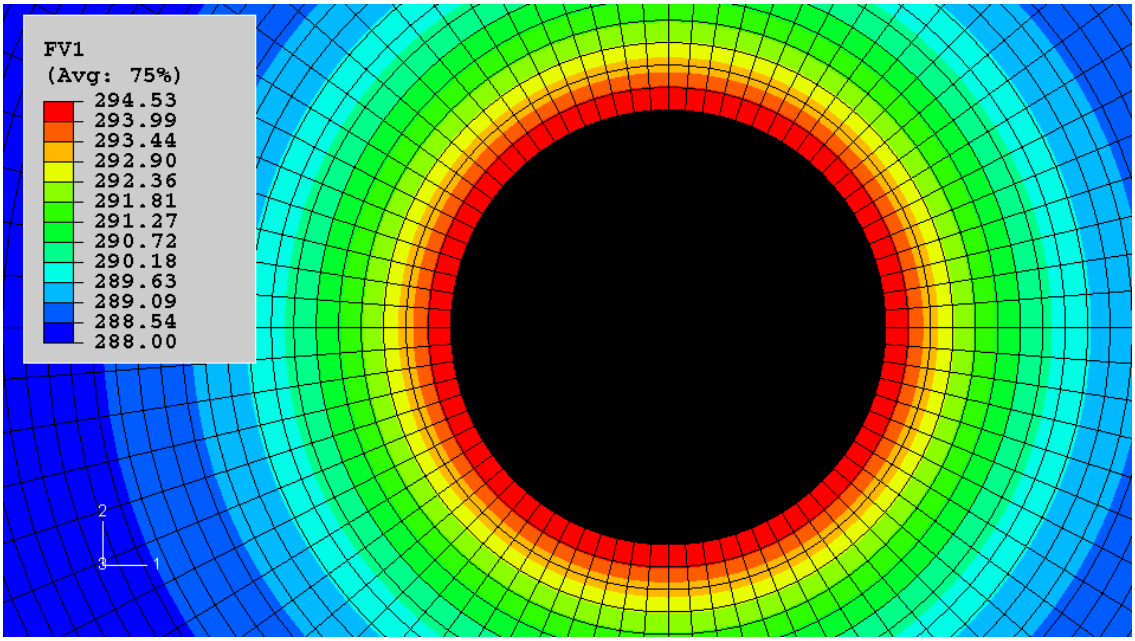

Figure 5.8 Temperature distribution in the models

The temperature distribution shown in Figure 5.8 resulted from drilling the next section of the wellbore in gas hydrate bearing sediments after 8 days. In other words it was generated by increasing the temperature at nodes adjacent to the wellbore by 10 K compared to the initial temperature as assumed by Freij-Ayoub, et al [5.10]. Figure 5.9 also shows the temperature distribution in the models at different times after starting drilling the next section of the wellbore.

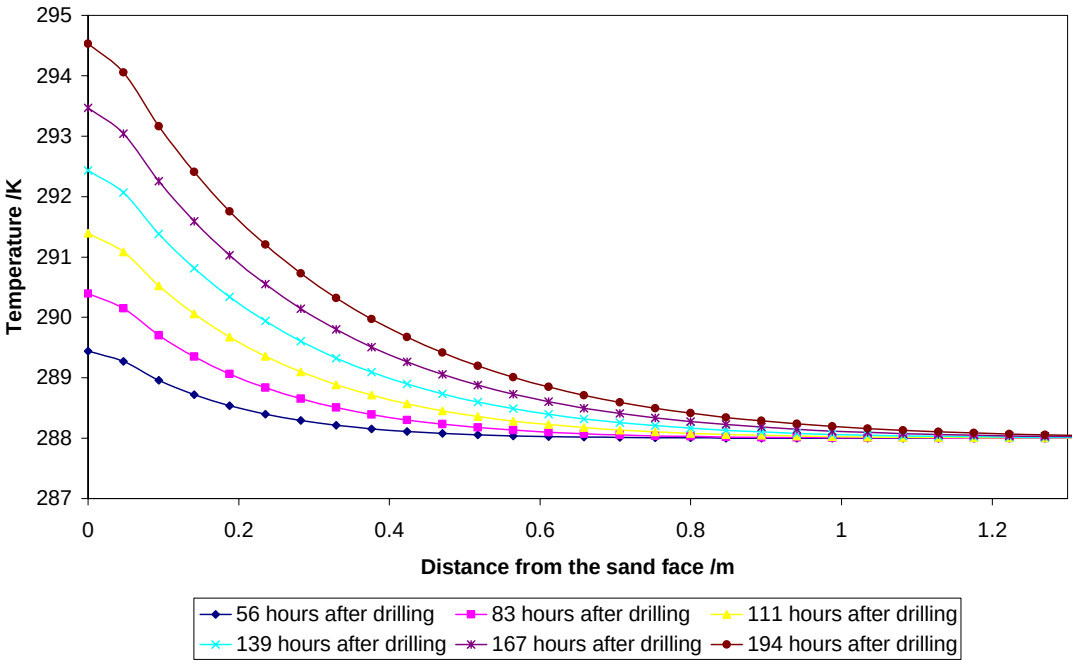

Figure 5.9 Transient temperature distribution in the models

Figures 5.10 to 5.12 show the pore pressure distribution in Cases-1 to 3, respectively.

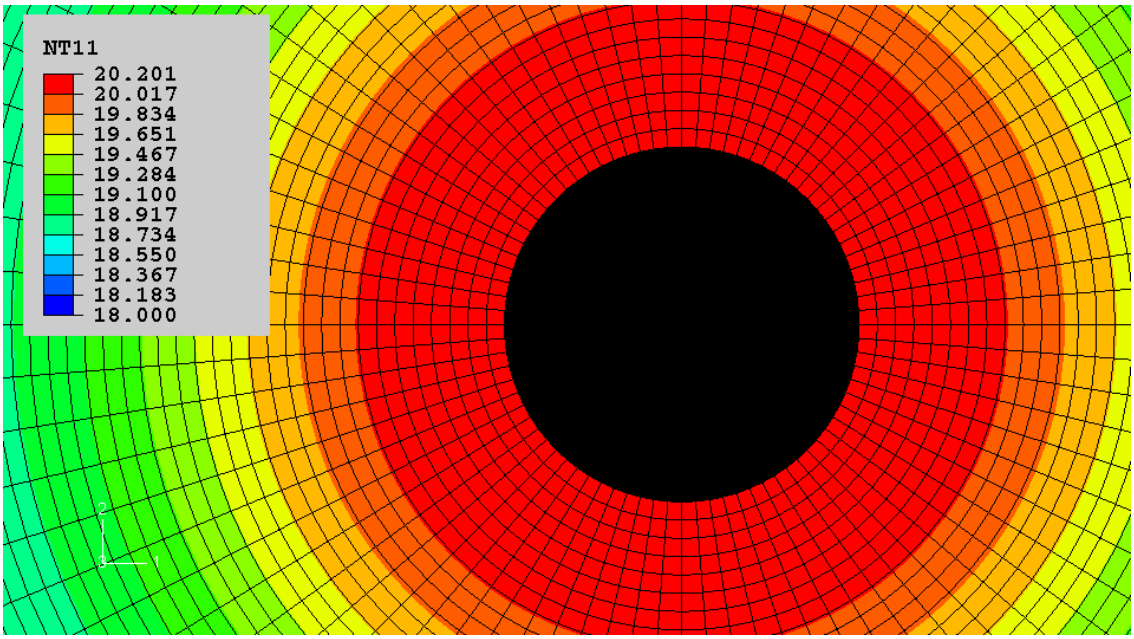

Figure 5.10 Pore pressure distribution in Case-1

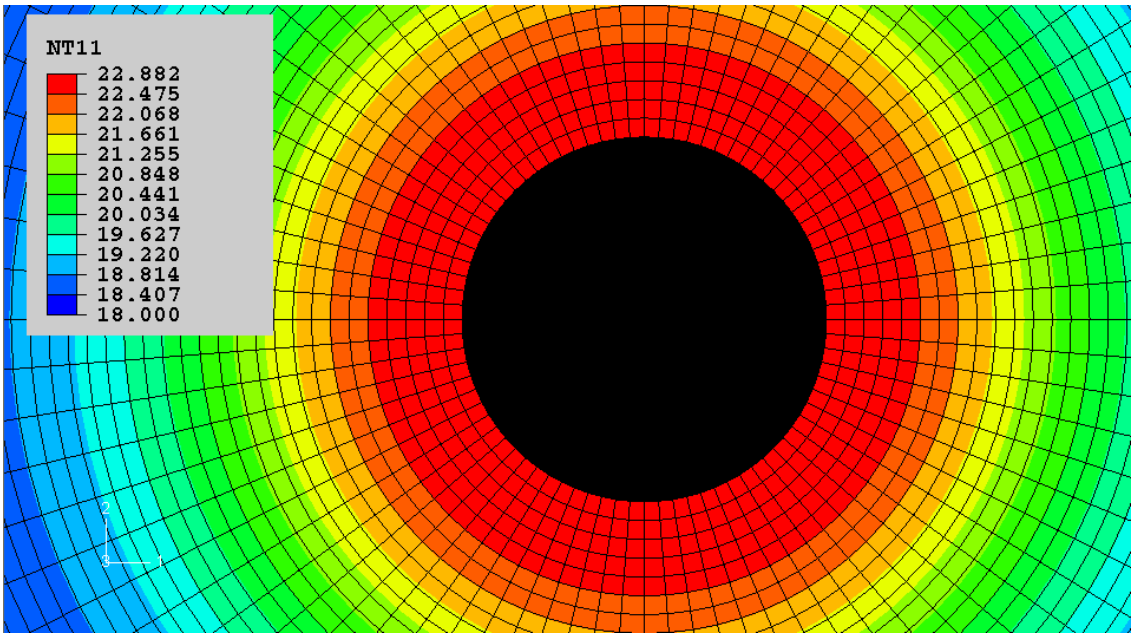

Figure 5.11 Pore pressure distribution in Case-2

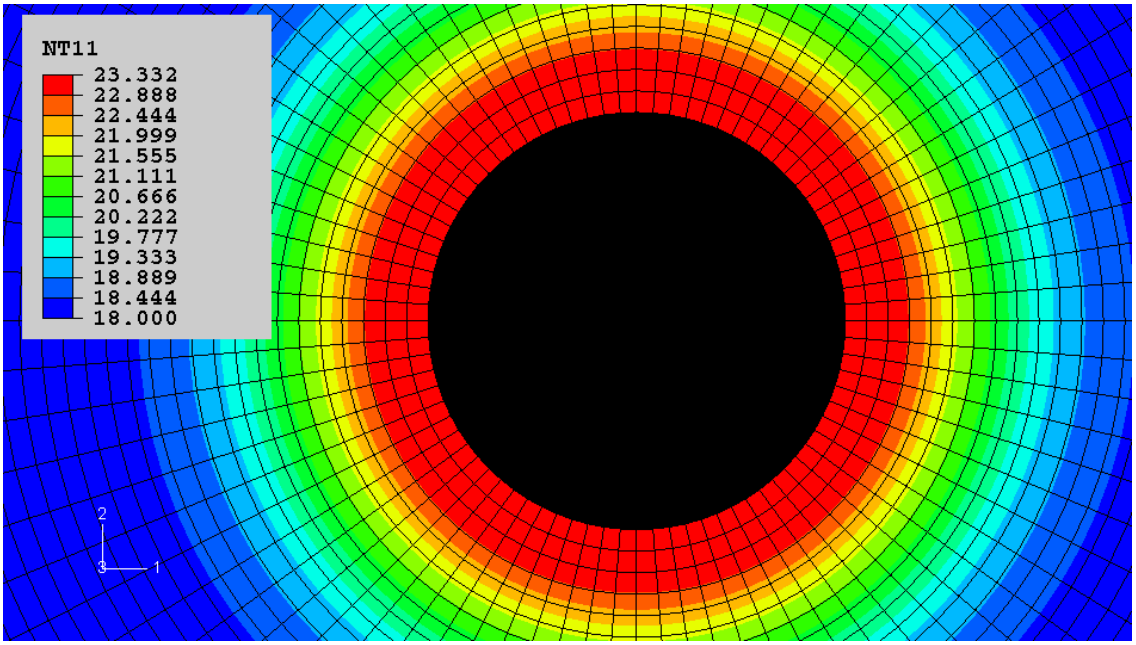

Figure 5.12 Pore pressure distribution in Case-3

As shown in the above figures, the magnitude of pore pressure increases by decreasing the permeability of the formation. When the formation permeability is high the fluids generated during gas hydrate dissociation will flow away from the wellbore decreasing the pore pressure. Pore pressure in the near wellbore area which has being affected by

the fluids generated during gas hydrate dissociation also increases by increasing the formation permeability. Figures 5.13 to 5.15 show the pore pressure distribution in the formation at different times after starting drilling the next section of the wellbore.

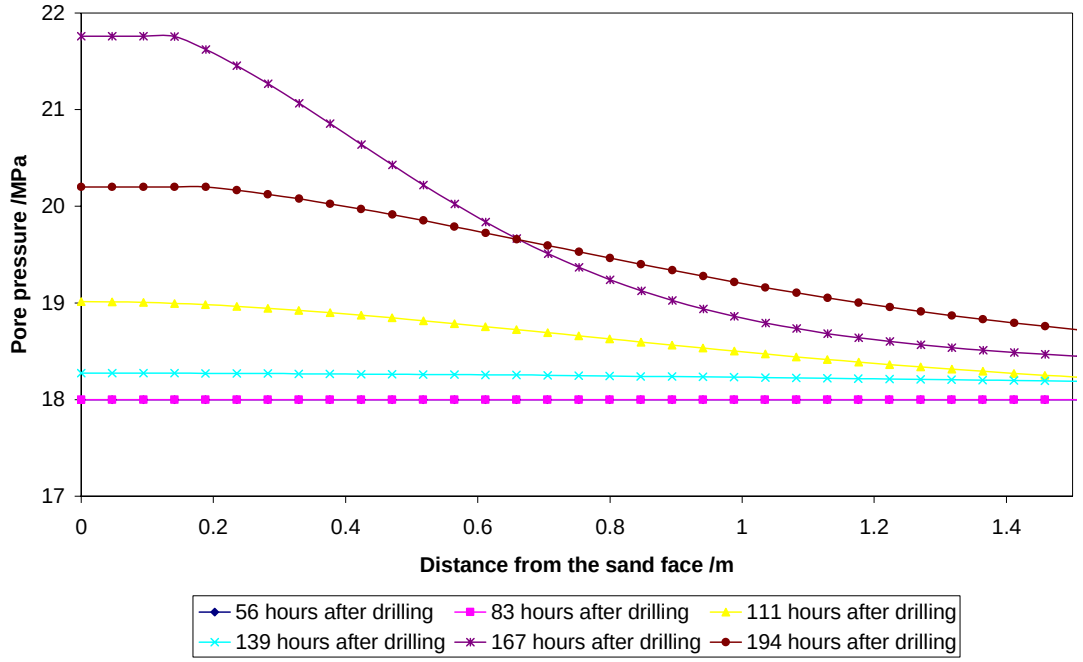

Figure 5.13 Pore pressure distribution in Case-1(i.e., with permeability of 97.98 E-13 m^2) at different times after drilling the next section of the wellbore

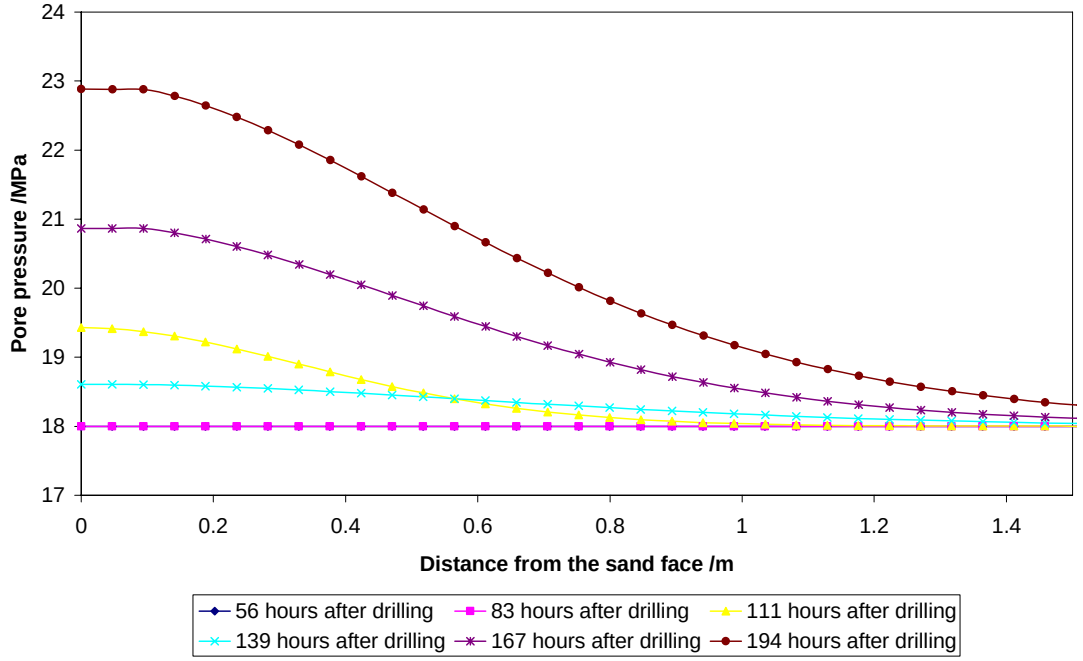

Figure 5.14 Pore pressure distribution in Case-2 (i.e., with permeability of 97.98 E-14 m^2) at different times after drilling the next section of the wellbore

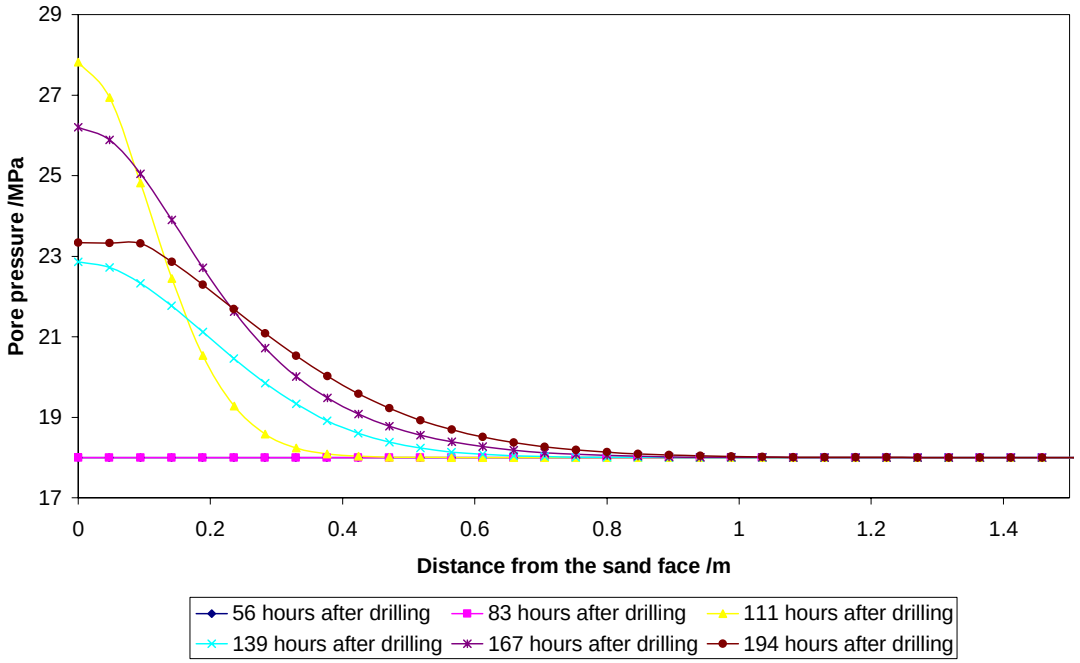

Figure 5.15 Pore pressure distribution in Case-3 (i.e., with permeability of 97.98 E-15 m^2) at different times after drilling the next section of the wellbore

Figures 5.16 shows that less gas hydrate will dissociate behind the casing by decreasing the formation permeability.

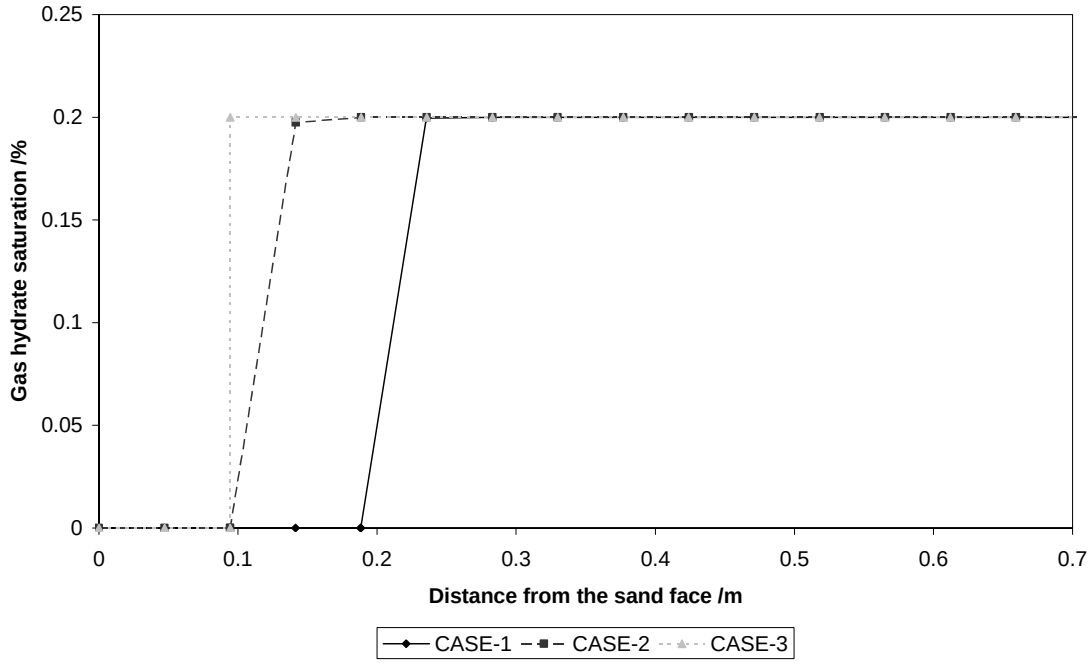

Figure 5.16 Gas hydrate saturation as a function of distance from the sand face in Cases-1 to 3

The pore pressure distribution in Cases-1 to 3 is shown in Figure 5.17. The pore pressure distribution resulted from a model considering the formation with very low permeability so that fluids generated during gas hydrate dissociation can not flow away from the wellbore region (i.e., as mentioned in the previous chapter) is also shown in Figure 5.17 for comparison. Figure 5.17 shows that the magnitude of pore pressure resulted from the model considering the formation with very low permeability is very high.

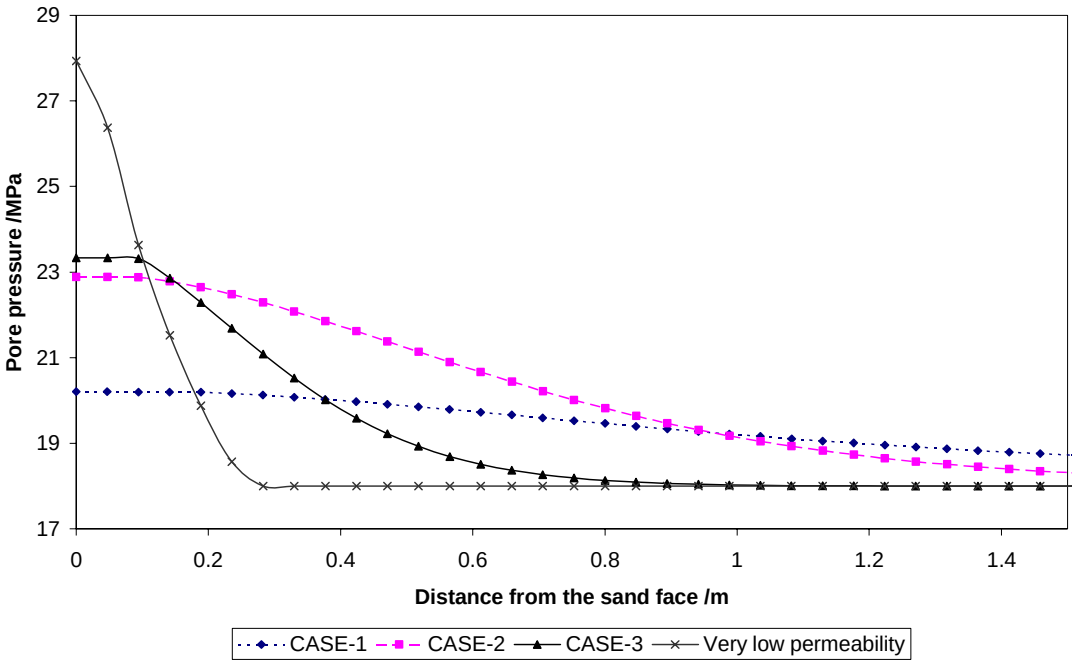

Figure 5.17 Pore pressure as a function of distance from the sand face in Cases-1 to 3 and a model considering formation with very low permeability (i.e., the model developed in previous chapter)

The maximum Von Mises stress generated in the casing during gas hydrate dissociation in Cases-1, 2 and 3 is 64.87, 64.83 and 64.80 MPa, respectively.

5.4 Discussion

It can be found from Figures 5.13 to 5.15 that the pore pressure builds up after hydrate dissociation but it decreases as fluids generated during hydrate dissociation flow away. The pore pressure profile resulting from hydrate dissociation depends on the permeability of the formation. Formations with low permeability have a narrow pore pressure profile while formations with high permeability have a wider pore pressure profile. In other words, the pore pressure build up due to hydrate dissociation in formations with low permeability is localized to the near wellbore region while in formations with high permeability the pore pressure build up zone covers larger areas than just the near wellbore region.

As mentioned before, less gas hydrate will dissociate behind the casing by decreasing the formation permeability as shown in Figure 5.16. It can be explained by the fact that, the fluids generated during gas hydrate dissociation in formations with low permeability increase the pore pressure and bring the thermodynamic conditions inside

the hydrate phase boundary. This means that less gas hydrate will dissociate as the generated fluids can not flow away from the wellbore region and the reverse is true when the formation permeability is high.

It can be found from Figure 5.17 that the pore pressure increase during gas hydrate dissociation is higher when the permeability of the formation is low. The figure shows that in formations with low permeability, the zone with increased pore pressure due to gas hydrate dissociation is limited to the area close to the near wellbore. In spite of this fact, the zone with increased pore pressure due to gas hydrate dissociation covers a larger area behind the casing in the formations with high permeability. This can be explained by the fact that the fluids generated during gas hydrate dissociation can flow away and increase the pore pressure of a larger area.

The low maximum Von Mises stress generated in the casing in the studied models can be explained by the fact that the mechanical degradation of hydrate bearing formations due to gas hydrate dissociation was not taken into account. To quantify mechanical degradation (for example, cohesion softening as a function of hydrate saturation), several triaxial experiments with different hydrate saturations are required. It is also required to further develop the model by taking into account the relation between mechanical degradation and hydrate saturation for different sediment mineralogies.

5.5 Summary

The numerical model that couples a well-proven thermodynamic PVT-Hydrate model (i.e., HWHYD) with ABAQUS was further developed with consideration to the kinetic of hydrate dissociation. The kinetics of hydrate dissociation was added to the model by considering the fluids generated during hydrate dissociation as a source term.

The mass balance equation used for fluid flow modelling in ABAQUS does not have a source term. As a result, there is a limitation for adding the kinetics of hydrate dissociation to the model (in order to relax the fixed pore pressure boundary conditions used in the previous chapter). It was shown that heat balance equation with conduction only is similar to the mass equation in fluid flow. As a result, a thermal model including a source term was used as analogue of the hydraulic model.

The developed model including the kinetics of hydrate dissociation was used to study the effects of formation permeability on pore pressure distribution resulting from the

hydrate dissociation. It was found that the magnitude of the pore pressure during gas hydrate dissociation in formations with high permeability is less than formations with low permeability. It was also found that the dissociated region behind the casing is higher in formations with high permeability than formations with low permeability. Furthermore, the results show that the area where the pore pressure has been increased due to gas hydrate dissociation, is larger in formations with high permeability than formations with low permeability.

5.6 References

5.1 H. C. Kim, P.R. Bishnoi, R.A.Heidemann, S.S.H.Rizvi, *Kinetics of gas hydrate decomposition,* Chemical Engineering Science, 42, 1645-1653, 1987

5.2 S. Gerami, M. Pooladi-Darvish, *Predicting gas generation by depressurization of gas hydrates where sharp-interface assumption is not valid,* Journal of Petroleum Science and Engineering, 56,146-164, 2007

5.3 N. Goel, M. Wiggins, S. Shah, *Analytical modeling of gas recovery from in sit hydrates dissociation,* Journal of Petroleum and Engineering, 29, 115-127, 2001

5.4 G. J. Moridis, *Numerical studies of gas production from methane hydrates,* SPE Gas Technology Symposium, Calgary, Canada, 2002

5.5 R. W. Lewis, P. N. Kankanhally, N. Seetharamu, *Fundamentals of the Finite Element Method for Heat and Fluid Flow*, Wiley, 2004

5.6 M. A. Aghighi, *Fully Coupled Fluid Flow and Geomechanics in the Study of Hydraulic Fracturing and Post-Fracture Production*, Petroleum Engineering, The University of New South Wales, Sydney, 2007

5.7 *ABAQUS User`s Manual, Version 6-7, Http://www.simulia.com/*

5.8 K. Nazirdoust, G. Ahmadi, *Computational modeling of methane hydrate dissociation in a sandstone core*, Chemical Engineering Science, 62, 6155-6177, 2007

5.9 Y.Masuda, Y.Fujinaga, S.Naganawa, K.Fujita, K.Sato, Y.Hayashi, *Modelling and experimental studies on dissociation of methane gas hydrates in berea sandstone cores*, Proceedings of Third International Conference on Gas Hydrates, USA, 1999

5.10 R. Freij-Ayoub, B. Clennell, B. Tohidi, J. Yang, R. Hutcheon, *Casing integrity in hydrate bearing sediments,* Offshore Site Investigation and Geotechnics, London, 2007

Chapter 6 – Experimental Study of the Potential of CO_2 Sealing for CO_2 Sequestration in Subsea Sediments

6-1 Introduction

Underground CO_2 storage offers interesting and potentially permanent or long-term environmentally safe possibilities. However, one of the main issues in underground CO_2 storage is the long term safety of the stored CO_2 with respect to potential leakage. Sudden release of large quantities of stored CO_2 could have a negative impact on marine environment as the leaked CO_2 could increase the acidity of the surrounding ocean. Therefore the selection of an appropriate reservoir or geological host formation is critical to ensure storage integrity and safety regarding CO_2 leaks into the ocean.

.As mentioned before, gas hydrates form over a limited pressure and temperature range (i.e., relatively high pressure and low temperature conditions). They are typically found in sediments within a few hundred meters of the seafloor, in water depths usually of greater than a few hundred meters, depending on bottom-water temperatures (Figures 1.2 to 1.4 refer to both methane and CO_2 phase boundaries and the Kvenvolden-style depth/temperature phase boundary in Chapter 1). This phenomenon could be an important factor for improving safety in long term storage of CO_2 in geological structures (e.g., depleted reservoirs, saline aquifers) beneath the GHSZ (Gas Hydrate Stability Zone). If any CO_2 leakage happens during long term storage through the cap rock of the geological structures, theoretically the CO_2 will move upward through pore space into GHSZ and form CO_2 hydrate. CO_2 hydrate is solid and immobile therefore the CO_2 hydrate formation process in the GHSZ traps leaked CO_2 in the form of CO_2 hydrate. In addition, CO_2 hydrate could clog the pore spaces of host formation results in decreasing the permeability of formation and over a long period of time (i.e., geological time scale) could form a CO_2 hydrate cap (i.e., secondary sealing layer) as shown in Figure 6.1.

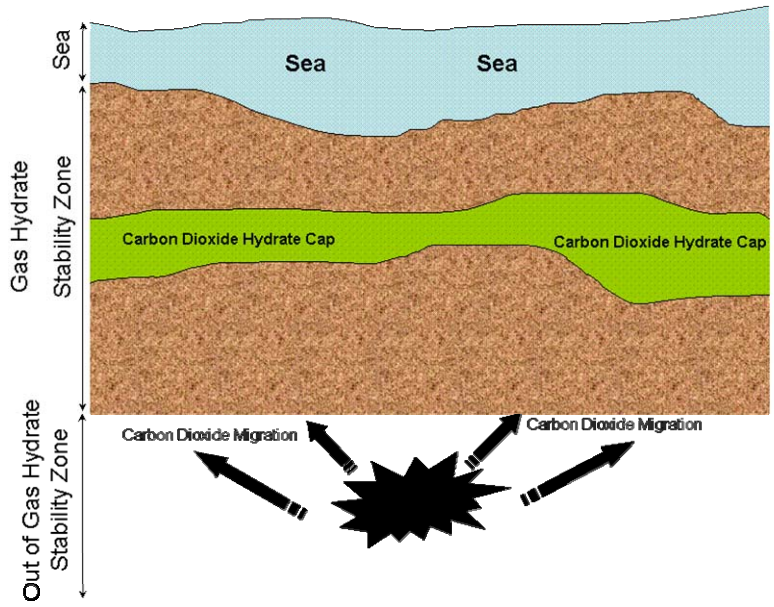

Figure 6.1 Formation of secondary CO_2 hydrate cap by migration of CO_2 into the GHSZ

In this study, the aim was to examine the effects of the GHSZ on the concentration of leaked CO_2 at seafloor (i.e., monitoring point). As a result, it was assumed that stored CO_2 in a geological structure beneath gas hydrate stability zone leaks through its cap rock and migrates upward to the GHSZ by diffusion and natural convection as shown in Figure 6.2.

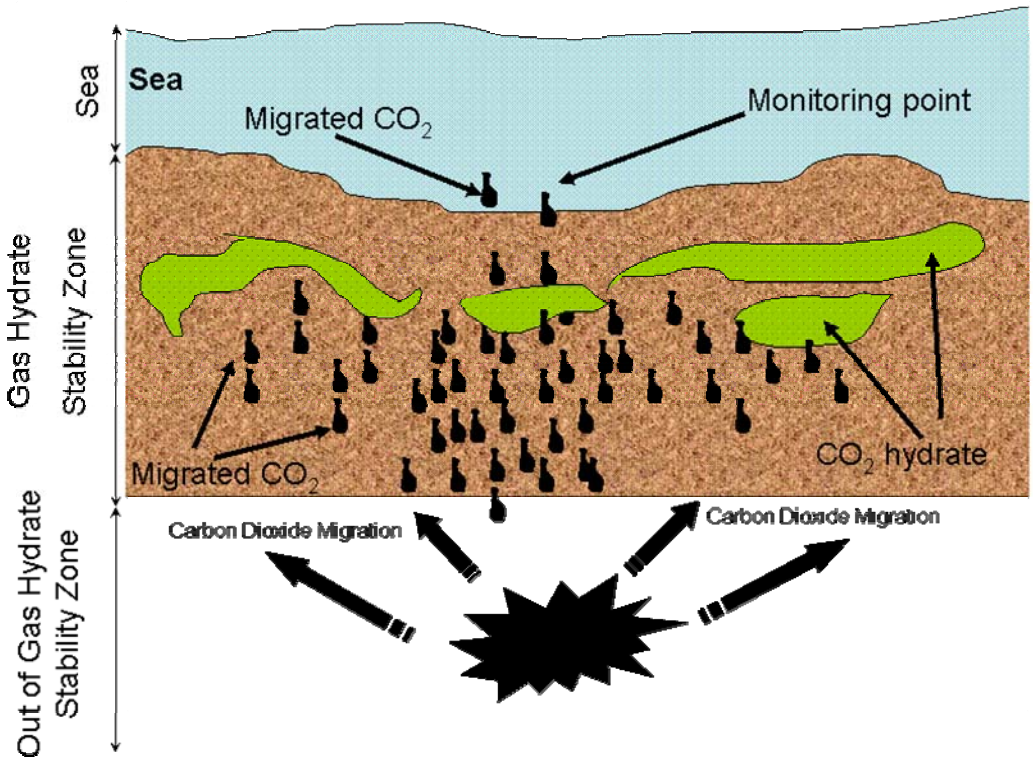

Figure 6.2 Migration of CO_2 into the GHSZ and forming CO_2 hydrate

Black spots in Figure 6.2 show leaked CO_2 migrating upward into the GHSZ and forming CO_2 hydrate marked with green colour. The concentration of CO_2 at a monitoring point (i.e., seafloor) was observed by taking samples. To simulate the process shown in Figure 6.2, a unique apparatus was built to study (i.e., simulate) CO_2 migration by diffusion and natural convection through GHSZ and CO_2 hydrate formation following CO_2 introduction from the bottom. The setup simulates seafloor conditions found in deep offshore environments. Several experiments were carried out with different sediments under seafloor conditions in deep water environments to examine the effects of the presence of GHSZ (i.e., CO_2 hydrate formation) on the concentration of CO_2 at a monitoring point (i.e., seafloor) as shown in Figure 6.2. The details of the setup and experiments are presented below.

6.2 Experimental Apparatus

All the experiments were conducted using the set-up developed at the Centre for Gas Hydrate Research at the Institute of Petroleum Engineering, Heriot-Watt University. Figure 6.3 shows the schematic of the set-up. It was built to mimic seafloor conditions in deep water offshore environments.

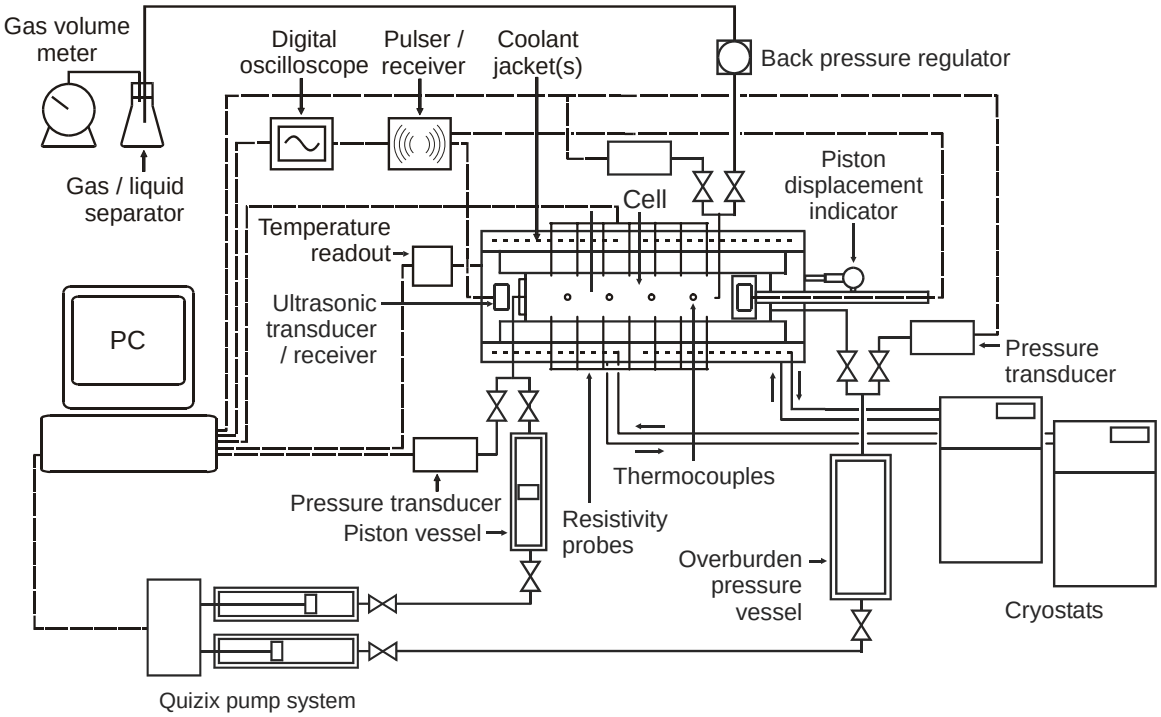

Figure 6.3 Schematic diagram of the developed set-up

It consists of a high-pressure stainless steel cylindrical cell and a feed system for CO_2 and water injection. The axial stress and pore fluid pressures are controlled independently with the aid of a piston assembly and quizix pumps. The pore pressure at the top and bottom of the cell is measured by pressure transducers. The overburden pressure is measured by the pressure transducer placed at the bottom of the cell. The pressure transducers were calibrated using a dead-weight-tester with an accuracy of $\pm$0.008 MPa in the range of 0 to 138 MPa. The temperature sensors placed inside of the cell are PRT (Platinum Resistance Thermometer) calibrated using a Prema Precise Temperature Metre over a range from 273.15 to 323.15 K.

The high-pressure cell is 500 mm in length and 75 mm in diameter and can work up to 40 MPa. It is surrounded by two cooling jackets connected to two separate temperature

control baths (bath No.1 and 2). The two cooling jackets are used to provide a thermal gradient in the cell, simulating the geothermal and hydrothermal gradients in deep offshore environments. In term of gas hydrate formation conditions, the thermal gradient divides subsea sedimentary formation into two zones. One zone dominating the upper part of the cell is set at lower temperature inside the gas hydrate stability zone so that CO_2 in the presence of water could form CO_2 hydrates. The other zone dominating the bottom of the cell is set at a higher temperature to represent conditions outside the gas hydrate stability zone. Using two separate cooling jackets and baths, it is therefore possible to simulate the conditions in seabed sediments, i.e., gas hydrate stability zone at the top of the cell and out of gas hydrate stability zone at the bottom of the cell. The temperature of the cooling baths can be kept stable within $\pm$ 0.05 K. One end of the cell is fitted with a movable piston for adjusting the overburden pressure. A LVDT (linear variable differential transformer) is fixed to the rod of the movable piston to measure the piston displacement. There are seven pairs of electrodes to measure the electrical resistivity across the sediment and also four temperature probes to measure the temperature gradient in the sediment.

In the original design, the electrodes and temperature probes were placed on the body of the cell as shown in Figure 6.4. In order to avoid electrical shortcut between the electrodes and the cell body, the internal surface of the cell was coated with a thin layer of special plastic insulation.

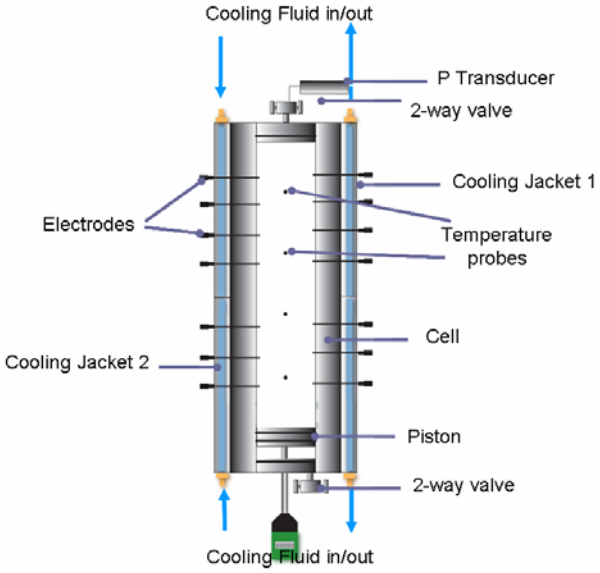

Figure 6.4 The original design of the set-up

The insulation layer was damaged after conducting a couple of experiments (i.e., Experiments 1 and 2). The recoating was a time consuming (i.e., 6 months) and costly process as it was required to send the cell to another company. As a result, the design of the setup was modified and all the sensors including the temperature probes and electrodes were mounted on the frame as shown in Figures 6.5 and 6.6. The frame was made of special plastic which was nonconductive and strong enough against certain axial stress.

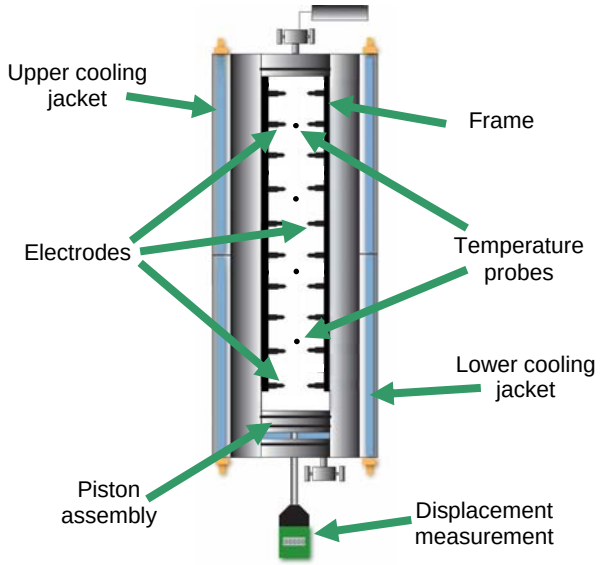

Figure 6.5 Schematic of the re-designed cell with a frame for mounting the sensors

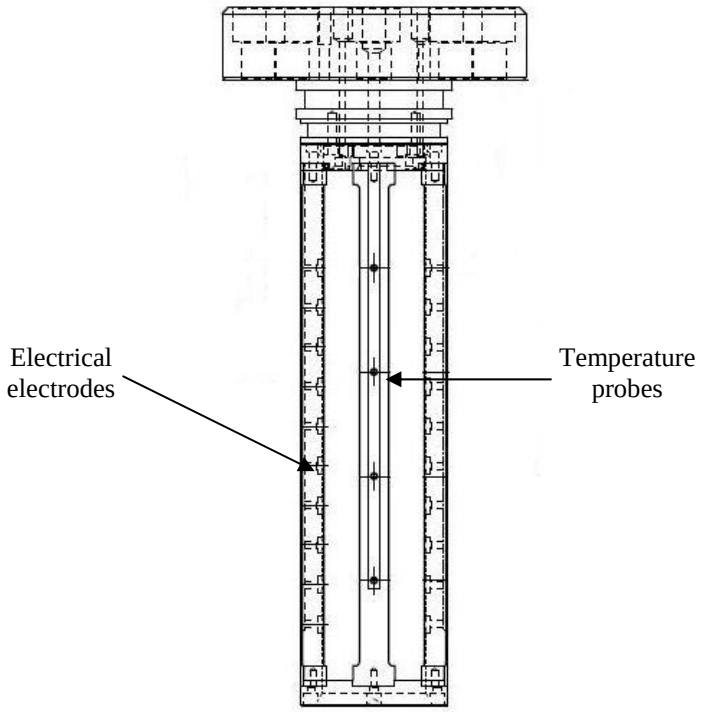

Figure 6.6 Detailed schematic of the frame with all sensors mounted

The results of resistivity measurements are not reported in this study as they still require further investigations.

6.3 Test Material

6.3.1 CO_2

The gas and liquid carbon dioxide for the experiments were obtained from Air Products PLC, with a certified purity 99.995 %.

6.3.2 Sand

The same sand was used in these experiments as described in Section 2.3.2.

6.3.3 Clay

One type of clay, (i.e., kaolinite) was used in the experiments.

6.4 Experimental Methodology

6.4.1 Sample preparation

The sensors frame was placed inside the cell, positioned vertically, and then the cell was filled with sediments. The sediment (i.e., sand) was poured into the cell until it was completely filled. The approximate weight of sediment required to fill the cell was kept constant for each type of sediment. After filling the cell with the sediments, vacuum was applied to the cell and then the data logging system was set to record. The sediments were completely saturated with water. The water injection process was stopped when the desired magnitude of pore and over burden pressures were reached. The pore pressure was kept constant around 6.89-7.24 MPa. The overburden pressure was limited to 7.24-7.58 MPa meaning the effective stress was 0.34-0.69 MPa. The presence of the frame inside the cell limited the magnitude of the applied effective axial stress (i.e., overburden pressure). If the applied axial stress was higher than the strength of the frame, it might deform or even damage the frame that was practically buried in the sediments. Throughout the experiments the effective axial stress was kept constant around 0.34-0.69 MPa. The temperatures in the cooling baths were set to have the required temperature distribution, as typically described in Section 6.4.2. It was assumed that stored CO_2 in an underground reservoir placed beneath GHSZ, leaks through the cap rock of the reservoir and moves upward by diffusion and natural convection. In these experiments therefore, CO_2 was introduced at the bottom of the cell and the bottom of the cell was exposed to the CO_2 reservoir throughout the experiments. Each experiment took a long time to be completed as diffusion and natural convection of CO_2 was a very slow process.

6.4.2 Thermodynamic conditions

The experiments were conducted under two different thermodynamic conditions.

Condition A

The temperatures of bath No 1 (to the upper part of the cell) and bath No 2 (to the lower part of the cell) were separately set to achieve the required thermal gradient along the core length. The thermodynamic conditions in both the upper and lower part of the cell were outside the hydrate stability zone as shown in Figure 6.7.

Condition B

In this condition, the temperature of bath No 1 and bath No 2 were set to have a similar thermal gradient profile along the core length to Condition A but with different temperature magnitudes. Using this thermodynamic condition, the upper part of the cell was set inside the hydrate stability zone (to simulate the GHSZ condition), while the lower part of the cell was outside the hydrate stability zone as shown in Figure 6.8.

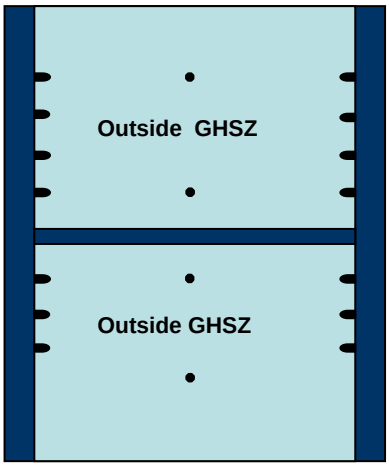

Figure 6.7 Schematic of Condition A

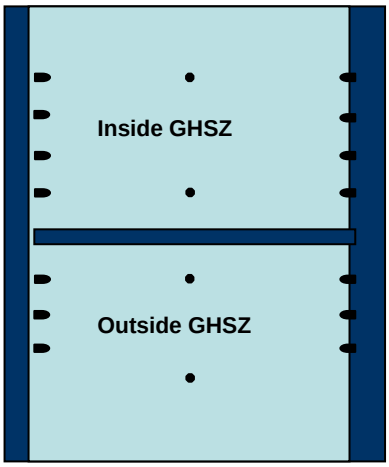

Figure 6.8 Schematic of Condition B

6.4.3 Sampling and analysis procedures

During the experiments, it was necessary to take a sample from the top of the cell to analyse the concentration of CO_2 in the pore fluid. The procedure of taking and analysing the sample is explained in this section.

Procedure for taking the sample

A piston vessel of 10 cm^3 volume was used for taking the sample from the cell. The piston inside the vessel divides it into two parts, as shown in Figure 6.9. One side of the piston vessel was attached to the top of the cell and the other side was attached to a Quizix pump.

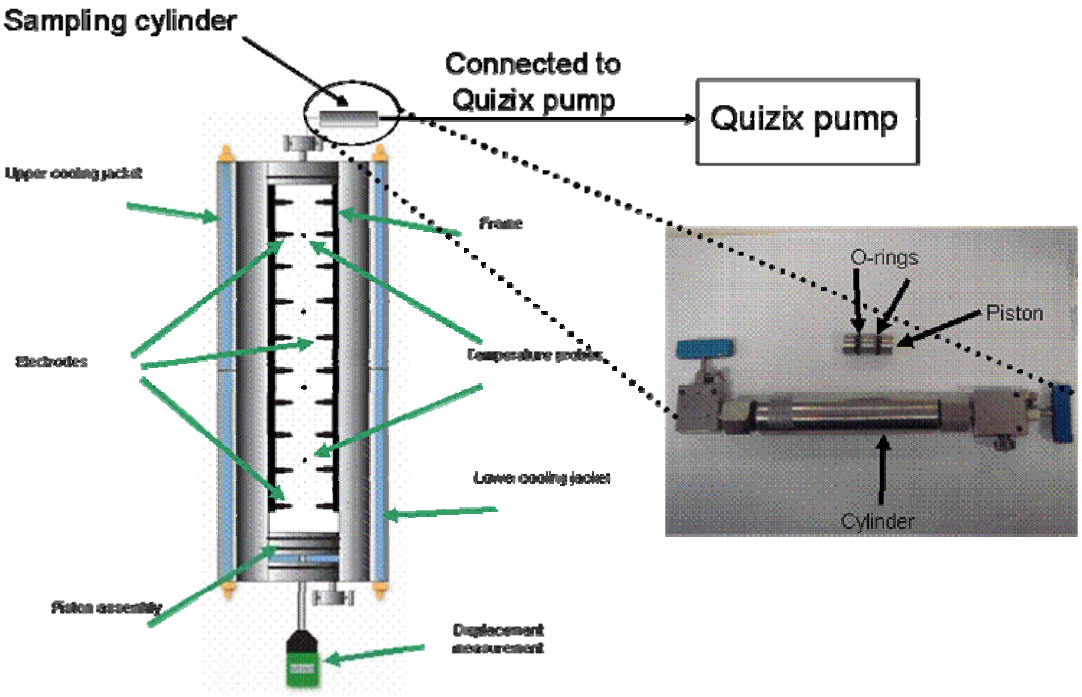

Figure 6.9 The schematic of the piston vessel

The side connected to the top of the cell, was pressurised to the pore pressure of the sediment inside the cell, by pumping water using the Quizix pump to the opposite side as shown in Figure 6.9. The cylinder was then opened to the cell fluid. After the pressure at both sides of the cylinder reached equilibrium, the water inside of the cylinder at the Quizix pump side was drained at a constant rate of 0.18 cm^3/min. The pore pressure in the cell was held constant by the continuing injection of CO_2 from the bottom of the cell as it was opened to the CO_2 reservoir. If the CO_2 was not injected from the bottom, the pore pressure might have dropped below the hydrate dissociation pressure. Approximately 5 cm^3 pore fluid was taken from the top of the cell under the pore pressure condition.

Analysis of samples

The analysis of fluid samples taken from the cell was conducted using a gas chromatograph (GC), VARIAN CP-3600, at the Centre for Gas Hydrate Research at the Institute of Petroleum Engineering, Heriot-Watt University. The GC was initially calibrated by injecting different solutions containing known amounts of CO_2 and water. The fluid samples were manually injected into the GC at a pressure that was similar to the pore pressure at which the fluid samples were taken. This was to ensure there was no CO_2 gas coming out from the liquid samples and forming gas-liquid phases.

6.5 Experiments

In order to examine the effect of the CO_2 state (liquid or gas) on the migration rate of CO_2 through the GHSZ, the first two experiments were conducted using gas and liquid CO_2 using the same sediments and under the same thermodynamic conditions. The changes in the CO_2 concentration at the top of the cell were monitored by taking samples.

Furthermore, several pairs of experiments were conducted under Condition A and Condition B. It meant that for each type of sediment two sets of experiments were conducted. One experiment was conducted under Condition A and the other one was conducted under Condition B. The results of these experiments were compared to examine the effect of CO_2 hydrate formation in the hydrate stability zone on the rate of CO_2 migration through GHSZ. In order to minimize the effects of other minerals on the results and to better understand the fundamental of the CO_2 migration through GHSZ, most of the experiments were conducted using sand.

Studies of natural gas hydrate sediments in deep offshore environments have shown that they are mainly found in sediments containing very fine grained sand with high clay content [6.1],[6.2]. In order to investigate the effect of sediments containing clay on the rate of CO_2 migration through the gas hydrate stability zone by diffusion and natural convection, two experiments were conducted using a mixture of sand and clay. Kaolinite was used in these experiments as clay.

In addition to the above experiments, a monitoring technique based on a two-tracer technique was investigated to detect hydrate formation/dissociation in GHSZ. The technique included two tracers; one hydrate former and one non-hydrate former. The

objective is to detect CO_2 hydrate formation (i.e., success in CO_2 trapping) and/or CO_2 leakage. If there is no sign of either of the two tracers, it means that CO_2 hydrates have provided an effective seal which can prevent any leakage. If tracers are detected with no change in the original ratio, this could mean that the injected CO_2 leaked and no CO_2 hydrate formed. If the relative concentration of non-hydrate forming compound is higher than that of the hydrate forming compound, this could mean the injected CO_2 is leaking to the monitoring point and CO_2 hydrate is also forming (which may provide a better seal in the future when pore space is filled with CO_2 hydrates) as shown in Figure 6.10. If only non-hydrate forming compound is leaking, this could mean that CO_2 hydrate formation is the main mechanism for CO_2 trapping as shown in Figure 6.11. If the ratio of hydrate forming tracer is higher than non-hydrate forming tracer, this could mean that CO_2 hydrates are dissociating. Prior to the application of the tracer technique to the CO_2 diffusion experiments, a few initial experiments were conducted to identify suitable tracers. A summary of the experimental parameters and conditions are presented in Table 6.1.

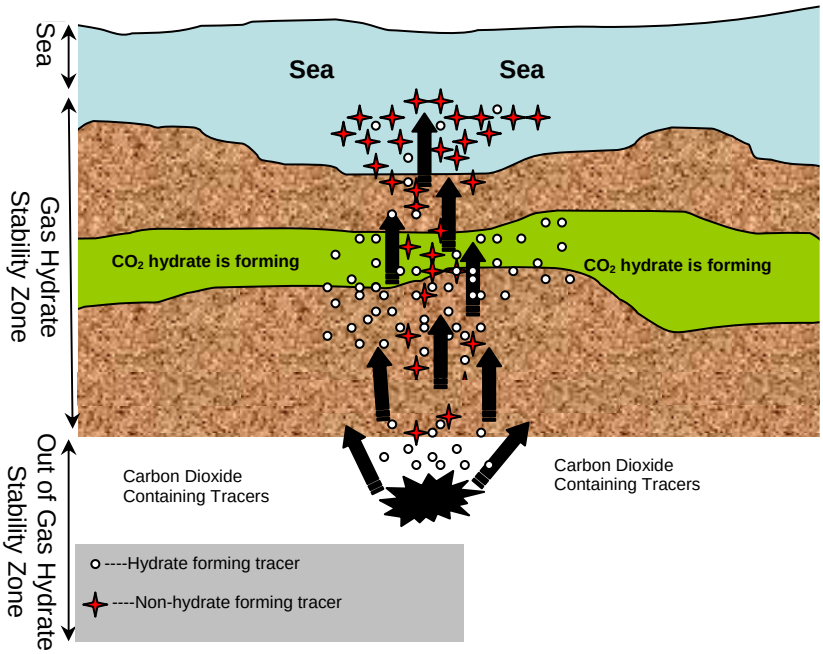

Figure 6.10 Schematic of a scenario where the relative concentration of non-hydrate forming tracer is higher than that of the hydrate forming tracer

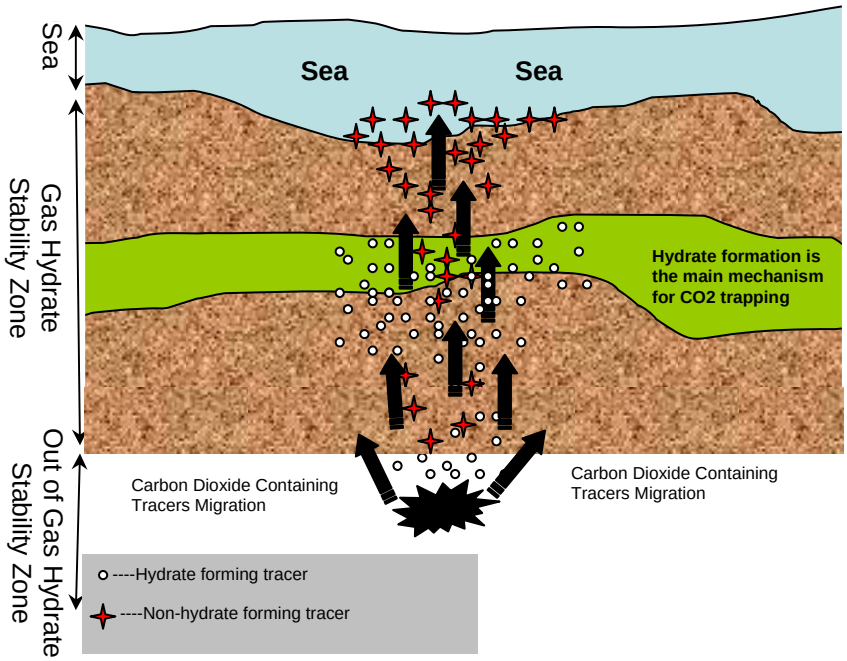

Figure 6.11 Schematic of a scenario where only non-hydrate forming tracer is leaking

Table 6.1 Summary of the experimental parameters and conditions

Experiment	Sediment	Pore pressure /MPa	Axial stress /MPa	CO_2 status	Experiment Condition	
1	Sand	6.89	7.28	Liquid	B	Inside GHSZ
2	Sand	4.7	4.88	Gas	B	Inside GHSZ
3	Sand	7.26	7.78	Liquid	A	Outside GHSZ
4	Sand	7.24	7.82	Liquid	B	Inside GHSZ
5	Sand	7.17	7.82	Liquid	B	Inside GHSZ
6	Sand+20% Clay	7.25	7.88	Liquid	A	Outside GHSZ
7	Sand+20% Clay	7.28	7.89	Liquid	B	Inside GHSZ
8	Sand	7.22	7.8	Liquid + Tracers	A	Outside GHSZ
9	Sand	7.13	7.6	Liquid + Tracers	B	Inside GHSZ

6.5.1 Experiments 1 and 2

Experiment 1 was conducted under Condition B and sand was used as the sediment. After charging sand into the cell, liquid CO_2 was introduced at the bottom of the cell and the pore pressure was kept constant at 6.89 MPa. The axial stress was 7.28 MPa. The experiment was conducted using the original design of the rig. Similar to Experiment 1, Experiment 2 was conducted under Condition B where the upper part of the cell was inside the GHSZ. Unlike the Experiment 1, gas CO_2 was introduced at the

bottom of the cell and the pore pressure was kept constant around 4.7 MPa. The axial stress was kept constant throughout the experiment at 4.88 MPa. This experiment like the previous one was conducted using the original design of the rig.

6.5.2 Experiments 3 and 4

Experiment 3 was conducted under Condition A where the upper part of the cell was out of the GHSZ. Liquid CO_2 was introduced at the bottom of the cell and the pore pressure was kept constant around 7.26 MPa. The axial stress was kept constant at 7.78 MPa. Like Experiment 3, Experiment 4 was conducted with sand but the thermodynamic condition was according to Condition B where the upper part of the cell was inside the GHSZ. The pore pressure and axial stress were 7.24 and 7.82 MPa, respectively, which were constant throughout the experiment.

6.5.3 Experiment 5

This experiment was exactly similar to that of Experiment 4. The aim was to check the repeatability of the CO_2 concentration at the top of the cell in Experiment 4. The axial stress and pore pressure were kept constant at 7.17 and 7.82 MPa, respectively.

6.5.4 Experiment 6 and 7

Experiment 6 was conducted with a mixture of sand and 20% kaolinite. The thermodynamic condition inside the cell was according to Condition A. The pore pressure and axial stress were kept constant at 7.25 and 7.88 MPa, respectively. Similar to Experiment 6, Experiment 7 was conducted with a mixture of sand and 20% kaolinite. The thermodynamic conditions inside the cell were according to Condition B where hydrate can form at the top of the cell. The pore pressure and axial stress were kept constant at 7.28 and 7.89 MPa, respectively.

6.5.5 Experiments with tracers

Von Stackelberg determined the relationship between the size of the guest molecule and the type of hydrate formed, as shown in Figure 6.12 [6.3].

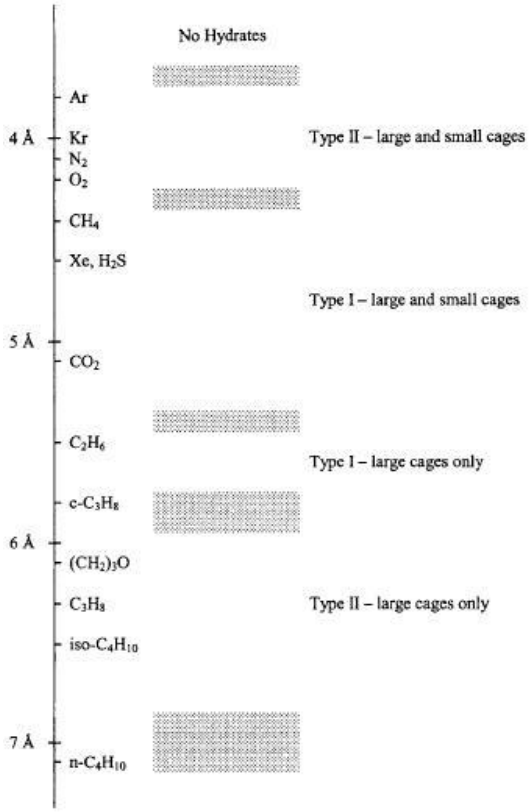

Figure 6.12 Relationship between guest molecule size and formed hydrate [6.3]

At the top of Figure 6.12 are small size guest molecules and the size of guest molecule increases as one goes downward on the figure. The small size guest molecules fill both small and large cages but the large guest molecule sizes fill large cages and mainly form structure II hydrates.

The hydrate forming tracer should form the same structure of hydrate that CO_2 forms. As shown in Figure 6.12, similar to CO_2, methane also forms structure I hydrates, therefore, methane could be a good candidate for hydrate forming tracer in this case. Argon can be a hydrate forming candidate as well since it fills only the small cages of structure II hydrates which are common in structure I and structure II hydrates. As a result, hydrate forming candidates can be either methane or argon.

Candidates for non hydrate forming in this case can be any component which cannot form hydrate. In addition to this fact the economical issue including the availability and price of the tracer needed to be taken into account as well. The non hydrate

forming tracer can be n-butane, as n-butane does not take part in hydrate formation of structure I dominated system as shown in Figure 6.12.

A gas Chromatograph (GC) technique was used to analysis the fluid samples taken from the top of the cell. It was found that the GC peak of argon coincided with the peak of dissolved nitrogen in the water and therefore it was very difficult to distinguish argon from nitrogen. As a result, methane and n-butane were selected as hydrate forming and non-hydrate forming tracers, respectively.

In order to examine the performance of methane and n-butane as tracers, an experiment was conducted using a kinetic rig developed at the Centre for Gas Hydrate Research at the Institute of Petroleum Engineering, Heriot-Watt University. The aim of this experiment was to check if methane and n-butane could be used in a desired two-tracer system, i.e., where the methane molecules could take part in forming CO_2-CH_4 mixed hydrate but the n-butane molecules are not.

The kinetic rig is made of an equilibrium cell surrounded by a cooling jacket to control the temperature inside the cell as shown in Figure 6.13. The cell itself is made of stainless steel with 500 cm^3 volume and can be pressurized up to 40 MPa. The temperature inside the cell can be controlled by circulating coolant through the cooling jacket using a cooling bath (i.e., GD 120 R series, Grant Instruments). The temperature can be monitored with ± 0.2 K using a PRT (Platinum Resistance Thermometer) temperature probe. The cell pressure can be measured using PDCR 4060 pressure transducer calibrated within an error range of ± 0.027 MPa. A magnetic stirrer is used to mix the test fluids inside the cell.

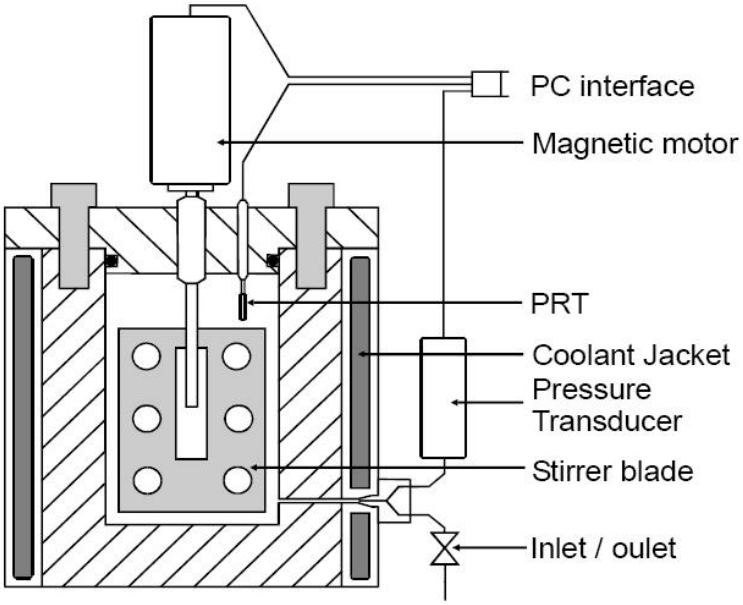

Figure 6.13 Schematic of the kinetic rig

The rig was first filled with 301 cm^3 water then equal amounts of methane and n-butane gas (i.e., 1 mol% each) were injected into the cell. The cell pressure was increased to 3.9 MPa by injecting CO_2 at 293.95 K. The stirrer was started to mix the system and speed up the dissolution of CO_2 in water. The cell temperature was cooled down to 274.45 K to form hydrate. The hydrate formation was manifested by sudden (and significant) pressure drop and a reduction in the stirrer's rpm which led to the final stoppage of the stirrer.

Finally, the formed hydrates were dissociated by step-heating and regular samples were taken from the cell to check the composition of the gas phase during hydrate dissociation as shown in Table 6.2 and Figure 6.14.

Table 6.2 Results of the tracer selection experiment

Variable	Sample-1	Sample-2	Sample-3	Sample-4	Sample-5	Sample-6
CO_2 / mol%	96.90	97.23	97.83	97.96	98.40	98.36
Methane / mol%	1.25	1.16	1.16	1.16	0.95	0.98
n-Butane / mol%	1.85	1.61	1.01	0.88	0.65	0.66
$\frac{\text{n - Butane}}{\text{Methane}}$	1.48	1.38	0.87	0.75	0.68	0.67
Temperature /K	274.45	275.95	279.35	280.05	293.55	293.75
Pressure /MPa	1.37	1.64	2.55	2.79	3.78	3.74

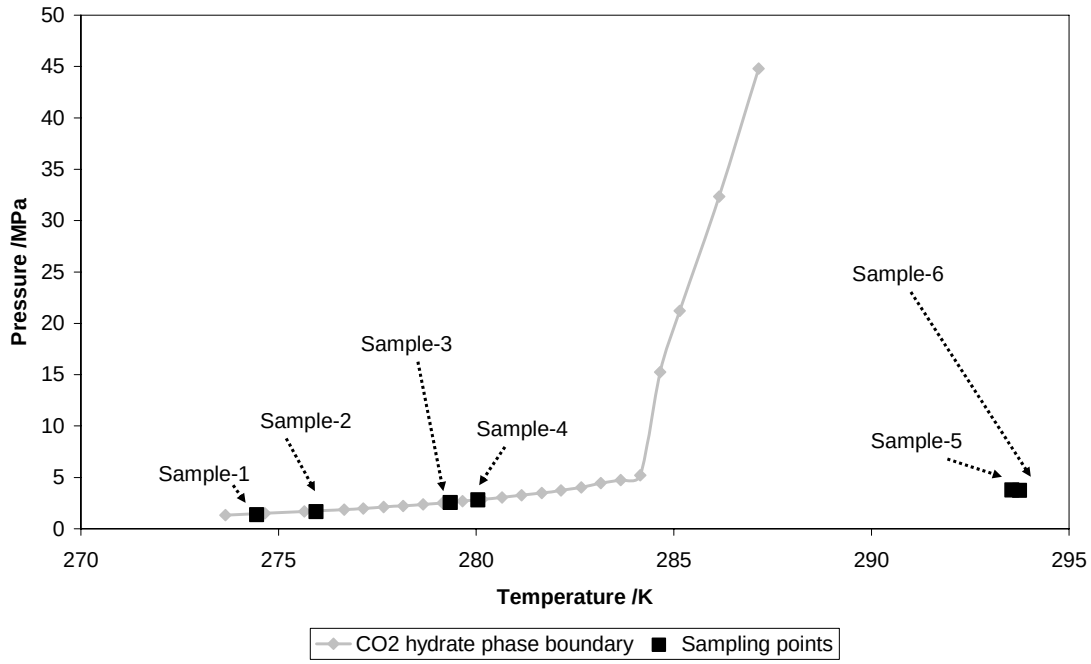

Figure 6.14 CO_2 hydrate phase boundary and sampling points

As shown in Table 6.2 the concentration of n-butane decreases during hydrate dissociation (which means that n-butane did not take part in the hydrate formation and the release of other gases dilutes the concentration of n-butane in the gas phase). In

contrast, the concentration of CO_2 increases and the concentration of methane remains relatively constant. The concentration of methane changes means that the methane is added to the system (from dissociating hydrates) otherwise its concentration would decrease as the concentration of the CO_2 is increasing due to the hydrate dissociation. In other word the decrease in the concentration of the n-butane means that its concentration remains with no noticeable changes during hydrate dissociation. Table 6.2 shows that the ratio of $\frac{\text{n - butane}}{\text{methane}}$ decreases during hydrate dissociation which means that the concentration of methane is increasing while the concentration of n-butane remains relatively constant.

In summary, the result of this experiment showed that CO_2 hydrate formation can be monitored by tracking the changes in the ratio of $\frac{\text{n - butane}}{\text{methane}}$.

Experiments 8 and 9

The sediment used in Experiment 8 was sand. The condition of the experiment was according to Condition A where hydrate can not form inside the cell. The liquid CO_2 was injected at the bottom of the cell containing 1 mol% methane and 1 mol% n-butane as tracers. The pore pressure and axial stress were kept constant at 7.22 and 7.8 MPa, respectively.

Like Experiment 8, Experiment 9 was conducted with sand but the thermodynamic condition was according to Condition B where hydrate can form at the top of the cell. The liquid CO_2 injected from the bottom of the cell contained 1 mol% of methane and 1 mol% of n-butane as the tracers. The pore pressure and axial stress were 7.13 and 7.6 MPa, respectively, which were constant throughout the experiment.

6.6 Results

6.6.1 CO_2 migration in Experiments 1 and 2

Figures 6.15 and 6.16 show the temperature distribution inside the cell in Experiments 1 and 2. It should be mentioned again that these two experiments were conducted with the original rig design therefore the positions of temperature probes (i.e., distance of temperature probes from the top of the cell) in the cell were different from the rest of

the experiments. The CO_2 concentration at the top of the cell in Experiments 1 and 2 are presented in Tables 6.3 and 6.4.

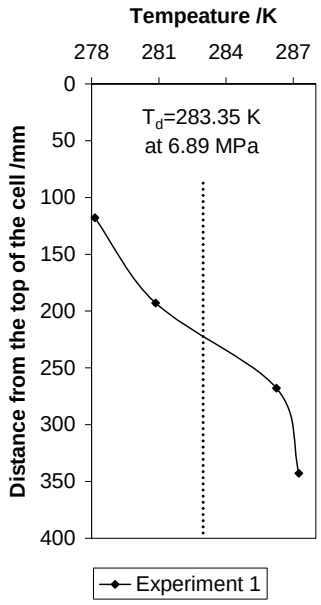

Figure 6.15 Temperature distribution in Experiment 1 (liquid CO_2)

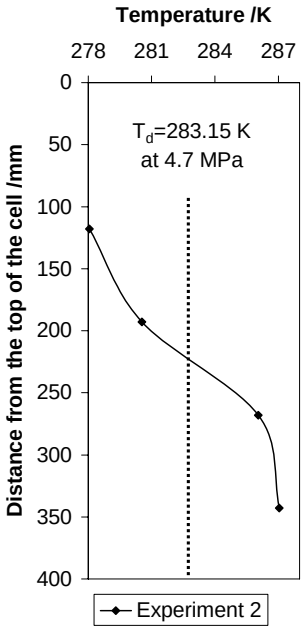

Figure 6.16 Temperature distribution in Experiment 2 (gaseous CO_2)

Table 6.3 CO_2 concentrations in Experiment 1 (liquid CO_2)

Time /hours	CO_2 concentration /mol%
0	0
21	0.028
69	0.031
169	0.03
238	0.028
358	0.04
406	0.136
478	0.249
574	0.316
645	0.361
741	0.415
790	0.471

Table 6.4 CO_2 concentrations in Experiment 2 (gaseous CO_2)

Time /hours	CO_2 concentration /mol%
0	0
23	0.00273
46	0.0212
142	0.0217
214	0.0219
286	0.44
311	0.49
382	0.53
483	0.57
623	0.75
816	0.78
892	0.82

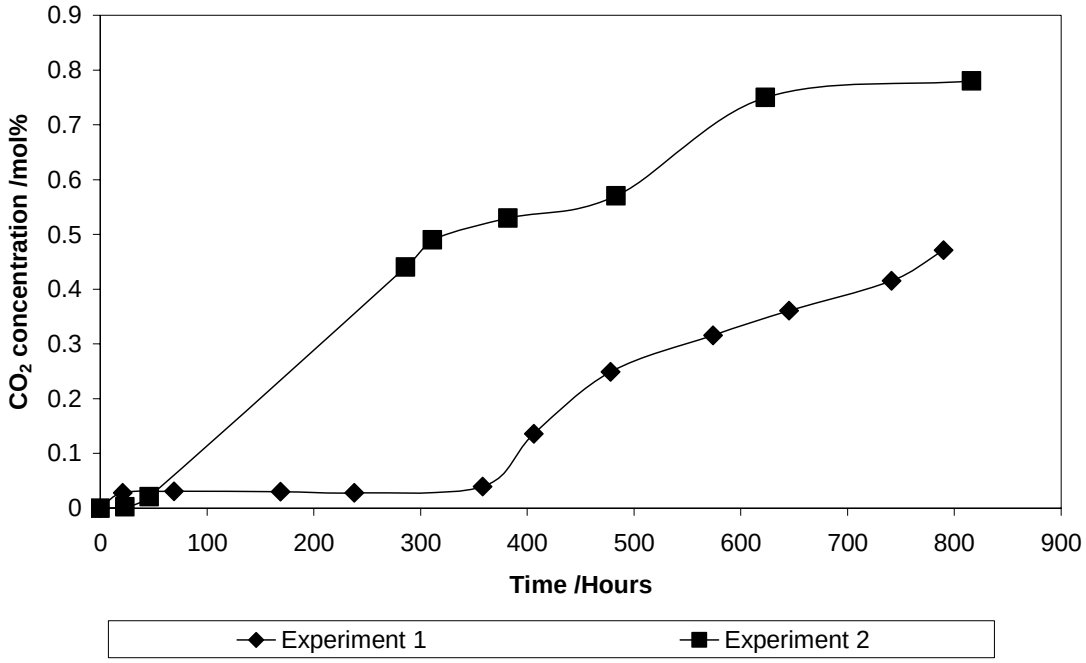

Figure 6.17 Concentration of CO_2 at the top of the cell in Experiments 1 and 2

Figure 6.17 shows the CO_2 concentration at the top of the cell versus time in Experiments 1 and 2. Although great care was taken to conduct these experiments under conditions in which CO_2 migrates through the GHSZ by diffusion and natural convection, it should be mentioned that the sampling process might cause slightly forced convection as the pore pressure was kept constant during sampling using the Quizix pump by injecting CO_2 at the bottom of the cell.

6.6.2 CO_2 migration in Experiments 3, 4, 6 and 7

Figures 6.18 to 6.21 show the temperature distributions inside the cell in Experiments 3, 4, 6 and 7. The CO_2 concentration in the samples taken from the top of the cell in Experiments 3 to 7 is shown in Table 6.5. It should be mentioned that the results presented in Table 6.5 are CO_2 concentrations in the first sample taken after CO_2 introduction at the bottom of the cell; therefore there were no forced convection at all.

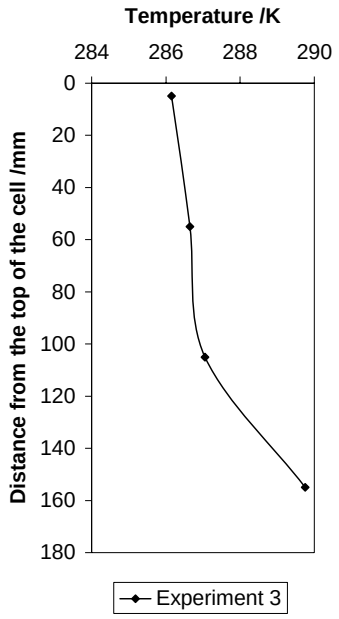

Figure 6.18 Temperature distribution in Experiment 3

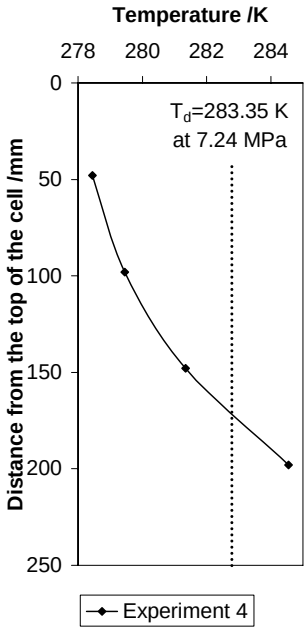

Figure 6.19 Temperature distribution in Experiment 4

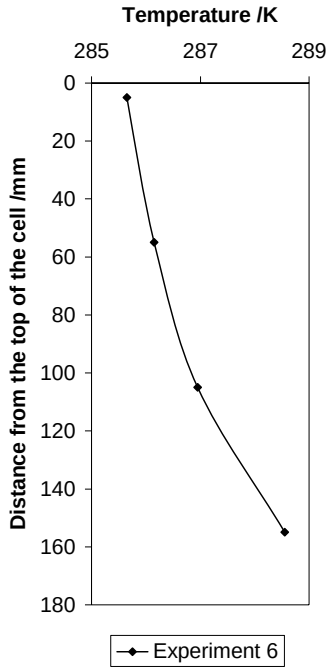

Figure 6.20 Temperature distribution in Experiment 6

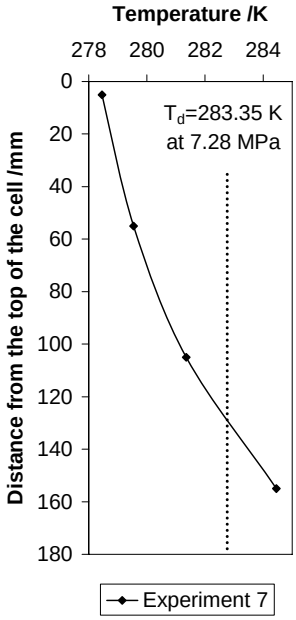

Figure 6.21 Temperature distribution in Experiment 7

Table 6.5 CO_2 concentration measured at the top of the cell

Experiment	Sediment	Thermodynamic condition	Time /hours	CO_2 /mol%	Average concentration over the time / $\frac{\text{mol\%}}{\text{day}}$
3	Sand	Outside GHSZ	175.5	26.3	3.60
4	Sand	Inside GHSZ	888	0.056	0.0015
5	Sand	Inside GHSZ	1205.5	0.084	0.0016
6	Sand+20% Clay	Outside GHSZ	506	0.16	0.0076
7	Sand+20% Clay	Inside GHSZ	1009	0.077	0.0018

As shown in Table 6.5 the presence of the GHSZ or CO_2 hydrate formation decreases the average concentration of CO_2 at the top of the cell in sediments containing sand or a mixture of sand and 20% clay significantly. This effect is stronger in sandy sediments particularly over short time periods. It is manifested by the fact that the ratio of the average concentration of CO_2 at the top of the cell, when thermodynamic conditions was outside GHSZ, over that when the thermodynamic conditions was inside GHSZ, in sediments containing sand is more than 2300 but in sediments containing a mixture of sand and clay it is 4. By comparing the results of Experiments 6 and 7, it is clear that the presence of clay in the sediments decreases the average concentration of CO_2 at the top of the cell but it seems that the combination of the clay and hydrate formation does not affect the average concentration of CO_2 at the top of the cell significantly at least over a short period of time (i.e., Experiments 4 and 7).

6.6.3 Effect of sampling

It was mentioned that during the sampling process the pore pressure was kept constant by injecting CO_2 at the bottom of the cell connected to the liquid CO_2 reservoir. This phenomenon could cause forced convection and affect the average concentration of CO_2 at the top of the cell in experiments in which the fluid samples were taken regularly at the top of the cell. In order to examine the effect of the sampling process on the average concentration of CO_2 at the top of the cell, the results of Experiment 1 were compared with the results of Experiments 4 and 5. It can be found that the

sampling process increased the average concentration of CO_2 from 0.0015-0.0016 $\frac{\text{mol\%}}{\text{day}}$ to 0.023 $\frac{\text{mol\%}}{\text{day}}$ (i.e., 14 times).

6.6.4 Experiments with tracers

Figures 6.22 to 6.23 show the temperature distribution inside the cell in Experiments 8 and 9. The concentrations of CO_2, methane and n-butane at the top of the cell in Experiments 8 and 9 are presented in Table 6.6 and 6.7. Experiment 8 was stopped after 770 hours when the CO_2 concentration at the top of the cell exceeded the solubility of CO_2 in water (1.8 mol%) [6.4] meaning that CO_2 is leaking.

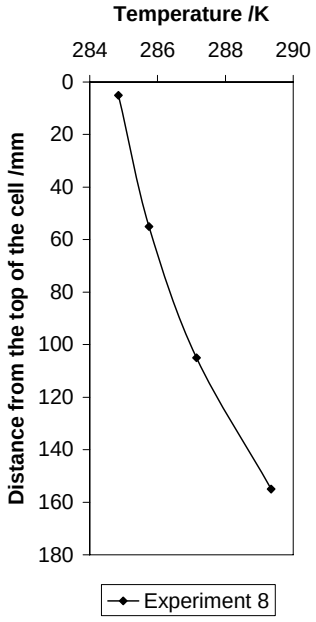

Figure 6.22 Temperature distributions in Experiment 8

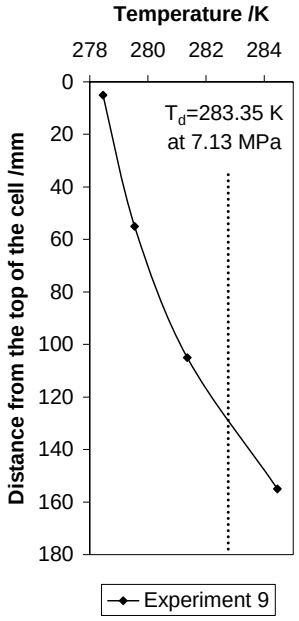

Figure 6.23 Temperature distributions in Experiment 9

Table 6.6 Concentrations of CO_2, methane and n-butane in Experiment 8

Time /hours	Methane /mol%	n-Butane /mol%	CO_2 /mol%	$\frac{\text{n - Butane}}{\text{Methane}}$
0	0.000960	0.0000	0.17	0.000
97	0.000000	0.0000	0.16	-
192	0.002700	0.0000	0.25	0.000
264	0.004800	0.0000	0.33	0.000
360	0.015000	0.0017	0.76	0.113
432.5	0.108000	0.0109	2.00	0.101
528	0.024000	0.0011	1.01	0.046
600	0.1095	0.00535	3.3	0.049
769.5	0.022150	0.0013	2.10	0.056

Table 6.7 Concentrations of CO_2, methane and n-butane in Experiment 9

Time /hours	Methane /mol%	n-Butane /mol%	CO_2 /mol%	$\frac{\text{n - Butane}}{\text{Methane}}$
0.0	0.0000	0.00000	0.000	-
40.5	0.0017	0.00000	0.170	0.0000
113.0	0.0025	0.00000	0.046	0.0000
280.5	0.0008	0.00000	0.096	0.0000
375.5	0.0041	0.00033	0.195	0.0793
544.5	0.0140	0.00110	0.565	0.0786
713.0	0.0145	0.00101	0.670	0.0697
1217.5	0.0450	0.00208	1.550	0.0462
1361.5	0.0625	0.00390	2.150	0.0624
1528.5	0.0395	0.00220	2.050	0.0557
1698.5	0.0291	0.00300	1.285	0.1033
1864.5	0.1010	0.02075	3.250	0.2054

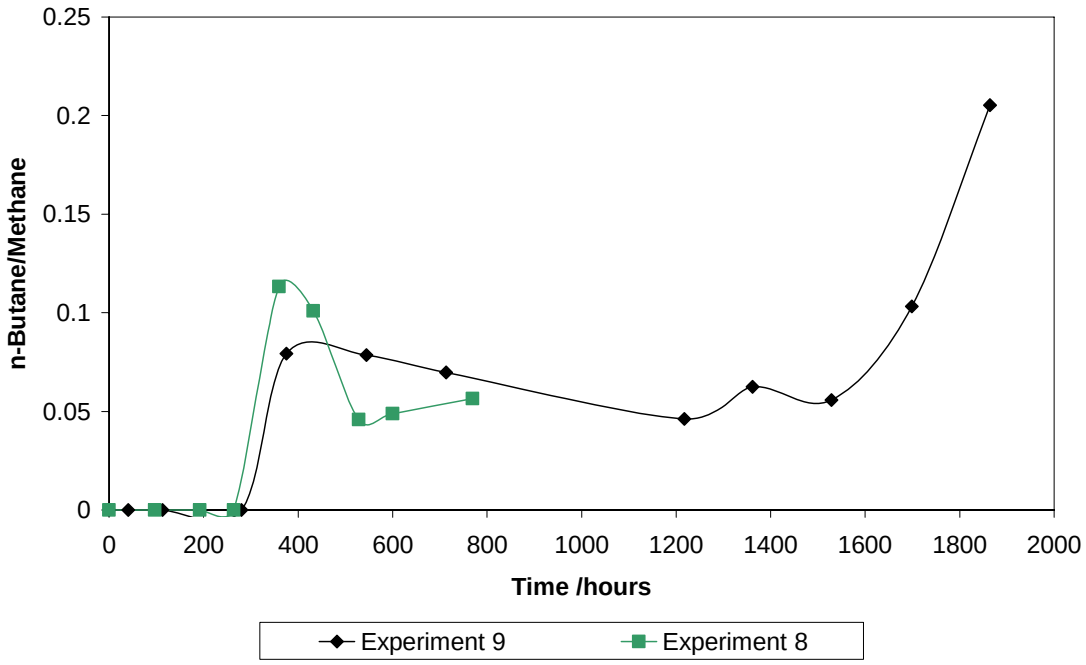

Figure 6.24 Ratio of $\frac{\text{n - butane}}{\text{methane}}$ versus time in Experiments 8 and 9

Figure 6.24 shows the ratio of $\frac{\text{n - butane}}{\text{methane}}$ in Experiments 8 and 9 versus time. As shown in the figure when the thermodynamic condition is not favourable for hydrate formation (i.e., Experiment 8), the ratio of $\frac{\text{n - butane}}{\text{methane}}$ is lower than that in Experiment 9 where the top part of the cell was inside the CO_2 GHSZ for more than 1000 hours. However there are some fluctuations in $\frac{\text{n - butane}}{\text{methane}}$ at the initial point of CO_2 introduction which can be related to the time that the components at the top of the cell need to reach equilibrium due to their different solubility in water during upward migration. The solubility of methane and n-butane in water at 285.15 K and different pressures is presented in Figure 6.25.

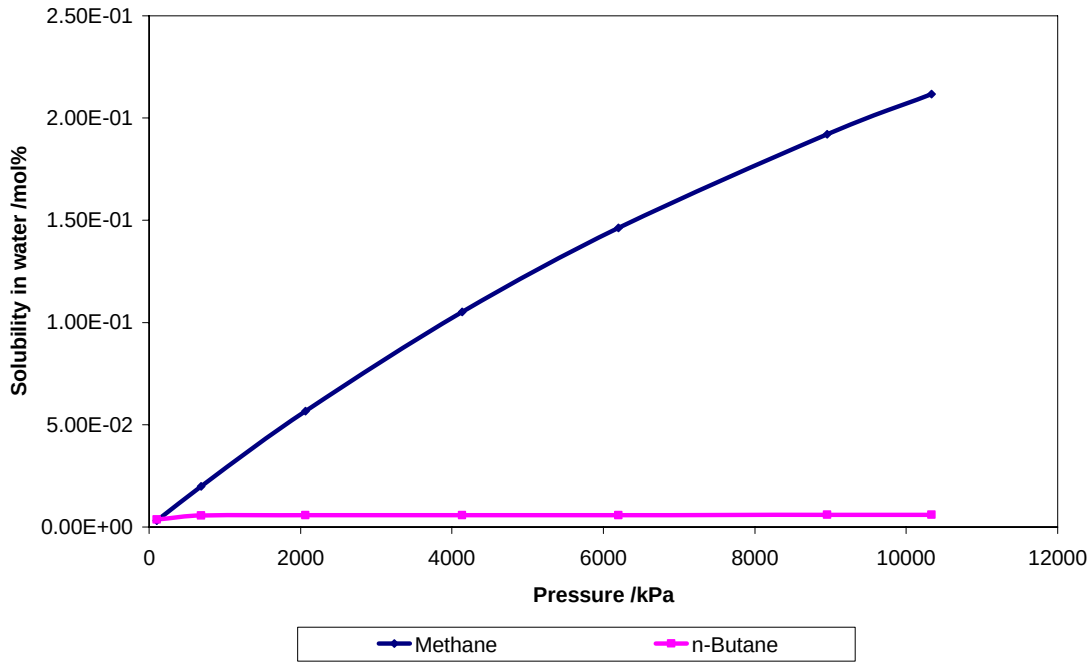

Figure 6.25 Solubility of methane and n-butane in water at 285.15 K [6.4]

The figure shows that the solubility of methane is significantly higher than that of n-butane. This fact may explain the initial fluctuations in the ratio of $\frac{\text{n - butane}}{\text{methane}}$ in Experiments 8 and 9 as the difference in the solubility of methane and n-butane in water, causes delay in the equilibrium of methane and n-butane at the top of the cell.

The ratio of $\frac{\text{n - butane}}{\text{methane}}$ in Experiment 9 where the top of the cell was inside GHSZ, fluctuates after CO_2 introduction at the bottom of the cell similar to Experiment 8. The ratio of $\frac{\text{n - butane}}{\text{methane}}$ then increases significantly, and this increase may suggest that methane along with CO_2 can be converted to a mixture hydrate at the top of the cell. However, further investigations are required to confirm these preliminary results and also to relate the changes of $\frac{\text{n - butane}}{\text{methane}}$ over the time to the amount of the hydrate formed at the top of the cell.

6.7 Discussion

As shown in Figure 6.17 the upward migration of CO_2 through GHSZ is slower when CO_2 is in the liquid state. This phenomenon can be related to the difference in the mobility of gaseous CO_2 and liquid CO_2 as the mobility of gaseous CO_2 is higher than liquid CO_2. Moreover, slower migration of liquid CO_2 in comparison with gaseous CO_2 through the GHSZ can be considered as a criterion for storing CO_2 in a geological reservoir under GHSZ. This is an additional benefit of storing CO_2 in the form of liquid added to the other benefits of storing CO_2 in this form.

Table 6.5 shows that CO_2 hydrate formation decreases the concentration of the CO_2 at the top of the cell (i.e., leaked CO_2 to ocean) significantly. As shown in the last column of the table, the average CO_2 concentration increase at the top of the cell for sand system is 3.6 $\frac{\text{mol\%}}{\text{day}}$ when the thermodynamic conditions are outside the GHSZ compared to 0.0015 $\frac{\text{mol\%}}{\text{day}}$ when the thermodynamic conditions are inside the GHSZ. The results presented in Table 6.5 also demonstrate the effect of sediment mineralogy on the rate of CO_2 leakage. As shown in the table, the presence of 20% clay has a significant impact on reducing the average rate of CO_2 leakage at least in the relatively short experimental time scale. The exact mechanism is not clear at this stage, but it could due to a reduction in relative permeability (it is referred to the ratio of effective

permeability of a particular fluid at a particular saturation to absolute permeability of that fluid at total saturation).

Table 6.5 also shows that a hydrate cap (i.e., secondary sealing layer), blocking the supply of CO_2 from below and preventing CO_2 leakage to seafloor as shown in Figure 6.1, can not form over a short period of time in laboratory surroundings (though the ultimate objective of preventing CO_2 leakage to ocean is achieved through hydrate formation and CO_2 trapping in solid hydrates). In other words, the formation of a synthetic physical barrier using CO_2 hydrate or an emergency synthetic CO_2 hydrate cap in the GHSZ, by introducing CO_2 to the GHSZ with diffusion and natural convection is not feasible over a short period of time. The reason might be the low saturation of CO_2 hydrate formed in the GHSZ over the shorten time. However, it is believed that within the geological timescale, the saturation of CO_2 hydrate in the sediments which are inside the GHSZ will increase and form a hydrate cap acting as a physical barrier which completely seals the leakage of CO_2 to the seafloor. The results of Table 6.5 can be used to identify suitable geological structures for CO_2 storage. For example CO_2 leakage to the seafloor in geological structures placed beneath the GHSZ containing clay is significantly low as the presence of clay and CO_2 hydrate formation reduces CO_2 leakage to the ocean.

The tracer technique could be used as an early warning system for CO_2 hydrate formation and/or CO_2 leakage. Changes in the ratio of non hydrate forming tracer over hydrate forming tracer at a monitoring point, is an indication of CO_2 hydrate formation. Significant increase in the ratio of non hydrate forming tracer over hydrate forming tracer means that CO_2 hydrate is forming. In addition the presence of either non-hydrate forming or hydrate forming tracer at the monitoring point means that stored CO_2 is leaking. This phenomenon could be useful in situations where the detection of leaked CO_2 is more difficult than the detection of non-hydrate or hydrate forming tracers.

There are also limitations in using a tracer technique considering methane and n-butane as hydrate forming and non-hydrate forming tracers respectively. Methane and n-butane are components that can be found with high concentration in depleted

hydrocarbon reservoirs placed beneath the GHSZ and as a result theses components can not be mixed with stored CO_2 as tracers.

6.8 Summary

In this chapter, several experiments were conducted to address the potential of CO_2 hydrates to act as a secondary seal in subsurface storage of CO_2 (e.g., depleted reservoirs, aquifers). The objective was to examine the potential of CO_2 hydrates and to prevent any CO_2 leakage to the environment, as well as to develop a tracer technique to monitor the safety of CO_2 hydrate trapping mechanism.

In order to address the above question, a unique apparatus was built to mimic the seabed conditions in deep offshore environments. The apparatus includes two cooling jackets connected to two separate temperature control baths in order to simulate the geothermal gradients in subsea sediments. The geothermal gradient results in an upper hydrate stability zone, followed with a deeper non-hydrate forming zone.

The experiments were conducted by introducing CO_2 at the bottom of the cell and monitoring the concentration of CO_2 along the length of the cell (by monitoring the changes in electrical resistivity) and at the top of the cell (by taking fluid samples). The experiments were conducted in pairs for each type of sediment. In other words, for each type of sediments, two experiments were conducted. In one experiment the thermodynamic conditions at the top of the cell were inside the GHSZ and in the other experiment the thermodynamic conditions in the entire cell were outside the GHSZ (while observing similar geothermal temperature gradient).

The results of the experiments showed that upward migration of liquid CO_2 through the GHSZ is slower than gaseous CO_2, which is an additional advantage to the storage of CO_2 in the liquid state in geological structures beneath GHSZ (rather than gaseous CO_2). The results of the experiments also showed that CO_2 hydrate formation decreases the concentration of the CO_2 at the top of the cell (i.e., leaked CO_2 to ocean) significantly.

The presence of clay in the sediments and its combination with CO_2 hydrate formation conditions did not reduce the average concentration of CO_2 at the top of the cell considerably in comparison with the results of sand sediments over short time periods.

A monitoring technique based on gas hydrate formation and two tracers was investigated to monitor the success of the CO_2 hydrate trapping mechanism in the GHSZ. Methane and n-butane were selected as hydrate forming and non-hydrate forming tracers, respectively. CO_2 containing 1 mol % of each tracer was injected at the bottom of the cell. It was found that this technique could be applicable for detecting CO_2 hydrate formation and CO_2 leakage based on the relative concentration of n-butane and methane. However further investigations are required to confirm the applicability of the two tracer technique.

6.9 References

6.1 A. M. Trehu, G. Bohrmann, M. E. Torres, F. S. Clowell, *Grain-Size and bulk and clay mineralogy of sediments from the summit and flanks of southern hydrate ridge, sites 1244-1250, ODP leg 204*, Proceeding of the Ocean Drilling Program

6.2 G. Ginsburg, V. Soloviev, T. Matveeva , I. Andreeva, *Sediment grain-size control on gas hydrate presence , sites 994 ,995 and 997*, Proceeding of the Ocean Drilling Program

6.3 J. Carroll, *Natural gas hydrates: A guide for engineers*, Elsevier Science and Technology, 2002

6.4 B. Tohidi, A. Danesh, A. C. Todd, *Modelling single and mixed electrolyte-solutions and its applications to gas hydrates,* Chemical Engineering Research & Design, 73, 464-472, 1995

Chapter 7: Conclusions and Recommendations for Further Work

Despite great interest in gas hydrate bearing sediments, their properties and roles in wellbore/casing integrity in deep offshore environments and CO_2 sequestration are still fairly unknown. In this study, a series of experiments were conducted to measure the geophysical and mechanical properties of gas hydrate-bearing sediments. These are new experiments in the composition of samples and experimental conditions. A new procedure is also used to develop a numerical model with ABAQUS to investigate the casing stability in` a wellbore drilled in gas hydrate bearing sediments in deep offshore environment. The model was further improved by considering the kinetics of hydrate dissociation, in order to remove the simplifying assumption in relation to very low permeability for gas hydrate bearing sediments.

A unique apparatus was built to study (i.e., simulate) CO_2 migration by diffusion and natural convection through GHSZ and CO_2 hydrate formation following CO_2 introduction from the bottom of the cell. The experiments were carried out with different sediments under seafloor conditions in deep water environments. The following sections summarise the findings/conclusions of this work:

7.1 Conclusions

1. The rate of applied load may alter the measured static uniaxial compaction modulus of sediments containing gas hydrate, the higher the rate of loading the higher the static uniaxial compaction modulus and vice versa. Therefore, it could be inferred that the properties of gas hydrate bearing sediments particularly mechanical and hydraulic properties are stress dependent. For example, the hydraulic properties of gas hydrate bearing sediments may change during methane gas production from natural gas hydrate reservoirs by reducing pore pressure resulting in an increase of effective stress.
2. Hydrate dissociation degrades the mechanical properties of gas hydrate bearing sediments significantly. The mechanical degradation of gas hydrate bearing sediments during gas hydrate dissociation was quantified as a function of temperature.
3. Sediments containing methane hydrate show deformation due to abrupt drops of stress during continuous compaction. The cause of the stress drops might be

described using the compaction theory because of the separation of hydrate particles from grains and the twisting of hydrate particles and grains into the available pore space. These results can be used to analyse the load carrying capacity of gas hydrate bearing sediments and the deformations caused by the weight of surface facilities placed on the seabed in deep offshore oil and gas operations. Surface facilities are placed on the seabed in deep offshore environments and work as a foundation for subsequent operations and therefore their stability over a long period of time are important in oil and gas operations.

4. It was shown that gas hydrates grow within pore space as described by the pore filling model at low gas hydrate saturation, although when gas hydrate saturation increases (i.e, > 50%) gas hydrates may form as described by the cementing model within pore space and cement sediments grain particularly in silt samples. A gas hydrate cementing model was manifested by a significant increase in sonic velocities. These results are important for the improvement of understanding the interactions of sediment grains and gas hydrate particles in pore scale and their effects on the mechanical and geophysical properties of gas hydrate bearing sediments.
5. It was also found that geophysical and mechanical properties of sediments containing gas hydrates are dependant not only on gas hydrate saturation but also the mineralogy of the host sediment.
6. A numerical model that couples HWHYD (i.e., a well-proven thermodynamic PVT-Hydrate model) with ABAQUS was developed. The model was used to investigate the effects of uniform and non-uniform loadings on the casing stability analysis of a wellbore drilled in gas hydrate bearing sediments. The results of the modelling confirm the common engineering sense of using cement with low thermal properties (i.e., low thermal conductivity and high heat capacity) in sediments containing gas hydrates. However, the results of modelling showed that the maximum Von Mises stress generated in an eccentric casing (i.e., non-uniform loading) with low thermal properties is higher than cement with high thermal properties (i.e., high thermal conductivity and low heat capacity) demonstrating the importance of the drilling and cementing operations in hydrate bearing sediments. It is therefore recommended to place enough centralizers on the casing during running it in gas hydrate bearing

sections to hold the casing at the centre of the wellbore when using cement with low thermal properties.

7. The numerical model was further improved by taking into account the kinetics of gas hydrate dissociation. The developed model was used to investigate the pore pressure distribution during gas hydrate dissociation considering the permeability of gas hydrate bearing sediments. It was found that the magnitude of pore pressure during gas hydrate dissociation in formations with high permeability is less than formations with low permeability and also found that the area where pore pressure has been increased due to gas hydrate dissociation is larger in formations with high permeability than formations with low permeability. The developed numerical model can be used to understand the behaviour of wellbores drilled in gas hydrate bearing sediments.
8. A unique experimental set-up was built to simulate pressure and temperature conditions in deep offshore environments. It simulates the gas hydrate stability zone and the zone where the thermodynamic conditions are outside the gas hydrate stability zone.
9. It can be inferred that the presence of GHSZ and CO_2 hydrate formation capture any leaked CO_2 and decrease the leakage rate of stored CO_2 in the geological structures beneath GHSZ into the ocean significantly, initially by forming CO_2 hydrates and trapping CO_2 in solid hydrate structure and later by forming a low permeability hydrate barrier region (preventing physically the leakage to the ocean). This means that CO_2 hydrate formation from leaked CO_2 by diffusion and natural convection in the sediments within GHSZ cannot provide a physical barrier in the short time. However, it is believed that in longer time periods, the formation of CO_2 hydrates in subsea sediments will form a secondary seal reducing the permeability of the hosted formation, in particular in sediments containing a high concentration of clay.
10. The results of this study can be used to identify suitable geological structures for CO_2 storage in offshore environments. As an example, geological structures placed beneath the GHSZ where formations contain clay are suitable for CO_2 sequestration. It was demonstrated throughout this study that if any CO_2 leaks from the geological structures, the presence of clay in combination of CO_2 hydrate formation will reduce CO_2 leakage to the ocean significantly.

11. A two-tracer technique was investigated to detect both CO_2 leakage from the underground structure and CO_2 hydrate formation. The established two-tracer system includes methane and n-butane. Methane and n-butane were selected as hydrate forming and non-hydrate forming tracers, respectively. The initial results of the experiments show that this technique seems to be applicable for detecting/monitoring CO_2 hydrate formation and CO_2 leakage by analysis of the relative concentration of n-butane and methane, although, its applicability and feasibility should be further investigated in the future.

7.2 Recommendations for further work

1. The confining stress can be controlled in the Triaxial set-up therefore, it is recommended that further experiments are conducted using the Triaxial set-up with wider range of gas hydrate saturation than this study to quantify the plasticity properties of gas hydrate bearing sediments and their mechanical degradation during gas hydrate dissociation. The results of experiments conducted with the Triaxial set-up can also be used for studying and quantifying the mechanical behaviour of sediments containing gas hydrate.
2. It is believed that hydraulic property of sediments containing gas hydrate not only depends on the hydrate saturation but also on the stress state. As a result, it is recommended that the hydraulic properties of sediments containing gas hydrate (i.e., permeability) using the Triaxial set-up at different stress state are measured.
3. It is suggested that:
    a. Experiments are conducted using the Triaxial setup on samples made with a mixture of silt and montmorillonite to understand dynamic bulk modulus increase as a function of temperature before the gas hydrate dissociation point.
    b. Experiments are conducted using the Triaxial setup on silt and sand samples containing low gas hydrate saturations in order to understand the difference between their dynamic bulk and shear and/or static bulk and shear modulus.

   c. Further experiments are conducted on silt and sand samples without gas hydrate in order to understand the difference between their dynamic bulk and shear modulus (i.e., the velocity of S-wave and P-wave).

4. It is recommended that:
   a. Experiments are conducted with samples containing gas hydrates to quantify sample deformation (i.e., subsidence) after gas hydrate dissociation by depressurisation.
   b. Experiments are conducted with samples containing gas hydrates and illite as a clay to understand the effects of clay minerals (i.e., montmorillonite, kaolinite and illite) on the behaviour of samples.
   c. Further experiments are conducted with higher concentrations of clay to investigate the effects of clay on the leakage rate of stored CO_2 into the ocean.
5. The results of the casing stability analysis in this study showed that the maximum Von Mises stress generated in the casing due to gas hydrate dissociation was less than the casing yield strength meaning that the casing was stable. However, the formation behind the casing may fracture due to pore pressure increase; as a result, the use of the developed numerical model to investigate the possibility of the formation fracture behind the casing is suggested.
6. The developed numerical model considers the fluids generated during gas hydrate dissociation as a single phase. It is recommended to develop the model further by considering multi phase flow in order to achieve more realistic pore pressure magnitude/distribution resulted from gas hydrate dissociation.
7. The thermal model does not consider the endothermic process of hydrate dissociation (i.e., absorbing heat during dissociation) therefore it is recommended to consider the endothermic process of hydrate dissociation in further development of the model.
8. Further studies are recommended to investigate the effects of low concentration of CO_2 and CO_2 hydrate on the electrical resistivity in the porous media. The results could be helpful to interpret and map the hydrate distribution inside the sediments using the measured electrical resistivities.
9. A monitoring technique based on the gas hydrate formation and a two-tracer technique was preliminarily investigated in this study. The results of this study

were the initial results, and therefore further experiments are recommended in order to prove the applicability of this technique and to investigate the effect of sediments mineralogy on the results, and also to examine other components as potential hydrate forming and non-hydrate forming tracers.